BULETINUL INSTITUTULUI POLITEHNIC DIN IAŞI

Publicat de
UNIVERSITATEA TEHNICĂ "GH.ASACHI", IAŞI

Tomul LIII (LVII)

Fasc. 2

Secția

ŞTIINȚA ŞI INGINERIA MATERIALELOR

2007

President of the Editorial Board of Bulletin of the Polytechnic Institute
Prof. dr. eng. Nicolae Badea, Technical University "Gh. Asachi" Iasi, Romania
Rector of Technical University "Gh. Asachi" of Iasi

Editor-in-Chief of Bulletin of the Polytechnic Institute
Prof. dr. eng. Ion Giurma, Technical University "Gh. Asachi" Iasi, Romania
Vice-Rector of Technical University "Gh. Asachi" of Iasi

Managing Editor of Bulletin of the Polytechnic Institute
Prof. dr. eng. Dan Galusca, Technical University "Gh. Asachi" Iasi, Romania
Dean of the Faculty of Materials Science and Engineering

Managing Editor of the MATERIALS SCIENCE AND ENGINEERING
Assoc. prof. dr. eng. Iulian Ionita, Technical University "Gh. Asachi" Iasi, Romania
Scientific secretary of the Faculty of Materials Science and Engineering

Editorial Board of the Section MATERIALS SCIENCE AND ENGINEERING
Prof. dr. eng. Yuri A. Burennikov, Vinnitsia State Technical University, Ukraine
Prof. dr. eng. Borivoje Miškovic, Yugoslav Association of Metallurgical Engineers, Belgrad, Serbia-Muntenegru
Prof. dr. eng. Paolo Nanni, Universitad egli Studi da Genova, Italy
Prof. dr. eng. Strul Moisa, Ben-Gurion University of the Negev, Beer-Sheva, Israel
Prof. dr. eng. Corneliu Munteanu, Technical University "Gh. Asachi" Iasi, Romania
Prof. dr. eng. Vasile Cojocaru-Filipiuc, Technical University "Gh. Asachi" Iasi, Romania
Prof. dr. eng. Constantin Baciu, Technical University "Gh. Asachi" Iasi, Romania
Prof. dr. eng. Luchian Zaharia, Technical University "Gh. Asachi" Iasi, Romania
Prof. dr. eng. Ioan Carcea, Technical University "Gh. Asachi" Iasi, Romania
Prof. dr. eng. Adrian Dima, Technical University "Gh. Asachi" Iasi, Romania
Prof. dr. eng. Ioan Alexandru, Technical University "Gh. Asachi" Iasi, Romania
Prof.dr.eng. Gelu Barbu, Technical University "Gh. Asachi" Iasi, Romania
Assoc. prof. dr. eng. Leandru Gheorghe Bujoreanu, Technical University "Gh. Asachi" Iasi, Romania
Assoc. prof. dr. eng. Ioan Rusu, Technical University "Gh. Asachi" Iasi, Romania
Assoc. prof. dr. eng. Gheorghe Badarau, Technical University "Gh. Asachi" Iasi, Romania
Assoc. prof. dr. eng. Petrica Vizureanu, Technical University "Gh. Asachi" Iasi, Romania

Editorial Secretary of the MATERIALS SCIENCE AND ENGINEERING
Assoc. prof. dr. eng. Gheorghe Badarau, Technical University "Gh. Asachi" Iasi, Romania

BULETINUL INSTITUTULUI POLITEHNIC DIN IAŞI
BULLETIN OF THE POLYTECHNIC INSTITUTE OF JASSY
Tomul LIII (LVII) 2007

MATERIALS SCIENCE AND ENGINEERING

CONTENTS

BULETINUL INSTITUTULUI POLITEHNIC DIN IAŞI
BULLETIN OF THE POLYTECHNIC INSTITUTE OF JASSY
Tomul LIII (LVII) 2007

ŞTIINȚA ŞI INGINERIA MATERIALELOR

CUPRINS

BULETINUL INSTITUTULUI POLITEHNIC DIN IAŞI
Tomul LIII (LVII), Fasc. 2, 2007
Secția
ŞTIINȚA ŞI INGINERIA MATERIALELOR

STUDIES CONCERNING THE INFLUENCE OF PRESSURE AND TEMPERATURE ON LUMINESCENCE DISCHARGE MECHANISM IN PLASMA NITRIDING

DAN GELU GĂLUŞCĂ, CARMEN NEJNERU, MIHAI AXINTE, GHEORGHE POPA

Abstract

The paper presents experimental studies that refer to the variation of specific power and of the cathode drop thickness function the cathode temperature and azote and hydrogen ratio in constant nitriding pressure of 5 mm Hg. It also presents experimental studies referring to the variation of cathode drop and the tension function the total pressure from the nitriding chamber and the ratio of the gases at 500 °C temperature.

Keywords: *ion nitriding, luminescent discharge,ionization process*

1. Introduction

The ionic nitriding bases on the principles of electric discharge in gases respectively the plasma state reached under certain pressure and temperature conditions.

The ionic nitriding realizes in abnormal luminescent discharge regime in a N_2 and H_2 atmosphere or in dissociated NH_3 to a pressure of 0,1…10 torr and when between the cathode, represented by the sample and the anode represented of the work chamber is applied o potential difference of 500…1000 V. From physical point of view, the electric discharges in thin gases imply three phenomena groups:

- the formation of charge carrier: electrons and positive ions;
- the movement of charge carrier in the electric field applied between the electrodes;
- the charge carrier neutralizing.

The primary ionization coefficient α is dependent on the pressure and the nature of the gas. The multiplication of the charge carrier through secondary processes at the electrodes is characterized through γ coefficient that gives indications referring to the number of electrodes emitted by the cathode through positive ions incidents firing, incident photons, rapid neutral atoms etc. The increase of the potential applied to the electrodes determines the amplification of ionization processes and the density of the current could increase until the limited value of impedance of the current supply.

2. Researches concerning the influence of the work conditions on the luminescent discharge mechanism in plasma nitriding

The luminescent discharge under normal regime presents different zones like cathode dark space, cathode light. The dimensions of the cathode dark space depend on the gas pressure, the chemical nature of the gases, the ration of the partial pressures

of the gases and the difference of applied potential. The correlations between the specific power P=UI/S, the thickness of the cathode fall d_c and the temperature of the T cathode are presented in the first figure.

The established correlations between the tension of cathode fall and the total pressure within the nitriding chamber are presented in the second figure.

Table 1

The variation of P [W/cm^2]								
T[°C] / 100%$P_{N2}/P_{N2}+P_{H2}$	400	420	440	460	480	500	520	540
0	3,54	3,83	4,16	4,58	4,91	5,33	5,71	6,00
20	3,08	3,46	3,75	4,16	4,58	4,87	5,33	5,87
40	2,63	2,91	3,16	3,51	3,86	4,30	4,80	5,30
50	2,43	2,71	2,96	3,34	3,67	4,16	4,54	5,12
60	2,51	2,87	3,12	3,46	3,62	3,92	4,37	4,88
80	2,08	2,38	2,54	2,79	3,04	3,33	3,54	3,83
100	2,21	2,42	2,67	2,88	3,17	3,51	3,75	4,08

Table 2

The variation of d_c [mm]								
T[°C] / 100%$P_{N2}/P_{N2}+P_{H2}$	400	420	440	460	480	500	520	540
0	4,4	4,4	4,25	4,4	4,5	4,45	4,6	4,6
20	3,01	3,02	3,05	3,1	3,1	3,1	3,3	3,3
40	2,7	2,7	2,85	2,85	2,9	2,9	3,0	3,0
50	1,95	2,0	2,1	2,05	2,2	2,25	2,22	2,3
60	2,3	2,3	2,4	2,35	2,43	2,5	2,5	2,6
80	1,7	1,7	1,7	1,7	1,9	1,85	1,88	1,85
100	1,45	1,5	1,5	1,52	1,6	1,6	1,65	1,65

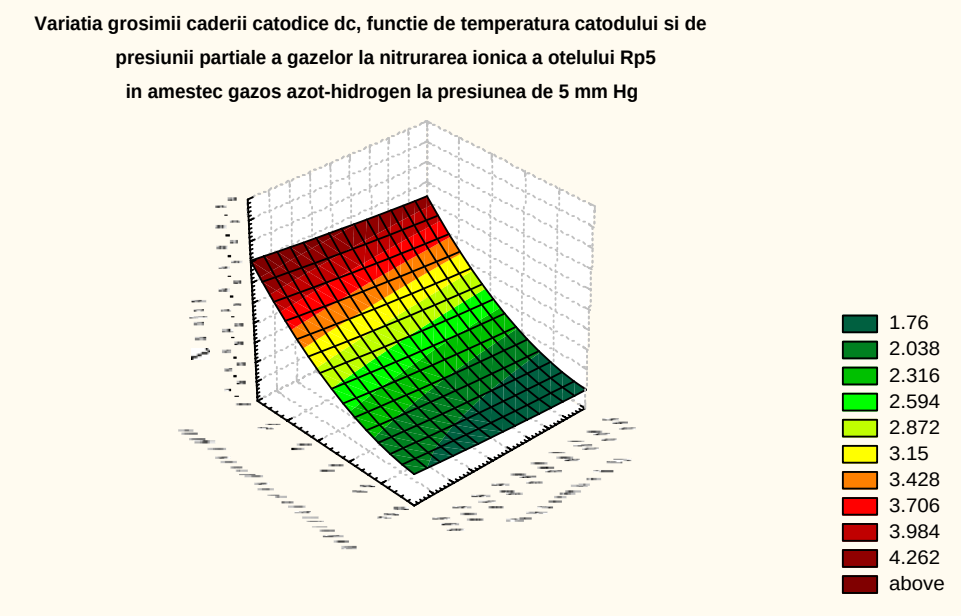

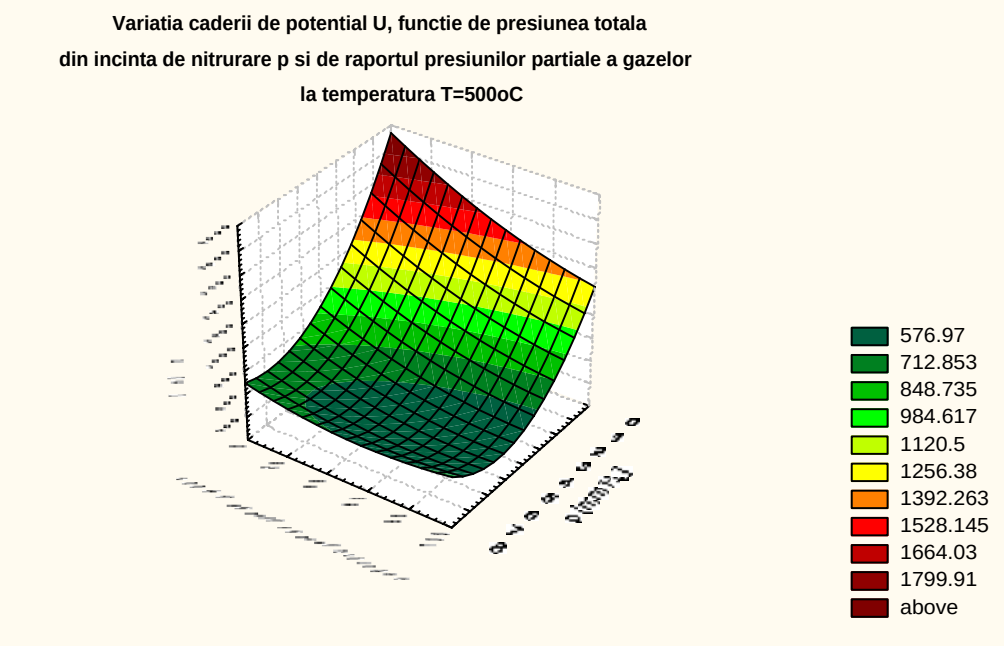

Table 3

The variation of P [W/cm^2]							
P [mmHg]	1	2	3	4	5	6	7
100%PN_2/PN_2+PH_2							
0	1588	1192	984	879	750	681	622
20	1574	1121	935	828	725	622	591
50	1276	892	691	578	523	493	469
60	1173	858	662	590	531	500	490
80	921	722	554	502	468	422	402
100	1053	782	614	540	510	505	492

Table 4

The variation of d_c [mm]							
P [mmHg]	1	2	3	4	5	6	7
100%PN_2/PN_2+PH_2							
0	10,4	6,3	4,8	3,9	2,6	2,05	1,8
20	7,3	4,6	3,4	2,6	1,9	1,82	1,78
50	5,8	3,05	2,05	1,65	1,3	1,15	1,12
60	4,9	2,92	1,9	1,42	1,3	1,1	1,08
80	3,2	1,6	1,57	1,45	1,37	1,18	1,16
100	4,0	2,2	1,8	1,4	1,38	1,16	1,14

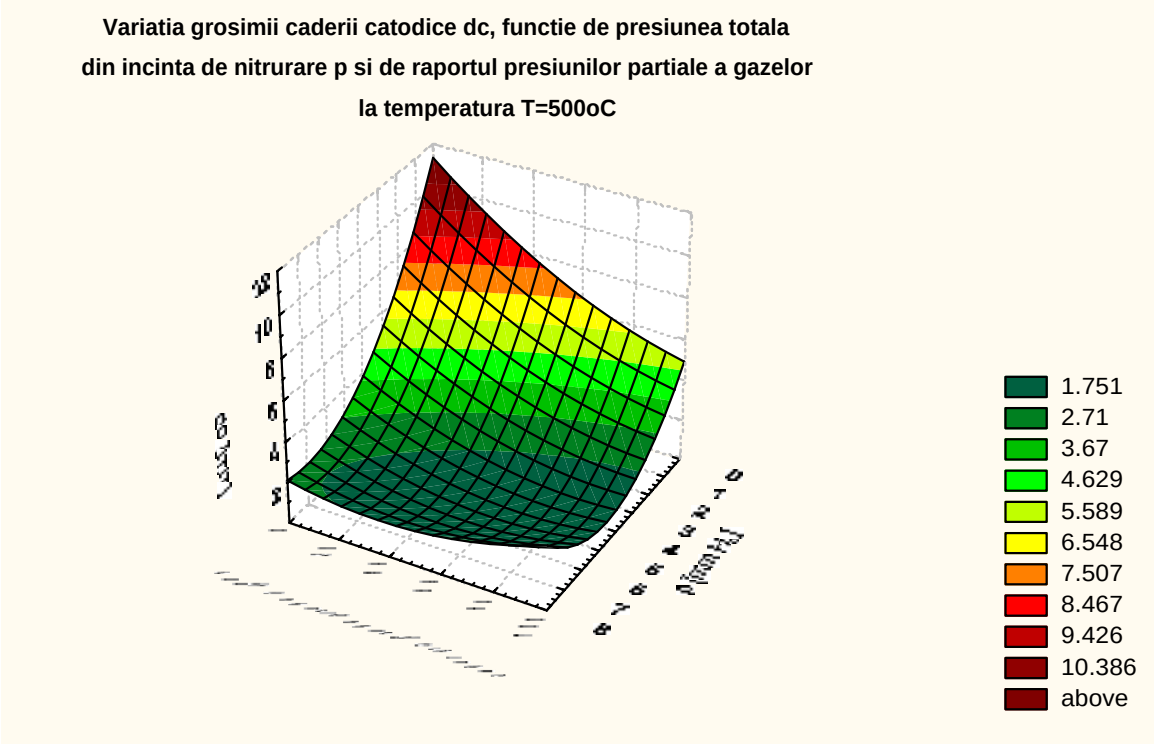

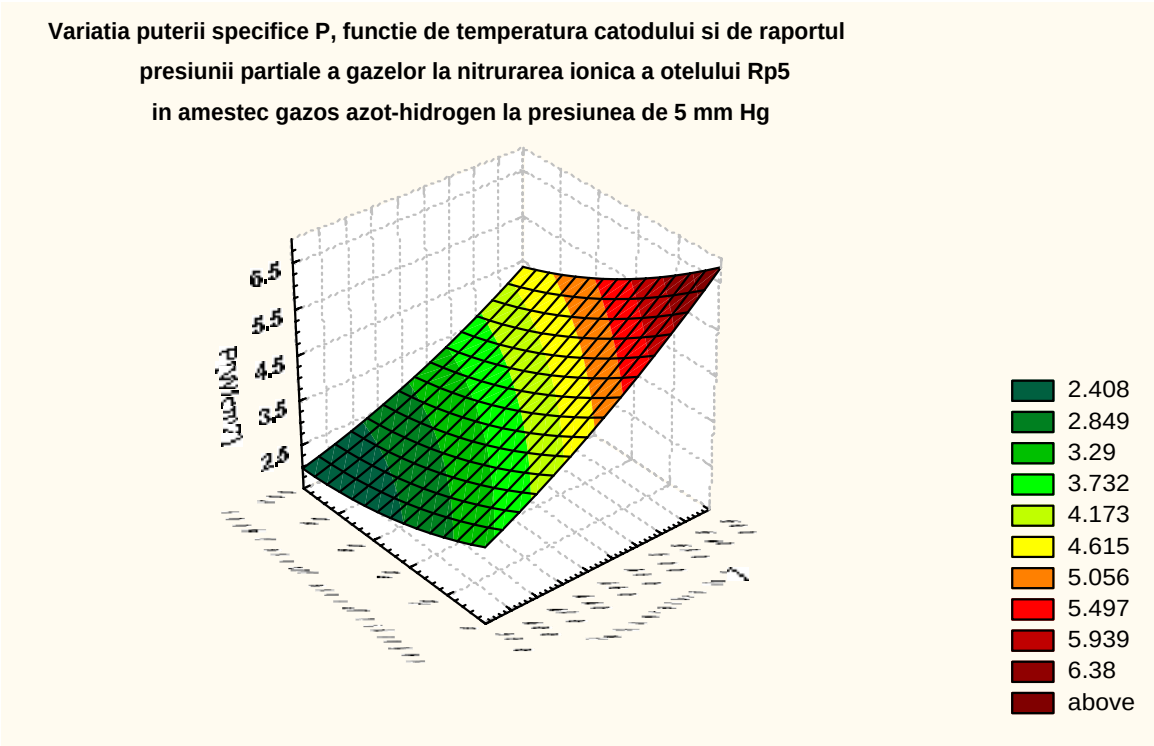

3. Conclusions

- the specific power increases with the temperature of the differential cathode based on the chemical composition of the gas;

- the increases of power specified in increase temperature are determined of the growth of temperature gradient and the increase of the radiated cathode power;

- the increases of specific power are almost linear;

- Hydrogen has a conductibility coefficient bigger than the azote and the gases put in hydrogen need specific powers bigger in order to reach the desired temperature comparing those which are enriched with azote;

- for pressures ratio $(P_{N2}/ P_{N2} + P_{H2})x100\% = 80\%$ it is obtained an imposed temperature at the cathode with a minimum power consumption;

- the thickness of the cathode fall is temperature independent but is gas nature dependent; the thickness of the cathode fall is smaller as the gaseous mixture is richer in azote;

- the discharge parameters are influenced by the chemical composition of the gas meaning that for electric discharges in gaseous mixture rich with hydrogen the formation stresses of the plasma and the thicknesses of the cathode falls are bigger;

- in order to obtain thin cathode falls, in ionic nitriding, of the tools executed from rapid steels and in order to obtain a minimum power consumption it must be worked with big pressures (P = 5...10 torr) and tensions of 500…600 V using a gaseous mixture rich in azote or dissociated ammonia.

References

1.**D.G.Găluşcă, A. Dima, R. Comăneci** – Nitrurarea ionică, Editura Sedcom Libris, Iaşi, 1997, ISBN 973-98187-0-6

Received March 15, 2007

Technical.University"Gh. Asachi", Iasi
University "A.I. Cuza", Iasi

STUDII PRIVIND INFLUENȚA PRESIUNII ŞI TEMPERATURII ASUPRA MECANISMULUI DESCĂRCĂRII LUMINISCENTE LA NITRURAREA ÎN PLASMĂ

(Rezumat)

Lucrearea prezintă studii experimentale referitoare la variația puterii specifice şi a grosimii căderii catodice funcție de temperatura catodului şi de raportul dintre azot şi hidrogen la presiunea constantă de nitrurare ionică de 5mm Hg, precum şi studii experimentale referitoare la variația căderii catodice şi a tensiunii, funcție de presiunea totală din incinta de nitrurare şi raportul gazelor la temperatura de 500°C.

BULETINUL INSTITUTULUI POLITEHNIC DIN IAŞI
Tomul LIII (LVII), Fasc. 2, 2007
Secția
ŞTIINȚA ŞI INGINERIA MATERIALELOR

OPTIMIZATION OF EAF'S TECHNOLOGICAL BLOWING PROCESS BY MODELLING

ADRIAN IOANA

Abstract

The liquid steel's quality is strongly influenced by the reactive power's blowing process in Electric Arc Furnaces (EAF). This is mainly reflected by: the gases' content decrease, advanced desulphuration, impurities' content decrease.

The paper presents the main steps of a power blowing process in the EAF modelation algorithm.

The conceived mathematical model has as a goal both determining oxygen's and sulphur's concentrations dependences on the blowing regime (based on modelating the weight transfer), and determining the velocity field and the system's turbulence characteristics.

Key Words: *EAF, Modelling, Blowing Process, Steel Quality, Weight Transfer, Velocity Field.*

1. INTRODUCTION

The mathematical model has the following goals:

A. Determining the dependence between oxygen and sulphur concentration and the blowing conditions on the basis of mass transferring modelling (with its diffusive and conductive elements).

B. Determining the speed area and the system's turbulence characteristic.

2. DESCRIBE OF ALGORITHM

The scheme of the system that blows the reactive powder into the liquid steel is presented in figure 1.

Figure 1. The scheme of the system that blows the reactive powder into liquid steel

1. Liquid steel area
2. Liquid slag area
3. Three-phased area

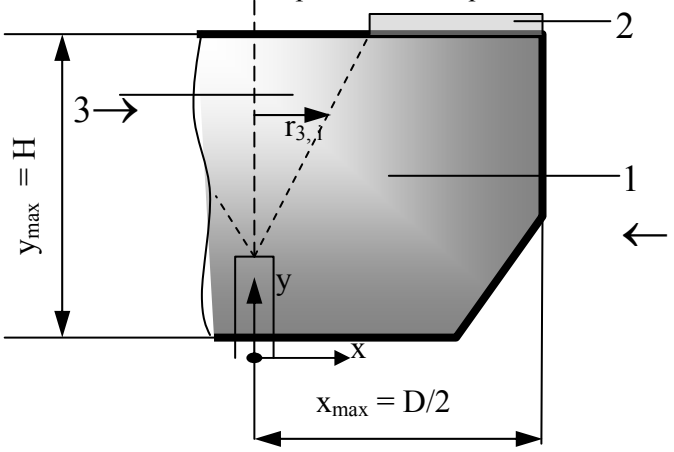

The three-phased area refer to: spurt of inert corrying gas (bubbles), solid particles (reactive powder) and liquid steel.

The modelling algorithm main stages are:

1. Continuity law: $$\frac{1}{x}\cdot\frac{\partial}{\partial x}\left(\rho_x\cdot v_x\right)+\frac{\partial}{\partial y}\left(\rho_y\cdot v_y\right)=0 \qquad (1)$$

Where: ρ_x, ρ_y – are the densities of the afferent environment of the area in the radial direction x, respective longitudinal y;

v_x, v_y – are the radial (in the x direction) and the longitudinal (in the y direction) components of the velocity.

Evidently:

- for $x > r_{3,i} \Rightarrow \rho = \rho_{steel}$ (2)
- for $x < r_{3,i} \Rightarrow \rho = d_f\,\rho_{gas} + (1 - d_f)\cdot\rho_{steel}$ (3)

Where d_f is the phases distribution parameter given by relation:

$$d_f = \frac{Q_{gaz}}{2\pi\cdot\int_o^x v_y dx} \qquad (4)$$

Where Q_{gaz} is the blowed rare gas flow (m^3/h)

2. The movement low in the radial direction x:

$$\frac{1}{x}\cdot\frac{\partial}{\partial x}\left(\rho\cdot x\cdot v_x^2\right)+\frac{\partial}{\partial y}\left(\rho\cdot v_x\cdot v_y\right)=\frac{1}{x}\cdot\frac{\partial}{\partial x}\left[x\cdot\mu_{ef}\,\frac{\partial v_x}{\partial x}\right]+ + \frac{\partial}{\partial y}\left[\mu_{ef}\,\frac{\partial v_x}{\partial y}\right]-\frac{\mu_{ef}\cdot v_x}{x^2} \qquad (5)$$

Where μ_{ef} – is the real viscosity, witch is calculated with:

$$\mu_{ef} = \mu_m + \mu_t \qquad (6)$$

In which: μ_m – is the molecular viscosity;

μ_t – is the turbulent viscosity.

The turbulent viscosity can be calculated on the basis of the model:

$$\mu_t = \frac{K}{\sqrt{W}} \qquad (7)$$

Where: K is the kinetic turbulent energy of the fluid; W is the frequency of the turbulent fluctuation.

3. The movement law in y direction

$$\frac{1}{x}\cdot\frac{\partial}{\partial x}\left(\rho_x\cdot v_x\cdot v_y\right)+\frac{\partial}{\partial y}\left(\rho\cdot v_y\right)=\frac{1}{x}\cdot\frac{\partial}{\partial x}\left[x\cdot\mu_{ef}\,\frac{\partial v_y}{\partial x}\right]+ + \frac{\partial}{\partial y}\left[\mu_{ef}\,\frac{\partial v_y}{\partial y}\right]+\rho\cdot g \qquad (8)$$

Where "g" is the gravity acceleration.

4. Determining the speed potential's transport law p_v :

$$x^2 \cdot \left[\frac{\partial}{\partial y}\left(\frac{p_v}{x} \cdot \frac{\partial f_c}{\partial x} \right) - \frac{\partial}{\partial x}\left(\frac{p_v}{x} \cdot \frac{\partial f_c}{\partial y} \right) \right] - \\ - \left[\frac{\partial}{\partial y}\left(x^3 \frac{\partial}{\partial y}\left(\mu_{ef} \frac{p_v}{x} \right) \right) + \frac{\partial}{\partial x}\left(x^3 \frac{\partial}{\partial y}\left(\mu_{ef} \frac{p_v}{x} \right) \right) \right] = 0 \qquad (9)$$

5. Determining the current correlation:

$$\frac{\partial}{\partial y}\left[\frac{1}{\rho x} \cdot \frac{\partial f_c}{\partial y} \right] + \frac{\partial}{\partial y}\left[\frac{1}{\rho x} \frac{\partial f_c}{\partial x} \right] + p_v = 0 \qquad (10)$$

6. In the system formed by (9) and (10) correlation, by imposing the constraints specific for the blowing of reactive powder into the liquid steel (on basis of inert gas), the following should be determined:

6.1. The distribution of the speed's components in the two analysed directions: radial (x) and longitudinal (y), (m/s).
6.2. The distribution of the current lines, (kg/s).
6.3. The distribution of the turbulent function, (1/s).
6.4. The distribution of the effective viscosity, (kg/m.s).

7. Determining the oxygen and sulphur law of diffusion within the system.

$$\frac{\partial C}{\partial t} + v_x \frac{\partial C}{\partial x} + v_y \frac{\partial C}{\partial y} = D_t \cdot \left[\frac{\partial^2 C}{\partial y^2} + \frac{1}{x} \cdot \frac{\partial}{\partial x}\left(x \frac{\partial C}{\partial x} \right) \right] + P \qquad (11)$$

Where C is the concentration; D_t is the diffusivity in the state of turbulent movement ($D_t = \rho / \mu_t$); P is the steel's of purity (expressed by the specific dezoxidation of the liquid steel's volume unit or the specific desulphuration).

3. RESULTS OF THE MATHEMATICAL MODELLING AND CONCLUSION

The simulation of the process of blowing reactive powder in liquid steel was made in the following conditions:

- a 50 t recipient;
- brant: non-alloyed steel (OL37);
- the blowing deepness (penetration): 2000 mm from the basic level of the steel;
- the diameter of the blowing tube: 20 mm;
- the debit of the gas (Ar);
- the mass debit of the powder;
- the CaSi composition;
- the CaSi granulation;
- the duration of the process: 15 min.

The hydrodynamic behaviour of the liquid steel and slag, under the influence of the argon and CaSi powder spurt, can be characterized, on the basis of the analyse of the results obtained after applying MIP, leads to the following conclusions:

- The phenomenon of transport on radial direction are emphasized in the superior area of the recipient, which is suggested by the higher values of the speed component on this direction: v_x = 0,4-0,6 cm/s. In this way, favourable conditions are settled for a good fluid shuffle.
- Assuring a relatively high value of the longitudinal component of the velocity in a sensitive size area: v_y = 1,2-2,5 cm/s, which lead's to good steel's recycling.
- The resulting velocities' field (v) assures maintaining continuous injected fluids (argon and Ca vapours) and the reaction products' accelerating. Creating and maintaining this velocities regime and, therefore, the continuous areas of transport of the liquid steel are ensured by the mentioned injection parameters.

The utility and finality of the mathematical model for calculating the reactive powders' blast in the EAF consists of the possibility to analyze through simulating the triphasal liquid steel-powder and supporting gas-slag system's hydrodynamics. On the basis of this analysis, one can present the best constructive and functional parameters of the blast plant, in direct correlation with the technological performances (gas purity, enclosure purity) that the process imposes.

REFERERENCES

1. Ioana, A. - "The Electric Arc Furnaces (EAF) Functional and Technological Performances with the Preheating of the Load and Powder Blowing Optimisation for the High Quality Steel Processing", Master Degree Paper, University 'POLITEHNICA' of Bucharest, 1998.
2. Ioana, A., Dimitriu, S. - Management Elements of the Metallurgical Technological Plants, Conferința Internațională ISMT-Oradea, 2004.
3. Ioana, A., Nicolae, A., Dumitrescu, D., Ivănescu, S. - Modelling and Simulation of EAF' Processes, Conferința Internațională BRAMAT 2003, Braşov, 2003.
4. Ioana, A., Predescu, C., Sandu, I. F., Sohaciu, M., Calea, Gh., Nicolae, A. – "Optimal Managing of Electric Arc Furnaces", Fair Partners Publishing, Bucharest, 2002.
5. Ioana, A., Bălescu, C. - Optimization of Steel Elaboration in EAF through Mathematical Modelling, Junior Euromat Conference 2006, Proceeding, Lausanne, 4 - 8 September 2006.
6. Ioana, A. - Technical – Economical Analysis Options for the Quality of the Steel Elaborated in the EAF, Conferința Internațională IMT, Proceeding, Oradea, 2006.
7. Ioana, A. - Methods for Reducing the EAF's Polluting, Conferința Internațională „PRIORITĂȚI PENTRU RESTAURAREA FACTORILOR DE MEDIU NATURALI ŞI ARTIFICIALI", Proceeding, Sulina, 2006.

Received March 15, 2007

University "POLITEHNICA" of Bucharest

Rezumat

Calitatea oțelului lichid este puternic influențată de procesele de suflare a pulberilor reactive în cuptorul cu arc electric (CAE). Această influență este reflectată în principal de conținutul scăzut de gaze In oțelul lichid, de desulfurarea avansată şi de conținutul scăzut de impurități.
Lucrarea prezintă etapele principale ale procesului de suflare în algoritmul de modelare a CAE.
Modelul matematic conceput are ca scop atât determinarea dependențelor concentrațiilor de O_2 şi S în funcție de regimul de suflare (bazat pe modelarea transferului de masă), cât şi determinarea caracteristicilor de viteză şi ale turbulențelor sistemului.

BULETINUL INSTITUTULUI POLITEHNIC DIN IAŞI
Tomul LIII (LVII), Fasc. 2, 2007
Secția
ŞTIINȚA ŞI INGINERIA MATERIALELOR

CHARACTERIZATION OF SOME WASTES FROM IRON AND STEEL INDUSTRY BY LEACHING TEST

CRISTIAN PREDESCU, ECATERINA MATEI, MIRELA SOHACIU, DIANA PARPALA, ANDREI BERBECARU

Abstract: *According to the new environmental regulations, it is necessary that the disposal of each type of waste to be made by help with some disposal criteria. For this, the applying of leaching test becomes compulsory, in order to establish the potential impact on environment of the waste, especially for the hazardous elements.*

Keywords: waste, leaching test, environment, heavy metals.

1. INTRODUCTION

The leachate means, according to Order 867 / 2002 any liquid washing the disposed wastes, emitted by deposit or retained by this. This leachate may contain hazardous substances, collection and treatment of this leachate being a very important activity for waste deposit.

Criteria for acceptance of a waste into a deposit are made according to waste characteristics:

- physical and chemical composition;
- organic content;
- biodegrability of organic compounds;
- hazardous elements content;
- leaching test / prognosis;
- ecotoxicological properties of the waste and the leachate.

Due to physical and chemical characteristics, wastes from iron and steel industry represent may be used in various industrial sectors. Today, in our country, these types of wastes are partially recovered. For example, the most current method for slag recovery is their use in cement industry and road construction, according to their properties. Their recycling is an environmental task that can lead to natural resource protection and soil pollution prevention by minimizing areas with slag deposit.

In order to establish if the types of slags from different iron and steel areas can be recovered as building materials for roads, it is necessary to assess their environmental impact, beginning with finding the content of the hazardous elements (heavy metals) and the risk of their leacheability into soil and groundwater by help of rain waters.

This assessment is made with *leaching test*, which consists from the extraction into a liquid medium, in this case is rainwater, of different hazardous elements from waste, based on theirs solubilities in that medium.

In this paper are presented the results obtained after the leaching test applied for slag and dust samples generated in iron and steel industry. The tested wastes are now disposed in dumps, without being reused, and their quantity increases continuously.

2. RESULTS FROM LEACHING TEST FOR DIFFERENT WASTES

The national standard referring to waste analysis by leaching test is SR EN 12457 - 2003: Waste characterization. Leaching test. Validation test for granular wastes and sludges.

The leaching test standard refers to a liquid / dry solid ratio of 2 l / kg dry solid and 10 l / kg dry solid for 3 types of acid liquid phase: pH about 6 (distillate water), pH about 5 (buffer solution), pH about 3,5 (acetic acid solution).

The optimum stirring time is about 4 hours. The granular sizes are 4 mm and 10 mm for the waste.

After filtration, form liquid phase the specific indicators are analyzed.

This standard has been adopted as national standard according to the Environmental Acquis. At European level, the leaching test is available as requirement in German, Dutch or French standards.

For these laboratory experiments had been followed SR EN 12457 - 2003: Waste characterization. Leaching test. Validation test for granular wastes and sludges.

This standard presents the method for the solubilization of the solid sample, the obtained solution being analyzed by atomic absorption technique.

The method is used for solid and plastics wastes, which can be crushed and is not suitable for those wastes for which the leachate volume (aqueous solution) is less than 2l.

The experiments had been made on basic oxygen and electric arc furnace slags and electric arc furnace dust. Their chemical characterization is presented in table 1 and figure 1.

Table 1. Chemical composition of some wastes from iron and steel industry

Chemical composition, (%)	Basic oxygen furnace (BOF) slag	Electric arc furnace (EAF) slag	Electric arc furnace (EAF) dust
Ca	39,84	33,26	31,9
SiO_2	9,82	14,55	1,60
Al_2O_3	0,90	0	ND
MnO	6,26	7,46	2,4
MgO	1,97	22,71	ND
P_2O_5	2,26	0,48	ND
Fe tot	12,86	12.09	49,13
Fire losses	0,002	5,60	ND

ND-unavailable; the element has not been analysed.

The test had been made in order to:

- Assessment of the soluble portion from waste samples;
- Assessment of the waste quality;
- Behavior assessment of pollutants from slag during leaching test.

Working procedure had involved the following steps:

- 1. Preparation of the samples for testing;
- 2. The contact between solid sample and aqueous solution;
- 3. Separation of the solid material from liquid medium (leachate);
- 4. Leachate analysis.

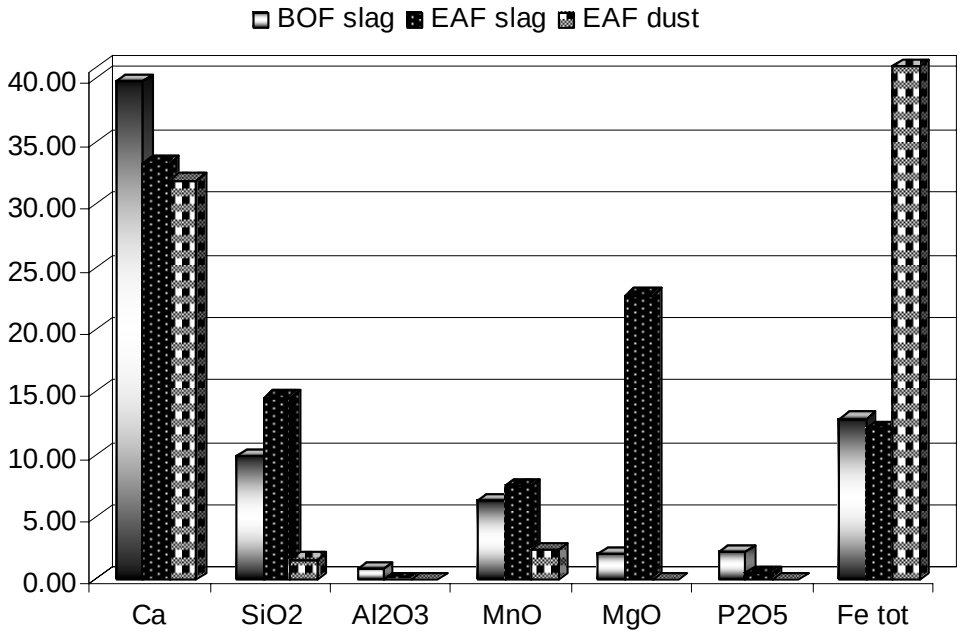

Fig. 1 Chemical composition of wastes

1) Preparation of the samples for testing

The procedure refers to the obtaining of the laboratory samples, after checking of the waste state (diameter, solid or slurry aspect, etc).

In the first step, the waste samples had been crushed in order to obtain the solid particles with size less than 4 mm.

According to standard, in case of a size higher than 4 mm, being impossible to reach at this size, the sample will be the subject of an especially analysis and will be establish depending by final objectives. The other recommended size is 10 mm.

By using the ball crusher and sieve set had been possible the obtaining of an adequate size.

2) The contact between solid sample and aqueous solution

This represents the main leaching step, when the waste is bring into the contact with aqueous phase and it takes place the transfer of the soluble compounds from the waste into liquid medium.

The contact time of the solid waste with the solution is an important parameter, the separation efficiency of the soluble compounds being related with this.

The contact time depends on the following factors:

- Material size;
- Composition of tested material and its compounds;
- Stirring frequency.

The optimum contact time, according with the standard SR EN 12457:2003 is about 4 hours under continuous stirring for the two phases, with the help of the magnetic stirrer, at 60 – 80 rot/min.

3) Separation of the solid material from liquid medium (leachate)

The standard recommends as a separation technique the filtration and/or centrifugal hydro extraction in order to obtain a higher efficiency. Filtration was made by a filter paper with pore sizes up to 0,45 μm, after a coarse filtration.

The liquid phase – *the leachate* will be available for chemical characterization in order to analyze *the heavy metal traces*, thus being possible to assess the negative impact of these metals on soil and ground waters.

4) Leachate analysis

The obtained leachate (the liquid medium) was analyzed in order to establish its chemical composition with help of atomic absorption spectrometry, using as apparatus for analysis a GBC932 AB PLUS atomic absorption spectrometer.

The work procedure was made according to SR EN 12506 – 2004: Wastes characterization. The elute analysis. Determination of: pH, As, Ba, Cd, Cl^-, Co, Cr, Cr^{6+}, Cu, Mo, Ni, NO_2^-, Pb, S total, SO_4^{2-}, V şi Zn. The metallic elements are analyzed by help with the atomic absorption method.

An overview of the activities applied during leaching test is presented in figure 2.

The experiments had been made for chemical characterization of the solution obtained by leaching test in static condition.

The chemical composition of the leachates (liquid solution after separation from slag samples) is presented in the table 2.

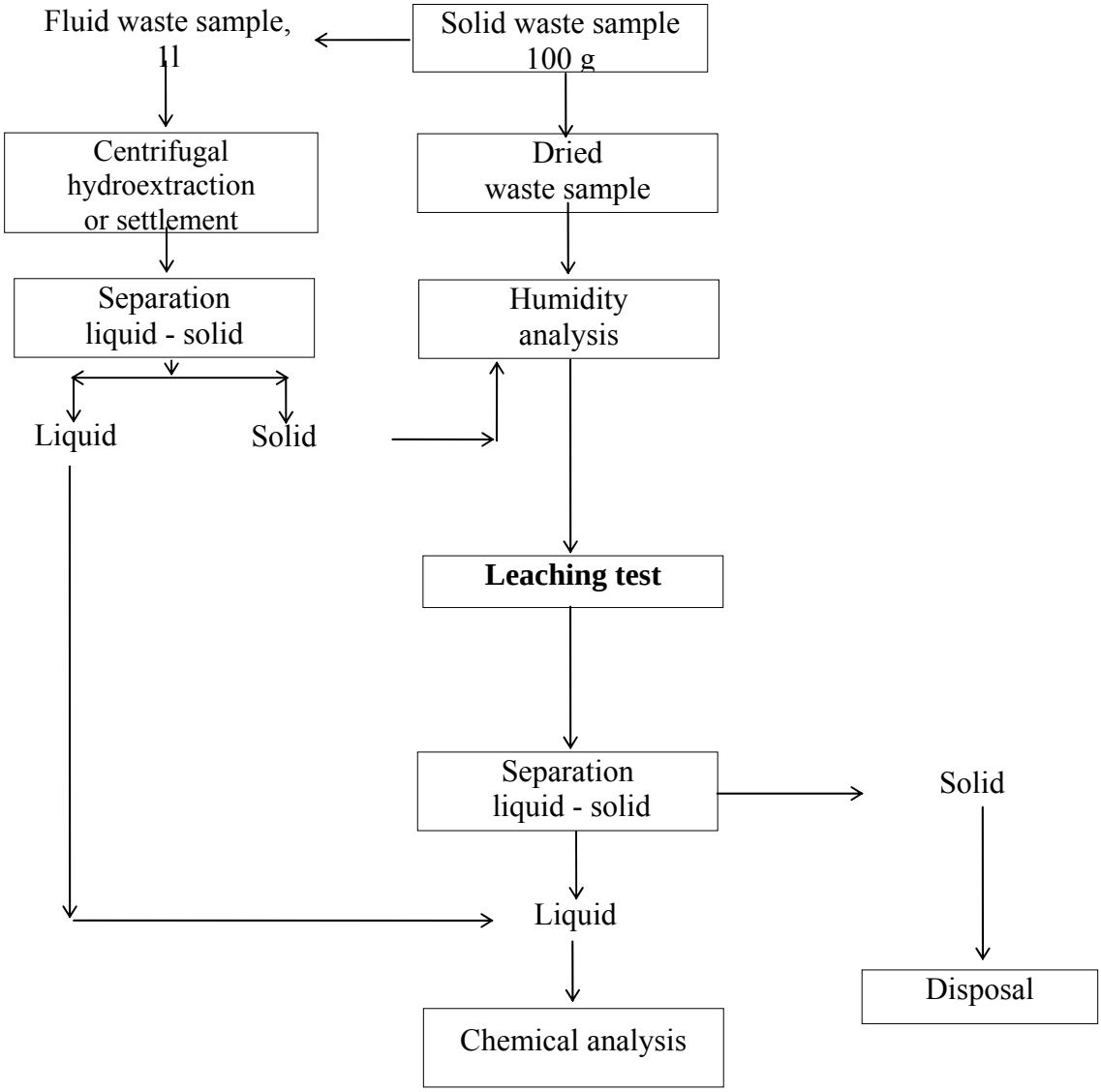

Fig. 2 Leaching test steps

The maximum admitted values are established in Order no. 867/2002 regarding *classification criteria of the wastes in order to be accepted in national list of the wastes and into different deposits.*

According with this Order, the iron and steel slags are classified into the deposit class of the nonhazardous wastes, 10 08 09 code – the others slags, 10 06 01 code – primary and secondary treatment slags, 01 03 08 code – dust and powder wastes.

Table 2. Chemical composition of leachate (mg/dm^3)

Indicators	BOF slag	EAF slag	EAF dust	Maximum admitted values, Order 867/2002	Analysis method
Ni	0,0006	0,0013	0	1,0	SR EN 12506 – 2004
Pb	0,021	0,016	0,005	0,5	
Zn	0,006	0,023	0,019	1,0	
Cd	0,003	0,003	0	0,3	
Cr tot	0,02	0,01	0,02	1,5	
Cr^{6+}	0,007	0,002	0,005	0,2	
Cu	0,01	0,014	0,009	0,2	
Ca	11,21	17,98	10,45	100*)	
Fe_{tot}	3	2,4	2,0	0,1*)	
pH	9	7 - 7,5	7,2	6,5 – 7,4*)	

**) the Ord. 867/2002 has not limited the calcium and iron content and also the pH value from leachate and these values were compared with STAS 1342 – 91 standard for potable water quality as reference.*

From laboratory tests it can be observed that some heavy metals ions can be solubilized by demineralized water.

The contact time for these samples was 4 hours. Thus, even if the initial composition of the wastes has not comprised the heavy metals content, which can be appear by accident, it could be observed, that some ions, due to contact between water and crushed samples of slags, were solubilized by demineralised water in small quantities.

Thus, for basic oxygen slag, where pH of the leachate has a basic value (pH=9), the heavy metal ions contents are important due to the impurities and fluxes content during the steel process (the similar effect is for electric arc furnace slag and dust).

In this case, it is expected the presence of some ions as Cd^{2+}, Pb^{2+}, Zn^{2+}.

The iron ions, due to slightly acid (amphoteric feature) characteristic of the ferric oxide Fe_2O_3 and the low water solubility of the ferrous oxide FeO (II), the efficiency values obtained for the total amount of iron are below 1 %.

For the calcium ions, the separation efficiency values are higher for electric arc furnace slag due to calcium oxide amount from initial composition of the wastes (and also the CaO has high water solubility).

Thus, for 1 t waste, the maximum iron and calcium quantities, expected to be extracted by about 10 m^3 water from one tone of slag into soil and groundwater are presented in table 3.

Table 3. Iron and calcium quantities extracted by leaching test application

Leachate from 1 t slag:	Ca^{2+}, g	Fe_{tot}, g
- basic oxygen furnace slag	220	60
- electric arc furnace slag	360	48
- electric arc furnace dust	209	40

It is important to observe that the heavy metal ions are not presented in high quantities.

After leachate analysis, it was observed that maximum admitted values are not exceeding, except iron, comparing with values admitted according with water quality standard. But, the iron quantity is expected due to its content in initial waste composition and its opportunity to be extracted into liquid medium.

3. CONCLUSIONS

Physical and chemical characterization and study of these types of wastes brought into contact with the water, according to leaching test, offer some information regarding the possible risk on environment of these wastes in case of theirs reuse as road construction materials, especially for analyzed slags.

The leaching test is important for assessment of the soluble portion from wastes samples and the waste quality and also for behavior study of pollutants from wastes during the test.

Three types of wastes were analyzed: BOF and EAF slags and EAF dust.

The samples were prepared according to working steps from the standard SR EN 12457:2003 and were analyzed according to SR EN 12506 – 2004 and Order 867/2002 requirements.

The obtained results show the presence of calcium, silicium and iron oxides, in the large amounts, as a result of used fluxes.

Applying this laboratory test on steel wastes (basic oxygen furnace slags and electric arc furnace slags) it is observed that:

- no one of these heavy metal ions are presented in high quantities in the leachate over the maximum admitted values:
- there are high quantities of some elements from leachate, such as iron and calcium, due to theirs presence in initial composition of the slags; the concentration values of these ions are not exceed the maximum admitted values for potable water (STAS 1342-91);
- the wastes from iron and steel industry are not hazardous wastes on environment, but the risk of some heavy metal ions appearance is possible, this being a reason for time to time testing of these waste types, having in mind the influence of these heavy metals on environment and life.

Received March 15, 2007

University POLITEHNICA of Bucharest

REFERENCES:

[1]. X X X, Environmental Control in the Steel Industry, Papers prepared for the 1991 ENCOSTEEL World Conference, International Iron and Steel Institute, 1992;

[2]. M. Abdelghafour, Realisation et mise au point d'un test de lixiviation sous pression. Application a la stabilisation des boues d'epuration d'eaux industrieles. Laboratoire de Chimie Physique Appliquee et Environnement, INSA, Lyon 1989;

[3]. X X X, MAPM Order nr. 867 / 2002;

[4]. X X X, SR ISO 8288 / 2001;

[5] X X X, NF X31-210 / 1992;

[6] SR EN 12457 / 2003;

[7] SR EN 12506 – 2004.

BULETINUL INSTITUTULUI POLITEHNIC DIN IAŞI
Tomul LIII (LVII), Fasc. 2, 2007
Secția
ŞTIINȚA ŞI INGINERIA MATERIALELOR

ASPECTS CONCERNING THE APPLICATION OF THE FUZZY LOGIC METHOD IN THE DESIGN OF TOOLS FOR DRAWING OF HEMISPHERICAL DRAW PARTS MADE FROM METAL SHEETS

G. BRABIE, M.RADU

Abstract: Springback of draw parts considerably affects their accuracy and deviations from the theoretical profile, this instability phenomenon determining the changes of the part shape and geometric parameters. The methods applied in order to reduce or eliminate springback are based on the following methods: tools correction after designing and testing, utilization of special tools and devices, optimization of process parameters based on some methods that establish a link among springback parameters and the influencing factors of this phenomenon. These methods are expensive and need a big number of experimental tests. Based on these conclusions, it is necessary to develop a method that will permit the reduction or the elimination of the springback from the designing stage of tools.
Keywords: *springback, hemispherical draw parts, tools correction, Fuzzy logic method*

Introduction

The springback is an elastic phenomenon, induced by the distribution of the residual stresses on the section of the deformed part (in our case, a hemispherical part), stresses that occur in addition to the internal stresses generated by the forming process. The springback phenomenon substantially affects the process accuracy, the deviations from the theoretical profile (figure 1) being recorded for the following parameters: the radius of the hemispherical part (Rp); the radius of connection between the flange and part (Rf); the angle between the flange and the horizontal axis (A).
To eliminate or to minimize the springback effects it is necessary to do this early in the conceptual phase of the tool and working process. An efficient way to solve this problem can be the application of the Fuzzy logic method. Based on the above mentioned method the influences of the process parameters on the geometrical parameters of the part can be quantified.
The system based on the Fuzzy logic allows to expand the true value to all numbers comprised in the [0, 1] interval. Each number from this interval can be considered as a possibility that the assertion to be true or false. One of the most important advantages of this method is its ability to formulate and manipulate the variables in a similar manner like in the case of a human expert. The Fuzzy logic allows a more flexible interpretation of the membership notion.
A procedure performed using fuzzy variables and rules starts with the understanding of the physic or by other nature phenomena. The Fuzzy logic method includes the following three phases**:**

- the fuzzyfication of the input variables which consists in their representation by a fuzzy set, defined by a membership degree; the Fuzzy variables are linguistic ones which don't describe the numerical data;
- the inference rule which realizes the connection between the input and output variables;
- the defuzzyfication of the input variables applied after the fuzzy set setting, set that is induced by the inference rule; that consists in the determination of a strictly singular value based on this set.

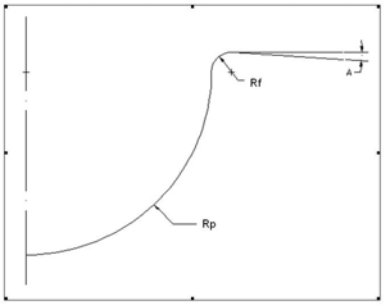

Figure 1 The geometrical parameters of the deformed part

The phases of the optimization method

Using Fuzzy logic in order to optimise the drawing process involves the setting of the input and output variables used to establish the influence of different factors on springback and on the geometrical parameters of the tool. The optimisation module searches for a combination of the factor levels, so that the requirements imposed equally to influence factors and to geometrical parameters of the tool to be simultaneous satisfied. Its application will allow also the optimisation of the tools geometry and the changing of several technological parameters of the drawing process. The precision of optimization can be increased by enlarging the number of the process influence factors that can be considered. The phases of the optimisation method are as follows:

- the setting of geometrical parameters of the part (Rp, Rf,A) ;
- the setting of parameters which influence the drawing process (Fr= blankholder force);
- the setting of the input variables (Rpn, Rm, Fr) ;
- the setting of the output variables (Rp, Rf, A) ;
- the setting of two levels of variation for each parameter: minimum and maximum ;
- the simulation of the process using Fuzzy logic ;
- the comparison between the resulted parameters and the nominal ones.

In figure no 2 it is presented the theoretical profile of the hemispherical draw part. The nominal parameters of the part are as follows: part radius Rp=55 mm, connection flange radius Rf=6 mm, flange angle with the horizontal axis A=0 and piece height h=62,6.

The geometrical parameters of the part which recorded considerable errors from the theoretical profile are as follows: the piece radius, the flange connection radius and the flange angle with the horizontal axis (figure 2).

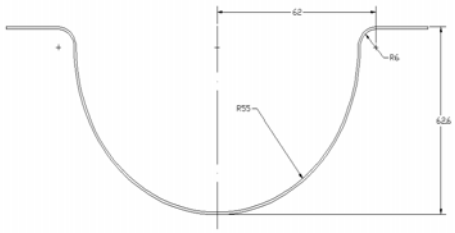

Figure 2 Theoretical profile of the drawpart

The setting the of the process parameters is one of the most important phase in the attempt to control the springback phenomenon. The original configuration of the tools used in the hemispherical drawing process is shown in figure no 3. The part made using the initial tool is shown in figure no 4.

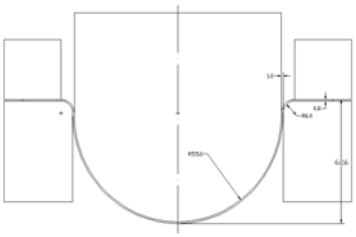

Figure 3 The initial tool

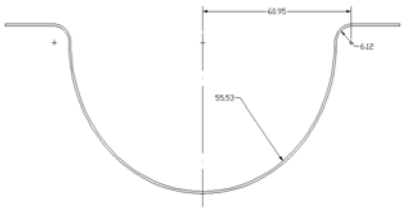

Figure 4 The part made using the initial tools

From the experimental tests it resulted that the blankholder force Fr has a significant effect on springback intensity and therefore it will be marked as the *input variable.* The tool radius R_{pn} (the punch radius) and the die radius R_m affects the springback intensity and therefore its will be marked as the *input variables.* So, the 3 input variables which affects the springback phenomenon are as follows: punch radius R_{pn}, die radius R_m and blankholder force F_r. These three parameters will directly influence the following parameters considered to be the *output variables:* the piece radius R_p, the connection flange radius R_f and the springback angle of the flange A.

For each of these parameters the following so - called *linguistic variables* which contain 3 "fuzzy sets" have been defined: "small" – it describes the minimum value of the input and output variables; "medium"- it describes the medium value of the input and output variables; "big"- it describes the maximum value of the input and output variables. Each of the above presented variables has a field of variation between a minimum and a maximum limit, as it is shown in the tables 1 and 2.

Table 1

Input variables	**minimum value**	**maximum value**
Die radius (Rm)	5 mm	7 mm
Punch radius (Rpn)	55 mm	56 mm
Blankholder force (Fr)	20 kN	70 kN

Table 2

Output variables	**minimum value**	**maximum value**
Piece radius (Rp)	55 mm	57 mm
Flange connection radius (Rf)	5 mm	7 mm
Springback angle (A)	0 mm	1mm

The simulation of the drawing process using Fuzzy logic

The manipulated variables of the proposed algorithm are the following: punch radius, die radius and blankholder force. For each of them a so called linguistic variable must be defined. For example the linguistic variable "die radius" which consists of three fuzzy sets: small: it describes the *small* radius; medium: it describes a *medium* radius: big: it describes a *big* radius. The set small is trapezoidal, having the big base of 1 and the small base of 0,5. The set big is also trapezoidal but using the big base of 1 and small base between 0,5. The set medium is triangular with the base of 1. The linguistic variable "punch radius" is very similar to the linguistic variable "die radius". The output variables are as follows: part radius, flange radius and the springback angle. All of them have the following characteristics: three fuzzy sets: small, medium and big; the small and big sets are trapezoidal and the medium set is triangular. The results of simulations are presented bellow

Simulation no 1

Input variables: punch radius (fig. 5a), die radius (fig. 5b). Output variables: piece radius (fig. 6a), flange radius (fig. 6b), springback angle (fig. 6c)

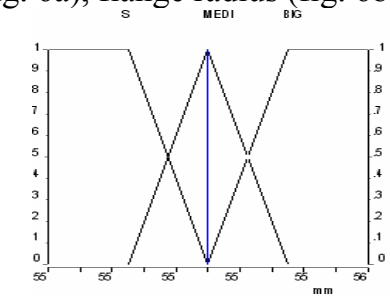

a

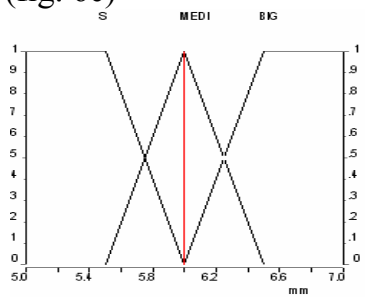

b

Input variable	Resulted value
Die radius	6 mm
Punch radius	55,5mm

Figure 5 Input variables

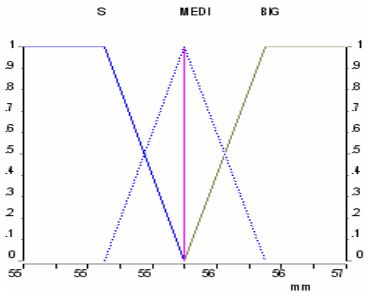

a.

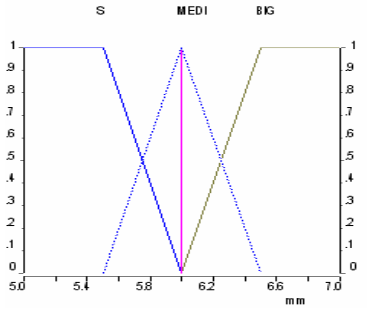

b.

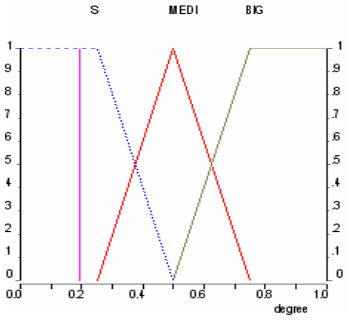

c.

Output variables	Resulted value
Piece radius	55,75 mm
Flange connection radius	6 mm
Springback angle	0,2degree

Figure 6 Output variables

Simulation no 2

Input variables: punch radius (fig. 7a), Blankholder force (fig. 7b). Output variables: piece radius (fig. 8a), flange radius (fig. 8b), springback angle (fig. 8c)

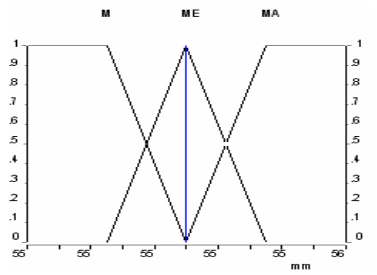

a.

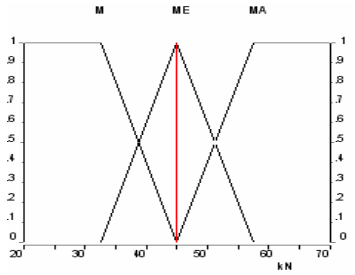

b

Input variables	Resulted values
Blankholder force	45 kN
Punch radius	55,5 mm

Figure 7 Input variables

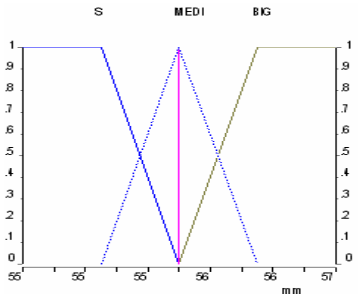

a.

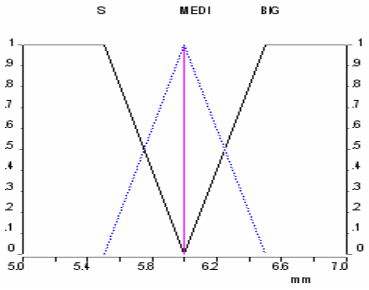

b.

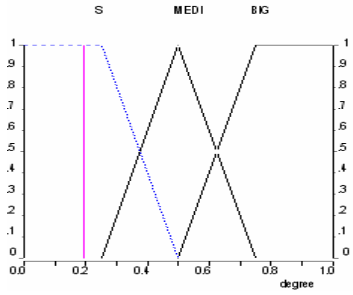

c.

Output variables	Resulted values
Piece radius	55,75 mm
Flange connection radius	6mm
Springback angle	0,2 degree

Figure 8 Output variables

Simulation no 3

Input variables: Die radius (fig. 9a), Blankholder force (fig. 9b). Output variables: piece radius (fig. 10a), flange radius (fig. 10b), springback angle (fig. 10c)

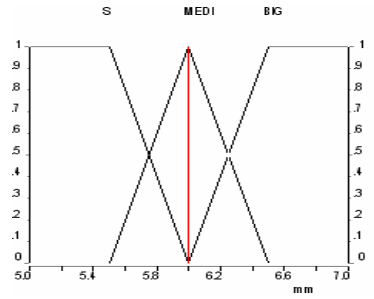

a.

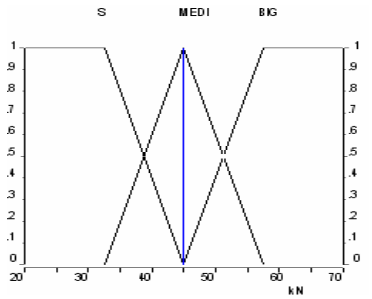

b.

Input variables	Resulted values
Blankholder force	45 kN
Die radius	6 mm

Figure 9 Input variables

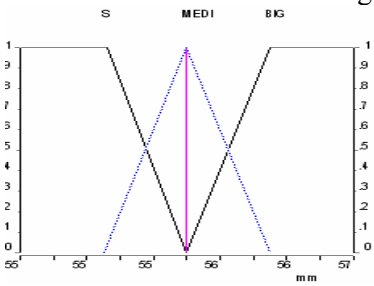

a.

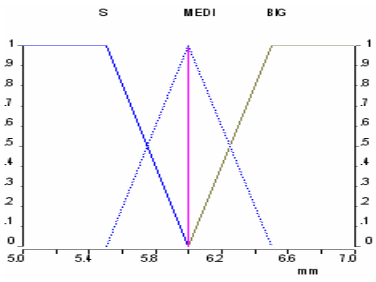

b.

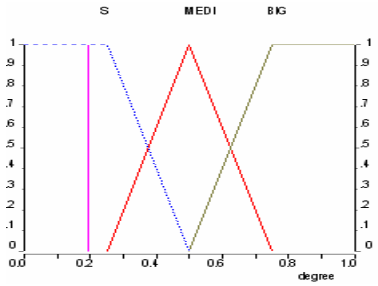

c.

Output variables	Resulted values
Piece radius	55,75 mm
Flange connection radius	6mm
Springback angle	0.2 degree

Figure 10 Output variables

Conclusions

A comparison between the theoretical parameters of the part, the parameters resulted from simulation based on Fuzzy logic and experiments presented in table no 3.

Table 3

	Blankholder force	Part radius	Flange connection radius	Springback angle
Theoretical values	35 kN	55mm	6 mm	0 degrees
Values resulted from experiment	35kN	55,53	6,12	0,4 degrees
Values resulted from simulation based on Fuzzy logic	45kN	55,75mm	6mm	0,2 degrees

By analysing the results presented in the table, we can observe some differences between the simulated by using Fuzzy logic and theoretical values, but a decrease of springback intensity obtained from experiment using initial tools.

Acknowledgments:
The present research was performed in the frame of the CEEX grant no 317/2006 with the financial support from the MEC - ANCS

References:

[1] Cox E., *"The fuzzy systems handbook"* Academic Press. Inc., 1994
[2] Ene C.F., Teza de doctorat, "*Cercetari privind optimizarea procesului de ambutisare a pieselor semisferice"*, Univ. Politehnica Bucuresti, 2006
[3] McNeill M.F., Thro E., "*Fuzzy logic a practical approach*" Academic Press. Inc., 1994
[4] Klir J., Yuan B., *"Fuzzy set and fuzzy logic Theory and applications"* , Prentice Hall PTR, 1995
[5] Kasabov N.K.,"*Foundations of Neural networks,Fuzzy systems,and Knowledge Engineering*", Massachusetts Institute of Technology 1996
[6] Brabie G., s.a., Dfeormarea tablelor metalice. Fenomene de instabilitate, Ed.Junimea, 2006

Received March 15, 2007

University of Bacau, Department of Production Systems Engineering

Rezumat
Revenirea elastică este un fenomen determinat de distribuţia tensiunilor reziduale pe secţiunea piesei deformate, tensiuni care apar suplimentar tensiunilor interne generate de procesul de deformare. În cazul ambutisării pieselor semisferice, fenomenul afectează în mod substanţial precizia procesului, abaterile de la profilul teoretic fiind înregistrate pentru următorii parametri: raza piesei semisferice, raza de racordare dintre flanşă şi corpul piesei, unghiul dintre flanşă şi axa orizontală. Eliminarea sau diminuarea efectelor revenirii elastice se realizează actualmente prin aplicarea unor corecţii la sculele de lucru, realizarea unor construcţii speciale de scule sau aplicarea unor proceduri de optimizare a parametrilor procesului. Aceste metode se caracterizează prin costuri ridicate şi consumuri mari de manoperă şi timp. Din aceste motive, este necesară aplicarea unei metode care să permită eliminarea sau diminuarea efectelor revenirii elastice încă din faza de proiectare a sculei şi procesului de deformare. O cale eficientă de rezolvare a problemei constă în aplicarea metodei Fuzzy Logic pe baza căreia pot fi cuantificaţi parametrii geometrici ai sculei şi ai procesului de lucru; aplicarea metodei în cazul pieselor semisferice a condus la eliminarea efectelor revenirii asupra unor parametri geometrici ai piesei şi la reducerea considerabilă a efectelor asupra altor parametri.

BULETINUL INSTITUTULUI POLITEHNIC DIN IAŞI
Tomul LIII (LVII), Fasc. 2, 2007
Secția
ŞTIINȚA ŞI INGINERIA MATERIALELOR

ASPECTS CONCERNING THE APPLICATION OF THE TAGUCHI METHOD FOR TOOLS OPTIMIZATION IN THE CASE OF CONICAL DRAW PARTS MADE BY USING CYLINDRICAL PUNCH

BRABIE G., NANU N.

Abstract: Springback of draw conical parts considerably affects their accuracy and deviations from the theoretical profile, this instability phenomenon determining the following changes of the part shape and geometric parameters: flange connection radius, bottom radius, flange angle between real profile and theoretical profile. The methods applied in order to reduce or eliminate springback are based on tools correction after designing and testing, on the utilization of special tools and devices, on the optimization of process parameters based on some methods that establish a link among springback parameters and the influencing factors of this phenomenon. These methods are expensive and necessitate a big number of experimental tests. Based on these conclusions, it is necessary the development of a method for the reduction or the elimination of the springback from the designing stage. The present paper analyses the possibilities to apply such method in the case of a conical part made from steel sheets.
Keywords*: springback, conical draw parts, tools correction, Taguchi's method*

Introduction

The elastic springback phenomenon in the case of conical draw parts is important because this phenomenon has as effect the following changes of shape of the draw part: flange connection radius, bottom radius, flange angle between real profile and theoretical profile. Generally, the elastic springback intensity is strongly influenced by the applied blankholder force and also by some parameters and working conditions like: material parameters, part geometry, tool geometry, friction coefficient.
The methods applied in order to obtain the springback minimization are based on the following theoretical and technical solutions:

- the tools correction after the designing, manufacturing and testing of the initial tools;
- the application of different models that consider the effects of different factors on springback intensity;
- the construction of special tools [1].

All the above mentioned methods lead to high costs and need many experiments.
Starting from the above presented aspects, we can conclude that in order to increase the accuracy of the drawing processes it is necessary the development of a method for the reduction or the elimination of the springback from the designing stage. An optimal solution can be obtained by using the process simulation in combination with a statistical modelling that allows the mathematical description of the influence of

different process parameters on the draw part geometry and accuracy. For this purpose, the factorial design offers the possibility to use a statistical method – for example Taguchi method. This method uses some predefined tables and on their basis it is possible to establish the relative importance of process parameters and their interactions on the springback intensity. The present paper analyses the possibilities to apply such method in the case of a conical part made from steel sheets.

Methodology of optimization

The Taguchi method uses some predefined tables and on their basis it is possible to establish the relative importance of processes parameters and their interaction on the springback intensity [3]. The optimization method of the forming process using Taguchi method has as purpose the reduction of elastic springback intensity of the draw part. Between the geometric parameters of the pieces and the parameters of the process can be established a dependence by using a quadratic or linear polynomial function. Taguchi's method suppose that by varying a number of factors (parameters of influence), the optimization process is more efficient if the number of tested factors is more important. Sometimes, the number of factorial plans that correspond to the number of tests can increase and hence the complexity of the problem that must be solved. Using this method we can optimize the tools geometry and also to modify some technical parameters of the drawing process. The main stages of the optimization method are as follows:

- the selection of geometrical parameters of the pieces that determine the deviations from the theoretical profile;
- the selection of the process parameters that influence the springback intensity;
- the establishing of two levels of variations for each of chosen parameters and the selection of the fractional factorial plans;
- the simulation of the drawing process using the finite element method combined with the experimental factorial planes;
- the selection of the model of linear or quadratic polynomial dependence and the construction of the factorial plane of experiment;
- the global optimization of the drawing process parameters by using an optimization function, so that the part geometrical parameters to be closer to nominal desired value;
- the verification of the resulted parameters obtained from the applied optimization method.

The Taguchi method was applied to optimize the drawing process in the case conical parts having the variation field of the considered parameters as it is shown in table no.1.

Table 1

Field a variation of the parameters used in optimization

Parameter	Initial value	Minimum value (-1)	Maximum value(+1)
Blanckholder force **(F_r)**	20 kN	20 kN	70 kN
Punch radius **(R_p)**	4 mm	4 mm	6 mm
Die radius **(R_m)**	4 mm	4 mm	6 mm

Selection of the part geometrical parameters that influence the deviations from the theoretic profile

Because the elastic springback phenomenon is characterized by many parameters, it is needed to determine all the parameters that affect the theoretical profile. In this order it is necessary to optimize the following parameters: flange radius, bottom radius, and curvature radius of the sidewall. The theoretical profile of the conical part is shown in figure 1.

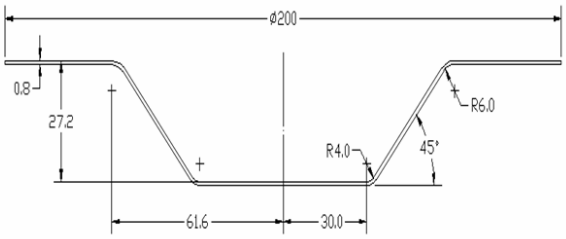

Figure 1 Theoretical profile of the conical part

After the drawing process we desire to obtain the following parameters of the draw part: the bottom radius R1=4 mm, the flange connection radius R2=6 mm and the curvature radius of the sidewall ρ that must be maximized (Figure 2)

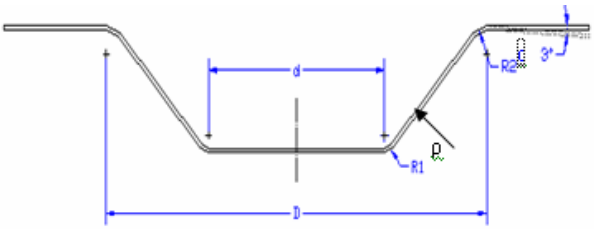

Figure 2 Real profile of the draw part

Selection of the process parameters that influence the drawing process

The process parameters must be carefully selected, because these parameters have an important influence on the accuracy of the finished part. The configuration of the initial tools is shown in figure 3 and the geometry of the part obtained using the initial tool is shown in figure 4.

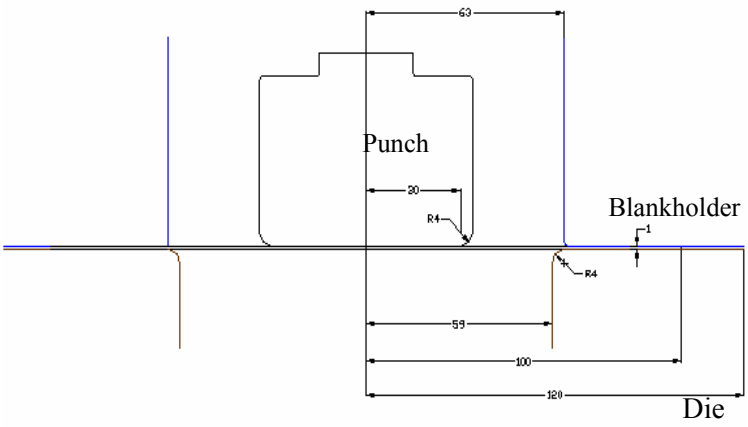

Figure 3 Initial tools

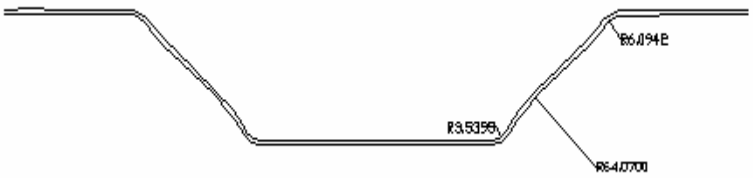

Figure 4 Shape of the part obtained using the initial tools

After the drawing process by using the initial tools, the configuration of the finished part presents a deviation from the given theoretical profile. On the basis of experimental researches, the process parameters which have an important influence on the springback intensity are as follows: *Blankholder force* $\boldsymbol{F_r}$ *, the radius of the punch* $\boldsymbol{R_p}$ *and radius of the die* $\boldsymbol{R}$**m**

Simulation of the drawing process using the finite element method and the factorial plane

The drawing process has been simulated using the ABAQUS-Explicit software. The simulation was performed for the conical parts made from E220 steel sheets - along and normal to the loading direction. The materials elastic properties used for simulation were as follows: Young's modulus 2.1×10^5 MPa, Poisson's ratio 0.3, density 7800 kg /m3. A three dimensional model used for simulation was created in order to ensure the simulation of the quasi-static problem and to obtain the state of equilibrium after the forming operation. The geometry of the models is shown for both parts in figure 5. The blank was considered deformable with a planar shell base [4]. The integration method was Gaussian with 5 integration points for every node, equal distributed through the thickness of the shell. The elements used for the blank mesh were of S4R type. The blank-holder, punch and die were modelled as rigid surfaces. Contact interactions between the blank and the tools were modelled using penalty method. In order to describe the plastic behaviour of the used material, 10 points were chosen from the stress – strain diagram. The materials were considered elastic-plastic with an isotropic hardening. The coefficient of friction used for the contact between blank, punch, die and blankholder was $\mu = 0.005$.
The process parameters were as follows: drawing depth = 30mm, drawing speed = 54 mm/s, blankholder force = 20 -70 kN. A symbolic mass of 1 kg is attached to the blankholder and an initially concentrated load of 20 kN is applied to the reference node of the holder.

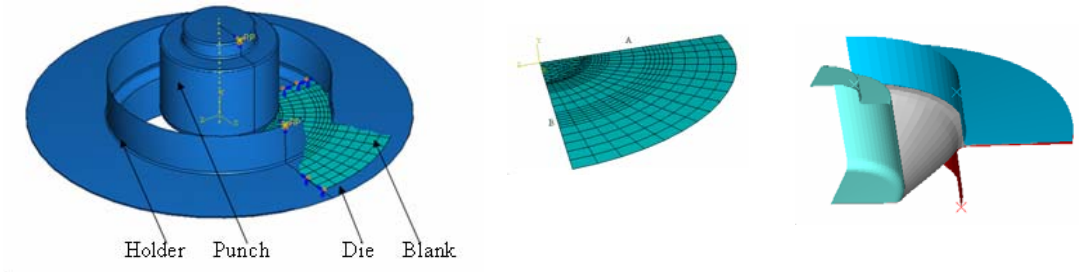

Figure 5 Geometrical model used in Abaqus

In order to establish a relation of dependence, Y(x), between the part geometrics parameters and process parameters two types of function, ***linear polynomial and quadratic functions***, can be used.[2]
In the case of determination of the linear polynomial function, we can use a factorial plan (experimental array) where for every factor of influence two variation levels (considered important for researching parameters evaluation) and a minimal level, coded(-1), and a maximal one, coded (+1) are assigned. For example, if we test ***k*** influence factors for a parameter and each factor is considered at two levels, we need an factorial experiment that requires 2^k experiences. In this case, because three influence factors have been selected, we should operate a number of 2^3 simulations. In order to minimize the number of simulation we only chosen the combinations that are representative for the main effects getting an ***fractioned factorial plan (2^{k-1})***.
In the case of determination of the quadratic polynomial function a fractioned factorial plan was used where, nearby first experiments, another three additional levels of each factors were used; the factors were coded as (-b), (0) and (+b) were b represents a real value (required to be smaller than -1 and bigger than +1).
First we used the factorial plans for determination of linear dependence function, and in the case when the obtained accuracy is not enough the experiments are continued according to fractioned factorial plan for quadratic function determination. But, by comparing the values resulted from simulation with that obtained using the above presented model a great difference was obtained especially in the case of the radii. Hence, we can conclude that the geometrical parameters considered in the linear model do not present a linear variation with the geometrical parameters of the tools. In this case it is needed to apply the optimization based on the quadratic model.
The following polynomial function of second degree was used in the quadratic model:

$$Y = a_0 + a_1X_1 + a_2X_2 + ... + a_nX_n + a_{11}X_{12} + ... + a_{nn}X_{n2} + a_{12}X_1X_2 + ... + a_{n-1,n}X_{n-1}X_n \quad (1)$$

where: Y represents the value that must be optimized (r_1, r_2, ρ) and $X_1..X_n$ represent the values of the input parameters that must be varied (F_r, R_p, R_m). In order to determine the coefficients of the model, a number of 10 additional simulations were used. The results of simulations are given in table no 2.

Table 2

Simulations with -b, 0, +b levels

	Fr	Rp	Rm	r1	r2	ρ
9	0	0	0	4.731	4.2259	103.5372
10	-1.287	0	0	4.3925	5.9578	217.9189
11	1.287	0	0	4.9855	4.7701	67.0711
12	0	-1.287	0	3.1929	4.3650	116.5062
13	0	1.287	0	5.6981	4.3445	75.1673
14	0	0	-1.287	4.8538	4.4366	80.6901
15	0	0	1.287	4.5953	5.0843	272.6595

The following models were obtained from calculation:

$$\boldsymbol{r1} = 4.71756 + 0.005\boldsymbol{F_r}' + 1.0309\boldsymbol{R_p}' - 0.14\boldsymbol{R_m}' - 0.148\boldsymbol{F_r}'\boldsymbol{R_p}' - 0.02\boldsymbol{F_r}'\boldsymbol{R_m} - 0.095\boldsymbol{R_p}'\boldsymbol{R_m}' - 0.01\boldsymbol{F_r}'^2 - 0.16\boldsymbol{R_p}'^2 + 0.01\boldsymbol{R_m}'^2$$

$r2 = 4.34689 - 0.616F_r' - 0.277R_p' + 0.3062R_m' + 0.3162F_r' R_p' + 0.109F_r' R_m - 0.083R_p'R_m' + \rho F_r'^2 \rho R_p'^2 1 \rho R_m'^2$

$\rho = 83.433 - 71.89F_r' + 43R_p' + 117.18R_m' - 39.16F_r' R_p' - 72.78F_r' R_m + 46.698R_p'R_m' + 44.69F_r'^2 + 16.52R_p'^2 + 65.33R_m'^2$

In order to test the obtained model, a simulation was performed for the case when: F_r=45 kN , R_p=5 mm, R_m=5mm. The obtained results are presented in table no 3.

Table 3

Simulation in the centre of the field

	F_r'	R_p'	R_m'	Values obtained from calculation	Values obtained from simulation	Deviation
r_1	0	0	0	4.7176	4.731	-0.013
r_2	0	0	0	4.3469	4.2259	0.121
ρ	0	0	0	83.433	103.5372	-20.1

By comparing the values resulted from simulation with that obtained using the above presented model, it was observed a diminution of the differences between the values obtained by applying the both methods. Also, if we compare the values obtained by applying the linear and quadratic models we can observe that in the case of quadratic model the differences are smaller than in the case of the linear model

Global optimization of drawing process parameters using an optimization function

To optimize the process parameters and to obtain simultaneously the three desired values for the part parameters (r_1 = 4 mm, r_2 =6 mm, ρ =1000 mm), the following function was applied:

$$F = (r_1 - 4)^2 + (r_2 - 6)^2 + (\rho - 1000)^2 \quad (2)$$

In the field of variation of the process parameters defined by the values -1 and +1, the function has some minima, but any of the minima is not equal to zero. The function F = 0 for r_1 = 4 mm, r_2 =6 mm, ρ =1000 mm. Hence we can choose in this field the lowest minimum value for the function F that must present the optimum value for which the above presented three conditions of optimization will be better and simultaneously satisfied. The values of the process parameters for which the function F will present the minimum value are given in table 4.

Table 4

Optimum values

	F_r'	R_p'	R_m'	r_1[mm]	r_2[mm]	ρ[mm]
Values obtained from calculation	-1.00 (20kN)	-0.26 (4.17 mm)	1.00 (6 mm)	4.19959	5.8498	387.059

By verifying the parameters resulted from optimization using the finite elements method the results presented in table no 5 were obtained.

Table 5

Values obtained from simulation

	r_1[mm]	r_2[mm]	ρ[mm]
Values obtained from simulation	4.16	6.2	315.047

The optimizated tools are shown in figure 6 and the part obtained by using the optimizated tools is shown in figure 7.

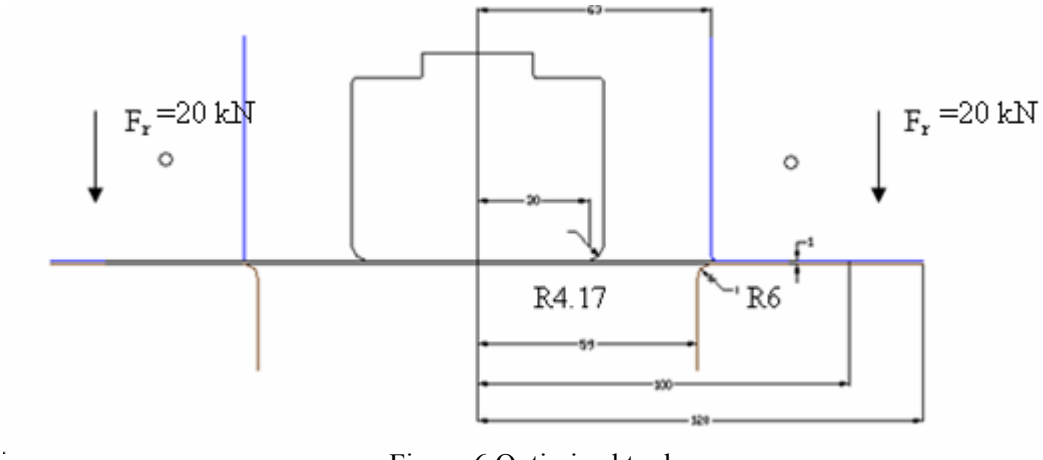

Figure 6 Optimized tools

Figure 7 The part obtained by optimizated tools

Conclusions

The values obtained after the process optimization are shown in table no 6.

Table 6

The values obtained after the optimization process

		r_1[mm]	r_2[mm]	ρ[mm]
Initial tools	**Values obtained from initial tools**	3.5395	6.0942	64.0755
Optimized tools	**Values obtained from calculation by applyng quadratic functions**	4.19959	5.8498	387.059
	Values obtained from simulation	4.16	6.2	315.047

In case of conical drawparts by using optimized tool and process parameters the springback intensity decreases . The best results are obtained by using quadratic functions. The method applied for the conical parts can be extended for all drawing processes.

Acknowledgments:
The present research was performed in the frame of the CEEX grant no 317/2006 with the financial support from the MEC - ANCS

References

[1] Ene C. F., "Cercetari privind optimizarea procesului de ambutisare a pieselor semisferice ", PhD thesis, T.U. of Bucharest, 2006
[2] E. Pairel, Y. Ledoux, R. Arrieux, L. Tabourot, O. Incandela " Correction of geometrical defects of stamping parts , by numerical simulation and design of experiment", Laboratory of Applied Mechanics, University of Savoy, BP 806, 74016 ANNECY Cedex, France.
[3] Bacivarov I., Bacivarov A., Ţipilică A." Ingineria calitaţii. Iniţiere în metoda Taguchi", Bucuresti 1998.
[4]Claes Arwidson " Numerical simulation of the sheet metal forming for high strenght steels", Lulea University of Technology, Department of Applied Physics and Mechanical Engineering, Division of Manufacturing Systems Engineering 2005.

Received March 15, 2007

University of Bacau, Department of Production Systems Engineering

Rezumat

Revenirea elastică este un fenomen determinat de distribuţia tensiunilor reziduale pe secţiunea piesei deformate, tensiuni care apar suplimentar tensiunilor interne generate de procesul de deformare. În cazul ambutisării pieselor semisferice, fenomenul afectează în mod substanţial precizia procesului, abaterile de la profilul teoretic fiind înregistrate pentru următorii parametri: raza piesei semisferice, raza de racordare dintre flanşă şi corpul piesei, unghiul dintre flanşă şi axa orizontală. Eliminarea sau diminuarea efectelor revenirii elastice se realizează actualmente prin aplicarea unor corecţii la sculele de lucru, realizarea unor construcţii speciale de scule sau aplicarea unor proceduri de optimizare a parametrilor procesului. Aceste metode se caracterizează prin costuri ridicate şi consumuri mari de manoperă şi timp. Din aceste motive, este necesară aplicarea unei metode care să permită eliminarea sau diminuarea efectelor revenirii elastice încă din faza de proiectare a sculei şi procesului de deformare. O cale eficientă de rezolvare a problemei constă în aplicarea metodei Taguchi pe baza căreia pot fi cuantificaţi parametrii geometrici ai sculei şi ai procesului de lucru; aplicarea metodei în cazul pieselor conice a condus la reducerea considerabilă a efectelor revenirii elastice asupra parametrilor geometrici ai piesei finite.

BULETINUL INSTITUTULUI POLITEHNIC DIN IAŞI
Tomul LIII (LVII), Fasc. 2, 2007
Secția
ŞTIINȚA ŞI INGINERIA MATERIALELOR

STUDY OF FATIGUE PHENOMENON IN NANOSTRUCTURED CARBON-BIOCOMPATIBLE ALLOY STRUCTURES

BY

ADRIANA SAVIN, RAIMOND GRIMBERG, LALITA UDPA

Abstract: This paper present the studies about fatigue phenomenon in complex structures made from nanostructured carbon- biocompatible alloy, as the components of Bjork Shiley convexo-concave prosthetic heart valves. For Haynes 25 alloy were determined the S-N curves and for occluder disk, the number of cycles until failure when a fatigue crack is growing, were determined

Keywords: BSCC prosthetic heart valve, fatigue phenomenon, fatigue cracks, Pyrolite carbon, biocompatible alloy

1. Introduction

Complex structures as nanostructured carbon - metallic alloy with biocompatible properties have uses more and more numerous, especially in different types of mechanical medical prosthesis [1]. A typical example of such structure is represented by Bjork-Shiley convexo-concave (BSCC) prosthetic heart valve [2], [3].

The BSCC prosthetic heart valve comprises a flange (orifice ring) an inlet strut, a disc occluder and a cloth sewing ring [4] (figure 1).

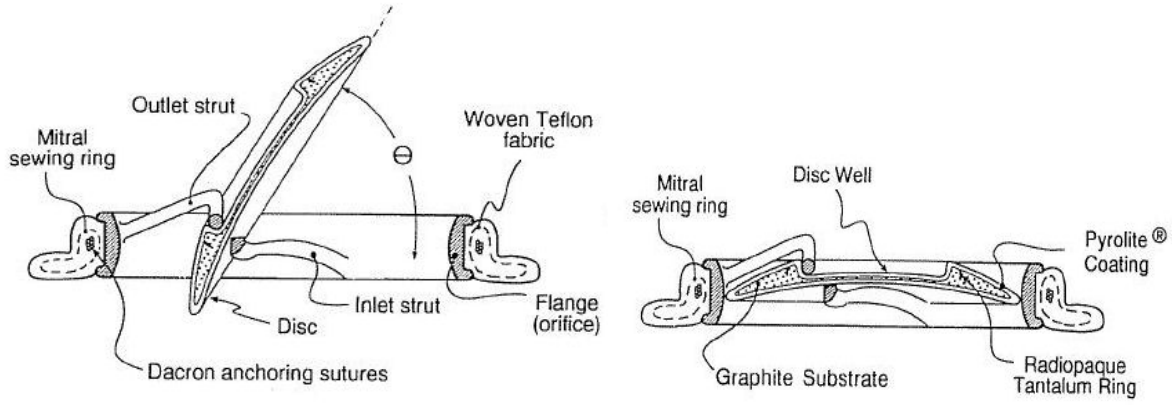

a b

Figure 1 The BSCC prosthetic heart valve – central cross – section drawing:
(a) Disc in open position (θ either 60^0 or 70^0)
(b) Disc closed

The flange and the inlet strut were fabricated as a single piece from a cylinder of cobalt based Haynes 25 alloy bar stack. The outlet strut was formed from a wire of

the same alloy and joined to the flange by tungsten inert gas (TIG) welding, which melted the ends of the two outlet strut legs and the surrounding flange metal to form integral welds, without filler material. The flange and struts were hand-polished to provide mirror finishes on the blood flaw contact surfaces.

The disc made by Carbo Medix Inc. is composed of an outer nanostructured carbon Pyrolite coating over graphite core that bias an embedded, radio-opaque tantalum ring. The marker ring is incomplete, with an intentional gap to allow thermal expansion during the carbon nanostructured coating. The disk was inserted into the flange orifice by cold-bending the outlet strut, making specific tolerance checks to ensure proper clearance around the perimeter of the disk and setting the hook-to-well gap between the outlet strut tip and the bottom of the well in the disc's convex surface. The disk well is engaged by the hook-shopped control tip of the outlet strut to limit disc opening translation and rotation about the inlet strut. On closing an outflow over inflow side pressure gradient strut's reverses flow forcing the disc to settle down on the inlet strut's convex surface and placing the disc in a neutral, mid-orifice, occlusive position, perpendicular to the orifice axis (figure 2).

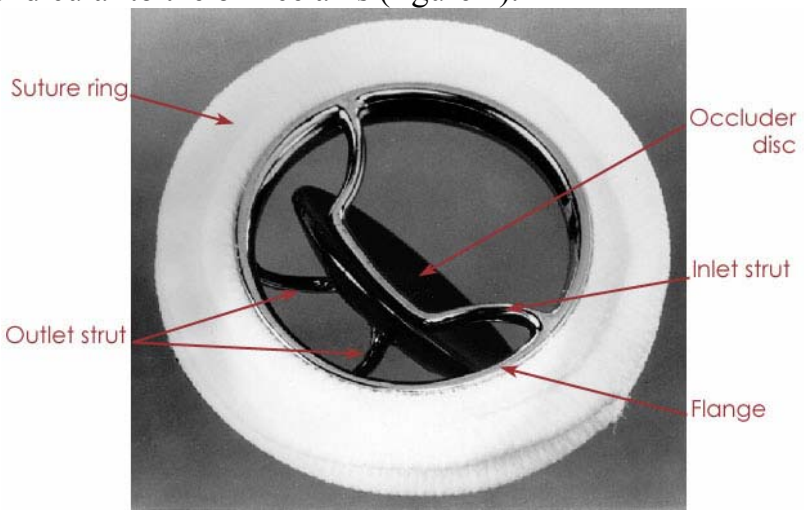

Figure 2. BSCC prosthetic heart valve

An epidemiological study [5] found 42 strut fracture and 8 occluder disc fractures during mean follow-up of 66 years. At present in all the world approximately 250.000 patients use such device.

Both types of fractures (outlet struts fractals and occludes disc fractals) are due especially to the degradations induced by fatigue. This paper is occupied with study of fatigue in alloy Haynes 25 type as well as in occluder disc coated with nanostructured carbon.

2. Samples taken in study

Because the epidemiological studies showed that maximum number of deteriorations of BSCC prosthetic heart valves are due to phenomenon associated with fatigue of outlet struts, the fatigue phenomenon on samples made by Haynes 25 wire alloy having 1.03mm diameter, identical with OS were studied. Chemical composition

for alloy is presented in table 1, the data being delivered of Haynes International Inc. USA.

Table 1 Chemical composition for Haynes 25 alloy (L605), according UNS-R30605

Element	Co	Cr	W	Ni	Fe	Mn	C	Si
Constituent [%wt.]	51*	20	15	10	3	2.0	0.1	0.4

* Balance

The principal mechanical characteristics indicated by producer are presented in table 2.

Table 2 Mechanical characteristics for Haynes 25 (L605) alloy

Characteristics	Young's modulus [GPa]	Strength [MPa]	Fracture toughness [MPa $\sqrt{m}$]	Fatigue threshold [MPa $\sqrt{m}$]
Value	209	450-1000	~60	4.5÷10

In case of prosthetic heart valves BSCC, occluder disc is manufactured by graphite core (show figure 1 and 2) on which a nanostructured carbon layer is deposited. The producer of disc, Carbo Madix Inc-USA had given the principal mechanical characteristics for this composite structure, sandwich type.

Table 3 Mechanical characteristics of nanostructured carbon

Characteristics	Young's modulus [GPa]	Strength [MPa]	Fracture toughness [MPa $\sqrt{m}$]	Fatigue threshold [MPa $\sqrt{m}$]
Value	27-31	350-530	1-2	0.7-2

The tests were made on samples of occluder disc with 18.8mm diameter, 0.9mm thickness and 5.5mm initial notch depth (measured from the load line). Razor micro notch were placed at the end of the saw cut notches by repeatedly slinding a razor blade over the notch under a light normal load (~1N) using a custom made ring in the presence of a 1μm diamond slurry. Using this method, notch root radii of 3÷5μm were readily achieved, as shown in figure 3.

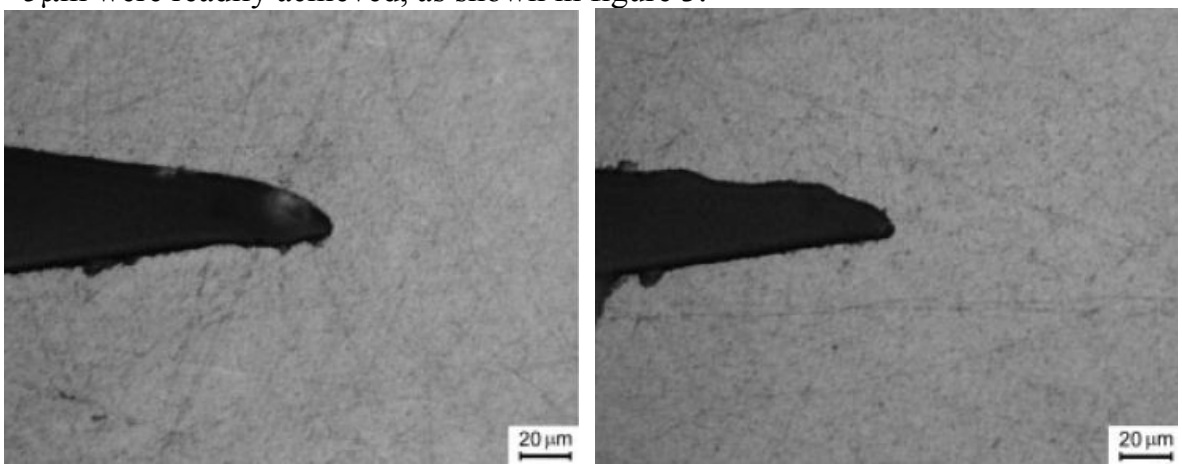

a *b*

Figure 3 Optical micrographs showing examples of razor micro notches in nanostructured carbon coated graphite: a) match root radii ~ 5μm; b) match root radii ~ 3μm

The image of strut of nanostructured Pyrolite carbon which cover graphite core (obtained with Atomic Force Microscopy) is presented in figure 4. The layer has advantage that is tromboresistive.

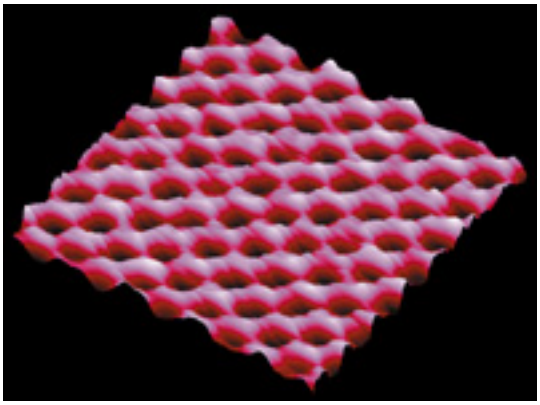

Figure 4. AFM imagine of nanostructured Pyrolite carbon

3. Experimental results

The fatigue tests were made at Michigan State University, College et Engineering, Mechanics Dept, using in this purpose the equipment INSTRON 1350 with ±100kN capacity of loading.

Samples of Haynes 25 wires were supposed at uniaxial cyclic extension-compression stress with 30Hz frequency. The tests were made in air at room temperature (+25^{0}C) as well as in solution Ringer lactate (a solution perfusable with electrolytic proprieties similarly with human blood).

In figure 5 are presented the curves S-N type for Haynes 25 alloy.

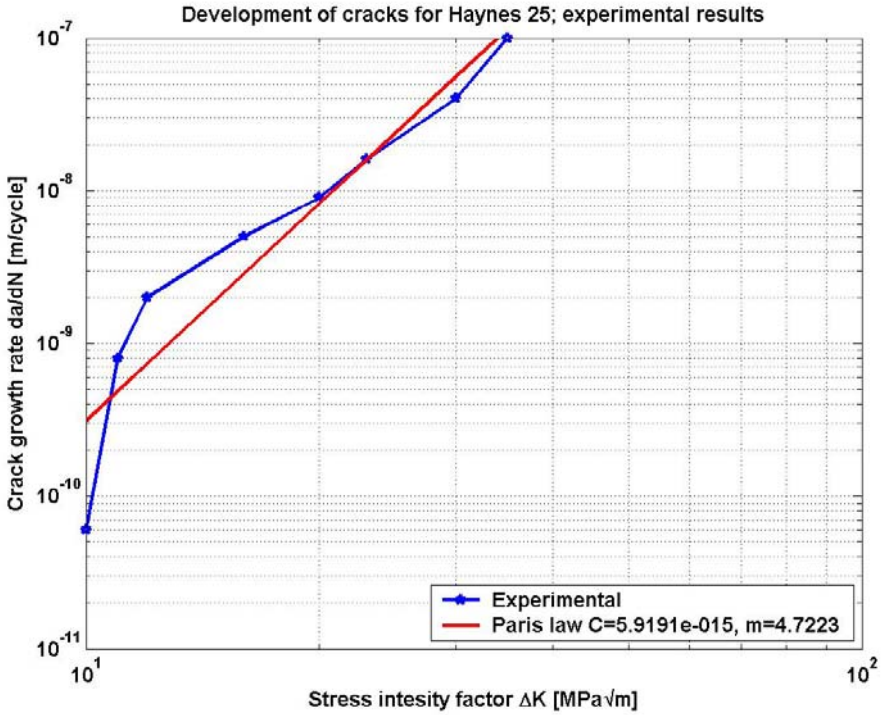

Figure 5 S-N curves for Hayes 25 Alloy

To measure fatigue – crack growth properties were used standard samples from Haynes 25, the measurement principle being presented in figure 6.

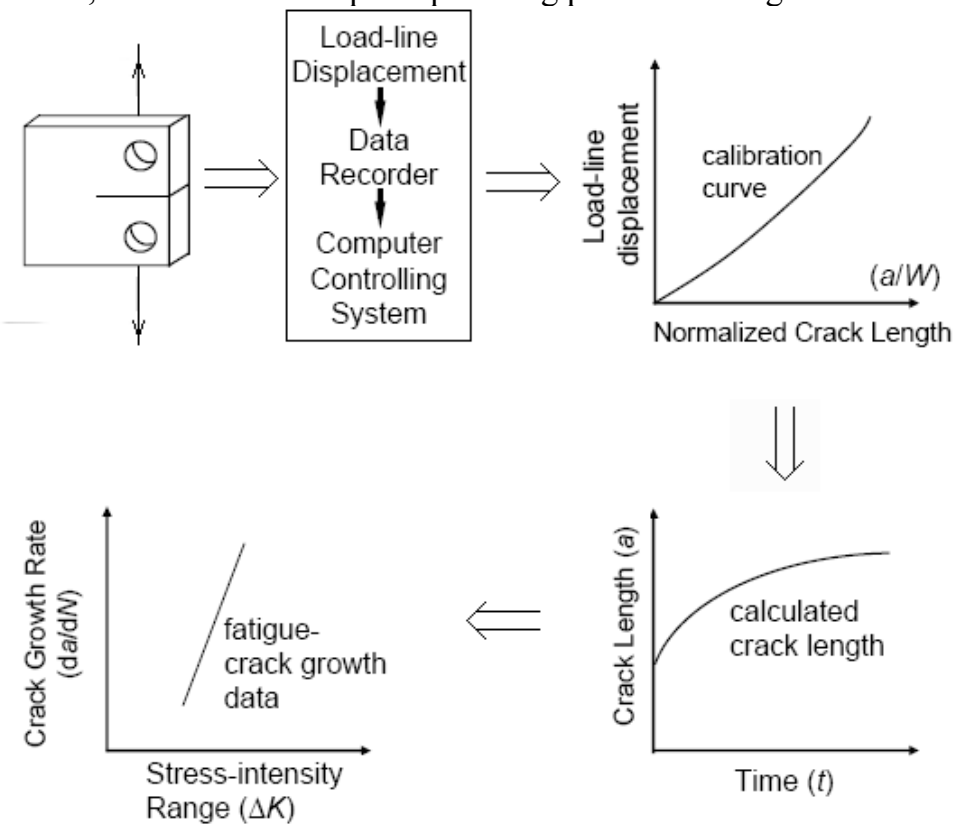

Figure 6 Measurement of Fatigue-Crack Growth

The results which describes the dependence of fatigue-crack propagation rate, da/dN, where *a* is crack length and N is number of cycles, are presented in figure 7 for samples immersed in Ringer lactate solution for coefficient: R = -1.

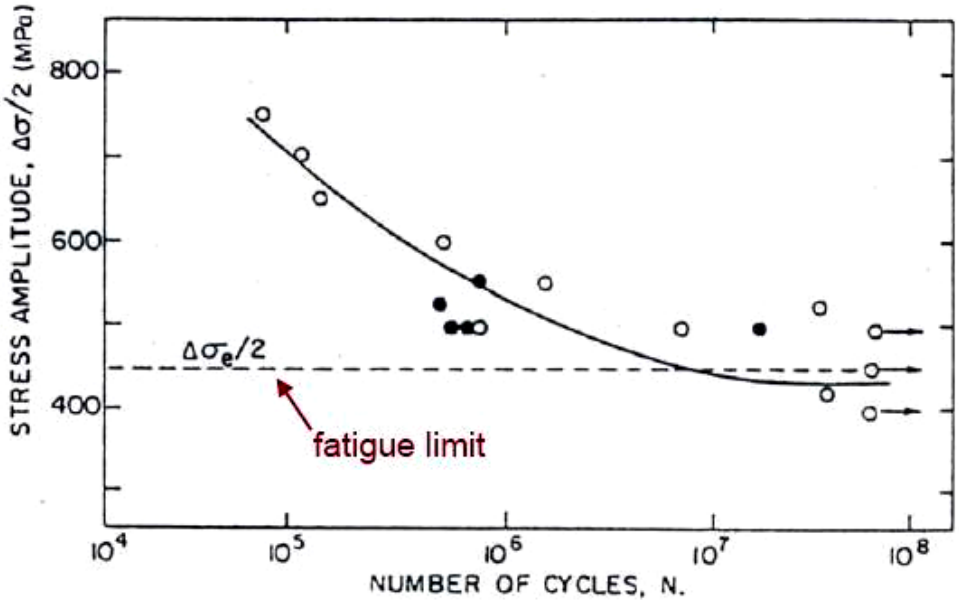

Figure 7 Fatigue crack propagation rate vs. Stress intensity factor

Occluder discs were tested in concordance with ASTM E-399. The discs were loaded with 0.44N/s loading rate until unstable fracture occurred. The critical stress intensity, K_c, for each sample was then computed from the peak load P and sample dimension, w is disk diameter, B is disk thickness, *a* is crack's length [7]:

$$K = \frac{P}{B\sqrt{w}} f\left(\frac{a}{w}\right) \tag{1}$$

where

$$f\left(\frac{a}{w}\right) = \frac{2+\frac{a}{w}}{\left(1-\frac{a}{w}\right)^{\frac{3}{2}}}\left[0.76+4.8\left(\frac{a}{w}\right)-11.58\left(\frac{a}{w}\right)^{2}+11.43\left(\frac{a}{w}\right)^{3}-4.08\left(\frac{a}{w}\right)^{4}\right] \tag{2}$$

Results to obtain are presented in table 4.

Table 4. Fracture Toughness Test Results for Micro matched Occludes Disks

Sample No.	K_c [MPa$\sqrt{m}$]
1	1.42
2	1.29
3	1.48
4	1.28
5	1.35
Mean ± Std. Dev	1.36 ± 0.08

4. Results and discussion

It was considered that the crack-growth relationship for Hayes 25 alloy is given by Paris law [8]:

$$\frac{da}{dN} = C\left(\Delta K\right)^{m} \tag{3}$$

the parameters being determined by best-fitting method.

The values C = 5.9191x10^{-15} and m = 4.7223 are obtained, on basis data by figure 7.

The form factor for fatigue cracks l/a (l = crack's length and a = crack depth) has average value ½ [8].

Stress intensity, K, can be expressed with relation:

$$K = Q\sigma\left(\pi a\right)^{\frac{1}{2}} \tag{4}$$

where

$$Q = \frac{2}{\pi} \quad \text{in case of} \quad \frac{\mathrm{l}}{\mathrm{a}} = \frac{1}{2} \tag{5}$$

Introducing (5) and (4) in (3) and effectuating the calculus, the number of cycles until failure of outlet strut for crack's fatigue can be found:

$$N_t = \frac{2}{(m-2)CQ^m \Delta\sigma^m \pi^{\frac{m}{2}}} \left[\frac{1}{a_0^{\frac{m-2}{2}}} - \frac{1}{a_t^{\frac{m-2}{2}}} \right] \tag{6}$$

where

$$a_t = \frac{1}{\pi} \left(\frac{K_{\max}}{Q_{\max}} \right)^2 \tag{7}$$

Experimental results are presented in figure 8.

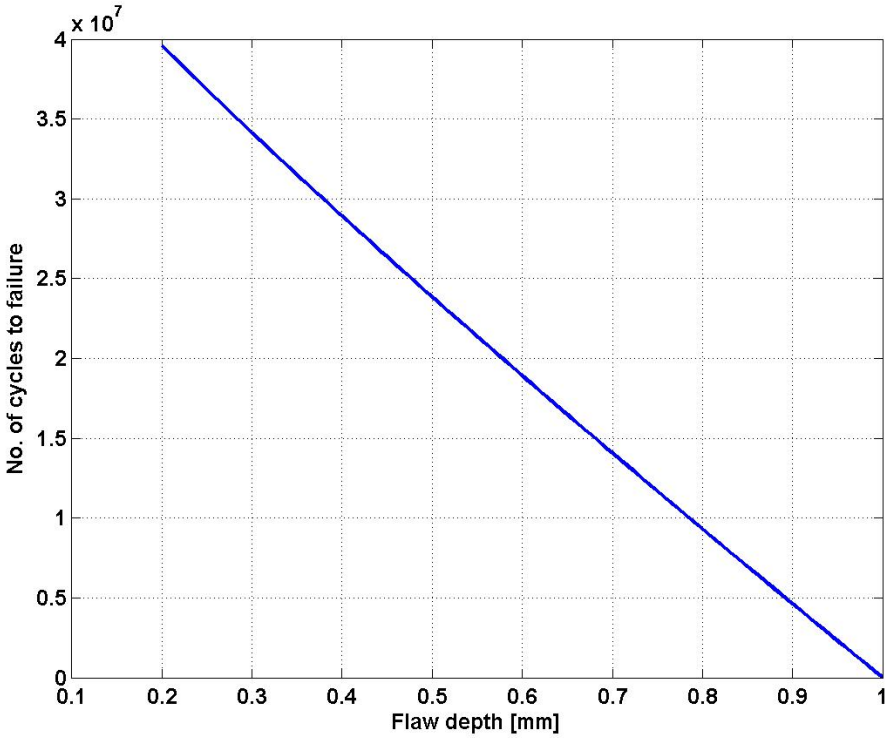

Figure 8 Number of cycles to failure vs. flaw depth

In case of occluder disk the propagation of cracks is made more slowly so that the number of cycles until break to exceed $8x10^8$, superior of BSCC heart valve prosthesis functioning time which is 53.8 years.

Examining the results presented in figure 8, we arrive at the conclusion that if a nondestructive examination method for heart BSCC prosthetic heart valve, which allow determination of fatigue crack with 0.6mm depth with probability of detection bigger or equal with 98% for imposed reliability coefficient, can be perfected, remain enough time for physician (cca 6 months for a heart rhythm of 72 battle/minutes) to prepare operation for explant – reimplant in good conditions.

Acknowledgements

This paper is supported by Romanian Ministry of Education and Research under the National University Research Council - Grant no.586/2006

Received March 1st , 2007

Nondestructive Testing Department,
National Institute of Research and Development for Technical Physics
47 D. Mangeron Blvd., Iasi, 700050, Romania
Michigan State University, 2120 Engineering Building,
East Lansing, MI 48824 – 1226, USA

REFERENCES

1. D. W. Weiting, A. C. Eberhardt, H. Reul, E. M. Breznock, S. G. Schreck, J. G. Chandler, "Strut Fracture Mechanisms of the Björk-Shiley Convexo-Concave Heart Valve", Journal of Heart Valve Disease, **8**, No.2, 206-217, (March 1999).
2. V.O. Bjork, *A new tilting disk valve prosthesis,* Second J. Thoroc. Cardiovascular Surg, 3 (1969), pp 1-10;
3. V.O. Bjork, *The improved Bjork-Shiley tilting disc valve prosthesis,* Second J. Thoroc. Cardiovascular Surg, 12 (1978), pp 81-84;
4. D.W. Wieting, A.C. Eberhardt, H. Reul, E.M. Breznoh, S.G. Schah, J.G. Chandler, *Strut Fracture Mechanism of the Bjork-Shiley Convexo-Concave heart valve,* J. Heart Valve Disc, 8, 2 (1999), pp. 206-217;
5. Y. vonder Grobf, P. de Ward, L.A van Herweden, J.J. Defauw, *Risk at strut fracture of Bjork-Shiley valves-Lancet*, 339 (1992), pp 257-261;
6. ASTM E 399-90, vol. 03.01, ASTM International, W. Consholochan, 2004;
7. J.J. Kruzic, S.J. Kuskowski, R.O. Ritchie, *Simple and accurate fracture toughness testing methods for pyrolitic carbon/graphite composites used in heart-valve prostheses,* Published online 22 June, 2005 in Wiley Inter Science;
8. J. Lemaitre, J.L. Cheboche, *Mechanics of solid materials,* Cambridge University Press, U.K, 1994.

STUDIUL FENOMENELOR DE OBOSEALA IN STRUCTURI CARBON NANOSTRUCTURAT-OTEL BIOCOMPATIBIL

Rezumat: Aceasta lucrare prezinta studiile asupra fenomenelor de oboseala in structurile complexe realizate din carbon nanostructurat- otel biocompatibil, asemeni componentelor valvelor de inima protetice tip Bjork Shiley convexo-concave. Pentru otelul Haynes 25 s-au determinat curbele S-N iar pentru cazul discului de inchidere a valve, s-a determinat numarul de cicli pana la fractura, in cazul existentei unei fisuri de oboseala.

BULETINUL INSTITUTULUI POLITEHNIC DIN IAŞI
Tomul LIII (LVII), Fasc. 2, 2007
Secţia
ŞTIINŢA ŞI INGINERIA MATERIALELOR

THE COMBUSTION FURNACES OPTIMISATION ASSISTED BY COMPUTER

BY

PETRICĂ VIZUREANU

Abstract. *The purpose of the heating operation is the metallic materials preparation for the forging processes in the technological flow. The heating technologies play an important part in the future quality of the product. For satisfying the production needs it is necessary to achieve a sharp control of heating processes' parameters. In such a context the development of the computer control system has a vital importance for obtaining the functional optimisation of the furnace through the mathematical model, by processing a big volume of data. The using of computer in the equipment designing and operation beside the using of new refractory materials and the burning equipment optimisation can lead at optimum heating furnaces from the constructive and operational point of view.*

Keywords: *furnace, combustion, heating, optimisation*

I. Heating regimes design for semi - products in view of forging

The heating process of metallic materials in view of forging has to ensure the achieving of the required temperature as more possible uniform distributed upon the entire section of semi - product, in a time as short as possible and without producing the fracturing or cracking of the material. The decreasing of heating time leads to the fuel consumption reducing and at the decreasing of oxidation and of decarburation of the heated material. The exaggerate decreasing of the heating time leads to a big temperature difference between the core and the semi - product surface and at stresses that lead to fractures and cracking in the material.

Taking into account the previous presented it results that, for achieving an optimum heating regime in the shortest time and without semi - product cracking danger, there is necessary such a leading of the furnace so the temperature difference between the core and the ingot surface be close to maximum acceptable value during heating. For the correct setting of the heating regime the values of the physical – mechanical parameters have to be those of the current material temperature during heating or at least average values for small temperature intervals.

For this it is necessary a computer programme with the help of which one can plot heating diagrams for the rang of polygonal ingots or round and prismatic semi-products. The programme starts from the heat transfer relations presented in the literature [4].

The initial data of this programme are:

• semi - product sizes;
• heating temperature;
• physical and mechanical feature of the steel that will be heated (λ, c, β, γ, E).
The programme is applicable for every kind of steel for which one know the physical - mechanical features values as function of temperature and the breaking limit function of material state (the cast reminded strains).

II. The combustion process optimisation by using of new burning equipment
There exists two trends in this direction:
• heat recovery from hot gases using regenerative burners;
• the using of gas analysers for burning control in heating furnaces.

II.1 Heat recovery from hot gases using regenerative burners
In the forge sections, important energy consumers, a special place was be represented by the heating furnaces for plastical deformation, which use as combustible the methane gas and at which during the technological processes there is a low degree of energy utilisation. The most part of the energy loss will be done by the gases vented from the working space and as it was be known, the most efficient recovery is that by which the energy was used in the charge heating process: primary recovery. Thus one can make appeal to the regenerative method by which the from the burned gases will be used to intensively preheat the combistion air using regenerative burners.
By this method the temperature of burned gases became 100-200ºC by comparison with the previous situation when the gases vented from the working space can have temperatures sensible equal with those of the furnace. One recommands the using of regenerative burners on heating furnaces with maximum working temperatures about 1250ºC with continuous or discontinuous operation. The regenerative method wasn't recommended to other gases due to its impurities.

II.2. The using of combustion gases analysers for burning control in heating furnaces
The advantages of the last burned gas analysers' generation were identified by the following features:
• they are made from a block of sensors placed on the pipes of burned gases of the boiler and from an electronic block placed in the furnace command desk zone, the link between them being achieved by a protective cable;
• the burned gases are being vented from the block of pipes passed through a floppy filter (which is permanently being cleaned from solid particles by reverse blowing of its inactive zone), or they filter themselves in the case of thermo-diffusive extraction and then they are being passed through the sensors and after that are sent back in the pipes (figure 1);
• the block of sensors has a ZrO_2 sensor for oxygen concentration measurement and the catalytic combustion sensor with platinum cataliser for combustible gases measurement;
• the block of sensors works at the high temperature making possible its location closer possible by the burner.
The electronic block is being endowed with a microprocessor that has several entrances and exits analogues and digital, playing the part of a general controller of burning. It fulfils the following functions:

• it displays oxygen and combustibles gases concentration values given by the block of sensors;
• it calculates and displays the values of optimum necessary and effective air excess;
• it accomplishes the adjustment through various adjustment laws and commands the execution elements (operation) for the getting of the required flow rates for combustible and air;

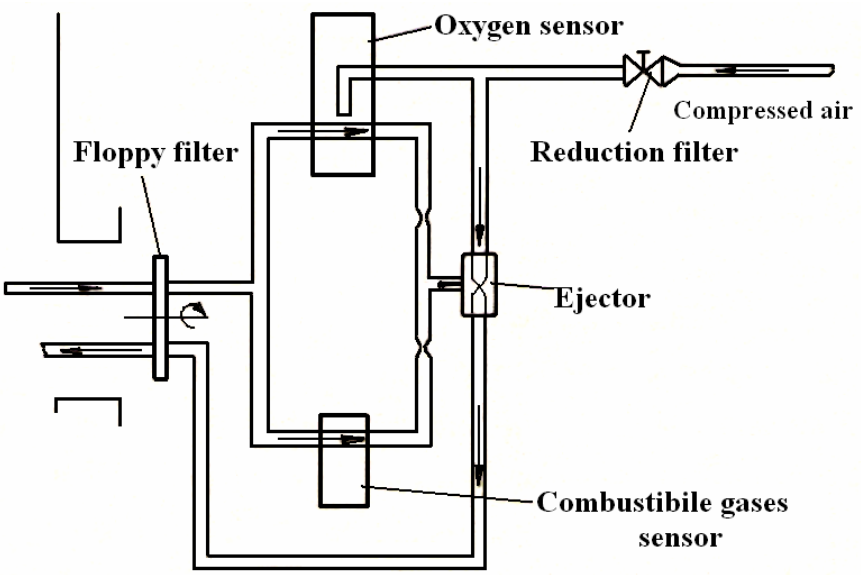

Figure 1.

• it facilitates an active dialogue with the operator which by means of a functional keyboard and of a display block can set the adjustment and advertising parameters and commands directly at the execution elements;
• it watches and commands the burners operation;
• in case of same disfunctionalities it brings the parameters at previous settled values.
This burning adjustment system optimises the efficiency of burning process by minimising the losses due to the air excess in the furnace or to unburned evacuate combustible. At the same time it helps at the maintaining of a proper fraction air /combustible despite the variation of caloric power, pressure, temperature or combustible density.

III. The computer assisted desiginig of heating equipment

As a result of the experience there follows that the designing of heating furnaces implies laborious calculation for the thermal regime as well as for the effective dimensioning. With the PC aid and with an advanced software one could elaborate sets of programmes for analytical designing of heating furnaces.
The designing methodology supposes the elaboration of a mathematic algorythm by which starting with a calculation of the combustible burning one pass to the designing of the thermal regime for the required heating technology and the proper heat recovery system.
An important chapter in the designing stages is the establishment of the thermal balance of the heating equipment that has to have optimum balance features [3].

Each section of the thermal balance of the furnace is being calculated using analytical relations that model the heat transfer. After the calculation of each type of heat flow rate one makes with the computer aid a feed-back cycle as in the case of the heat loss through to the walls. After the average temperature calculation of the middle layer of the furnace brickwork by means of feed-back cycle, these are being approximate such as the difference does not exceed 10 %. If this difference exists one makes the calculation again taking into account the average temperatures of the middle layers previously settled.
In this way one accomplish the calculation for the other chapters of the balance too, having in view the specificity of each.

References

1. Chelu, Gh. - Optimizarea regimurilor de încălzire a lingourilor şi semifabricatelor in vederea forjarii, Revista Metalurgia nr. 1, 1993, p. 5-11.
2. Grancea, V., Dima, A., Vizureanu P. - Necesitatea introducerii dimensionarii asistate de calculator a cuptoarelor de incalzire în procesul didactic - Sesiunea tiintificä "45 ani de învăţământ superior", Galaţi, oct. 1993, vol.2, p.170-174.
3. Dima, A., Grancea, V., Vizureanu P. - Computer Assisted Mathematic Modelling of Heating Processes in the Solidus Field of Fe-C Alloys - Heat Treatment Conference - Dunayvaros - Ungaria, 1993, p.85-90.
4. Grancea, V., Vizureanu, P., Alexandru, M. – New Trends in the Forging Furnaces Constructive and Operational Optimisation, Buletinul I.P. Iaşi, tomul XL (XLIV), secţia IX, Ştiinţa şi Ingineria Materialelor, vol. II, 1994, pp.613-618.

Received March 4, 2007

Technical University Iaşi

OPTIMIZAREA CUPTOARELOR CU COMBUSTIE CU AJUTORUL COMPUTERULUI

Rezumat. Încălzirea materialelor metalice în vederea deformării plastice la cald se face cu ajutorul cuptoarelor cu combustie. În acest sens este necesară optimizarea regimurilor termice din aceste utilaje mari consumatoare de energie. Optimizarea se referă la posibilităţi de recuperare a energiei termice furnizate prin intermediul elementelor încălzitoare.

BULETINUL INSTITUTULUI POLITEHNIC DIN IAŞI
Tomul LIII (LVII), Fasc. 2, 2007
Secția
ŞTIINȚA ŞI INGINERIA MATERIALELOR

NEURO-FUZZY EXPERT SYSTEMS FOR PREDICTION OF MECHANICAL PROPERTIES INDUCED BY THERMAL TREATMENTS

BY

PETRICA VIZUREANU[*], AUREL ANDREESCU[**], NICOLETA IFTIMIE[**], ADRIANA SAVIN[**], ROZINA STEIGMANN[**], SORIN LEITOIU[**], RAIMOND GRIMBERG[**]

Abstract: This paper presents an Expert System designed to be able to predict the mechanical properties - the yield strength and the tensile strength for some low alloy steels with the suitable heat treatment. The Expert System uses a neural network as the inference engine.

Keywords: expert system, neuro-fuzzy network, thermal treatment, low alloy steels.

1. Introduction

The heat treatment, as the technological process used in the obtaining the metallurgical products, involves the heating and cooling operations applied to the metals and alloys to achieve desired mechanical properties. The most heat treatments are made to improve ductility and toughness, to increase or reduce hardness, to increase strength and so on. The steels will have the desired properties according as the microstructure of alloys, which can be ferrite-pearlite, ferrite - pearlite - bainite or martensite.

There are a lot of recommended practices for conditions of heat treatment in function of chemical compositions and desired mechanical properties. These are looking for the austenitising temperature, the austenitising time, the heating and cooling rate, the tempering temperature and other parameters. The results are not always that we waited!

The possibility to predict or estimate the results of heat treatment leads to the development of physical and mathematical models regarding to the tensile strength, the yield strength, toughness, creep life, fatigue life etc. The lack of progress in predictions for the mechanical properties is due to their dependence on large number of variables. Nevertheless there are more patterns recognized by metallurgists, which are the guide for thermal treatment.

The neural networks as part of the artificial intelligence are using to model the complex systems in the engineering process where it is difficult to formulate an

analytical model. The Expert System (ES) offer a way to overtake the lack of experimental data and physical models in this domain and to realize the empirical quantitative model of great advantage in Materials Science [1].

The basic idea behind the Expert Systems is simply - the expertise, which is the vast body of task-specific knowledge, is transferred from a human to a computer.

The neural networks can achieve an exhaustive analysis by a non-linear relationship among sets of input and output data of the system. The advantage of Neural Networks is their capability to learn from the set of actual data. The transfer functions which realize the non-linear correlations between sets of input and output data are flexible and determined by interconnect- weights of input data. The encoding weights are been done by a learning technique by a special type. The combine effects of alloying elements for different mechanical properties are predicted when weights are chosen on the basis of metallurgical understanding. The realization of the Expert System depends on some problems which are the key of his performance: the data base which must created with a large experimental actual data, the selection of the adequate variable to describe the physical process and the use of artificial parameters so the Neural Networks system "discovere" the non-linear correlations.

The paper presents an Expert System designed to be able to predict the mechanical properties - the yield strength and the tensile strength for some low alloy steels with the suitable heat treatment.

The ES uses as inference engine a neural network back propagation type. The ES has three sets of neurons: one input layer with 10 neurons, a hidden layer with 2 neurons and the output layer with 2 neurons (fig. 1).

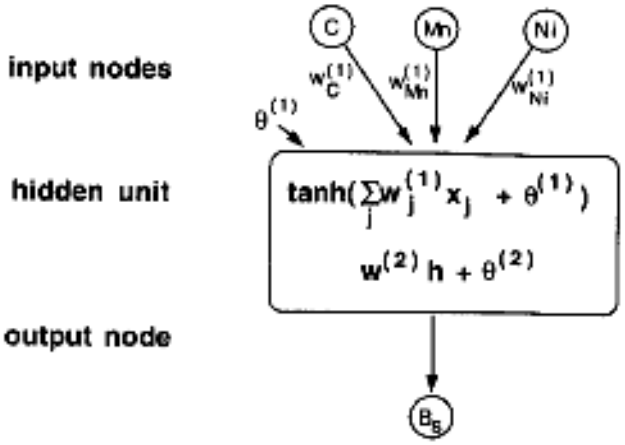

Figure 1. A non-linear network representation

The first layer includes one neuron for each input parameter, respectively the chemical composition (C, Mn, Si, Cr, Ni, Mo), the austenitising temperature, the austenitising time, the cooling rate (air cooling, oil cooling, water cooling). The second layer consists of a number of neurons as non-linear operators, the arguments of which are the weighting inputs from the first layer. The output layer has 2 neurons, one each for the output parameters: the yield stress and the tensile strength.

The transfer functions used in ES is a hyperbolic tangent function. The calculus relations are:

$$h = \tanh\left(\sum w_j^{(1)} x_j + \theta\right) \tag{1}$$

and

$$y = w^{(2)} h + \theta^{(2)} \tag{2}$$

The weights do not need to be known in advance. They will be adjusted by the Neural Network using a training algorithm in accordance with database for σ_y and σ_r. The encoding weights are been made by a learning technique by a special type. The combined effects of alloying elements for different mechanical properties are predicted when weights are chosen on the understanding metallurgical basis. The same thing is done using the regularization constants.

The database includes 50 sets of inputs data for the training and 25 sets of data for testing the ES. The sets of data relate to the low alloys cast steel and low alloy rolling steel used in machine construction**:** EN 10028, EN 10137, EN 10113.

The selection of input parameters are basis made on the literature data, where it is shown their influence on the mechanical properties [2], [3]. The yield and tensile strength has been modelled as a function of C, Mn, Si, Cr, Ni and Mo concentrations. The weight of concentrations is very important in determinate the mechanical properties as how it is known. On the metallurgical basis search the carbon concentration have the most significant influence on tensile strength (cca 80 MPa for each 0.1% C) and the yield strength (cca 50 MPa for each 0.1% C). The influence of Mn is smaller with the increases (10 MPa for each 0.1% Mn for σ_y and σ_r). The same thing we can say about Si but the Ni has a different influence for σ (80 MPa for each 1% Ni) respectively a minor influence about yield stress. The chrome has a similarity contribution as nickel.

The austenitising temperature allows materials to reach a γ-phase structure, in which the carbon element is interstitial lattice dissolved; that is in the temperature range $850^0 \div 980^0$C. The austenitising time allows the equalization temperature for the whole section of the material and a quantitative carbon element to dissolve in the austenite phase. The austenitising time may varies between 10 minute and 2 hours.

The cooling rate is function of the sample dimension, its surface temperature and the cooling medium. Its values varies between $0{,}3 \div 1^0$C/sec (air cooling), 75^0C/sec (oil cooling) or 360^0C/sec (water cooling). In function of the cooling rate, chemical composition of steel and the different austenitising stages the different metallurgical structure are formed: ferrite - pearlite, bainite - ferrite - pearlite or direct in martensite and so on

The tempering temperature of steel we taken in study varied between $570^0 \div 650^0$C.

The evaluation of the mechanical properties of the steel may be done with more hidden units in the second layer. More hidden units need more time of running program and more equivalent costs so it is necessary to make an optimum choice. The test error shows the optimum choise.

For the estimation of the yield and tensile strengths in the rolling plate as function of chemical compositions and rolling parameters it were reported 2 neurons in hidden layer [4]. For prediction of the Vickers hardness in austempered ductile iron it

was used 10 neurons correlating the hardness with the nominal composition, austenitisation temperature, austenitisation time, austempering temperature and austempering time [5].

Table1 The variables used in the analysis as the input parameters.

Analysis Parameters		**Minim**	**Maxim**
Input Parameter	Carbon, wt.%	0.09	0.55
	Manganese, wt.%	0.4	1.4
	Silicon, wt.%	0.2	0.8
	Crom, wt.%	0.3	1.8
	Molybdenum, wt.%	0.15	0.35
	Nickel, wt.%	0.3	3.55
	Austenitising temperature, ^{0}C	850	980
	Austenitising time, min	10	120
	Cooling rate, ^{0}C/sec	0.3	360
	Tempering temperature, ^{0}C	570	650
Analysis Parameters		**Minim**	**Maxim**
Output Parameter	Yield strength, MPa	275	1030
	Tensile strength, MPa	540	1320

2. Artificial neural network approach

In our model the network has one input layer, one hidden layer and one output layer. The input layer has 10 input parameters: the principal elements of chemical composition, austenitisation temperature, austenitisation time, cooling rate and tempering temperature.

One important step in our analysis is the normalization which brings the range of variations of all the variables between -0.5 and + 0.5 as follows:

$$x_N = \frac{\left(x - x_{\min}\right)}{\left(x_{\max} - x_{\min}\right)} - 0.5 \tag{3}$$

This is made to avoid the different scales of variations between the different input parameters and the important influence each parameter is shown. The transfer function is one hyperbolic tangent type. The argument of this function is *quantity* of type W.X+Θ with X (the vector input parameters) and W (the matrice of weights of input parameters). The output parameters are of form than (W.X+Θ). The output variables are a linear combination of hyperbolic tangent functions.

The calculated parameters are checking in regarding with the real parameter from the database. The error model is determined by minimized error function given by:

$$E_d = 1/n\ \Sigma(Y_{target} - Y_{calc})^2 \tag{4}$$

The error function is the sum squared error between the target and the prediction for a given choice of weights.

The weights are adjusted until the error is equal with the imposed limit.

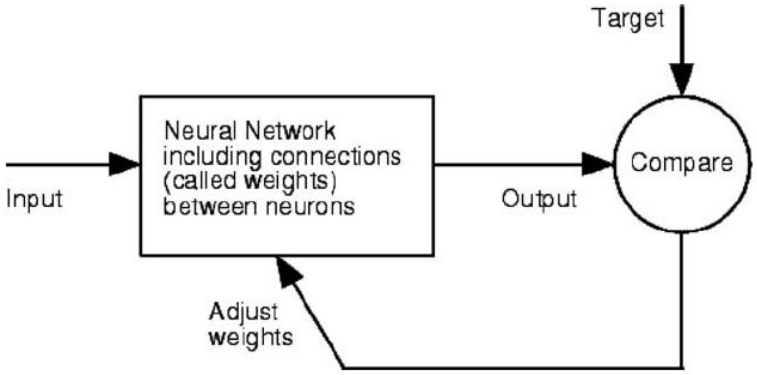

Figure 2. Training process for artificial neural networks

The algorithm used is a gradient descent type. The learning rate was taken 0.005. Numbers of iteration is 100.000. The algorithms automatically search the network configuration to avoid the over-fitting.

In order to reduce the search for the best training network to a reasonable time we used only network with one hidden layer.

3. Results

The predictions of the yield strength and tensile strength as a function of chemical composition are shown in figure 3 for wt% C, wt% Mn, wt% Cr.

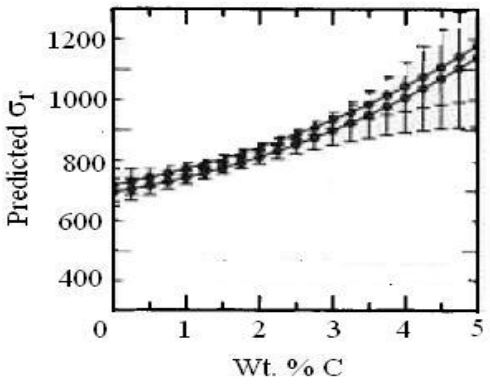

a

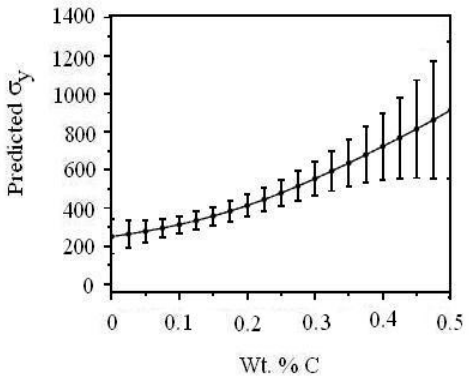

b

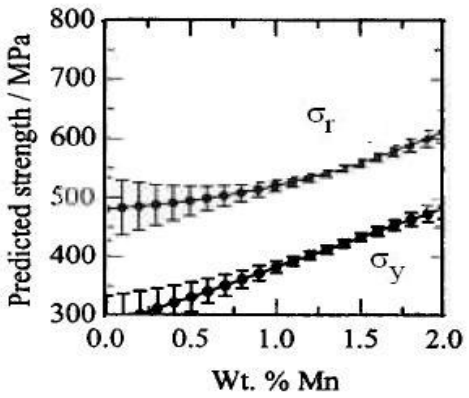

c

Figure 3. (a) and (b) Variation of σ_y and σ_r with carbon for steel without any micro alloying additions;
(c) Variation of σ_y and σ_r with manganese for steel without any micro alloying additions

The synergetic effect of all the input variables on the yield stress and the tensile strengths are shown in figure 4.

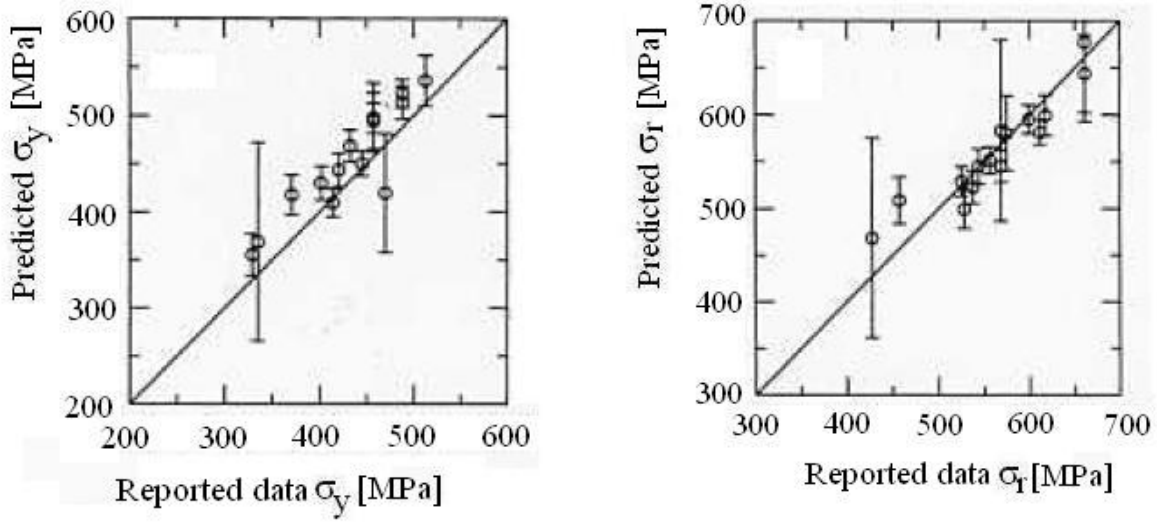

a b

Figure 4 Comparison of predicted σ_y (a) and σ_r (b)with data reported in literature standards

The comparison between the predicted and the measured values is good at the small concentrations of alloyed elements and the small cooling rate, so the treatment is in range of ferrite – pearlite microstructure.

Conclusions

The prediction of neural network model as a function of input parameter used is consistent with the metallurgical trends and can be used to study of the effect of each variable.

The one interesting results on the yield strength and the tensile strength but it is necessary a more database for the same class of steels.

Acknowledgements

This paper is supported by Romanian Ministry of Education and Research, Research of excellence Program, under Contract no. 171/2006 acronym PROTHERM.

Received March 1st , 2007

*Technical University Gh. Asachi Iasi
67 D. Mangeron Blvd., Tasi, 700050, Romania
**National Institute of R&D for Technical Physics Iasi
47 D. Mangeron Blvd., Tasi, 700050, Romania

REFERENCES

1. H.K.D.H. Bhadeshia, Neural Network is Materials Science, ISIJ International, vol. 39 (1999), No. 10, pp. 966-978;
2. Ovidiu Hatarescu, Indreptar de metalurgie, Ed. tehnica, Bucuresti, 1988 ;
3. George Vernescu, Tratamente termice, Editura Dacia, 1987 ;
4. S.B. Singh et al., Neural network analysis of steel plate processing, Iron making and Steel making 1998, vol. 25, no. 5, pp. 355-365;
5. M.A. Yescas, Prediction of the Vicker hardness in austempered ductile irons using neural networks, http://www.msm.cam.ac.uk/map/mapmain.html;

SISTEME EXPERT NEURO FUZZY PENTRU PREDICTIA PROPRIETATILOR MECANICE IDUSE DE TRATAMENTE TERMICE

Rezumat: Aceasta lucrare prezinta un sistem expert proiectat pentru a face predictii asupra proprietatilor mecanice ca limita de curegere si rezistenta la tractiune pentru o serie de oteluri slab aliate supuse tratamentelor termice specifice. O retea neuronala de tip feed –forward a fost antrenata sa coreleze limita de curgere si rezistenta la tractiune in functie de elementele de aliere, temeperatura si timpul de austenitizare, viteza de racire si temperatura de revenire.

BULETINUL INSTITUTULUI POLITEHNIC DIN IAŞI
Tomul LIII (LVII), Fasc. 2, 2007
Secția
ŞTIINȚA ŞI INGINERIA MATERIALELOR

EVALUATION OF CARBON EPOXY COMPOSITES DELAMINATIONS USING LAMB WAVES

BY

RAIMOND GRIMBERG*, PAUL BARSANESCU, ADRIANA SAVIN*, ROZINA STEIGMANN*, MARIUS MIHAI CAZACU*****

Abstract: This paper present a new nondestructive evaluation procedure for carbon- epoxy composites materials, based on production of low frequency Lamb wave in examined material using low frequency ultrasound transducers with Hertzian contact. Measuring the propagation speed for Lamb waves, using a triangulation method and a data fusion procedure, we can estimate more precisely the position and surface of delaminated area.

Keywords: carbon epoxy composites, low frequency ultrasound transducer, Hertzian contact, Lamb waves, delamination

1. Introduction

Carbon epoxy composites materials are used today in most different domains from aeronautics industry to sports goods. These materials consist by carbon fibre networks which forms composite reinforcing embedded in the matrix of epoxy resin. Carbon epoxy composites present a series of excellent advantages [1]:

- low density,
- great breaking limit,
- mechanical fatigue state is hard to establish,
- possibility to directly obtain complicate structures without being necessarily the mechanical processing and joints,
- reduced radar cross - section.

Between the disadvantages of carbon epoxy composites materials it can mention small resistance at impact after a perpendicular direction on the plan of the fibres arrangement. The impact induces a plastic deformation of the zone, appearing possible delamination accompanied or not by breaking of fibres, in function of impacted energy [2].

Calculation of lifetime prediction for the structures made from carbon- epoxy composites imposes knowledge of position and surface of delaminated area [3]. In this purpose, different methods of nondestructive evaluation methods were developed:

- ultrasounds methods [4], [5] with the disadvantage that is necessary to use coupling fluids between ultrasound transducers and examined material on one hand and on the other hand, the control operation lasts long;

- electromagnetic methods [6], [7] with the disadvantage that the estimated area of delaminated region evaluated by this method is in constant manner greater than real area.

Also, a series of monitoring methods of the structures from carbon-epoxy composites based on fibre Bragg gratings [8], on ultrasound transducers embedded in composites [9], and on acoustic emission [10] were developed.

In this paper is presented a new nondestructive evaluation procedure for carbon-epoxy composites materials, based on production of low frequency Lamb wave in examined material, using low frequency ultrasound transducers with Hertzian contact [11]. Measuring the propagation speed for Lamb waves, using a triangulation method and a data fusion procedure, we can estimate more precisely the position and surface of delaminated area.

2. Lamb waves in carbon-epoxy composite

Lamb waves are plane elastic wave guided between two free parallel interfaces. The theory of Lamb waves is developed in a series of references books [12], in this paper being presented only the mathematical development, absolute necessarily.

The analysis starts from the wave equations:

$$\begin{aligned} \frac{\partial^2 \Phi}{\partial x^2} + \frac{\partial^2 \Phi}{\partial y^2} + \frac{\omega^2}{c_L^2} \Phi = 0 \\ \frac{\partial^2 \Psi}{\partial x^2} + \frac{\partial^2 \Psi}{\partial y^2} + \frac{\omega^2}{c_T^2} \Psi = 0 \end{aligned} \tag{1}$$

where Φ and Ψ are two scalar potential functions,

$c_p^2 = \dfrac{\lambda + 2\mu}{\rho}$ - pressure (longitudinal) wave velocity,

$c_s^2 = \dfrac{\mu}{\rho}$ - shear (transversal) wave velocity,

λ, μ - Lamé constants, ρ - mass density.

The time degradation is assumed harmonic in the form: $e^{-j\omega t}$.

The general solution of eq. (1) is

$$\begin{aligned} \Phi = \left(A_1 \sin py + A_2 \cos py \right) e^{-j(\xi x - \omega t)} \\ \Psi = \left(B_1 \sin py + B_2 \cos py \right) e^{-j(\xi x - \omega t)} \end{aligned} \tag{2}$$

where $\xi = \dfrac{\omega}{c}$ - is the wave number

$$\begin{aligned} p^2 = \frac{\omega^2}{c_L^2} - \xi^2 \\ q^2 = \frac{\omega^2}{c_T^2} - \xi^2 \end{aligned} \tag{3}$$

The four integration constants, A_1, A_2, B_1, B_2 are to be found from the boundary conditions. Using the relations between the potential functions and the displacements, stress and strains:

$$\begin{aligned} u_x &= \frac{\partial \Phi}{\partial x} + \frac{\partial \Psi}{\partial y} \\ u_y &= \frac{\partial \Phi}{\partial y} - \frac{\partial \Psi}{\partial x} \\ \tau_{yx} &= \mu\left(2\frac{\partial^2 \Phi}{\partial x \partial y} - \frac{\partial^2 \Psi}{\partial x^2} + \frac{\partial^2 \Psi}{\partial y^2}\right) \\ \tau_{yy} &= \lambda\left(\frac{\partial^2 \Phi}{\partial x^2} + \frac{\partial^2 \Phi}{\partial y^2}\right) + 2\mu\left(\frac{\partial^2 \Phi}{\partial x^2} - \frac{\partial^2 \Phi}{\partial x \partial y}\right) \end{aligned} \tag{4}$$

we obtain:

$$\begin{aligned} u_x &= \left[\left(A_2 j\xi \cos py + B_1 q \cos qy\right) + \left(A_1 j \sin py - B_2 q \sin qy\right)\right] e^{j(\xi x - \omega t)} \\ u_y &= \left[-\left(A_2 p \sin py + B_1 j\xi \sin qy\right) + \left(A_1 p \cos py - B_2 \xi \cos py\right)\right] e^{j(\xi x - \omega t)} \end{aligned} \tag{5}$$

The terms in eq. (5) have been grouped into two ports, the first corresponding to symmetry motion and second to anti-symmetry motion (figure 1).

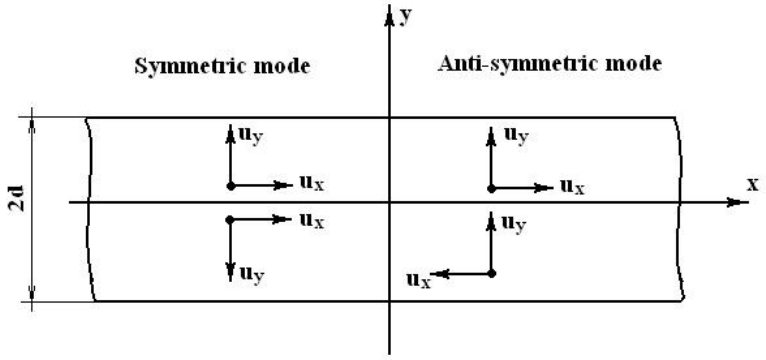

Figure 1 Symmetric and anti-symmetric particle motion across the plate thickness

For the free wave ratio, we derive the homogenous relation by applying the stress free boundary conditions at the upper and lower surfaces (y = ±d, where d is the plate half thickness). On obtains the characteristic equation for the operations (5):

$$\begin{gathered} \left(\xi^2 - q^2\right)\cos qd \sin qd + 4\xi^2 pq \sin pd \cos qd = 0 \\ \left(\text{symmetric motion}\right) \\ \left(\xi^2 - q^2\right)\sin qd \cos qd + 4\xi^2 pq \cos pd \sin qd = 0 \\ \left(\text{ anti-symmetric motion}\right) \end{gathered} \tag{6}$$

Equations (6) accept a number of eigenvalues $\xi_0^s, \xi_1^s, \ldots$, and $\xi_0^A, \xi_1^A, \ldots$, respectively. To each eigenvalues corresponds a set of eigencoefficients (A_2, B_1) for the symmetric case and (A_1, B_2) for the anti-symmetric case. Substitution of these

coefficients into eq. (5) yields the corresponding Lamb mode shapes. Since the coefficients p and q in eq. (6) depend on the angular frequency, ω, the eigenvalues ξ_i^s and ξ_i^A will change with also change with frequency. This phenomenon is named dispersion. Lamb wave are highly dispersion, and their speed depends on the product f·d.

3. Generation of Lamb waves in carbon-epoxy plates using Hertzian contact

If two solid bodies are superposed and pressed with relatively low forces, they get elastically deformed, giving rise to a Hertzian contact between each other. If one of the bodies is spherical of radius R and the other one is a plate material, the contact area is circular of radius a, which can be determined from the relation [12]:

$$a = (FDR)^{1/3} \tag{7}$$

where F is the force and D is give by

$$D = \frac{3}{4}\left(\frac{1-\nu_1^2}{E_1} - \frac{1-\nu_2^2}{E_2}\right) \tag{8}$$

ν_1, ν_2, E_1 and E_2 standing for the Poisson ratio and Young's module for the two bodies.

Thus, by means of the Hertzian contact it can excite in a plate the pressure and the shear ultrasonic wave in the case in which in buffer is generated pressure ultrasonic wave (figure 2).

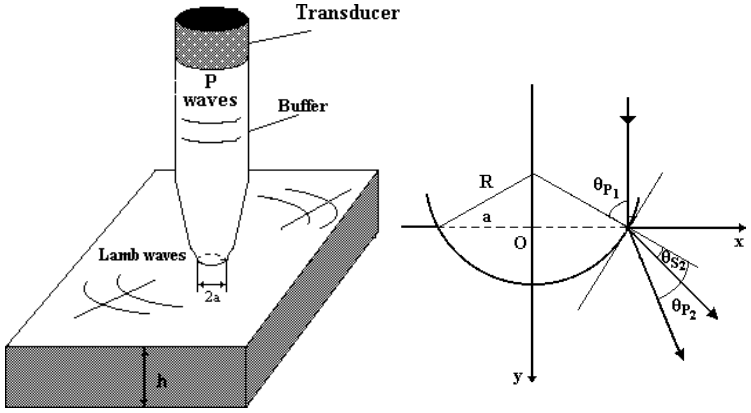

Figure 2 (a) Ultrasonic transducer with Hertzian contact
(b) Detail of the contact

The propagation speed for module A0 in a plane with 2d thickness and density ρ_2 is obtained using transcendental equation (6), for case Hertzian contact. Finally is obtained:

$$c_{AO} = \left(\frac{d}{2\rho_2 D}\right)^{\frac{1}{4}} \omega^{\frac{1}{2}} \tag{9}$$

For case a buffer having curvature radius of pick 2mm, Young modulus 208GPa and Poisson coefficient 0.29 in Hertzian contact with a plate by carbon-epoxy

with thickness 6mm having 48 layers of carbon fibres with orientations $\left[-45^0_2, 0^0_2, 45^0_2, 90^0_2\right]_s$ having density 1.78Kgm^{-3}, Young modulus perpendicular on fibres plane 104GPa and Poisson coefficient 0.31. It was calculated the dependence of propagation speed for module AO in function of plate thickness, the results being presented in figure 3.

The presence of delamination is equivalent with thickness plate composite decreasing and thus the propagation speed for module AO will decrease.

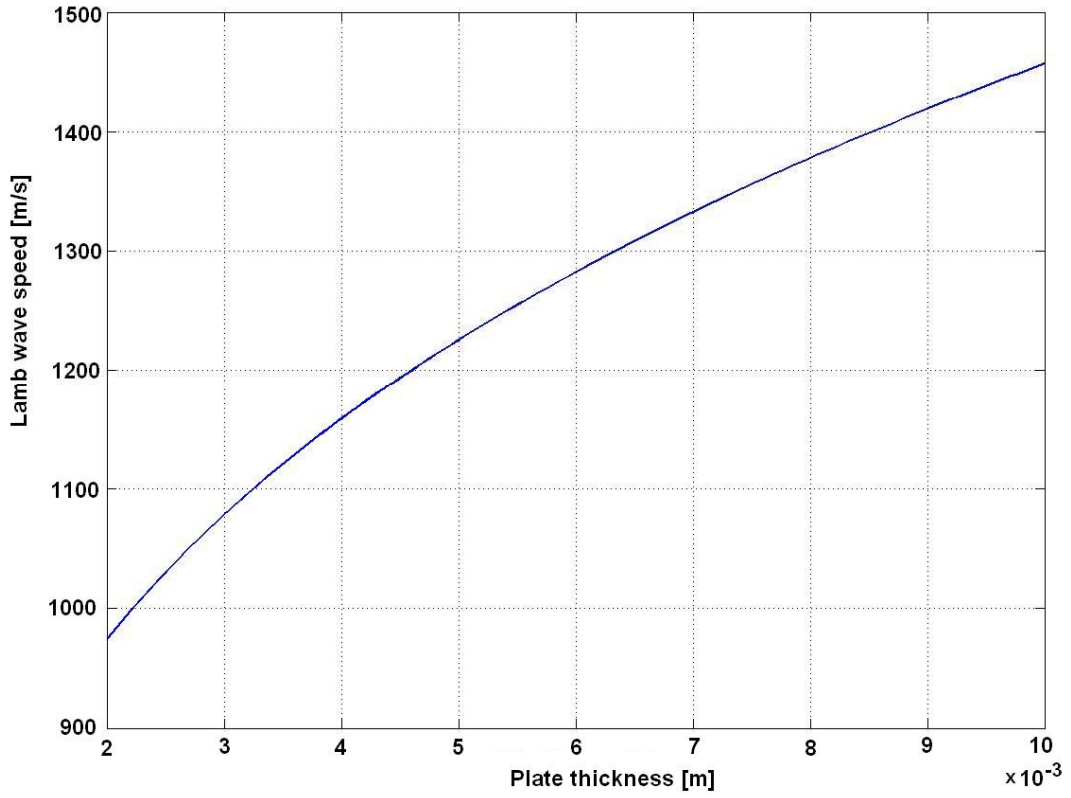

Figure 3 Wave speed for AO Lamb wave-ultrasound frequency 60 kHz

4. Studied samples, experimental set-up

Carbon-epoxy plates with thickness of 6mm having 48 layers of carbon fibres made of Boeing USA were taken in study. The plates were impacted with impact energies between 0.5J and 9J. To impact was made at ONERA – France.

The experimental set-up is presented in figure 4.

The emission transducer was pressed on the surface of composite with a force of approximately 20N. The electronic system allows the measurement of propagation speed with precision of $\pm 0.1\mu s$, the displacement system X-Y allows the positioning with precision $\pm 1\mu m$ and rotating system allows the rotation in step of 2".

During experiments, the emission and reception transducers were maintain at constant distance, only the composite plate bearing the motion.

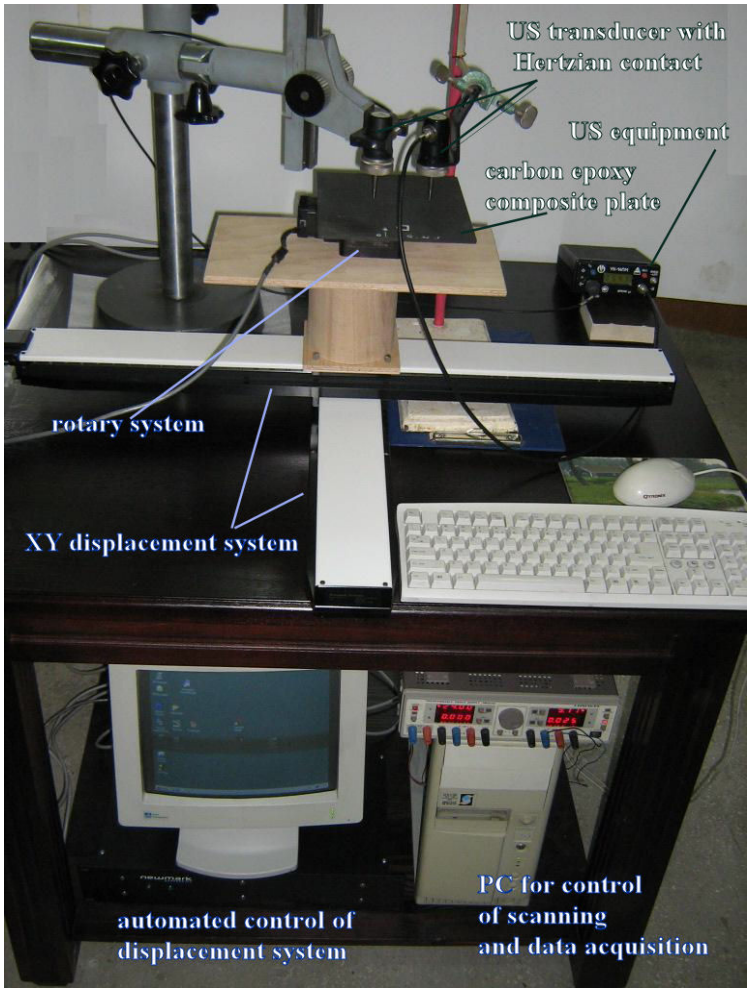

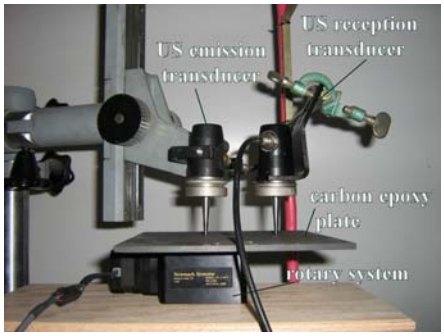

a b

Figure 4 (a) Experimental set-up; (b) Ultrasound transducer

5. Experimental results

A region of 65x65mm which contains the delamination was choose from composite plate. The emission transducer was positioned step by step in angular points shown in figure 5. The angles represent the regions in which speed of module AO decrease with more than $\bar{c}_{AO} - 3x\sigma$, where $\bar{c}_{AO}$ represent the means of propagation speed for module AO in region without delamination and σ is the dispersion of speed values.

Using the theory of evidence given by Shafer and Dempster [13] a data fusion between three measurements to accomplish on each plate imported was achieved.

In Figure 6 are shown the results of the fusion with correct indication of delaminated region and of the area of delaminated region. The impact of plate was made with 9J energy.

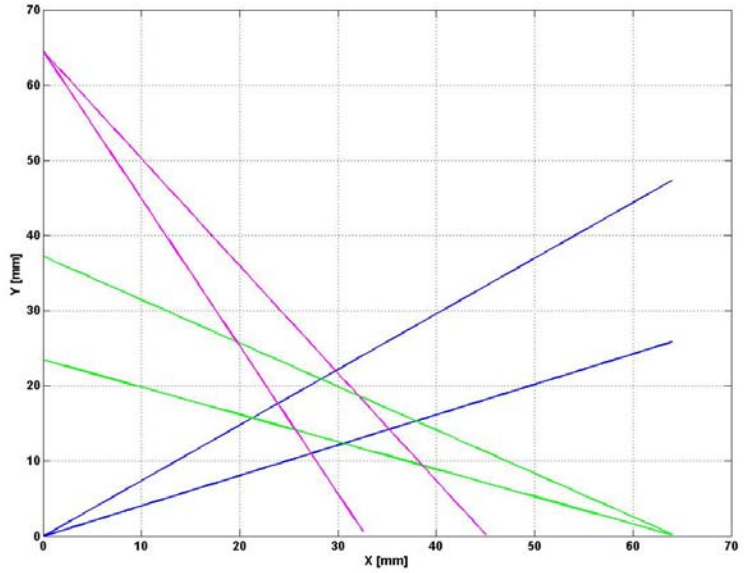

Figure 5. Angular positioning of transducers

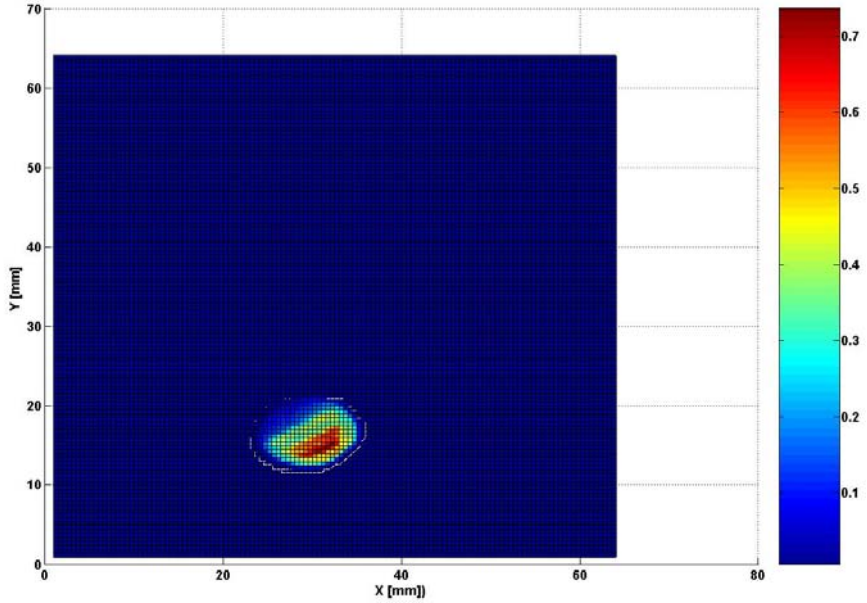

Figure 6 Results of data fusion for 9J impact energy

6. Conclusions

Lamb waves were generated in plates of carbon-epoxy composite using Hertzian contact method. It was calculated propagation speed for module AO, unique nodispersive mode, which is in very good concordance with experimental obtained results. Using 3*σ law, the angular regions in which delamination can be found, and then, predictions by data fusion using theory of evidence to determine position and area of delaminated region were determinate.

Acknowledgements

This paper is supported by Romanian Ministry of Education and Research, Research of excellence Program, under Contract no. 49/2006 acronym ROLIGHT.

Received March 1st , 2007

*National Institute of R&D for Technical Physics Iasi
47 D.Mangeron Blvd., Iasi, 700050, Romania
** Technical University Gh.Asachi Iasi
67 D.Mangeron Blvd., Iasi, 700050, Romania
*** Al.I.Cuza University
11 Carol I Blvd, Iasi, 700506, Romania

REFERENCES

1. L.A. Pilato, M.J. Michno, *Advanced Composite Materials,* Springer Verlag, Berlin, Germany, 1994;
2. M. Mauro, A.T. Marques, *Prediction of low velocity import danged in carbon-epoxy laminate,* Composites Part. A, 33 (2002), pp. 361-368;
3. J. Kim et. al, *Mechanical properties at waves laminates and felt composites using carbon fibers in plane properties,* Composites Science and Technology, 64 (2004), pp. 2221-2229;
4. M.M. Schwarts, *Composite Materials. Properties Nondestructive Testing and Repair,* vol. 1, Prentice Hall Inc., N.J., USA, 1997;
5. V. Giurgiutin, *Tuned Lamb Wave Excitation and Distortion with Piezoelectric wafer Active Sensors for Structural Health Monitoring,* J of Intelligent Material Systems and Structures, 16 (2005), pp. 291-305;
6. M. Lemistre, R. Gouyon, D. Balageas, *Electromagnetic Localization of Distortion in Carbon Epoxy Materials,* SPIE, vol. 3399 (1998), pp. 89-96;
7. R. Grimberg, D.Prémel, A.Savin, Y. Le Bihan, D.Placko, Eddy Current Holography Evaluation of Delamination in Carbon – Epoxy Composits, INSIGHT 43,4, UK,(2001), p.260-264
8. Eric Udd, Stephen T. Kreger, Sean G. Calvert, Marley Kunzler, and Tad Taylor, "Nondestructive Evaluation of Composite Materials Using Multi-axis Fiber Optic Grating Strain Sensors," Proceedings of SPIE, Vol. 5278, p. 1, 2003
9. V. Giurgiutin, j. Bao, W. Zhao, *Active Sensor Wave Propagation Health Monitoring of Beam and Plate Structures,* SPIE, (2001), pp. 1-12;
10. K.M. Holford, C.A. Featherston, R. Pullin, M.J. Eaton, Acoustic Emission Monitoring of Buckling Behaviour in Impact-Damaged Composite Plates, Proceedings of 26th European Conference on Acoustic Emission Testing, September 15-17, 2004 – Berlin
11. R. Grimberg, A.Savin, A.Lupu, L.Iancu, C.Rotundu, A Method to Determine the Debonding Zones in Multilayer Wood Materials, Proceedings of the 15th World Conference of Non-Destructive Testing, Roma, Italy, (2000), IDN 522 - The e-Journal of Nondestructive Testing & Ultrasonics Vol. 5 No. 10 - October 2000
12. L.Landau, E.M.Lifshitz,Theory of Elasticity, Pergamon, N.Y., 1959
13. G Shafer, *A Mathematical Theory of Evidence*, Princeton University Press, 1976

EVALUAREA DELAMINARILOR COMPOZITELOR CARBON EPOXY UTILIZAND UNDE LAMB

Rezumat: Aceasta lucrare prezinta o metoda de evaluare nedistructiva a materialelor compozite tip carbon epoxy bazata pe producerea undelor Lamb de joasa frecventa in materialul de examinat folosind traductori de ultrasunete de joasa frecventa cu contact Hertzian. Se poate estima mult mai precis pozitia si aria suprafetei delaminate, masurand viteza de propagare a undelor Lamb, utilizand metoda de triangulatie si un procedeu de fuziune de date.

BULETINUL INSTITUTULUI POLITEHNIC DIN IAŞI
Tomul LIII (LVII), Fasc. 2, 2007
Secția
ŞTIINȚA ŞI INGINERIA MATERIALELOR

NONDESTRUCTIVE EVALUATION WITH ULTRASOUND OF SANDWICH LIGNO-CELLULOSE COMPOSITES USING NONCONTACT TRANSDUCERS

BY

RAIMOND GRIMBERG*, IOAN CURTU, IOAN SZAVA**,
ADRIANA SAVIN*, ROZINA STEIGMANN*,
NICOLETA IFTIMIE*, MARIUS MIHAI CAZACU*****

Abstract. In this paper we present a method for non-destructive examination of wood based panels ultrasound method that allows the determination of physical and mechanical parameters of the product, as well the debonding of multi-layered wood based panels.

Keywords: ultrasound examination, non contact transducer, and wood based products.

1. Introduction

Wood is a natural composite whit complex structure and diverse properties function of essence, water content and testing direction. It can be used as timber, panels and batten boards. The timber utilized in the furniture industry can be upgraded by sticking veneer foils of noble essence on the basic materials. In this case, the basic material can be board or agglomerated wood chips stuck together in plates, a multi-layers structure being obtained. For other applications, the foils can be from composite materials, usually glass-epoxy.

In the latest time big efforts have made for the introduction of European quality standards, developing of new nondestructive evaluation techniques and adequate instruments for the wood and wood based products examination by ultrasound [1], [2], [3], visual [4], X rays [5]. These techniques shall emphasize and measure wood density, the presence and the surface occupied by knots, wood defects like decay, insect damage, splits, cracks, etc.

In the case of nondestructive examination of wood composites multi-layers, the mean issue is the determination of the regions in which isn't bonding between layers due to deficiency of glue. In the case in which the composite is ennobled by veneer layers applying, besides adherence, the problem of veneer quality evaluation is posed. The using of clasical ultrasound methods in which transducer-examined product coupling is assured through a layer of fluid isn't applicable due to hygroscopic property of wood and veneer damaging. Using the hertzian transducer-examined

product contact [3] even if the impress is very small, reduce the control speed, therefore such equipment can't be mounted on production line.

In this paper is presented a system for nondestructive evaluation of quality of gluing between the layers of plywood in 3 layers, using ultrasound non-contact transducers.

In the same time, to examine the state of veneer layer a visual examination method is used, employing images acquired and processed through typically image processing.

1. Physical principle of nondestructive examination method for multi-layer plywood ungluing using ultrasound non-contact transducer

Being a composite multi-layer plate that presents a ungluing between the layers. An ultrasound beam generated by a non-contact transducer perpendicularly on superior surface of plywood, is propagated through material and is received by the second transducer, identically with the first, placed face to face with the reception transducer, on the other side of plywood, Figure 1.

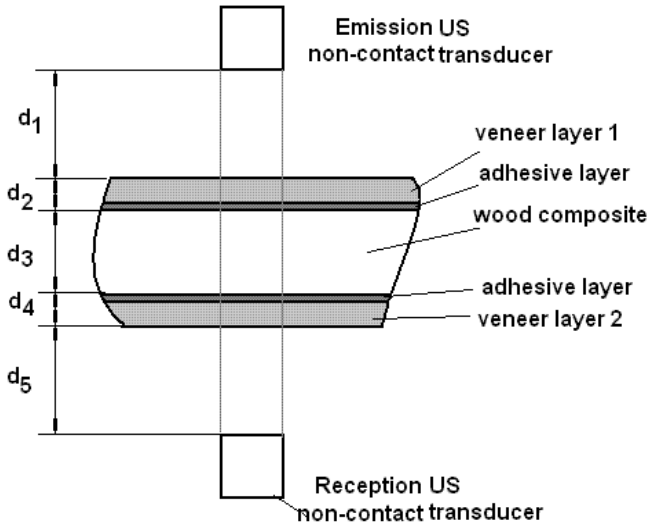

Fig.1: Physical principle

Usually, the thickness of the two veneer layers are identically, thus we can consider $d_2=d_4$. The thickness of adhesive layer is very small, and therefore, despite that the presence of adhesive influences the propagation, it wasn't considered in Fig. 1.

The time of flight, i.e. the time elapsed between the moment of emission and one of reception is given by the relation

$$t_t = \frac{d_1}{c_1} + \frac{d_2}{c_2} + \frac{d_3}{c_3} + \frac{d_2}{c_2} + \frac{d_5}{c_1} \tag{1}$$

where c_1 is the propagation speed of US in air at work temperature; c_2 is US propagation speed in veneer, c_3 is US propagation speed in wood material, d_1, ..., d_5 having the signification from Figure 1.

The arrangement from Figure1 was preferred because if the distance between emission transducer and the reception one remains fixed, the vibration of the plywood

didn't modify the distance traveled by ultrasound in air, then didn't influence the experimental results.

Considering the layered composite as a single material, for 100 KHz frequency of ultrasound beam, 4301±90m/s propagation speed was obtained. The wave length of ultrasound in composite will be approximate 4cm.

The presence of an ungluing in composite material is equivalent with the existence of a barrier in the way of US beam propagation, so that, on the barrier borders, the phenomenon of diffraction can appears [6], [7], (Figure 2)

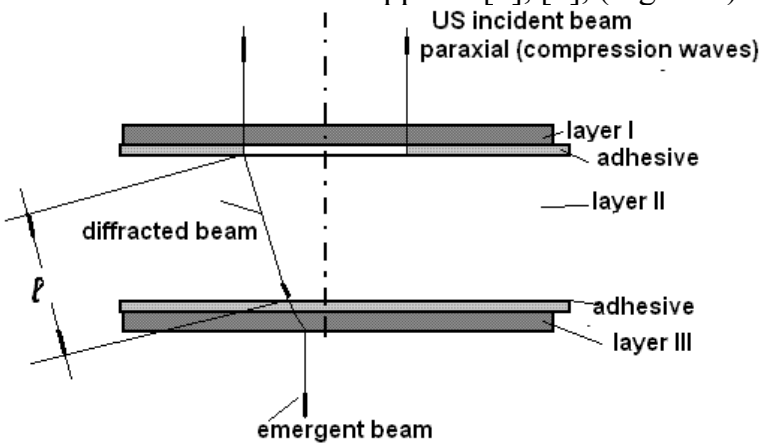

Fig.2: US diffraction

In the condition in which the adhesive layer is considered infinitely thin, the diffraction has take place on a barrier. For big angles of diffraction, function of elastic properties of the layers that the composite contain, a change into the propagation mode can take place; the compression waves could be transformed in shear waves (S wave). This phenomenon leads to an important attenuation of emergent ultrasound beam at the appearance of diffraction on a barrier.

Because the diffracted beam in layer II has lengthy bigger than d_3 ($\ell > d_3$) the total propagation time will increases.

Therefore, the measuring of the time of flight can serve as criteria for the determination of ungluing of multilayer wood composites.

To evaluate the states of veneer layers, the classical method of image processing is preferred. The composites are taken in picture with a video camera. The image is saved in *.BMP format, being presented as 3D matrix. This matrix can be decomposed in three 2D matrixes; each element of these matrixes contains information about the intensity of the three fundamental colors: red, green and blue (RGB). The red matrix contains the maximum of intensity about some possible defects that weren't emphasized at quality control operations of veneer and therefore, is the one with whom will work ahead.

2. The studied samples

The plywood consists in two layers 1mm thick beech veneer glued on two faces of a 2mm thick plate made of agglomerated poplar chips, Urelyte was used for gluing according to the usual procedure. The debonding was simulated by inserting

rectangular frames made of 80μm thin Raylon foil, the frame thickness being 0.5mm and no adhesive being applied inside the frame.

The diagram of the etalon is presented in Figure 3.

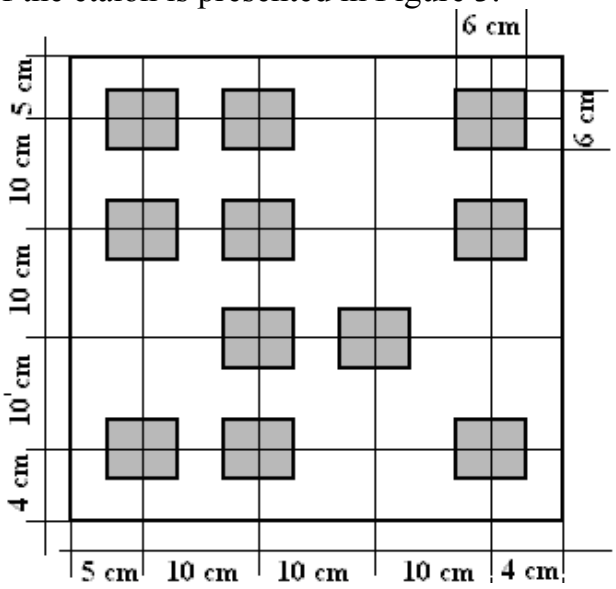

Fig.3: Diagram of etalon

Also, plywood plates, which, after inspection with ultrasound using non-contact transducer, were destructive, controlled to confirm the justness of the method.

3. Experimental set-up

The experimental set-up is presented in Figure 4.

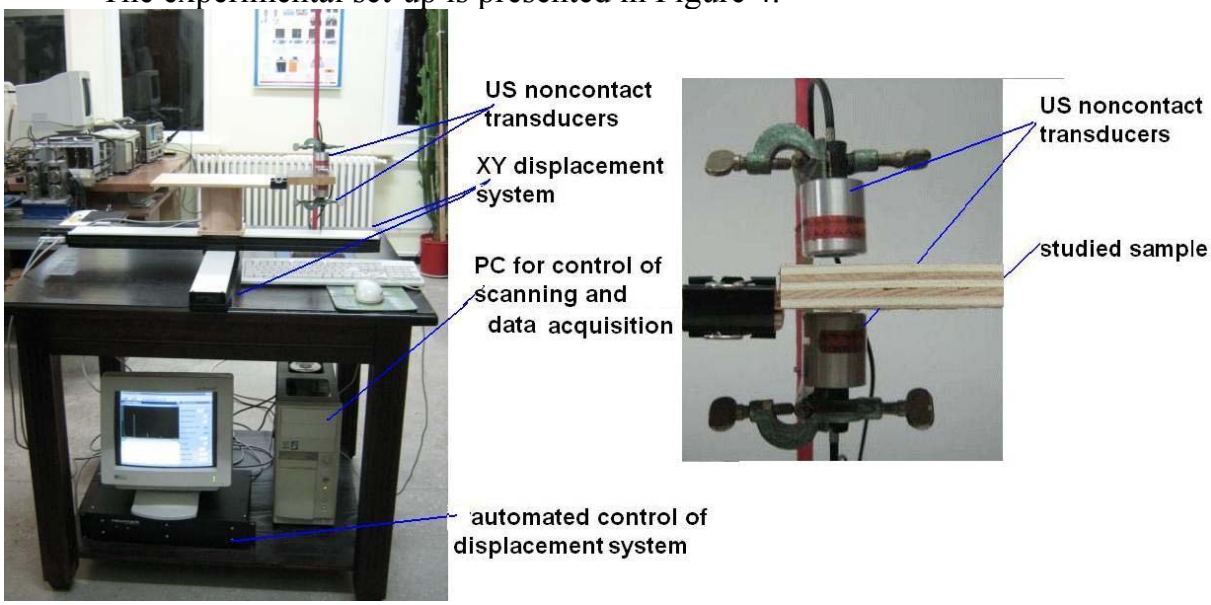

Fig.4: Experimental set-up

The emission and reception transducers are NCG100S25 type, produced by *ULTRAN GROUP* USA, having central frequency 100KHz, 25mm diameter of piezo-

composite plate and 10mm air column. The emission signal, chirps with 100kHz central frequency, is delivered by programmable function generator AWG7223 and amplified until 200V amplitude, value recommended by the transducer's producer.

The US beam is received by the reception transducer, amplified in a large band preamplifier and digital converted in a high speed A/D Converter SFT 4200 type.

The time of flight represents the interval elapsed between first sinusoid from chirps of emission until the reception one. This interval is measured with Programmable Counter/Timer, the data being inserted into PC Texas Micro through IEEE488 interface. To global command of the equipment, a graphical user interface (GUI) developed in MATLAB 6.5 was used. In the same media, the functions for the acquisition of data, image processing and final classification has write.

The plywood has an advance longitudinal moving with 5cm/s and the US transducers scan the examined surface after a transversal direction with 2cm/s speed. The time of flight data were obtained from millimeter to millimeter.

4. Work method

To execute the measurements, a plywood plate that presents ungluing between layers and which was nondestructive examined with the procedure described in [3] is placed between the transducers. The average value of time of flight and dispersion of results are calculated into significant number of points.

According to 3σ rule (σ is the dispersion of time of flight data) [8], so long as the time of flight is in the interval

$$\bar{t} - 3\sigma \le t \le \bar{t} + 3\sigma \tag{2}$$

where $\bar{t} = \dfrac{\sum_{i=1}^{N} t_i}{N}$ represents the average time of flight for a sample without debonding and

$\sigma = \sqrt{\dfrac{\sum_{i=1}^{n} (t_i - \bar{t})^2}{N(N-1)}}$ is the dispersion of data.

It can be considered that the multilayered wood composite plate has corresponding quality with 99.73% probability.

If

$$t > \bar{t} + 3\sigma \tag{3}$$

Results that in the controlled zone exist a ungluing.

If

$$t > \bar{t} - 3\sigma \tag{4}$$

results that in the basis layer of composite exists a fixed inclusion form a material of which propagation speed of compression waves is higher than this of wood, example being the metallic inclusion with an important surface.

For the veneer layers images processing we proceed hereby: the image is decomposed in the 3 matrixes on fundamental colors using ahead the red matrix. The region of interest (ROI) is delimited correlated with the displacing speed. It is searched that ROI

shall be free of distortions, especially keg type. The ROI matrix is filtered by convolution with a Gaussian kernel and then the image is binarized with a adaptive threshold. To emphasize cracks of veneer layer the morphologic operators are used: dilatation and erosion.

Because the two morphologic operators are complementarily, the images of knots and/or cracks appear at 1:1 scale, therefore the dimensions result directly.

At the image of time off flight, the debonding zones appear larger that they are in reality with a scan step, therefore with 1mm.

In the basis of these observations, for the data fusions, the common referential has created.

5. Results

The time of flight measurements made on a region of composite having total thickness 4.5mm, without debonding (the adhesive layer after polymerizing having 0.25mm thickness) show that:

- the average time of flight $\overline{t} = 1.5\mu s$
- the dispersion σ=0.12μs.

The time of flight measurements made on a region from the center of debonding zone show that:

- the average time of flight in the region with debonding $\overline{t} = 2.6\mu s$
- the dispersion σ=0.16μs.

In Figure 5 we present the image of the etalon presented in Figure 3

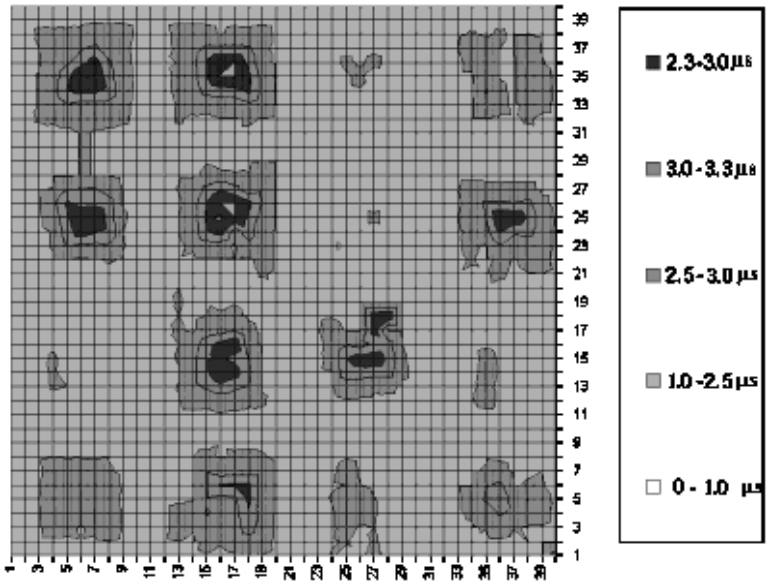

Fig.5: The original image of time of flight

To amplify the quality of the image, the filtering with Gaussian filter was applied, the results being presented in Figure 6.

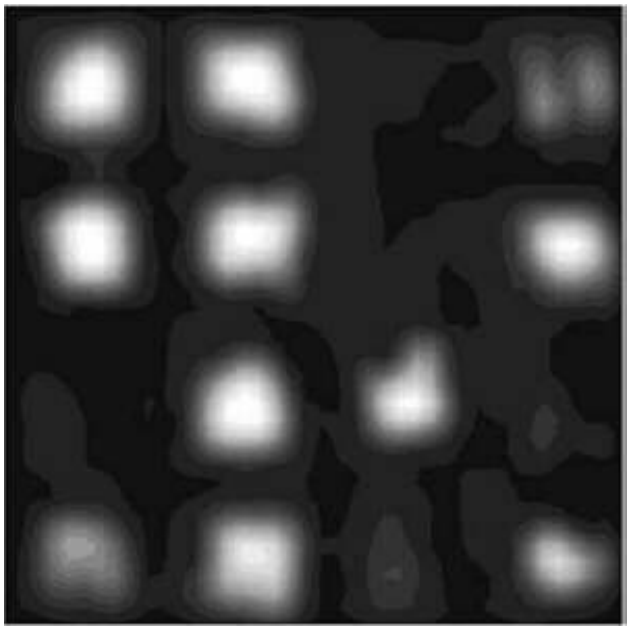

Fig.6: Filtered image of the etalon

6. Conclusions

The multilayered wood based composite materials can be nondestructive evaluated using the method of ultrasound generated and received by non-contact transducers, this method characterizing exactly the regions with debonding between the plywood layers.

To evaluate the quality of veneer layer, the numerical algorithm of image processing was used, that allow the emphasizing of knots, cracks or incorrect joint of veneer.

Acknowledgements

This paper is supported by Romanian Ministry of Education and Research, Research of excellence Program, under Contract no. 49/2006 acronym ROLIGHT.

Received March 1st , 2007

*National Institute of R&D for Technical Physics Iasi
47 D.Mangeron Blvd., Iasi, 700050, Romania
** Transilvania University Brasov,
29 Eroilor Blvd., Brasov, 500122, Romania
***Al.I.Cuza University
11 Carol I Blvd, Iasi, 700506, Romania

REFERENCES

[1] Bucur V, Ansell MP, Barlow CY, Pritchard J, Garros S, Deglise X. 'Physical methods for characterising wood composite panel products.' Holzforschung, 52 no 5 (1998) 553-561

[2] Sandoz J.L. Benoit Y., Demay L., Wood Testing using Acousto-Ultrasonic Technique, Proc. of the 12th Int.Symp. on Nondestructive Testing of Wood, Sopron, Hungary, 2000

[3] Grimberg R., Savin A., Lupu A., Iancu L., Rotundu C., A Method to Determine the Debonding Zones in Multilayer Wood Materials, Proceedings of the 15th World Conference of Non-Destructive Testing, Roma, Italy, (2000), IDN 522
[4] Grimberg R, Savin A., Andreescu A., Iancu L., Steigmann R, Nondestructive evaluation of timber, panels and batten board, The 1st INTERNATIONAL CONFERENCE ADVANCED CONCEPTS IN MECHANICAL ENGINEERING, Bul.Inst.Polit.Iasi, t. L(LIV), Fasc.6B, 2004, pg.147-152
[5] Lindgren O., Medical CAT Scanning X ray absorption coefficient, Proc. of 8th Int.Symp. on Nondestructive Testing of Wood, Vancouver, 1997
[6] Morse P.M., Feshbach H., Methods of Theoretical Physics, McGraw-Hill Ed., NY, 1953
[7] Schmerr Jr., Fundamentals of Ultrasonic Nondestructive Evaluation, ch.8, Plenum Press, NY, 1988
[8] Bendat J.S., Piersol A.G., Random Data: Analysis & Measurement Procedures, John Willey &Sons Inc., NY, 1986

EVALUAREA NEDISTRUCTIVA CU ULTRASUNETE A COMPOZITELOR LIGNOCELULOZICE TIP SANDWICH UTILIZAND TRADUCTORI FARA CONTACT

Rezumat: Aceasta lucrare prezinta o metoda de examinare nedistructiva a compozitelor lignocelulozice utilizand prin ultrasunete utilizand traductori fara contact, permitand determinarea parametrilor fizici si mecanici a compozitelor precum si zonele de dezlipiri din materiale lemnoase multistrat

BULETINUL INSTITUTULUI POLITEHNIC DIN IAŞI
Tomul LIII (LVII), Fasc. 2, 2007
Secția
ŞTIINȚA ŞI INGINERIA MATERIALELOR

NONDESTRUCTIVE EVALUATION OF IMPLANTED PROSTHETIC HEART VALVES BJORK SHILEY CONVEXO CONCAVE TYPE

BY

RAIMOND GRIMBERG[1], ADRIANA SAVIN[1], ROZINA STEIGMANN[1], SORIN LEITOIU[1], FLORINA PINTE[2], RAZVAN PALIHOVICI[3], ALINA BRUMA[4]

ABSTRACT. This paper presents a new electromagnetic method for evaluating Björk-Shiley Convexo-Concave (BSCC) prosthetic heart valves based on the use of a transducer with orthogonal coils. The approach examines the imaginary component of the transducer reception coil signal and uses the first harmonic of the component's power spectrum as the indicator of the condition of the valve. *In vitro* testing of this method with 32 BSCC heart valves has demonstrated 100% accuracy. The proposed method is suitable for detecting and characterizing fractures in BSCC heart valves with high accuracy.

Keywords: eddy current examination, nondestructive methods, transducer with orthogonal coils, Björk-Shiley convexo-concave prosthetic heart valves.

1. Introduction

Heart valves play a critical role in maintaining unidirectional blood flow through the cardiovascular system of the body. Due to reasons such as congenital defect, aging, disease and trauma, the proper functioning of one or more of the heart valves may be impaired. The treatment of such impairment include monitoring, medication, corrective surgery and, in severe cases, valve replacement. A replacement valve can be either a tissue (bioprosthetic) or mechanical in nature. Since a heart valve operates (opens and closes) an average of more than 40 million times a year [1], the design and construction of a prosthetic replacement valve must be both hemodynamically efficient to avoid thromboembolism, and mechanically reliable to prevent failure due to fatigue or stress corrosion [2], [3]. Current prosthetic heart valve devices are subject to strict regulatory ([5],[6]) and engineering controls in design evaluations, manufacturing quality control and *in vitro* verifications, and must demonstrate satisfactory results in both animal and human trials. Until its withdrawal from the market in 1986, the Björk-Shiley Convexo-Concave (BSCC) prosthetic heart valve (Figure 1) was one of the commonly implanted prosthetic heart valves. Between 1979 and 1986, approximately 86,000 BSCC valves were implanted worldwide.

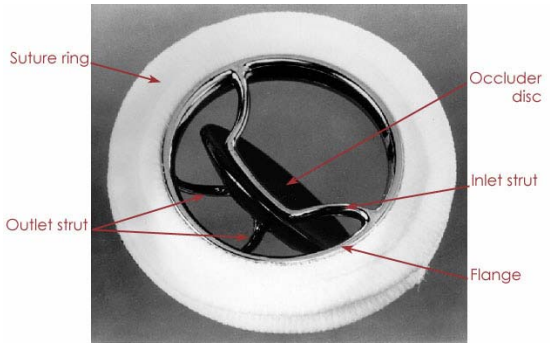

Fig. 1. The BSCC prosthetic heart valve

The BSCC heart valve comprises of a flange (orifice ring), an inlet strut, an outlet strut, a disc occluder and a woven Teflon fabric sewing ring for implantation. The flange and the inlet strut are manufactured as an integral unit from a cobalt-based Haynes-25 alloy bar stock. The outlet strut is formed from a wire of the same alloy and joined to the flange by TIG welding. The occluder disc is composed of an outer Pyrolite® coating over a graphite core. During valve assembly, the disc was inserted into the flange orifice and the outlet strut was cold-bended into place. The metallic parts of the heart valve were then hand-polished to provide mirror finishes, and checked for tolerance compliance. Occasionally, after years of use, the weld at one of the two sites on the outlet strut fractures, resulting in a single-leg separation (SLS) of the strut. This single-leg separation causes the load on the weld at the other end of the strut to increase, thereby setting the stage for it to fail eventually. If the outlet strut is severed from the flange, the occluder disc can escape, leading to loss of blood flow control and fatality in most cases. Although the failure mechanism of the BSCC heart valve is not yet completely understood, many reports ([2], [4]) have suggested material fatigue as the key cause of the fractures. There is, therefore, a necessity and considerable interest in developing techniques to detect cracks and SLS failures before a complete outlet strut fracture (OSF) occurs.

Many detection approaches have been proposed. They generally belong to one of the three categories:

a) High speed and energy cineradiography [7]. This approach is currently the only clinical diagnostic tool for detecting SLS in BSCC heart valve patients despite its less-than-satisfactory success rate. This approach is incapable of detecting and characterizing any fatigue cracks that may be under development.
b) Acoustic approaches [8]-[10]. Noninvasive active and passive acoustic approaches have been proposed to detect cracks and SLS cases in BSCC heart valves. These approaches are mostly under development at the time of this writing and are not yet ready for clinical applications.
c) Electromagnetic approaches [9], [10]. Gradiometer-based electromagnetic approaches have been developed for the detection of fractures in BSCC heart valves. These approaches are highly accurate and promising, but they also involve catherization procedures that carry risks to the patient.

This paper proposes a novel electromagnetic method for noninvasive *in vivo* detection of fatigue cracks in the outlet strut. In this method, an absolute send-receiver transducer ([11], [12]) with orthogonal coils for excitation and reception is used. The method is capable of detecting discontinuities in the outlet strut from a distance equal

to that from an implanted heart valve to the chest surface. Characterization of the detection system with heart valve replicas has demonstrated high system sensitivity to crack size as small as 0.4 mm. Meanwhile, *in vitro* testing of 32 BSCC heart valves with various outlet strut conditions using the proposed method has demonstrated 100% accuracy in indicating SLS failures.

2. Test Specimens

Two types of test specimens were used in the studies:

1. Replica valves made from Haynes-25 alloy using the same manufacturing technologies as the production valves. Each replica has the dimensions and tolerances of a 27 mm BSCC valve. On the outlet strut of each specimen, there is either no crack or an EDM notch with a depth of one of 0.2, 0.4 or 0.6 mm. The replicas do not contain occluder discs (Figure 2a). This is done without loss of accuracy since the contribution of conductivity from the disc is small, as is its influence on the results of the inspection.
2. BSCC heart valves with either intact or single-leg separated outlet struts (Figure 2b). The SLS cases consist of both manufactured and naturally occurring defects. In the manufactured SLS cases, a laser was used to sever one of the outlet strut legs. The valves with naturally occurring SLSs are obtained from either explantations or autopsies of BSCC heart valve patients. The occluder discs are present in these valves.

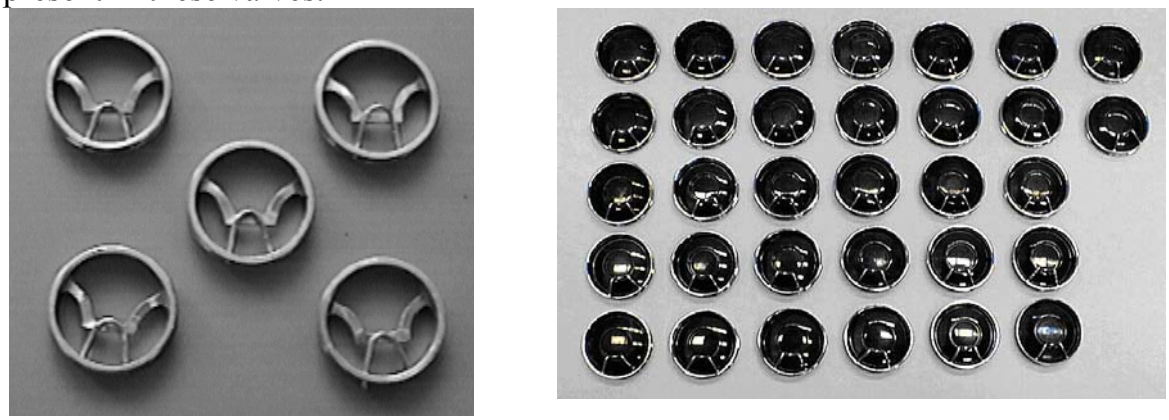

a b

Fig. 2. BSCC valves: a) replicas; b) real valves

2.1 Fatigue Growth Rate

The relationship between the fatigue growth rate per cycle, *da/dN*, and stress intensity range ΔK is given by Paris law [13]

$$\frac{da}{dN} = C\left(\Delta K\right)^n$$

For the Haynes-25 alloy, *da/dN* was also experimentally determined using alloy wire samples with a diameter of 1.2 mm, immersed in Ringer's lactate solution at 37^0C. Figure 3 shows a comparison between the experimental and theoretical results.

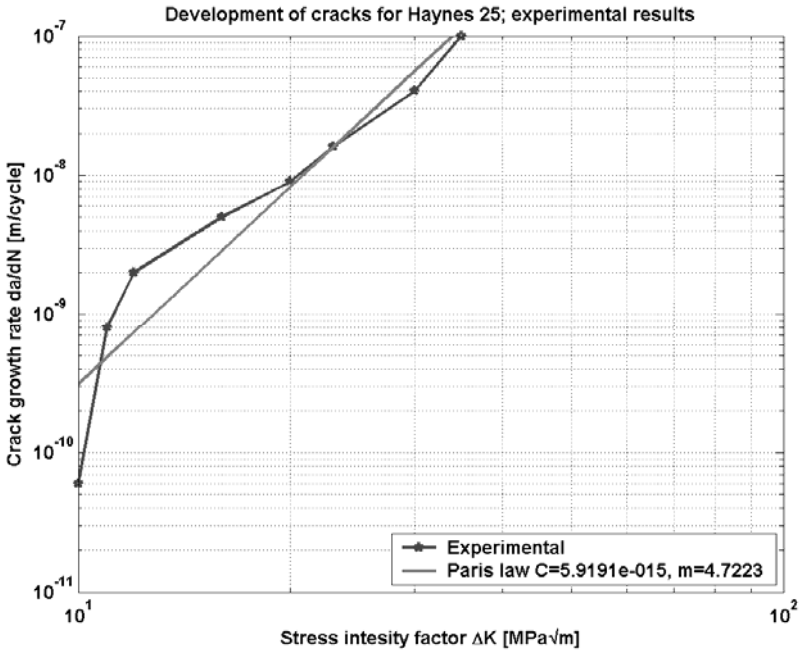

Fig. 3. Comparison of experimental and theoretical results

3. Experimental Setup

A test setup had been constructed to investigate the proposed approach involving the use of orthogonal coils and to demonstrate the method's ability to accurately detect and characterize discontinuities on outlet struts of BSCC heart valves. For each test, the heart valve is rotated 40^0 clockwise and tilted back 60^0 from the vertical, with the outlet side of the valve facing "up" towards the transducer. The transducer is placed approximately 70 mm away from the outlet strut of the valve. This particular valve orientation and test configuration resembles the situation when the transducer is placed on the chest surface of the patient.

During the heart valve inspection, the relative position and distance between the transducer and the heart valve continuously vary due to the cardiac cycle. In order to investigate the effects of this movement on the performance of the proposed orthogonal coils detection system, a cinegram of an unidentified BSCC heart valve patient was obtained and the *in situ* movement of the heart valve was traced from a series of fluoroscopic images [10]. The obtained travel path (Figure 4) was then used to program a motorized stage to simulate the relative movement between the transducer and the outlet strut. In the *in vitro* test setup, the heart valve was held at a fixed location by a silicon holder while the transducer was mounted on and moved by the motorized stage. The schematic diagram of the experimental setup is shown in Figure 5. The proposed detection system uses an absolute send-receiver electromagnetic transducer [11], [12]. The emission coil is 120 mm in diameter and has 300 turns. The reception coil is wounded in the plane orthogonal to the emission coil and also has 300 turns. The advantages of this transducer are its remarkable sensitivity and self-nulling property.

The emission coil was excited with a 60 kHz, $40V_{rms}$ sinusoidal signal. The motorized stages simulating the relative *in vivo* valve-transducer movement had a repetitive frequency of 1.2 Hz, corresponding to a 72 cycles/minute cardiac rhythm. The data acquisition frequency was 100 samples/second.

Fig. 4. Trajectory of a point on the outlet strut during a cardiac cycle

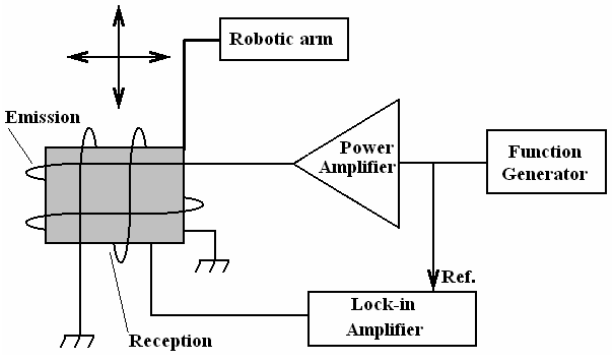

Fig. 5. Experimental setup

The real and imaginary components of the induced signal in the reception coil were measured. Figures 6a and 6b show the phase dependency of the received signal for testing the replica valves with no defect, and those with one of 0.2, 0.4 or 0.6 mm deep EDM notch, respectively.

These results suggest that a simple examination of either the signal amplitude or the phase angle, or both, cannot serve as an indicator of BSCC valve quality state.

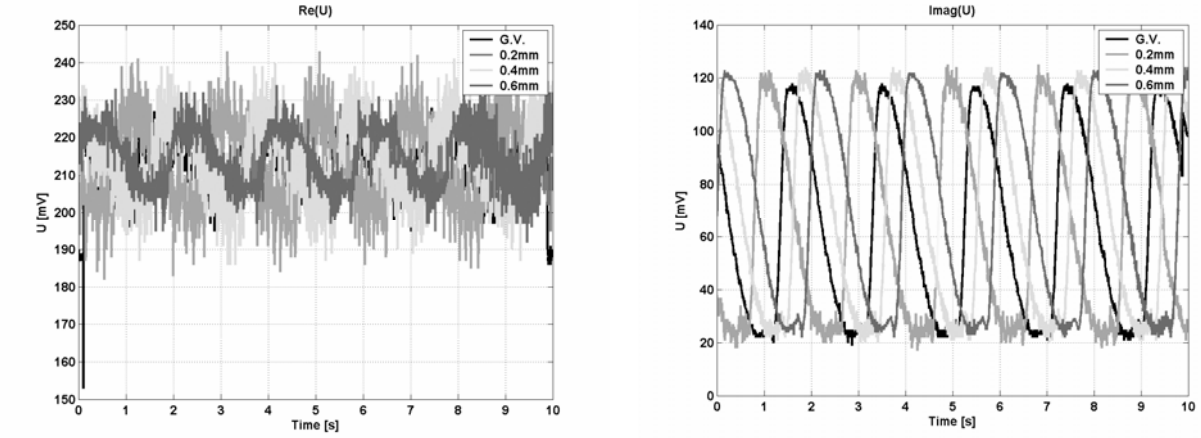

a) real component b) imaginary component

Fig. 6. Experimental measurements

4. Experimental Results

In the proposed detection system, the power spectrum is obtained for the imaginary component of the reception coil signal. The amplitude of the first harmonic of this power spectrum is then used as the indicator of BSCC valve quality state.

The power spectrum of a signal U is defined as

$$S = \frac{1}{N}\, fft\left(\mathrm{Im}(U)\right) * conj\left(\, fft\left(\mathrm{Im}(U)\right)\right)$$

where N is the number of samples and *fft* is the Fast Fourier Transform function. The power spectrum contains N harmonics.

4.1 Determination of Probability of Detection (POD)

One hundred measurements were taken on BSCC valve replicas with intact outlet struts as well as those with EDM slots of 0.2, 0.4 and 0.6 mm deep. The recorded signals were processed using the procedure described above. Examples of the processing scheme outputs are shown in Figure 7 for 12 of the measurements.

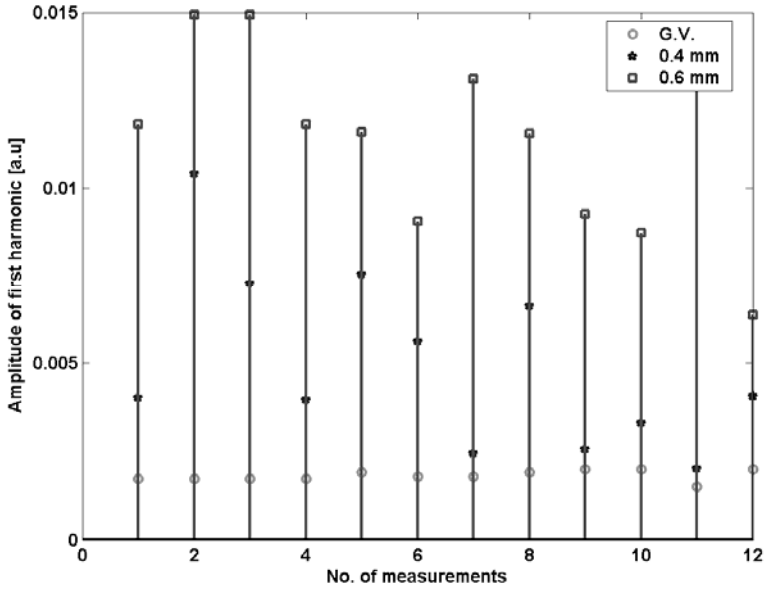

Fig. 7. Experimental results on BSCC replica valves

From the measured data, the lower-bound for the probability of detection with a 95% confidence level [14] was determined for each slot depth. The results are summarized in Table 1.

Table 1. The lower-bound probability of detection for a 95% confidence level for various slot depths

Slot depth [mm]	Probability of Detection (POD) [%]	Probability of Missing Flaw (PMF) [%]
0.2	41.3	58.7
0.4	84.6	15.4
0.6	97	3

Although all the 0.6 mm cases were correctly classified, the POD was less than 100% due to the imposed 95% confidence level and the fact that the number of measurement was 100.

4.2. In Vitro Testing with BSCC Heart Valves

Double-blind *in vitro* tests using 32 BSCC heart valves were also performed. The test samples consisted of 12 valves with intact outlet struts, 10 valves with manufactured SLSs and 10 explanted valves with SLSs. The data collected are

processed and the results are presented in Figure 8. In this figure, only the amplitude of the first harmonic of a signal's power spectrum is considered. The decision threshold was obtained using the 3σ law [13]: the mean plus three times the standard deviation of all the good valve data points:

$$Threshold = \mu_{g.v.} + 3\sigma_{g.v.}$$

Any valve with a data point located above this threshold was considered an SLS valve. Using this technique, the proposed detection method achieved a 100% correct classification with all the BSCC heart valves samples.

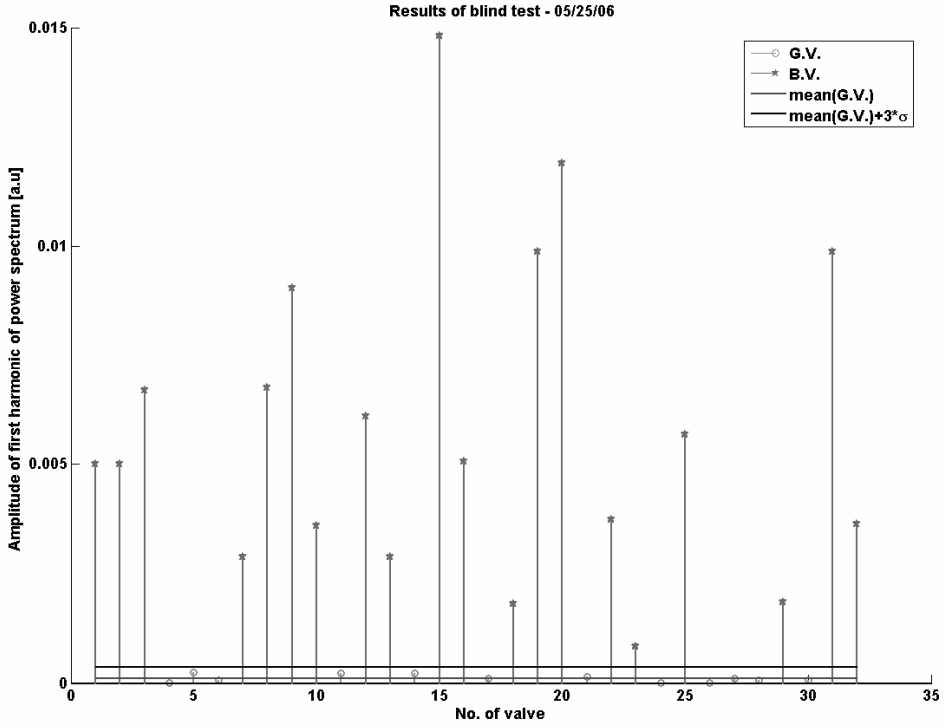

Fig. 8 Results of the double-blinded *in vitro* test

6. Conclusion

A novel electromagnetic method has been developed for noninvasive detection of cracks in the outlet strut of BSCC prosthetic heart valves. The method uses an absolute send-receiver transducer with a set of orthogonal coils for emission and signal reception, respectively. System characterization and performance evaluation have been performed with BSCC heart valves and replicas. With the valve replicas, this detection method has demonstrated a POD of 86.4% for a 0.4 mm deep crack, and a POD of 97% for a 0.6 mm deep slot in the strut.

An *in vitro* test system is constructed with motorized stages to simulate the relative movement between the heart valve and the transducer. Double-blind testing of 32 BSCC heart valves with various outlet strut conditions using this system resulted in 100% correct classification of single-leg separated valves. With the current clinical diagnostic success rate of 68% using cineradiography, the proposed detection method is highly promising.

Acknowledgements

This paper is supported by Romanian Ministry of Education and Research under the National University Research Council - Grant no.586/2006.

Received March 1st , 2007

[1]National Institute of R&D for Technical Physics Iasi
47 D.Mangeron Blvd., Iasi, 700050, Romania
[2] Central Army Hospital, 88, Int Furtuna Stefan, Bucharest, Romania
[3] Medical and Pharmacy University Gr. T. Popa Iasi, 16, Universitatii, 700115 Iasi,Romania
[4] Al.I.Cuza University,11 Carol I Blvd, Iasi, 700506, Romania

REFERENCES

[1] V.O. Bjork, Metallurgic and design development in response to mechanical dysfunction of Bjork-Shiley heart valves, Scand J Thorac Cardiovasc Surg. 1985; 19 (1), pp. 1-12
[2] R.O. Ritchie, P. Lubach, Fatigue life estimation procedures for endurance of cardiac valve prosthesis: Stress/life and damage-tolerant analysis, J. Biomechanical Eng., 108, (1986), pp. 153-160
[3] P. Hedger, Single-leg separations in explanted BSCC heart valves, Lancet, 343, (1994), pp. 294-295
[4] P. Hedger, Important updated information for physicians about patients with Björk-Shiley convexo-concave heart valves – Dear Doctor letters, Irvine, CA: Shiley Inc. March/April, 1993.
[5] ISO 5840:1996 (E) Cardio-vascular implants – cardiac valve prostheses
[6] EN 12006-1:1999 Non-active surgical implants – Particular requirements for cardiac and vascular implants : Part I. Heart valve substitutes
[7] W.W. O'Neil, J.G. Chandler, G.T. O'Connor, Radiographic detection of strut separation in BSCC valves, New Engl. J. Med, 333, (1995), pp. 414-419
[8] J.W. Candy, H.E. Jones, Classification of Prosthetic Heart Valve Sounds: A Parametric Approach, J. Acoustic Soc. of America, 97, 6, (1995), pp. 3675-3687
[9] S. Udpa, New electromagnetic methods for the evaluation of prosthetic heart valve, J. Appl. Phys., 90, (2002), pp. 1-5
[10] S.C. Chan, R. Clifford, S. Majunar, N. Nair, S. Ramakrishnan, Y. Li, P. Ramuhalli, L. Udpa, S. Udpa, Novel Methods for detecting fractures in prosthetic heart valves, INSIGHT, 47, (2005), pp.15-19
[11] E. Radu, R. Grimberg, A. Savin, O. Mihalache, Modelling the operation of the eddy current transducer with orthogonal coils in the presence of material discontinuities, Sensors and Actuators, A, 59, (1997), pp. 201-204
[12] R. Grimberg, A. Savin, E. Radu, O. Mihalache, Nondestructive Evaluation of the Severity of Discontinuities in Flat Conductive Materials Using the Eddy Current Transducer with Orthogonal Coils, IEEE Trans on Mag. 36, 1, (2000), pp. 299-307
[13] J. Lemaitre, J.L. Cheboche, Mechanics of Solids Materials, Cambridge University Press, 1990
[14]. R.C. McMaster, R.C.P. McIntire, M.L. Master, Nondestructive testing handbook (2nd Ed), 4 Electromagnetic testing, American Society for Nondestructive Testing, London, 1986
[15] D.W. Wieting et all., Strut fracture mechanism of the BSCC heart valve, J. Heart Valves Dis., 8, 2, (1999), pp. 206-217

EVALUAREA NEDISTRUCTIVA A PROTEZELOR DE VALVE PENTRU INIMA IMPLANTATE, TIP BJORK SHILEY CONVEXO CONCAVE

Rezumat . Aceasta lucrare prezinta o noua metoda electromagnetica pentru evaluarea valvelor protetice pentru inima tip Björk-Shiley convexo-concave (BSCC) utilizand un traductor cu bobine ortogonale. Abordarea examineaza componenta imaginata a semnalului receptionat de traductor si utilizeaza prima armonica a componentei spectrului de putere ca indicator al conditiei valvei. Testarile in vitro a acestei metode pe 32 de valve BSCC a demonstrat acuratetea metodei. Metoda propusa este convenabila pentru detectarea si caracterizarea cu acuratete a fisurilor in valvele BSCC.

BULETINUL INSTITUTULUI POLITEHNIC DIN IAŞI
Tomul LIII (LVII), Fasc. 2, 2007
Secția
ŞTIINȚA ŞI INGINERIA MATERIALELOR

LIFETIME PREDICTIONS FOR MEDICAL PROSTHESES MADE FROM NANOSTRUCTURED OXIDES OF ZR, HF, AL

BY

RAIMOND GRIMBERG*, ADRIANA SAVIN*, ROZINA STEIGMANN*, NICOLETA IFTIMIE*, ALINA BRUMA**

Abstract: In this paper, the fatigue of ceramics for biomedical implant devices is briefly described by examining the commonality of mechanisms affecting fatigue-crack growth in ductile and brittle materials, with particular focus on the methods for lifetime prediction.

Keywords: lifetime prediction, implanted prosthesis, fatigue-crack growth, ceramic materials

1. Introduction

Modern medical prosthesis as dental implant, knee prosthesis and hip stem are made from high strength brittle materials such ceramics, intermetallics and their respective composites for structural applications where cyclical loading is critical. More over, it is now known that they are susceptible to cyclic fatigue failure [1], [2]. Ironically, this fatigue susceptibility increases in microstructures designed for greater damage tolerance.

In brittle materials, such as monolithic and composites ceramics and intermetallics, the mechanism associated with fatigue-crack propagation are quite distinct from those encountered in metal fatigue. The sensitivity of crack-growth rates, da/dN, to the applied stress intensity K, for example, is markedly higher that in most metals. The notion that crack growth is a mutual competition between intrinsic microstructural damage mechanisms and extrinsic crack-tip shielding mechanisms provides a useful framework to compare fatigue mechanisms of ductile and brittle materials. Intrinsic mechanisms are defined as those which promote crack extension via processes at or ahead of the crack tip, while extrinsic mechanisms operate behind the crack tip and typically retard crack growth.

In this paper, the fatigue of ceramics for biomedical implant devices is briefly described by examining the commonality of mechanisms affecting fatigue-crack growth in ductile and brittle materials, with particular focus on the methods for lifetime prediction.

The importance of these researches is due in first row to the useful of these materials in different types of biological implants, figure 1.

a

b

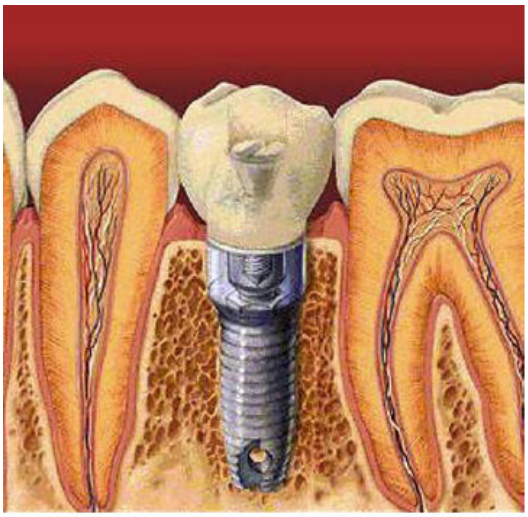

c

Figure 1. Biological implants
a) knee prosthesis,
b) hip stem
c) dental implant

2. Studied samples

Ceramic plates from ZrO_2 stabilized with HfO and Al_2O_3, were investigated.

The company Carma –Marseille, France, produces total hip prosthesis with ceramic-ceramic couple from these materials.

The plates have 2x2x15mm dimensions, being obtained through sintering from nanometric powders.

In the case of plates from Al_2O_3, the average dimension of grains was 1.3μm and in the case of ZrO_2, this was between 10nm and 1μm. the plates were cyclically loaded (sinwave R=0.1) in cantilever bending using mechanical test frame ELF 3200 produced by Endura TEC –USA. The frequency was 1Hz.

Cycling was periodically interrupted, after intervals of 500-1000cycles during which the sample was removed from the machine and the tensile side examined for cracking using bright-field optical microscope Olimpus STM-UM with 0.5μm resolution.

The stress –intensity range was calculated using solutions for surface cracks in bending [3]. The report between depth and semi-length was considered approximately 1.

Crack growth rates, da/dN, were computed by dividing crack extension by the number of cycles for each cycling interval.

Principal mechanical characteristics were put as our disposal by the producer and are indicated in table 1.

Table 1.

Mechanical parameter	***Al_2O_3***	***ZrO_2***
Young modulus [GPa]	380	220
Poisson coefficient	0.28	0.31
Density [kg/m^3]	3.9	6.1
Compression strength [GPa]	~4	~6

The crack – opening profiles has been measured using scanning electron microscope Jeal 7312 – Japan. All the measurements have been made in Characterization Laboratory – Mechanical Department – College of Engineering, Michigan State University.

3. Experimental results

In figure 2 is presented the dependence of fatigue growth rates da/dN function of applied stress intensity range Δk, for three average grain size of ZrO_2, certain 10nm, 70nm si 1μm.

Using a best fitting method for each samples, the Paris Law graphic was traced, corresponding, the constant being determined.

The classical form of Paris Law was taken into consideration [4]

$$\frac{da}{dN} = C\left(\Delta k\right)^m \tag{1}$$

The constant C and the exponent m were determined for each grain size, the results form table 2 being obtained.

Table 2. Paris Law coefficients

	Grain size (medium value) [nm]		
	10	70	1000
m	31.73	18.20	19.04
C	$3.16*10^{-18}$	$3.16*10^{-16}$	$5.012*10^{-22}$

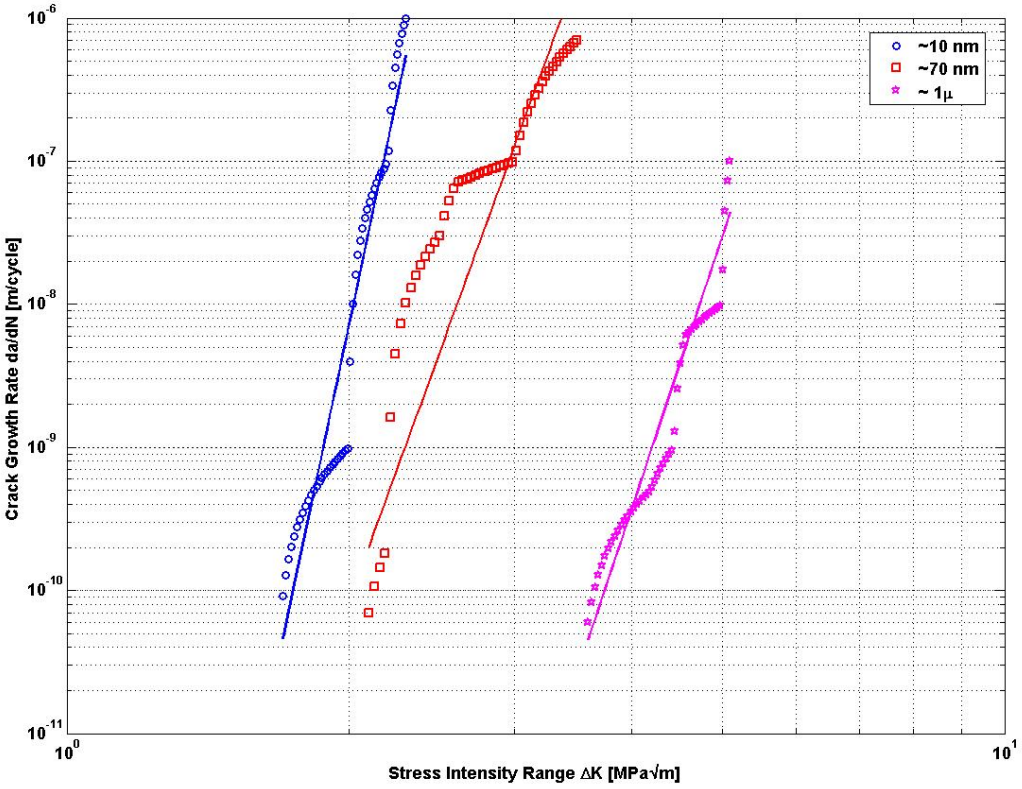

Figure 2. Fatigue-crack growth rates da/dN v.s the applied stress-intensity range for various grain size

Examining the curves from figure 2 as well as the data from table 2, it is observed that, in the case of ceramics and in the first row, in the case of ZrO_2, the exponent m takes high values, compared with values of metals, showing a mark sensitivity of growth rates to k_{max}, rather than to Δk [5]. From this reason, the Paris law can be write as

$$\frac{da}{dN} = C'\left(k_{\max}\right)^n \left(\Delta k\right)^p \tag{2}$$

where C' is scaling constant and n+p=m. The exponents n and p from modified Paris law [1] were determined, the results being presented in table 3.

Table 3. n and p exponents of modified Paris Law

	Grain size (medium value) [nm]		
	10	70	1000
n	~30	16.70	18.30
p	1.70	1.50	0.70

It is observed that in all cases p<<n and in the same time, the exponent p decrease together with average grains size.

The dependence of exponent p by average particle size is given in figure 3.

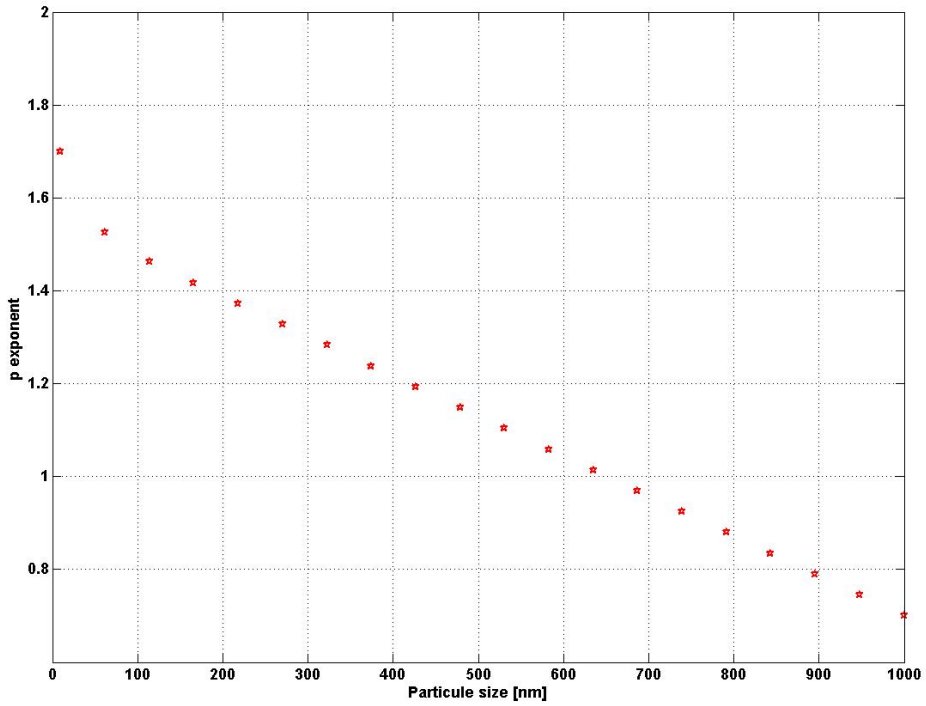

Figure 3. p- exponent vs particle size

4. Fatigue-crack propagation in ZrO_2 ceramics

Resistance to crack extension results from a competition between two classes of mechanisms. Crack growth is promoted ahead of the crack tip by intrinsic microstructural damage mechanisms, and impeded by extrinsic mechanisms acting primarily behind the crack tip, which serve to screen the crack tip from the far-field driving force.

Intrinsic mechanisms are an inherent property of the material, and thus are active irrespective of crack size or geometry. They control driving forces (or stress intensities) necessary to initiate cracking. Extrinsic mechanisms, conversely, act in the crack wake and are thus dependent on crack size and specimen geometry.

Whereas the cyclic processes in metal fatigue are predominantly intrinsic in nature, cyclic fatigue processes in ceramics are extrinsic. This is consistent with the marked dependency of growth rates on K_{max} in ceramics and a similarity in fracture surface appearance under cyclic and monotonic loading. Is considered the mechanism of fatigue degradation operating in ZrO_2 ceramics. In this case, decay in bridging is associated with the relative motion and subsequent frictional wear of ligaments or grain spanning the crack walls.

Under monotonic loading, the closing traction distribution associated with grain bridging, p(x), has been well documented. It can be expressed in terms of a bridging zone length, L, an exponent, k, and a peak bridging stress, P_{max}, as

$$P(x)=P_{max}\left(1-\frac{x}{L}\right)^{k} \tag{3}$$

The function p(x) describes the bridging stress distribution as a function of distance behind the crack tip, x, starting from a maximum value of P_{max} at the crack tip (x = 0), and falling to zero at the end of the bridging zone (x=L).

Under cyclic loads, the repetitive opening and closing of the crack results in a decrease in the toughening capacity of the bridging zone by reducing the grain bridging stress.

Bridging-traction distributions under specified loading conditions can be quantified by comparing measured crack-opening profiles, u(x), to known elastic solutions for bridged cracks [5]. The net crack-opening profile, u(x), for a linear-elastic crack under an applied far-field stress intensity, KA, with a bridging traction distribution, p(x), of length L acting across the crack faces can be expressed, in terms of the appropriate elastic modulus E', as:

$$u(x)=\frac{K_A}{E'}\left(\frac{8x}{\pi}\right)^{1/2}+\frac{2}{\pi E'}\int_0^L p(x')\ln\left|\frac{\sqrt{x'}+\sqrt{x}}{\sqrt{x'}-\sqrt{x}}\right|dx' \tag{4}$$

The first term in Eq. (4) reflects the traction free crack under tensile loading in small-scale yielding, and the second term accounts for contributions associated with the traction-stress distribution.

Because Eq. (4) is the near-tip solution and neglects specimen boundary or geometry effects, this description is only sufficient when bridging zones are small compared to specimen size and crack length, figure 4, figure 5.

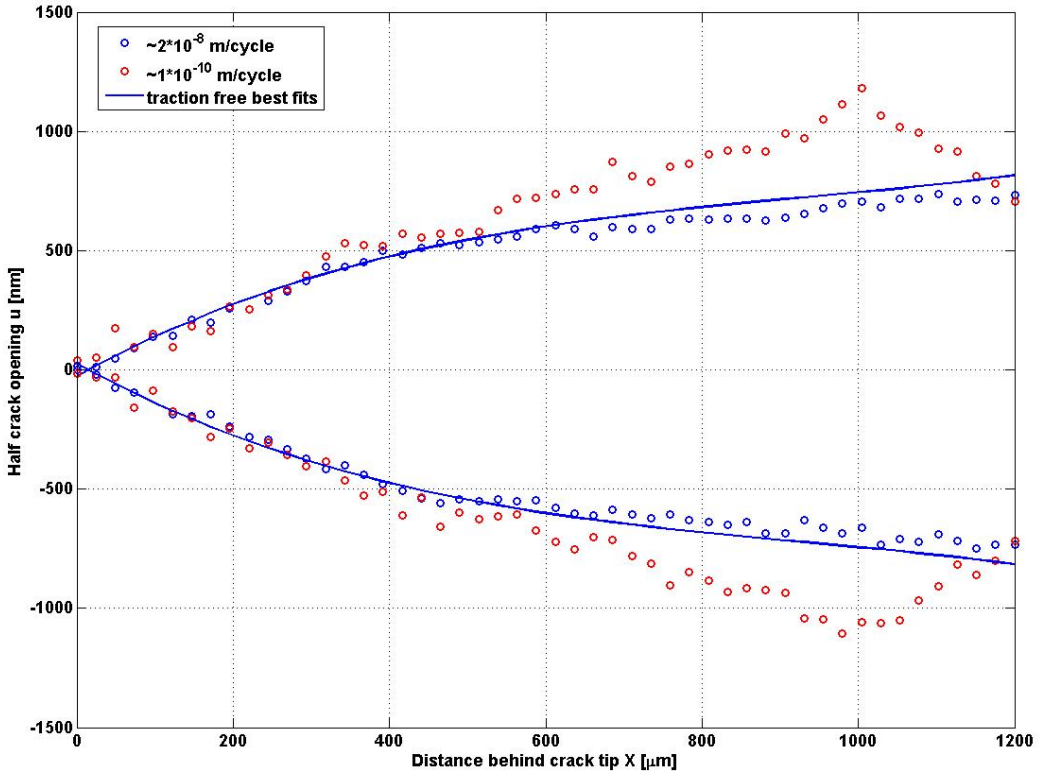

Figure 4

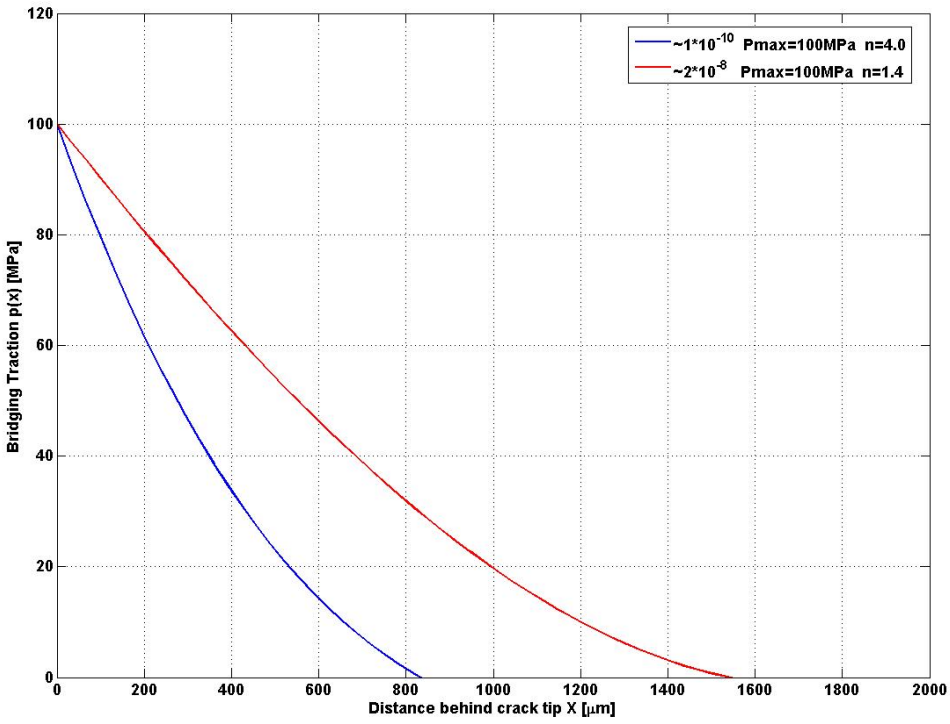

Figure 5

The bridging distribution can be estimated using Eq. (4), and fitting to the form of p(x) described in (3). Once p(x) is determined, it is possible to calculate the associated R-curve using the equation

$$K_B(\Delta a)=\left(\frac{2}{\pi}\right)^{1/2}\int_0^{\Delta a}\frac{p(x)}{\sqrt{x}}dx \tag{5}$$

where K_B is the bridging term and Δa is the amount of crack extension.

5. Lifetime estimation

Once the mechanisms of fatigue crack propagation are identified, is relatively simple to effectuate lifetime prediction.

Because in the case of fatigue crack, both for metals and ceramic materials, their aspect is semicircular

$$K = Q\sigma(\pi a)^{1/2} \tag{6}$$

where $Q=2/\pi$.

Large tolerant lifetime analyses can be performed for brittle implants in similar manner to metallic devices

$$N_t = \int_{a_0}^{a_t}\frac{da}{CQ^m\Delta\sigma^m\pi^{m/2}a^{m/2}} \tag{7}$$

Analyses are complicated by scatter in toughness and fatigue data and by large crack-growth exponents (m in Paris law).

If a lifetime ~100 years, which can correspond to 10^8 cycles is imposed, the value of preexistent crack shall be smaller than 30μm.

6. Conclusions

The ceramic materials from stabilized Al_2O_3 and ZrO_2 are utilized at larger scale in the construction of implantable prosthesis. The extreme high value of m exponent made these materials to become very sensitive at stress and at initial cracks dimensions. For the prosthesis having ~100 years lifetime, initial flaw size must, in this case, be less than ~30μm.

From quality control point of view, this imposes nondestructive detection methods able to reject components that contains cracks with depth bigger than 30μm.

Acknowledgements

This paper is supported by Romanian Ministry of Education and Research, Research of excellence Program, under Contract no. 6110/2005, acronym SINERMAT and Nucleus Program PN 06 - 38 01 03.

Received March 1st , 2007

**National Institute of Research and Development for Technical Physics Iasi*
47 D.Mangeron Blvd, 700050, Iasi, Romania
*** Al.I.Cuza University*
11 Carol I Blvd, Iasi, 700506, Romania

REFERENCES

[1] R.O. Ritchie*, C.J. Gilbert, J.M. McNaney, Mechanics and mechanisms of fatigue damage and crack growth in advanced materials, International Journal of Solids and Structures, 37, (2000) , pp 311-329

[2]. R.H. Dauskardt, , 1993. A frictional-wear mechanism for fatigue-crack growth in grain bridging ceramics. Acta Metallurgica et Materialia 41 (9), 2765±2781

[3] J.C.Newman, , I.S.Raju, , An empirical stress-intensity factor equation for the surface crack. Engineering Fracture Mechanics 15, (1981), pp.185–192.

[4] F Ellyin,., Fatigue Damage, Crack Growth and Life Prediction. Chapman & Hall, London, UK, 1997.

[5] J.Radel, J.Kelly, B.R. Lawn, In situ measurements of bridged crack interfaces in the scanning electron microscope, Journal of the American Ceramic Society 73 (11), 1990, pp 3313-3318.

PREDICTIA TIMPULUI DE VIATA PENTRU PROTEZE DIN OXIZI NANOSTRUCTURATI DE ZR, HF SI AL

Rezumat: Aceasta lucrare se prezinta pe scurt fenomenul de oboseala in materiale ceramice pentru implanturi biomedicale, examinand mecanismele afectate de cresterea fisurilor de oboseala in materiale ductile si casante, in particular metodele de predictie de timp de viata..

BULETINUL INSTITUTULUI POLITEHNIC DIN IAŞI
Tomul LIII (LVII), Fasc. 2, 2007
Secția
ŞTIINȚA ŞI INGINERIA MATERIALELOR

MODELING OF BEHAVIOR OF PRESSURE TUBES MADE FROM ZR 2.5%NB FROM CANDU NUCLEAR REACTORS

BY

RAIMOND GRIMBERG*, ADRIANA SAVIN*, ROZINA STEIGMANN*, SORIN LEITOIU*, ALINA BRUMA**

Abstract: In this paper it was elaborate a Markov model for life time prediction of pressure tubes in inspection of nuclear reactors PHWR type using MATLAB 7.0 program with a series of apriority knowledge; it was developed a soft using MATLAB 7.0.

Keywords: life time prediction, pressure tubes, degradation state.

1. Introduction

Pressure tubes (PT) assure the cooling fuel channels in nuclear power plant CANDU type. During the run of nuclear power plants, it appears hydrogen which is absorbed by the material of manufactured tubes, Zr-2.5%Nb alloy, due to the zirconium corrosion. The absorbed hydrogen forms the zirconium hydrates which are decreasing the materials resistance. Under the influence of hydrate, the incipient cracks in pressure tubes can develop in unstable and uncontrolled forms being named Delayed Hydrogen Cracking (DHC) phenomena. The nature of the crack's incipient can have a different reason among which degradation of spring garters which is designed to keep the pressure tube concentric with calandria tube, by cooler system for fuel bundles.

The statistically analysis for existent data is made by the IAEA Vienna and that indicates a slowly evolution to a dangerous state systems.

The Canadian Norms of flaw depth restriction to 1.6 mm by from wall thickness (4.1mm) for pressure tubes, after that it imposes the change of pressure tubes. Some thresholds are imposed to establish limit values for degradations indicator for materials or some mechanical-physical systems.

Improving the knowledge of degradation phenomenon is the key of industrial issue for the control of ageing of a plant unit. In this paper, the focus is placed on degradation mechanisms that affect passive components (such as crack length, corrosion loss of material etc) [2, 3].

The stochastic processes provide an interesting way of dealing with this uncertainty. As we shall see, these models rely on very simple considerations on

physics (e.g. linear or nonlinear trend) and complete this information by a statistical treatment of a degradation measures dataset, generally obtained via *non-destructive tests (NDT)* [4]. In such models, the degradation indicator becomes a *random variable.*

For a given environment, the aim is not to forecast the exact value of X_t, but rather the range of possible values weighted by a *probability distribution function (* P_r) denoted by f_{Xt} ; the more important $f_{Xt}(x)$, the more likely X_t to take values in ranges [a, b] is given of relation:

$$P_r\left(a \le X_t \le b\right) = \int f_{Xt}\left(x\right) dx \tag{1}$$

To describe the degradation processes we used Markov processes [3]. A Markov process is a stochastic process with the properties that the given value of X(t), at time τ, where τ > t, are independent of the values of X(u), u < t.

We assume that the system structure can be any one of N ≥ 0 discrete states. A Markov chain is a discrete-time stochastic process $\{X_n, n = 0, 1, 2, \ldots,\}$ for which the Markov process properties holds.

The conditional probability of moving into state *j* at time *n+1* gives that at the current time, *n,* the object is in state *I,* is given by:

$$P_{ij} = P_r\left\{X_{n+1} = j \middle| X_n = i\right\} \tag{2}$$

To define the Markov chain X_n, it is necessary to asses the transition probabilities between all possible condition state pairs. If there are N states, then this results in an NxN matrix:

$$P = \begin{bmatrix} P_{11} & P_{12} & \ldots & P_{1N} \\ P_{21} & P_{22} & \ldots & P_{2N} \\ . & . & . & . \\ P_{N1} & P_{N2} & \ldots & P_{NN} \end{bmatrix} \tag{3}$$

The transition probabilities by P matrix are difficult to evaluate and this reason to appeal to judgment experts or to evaluate by laboratory experiments.

2. Studied samples

To evaluate the life time for pressure tubes (PT) it is a probabilistic model made on basis if continue Markov chains. The system consists by pressure tubes by frame CNE – CANDU type.

Let's S denote the number of possible states for system at t time, finite number, and $X_n(t) \in S$ denote system state at t time. On during between two successively controller for pressure tubes,

$$nT \le t < T, \qquad n = 1, 2, \ldots, \tag{4}$$

where T denote the length control range, the pressure tubes system achieves as homogenous Markov chain. A Markov chain is governed by transition matrix P, where $P_{jk}(t)$ elements represent the transition probability of moving from the current state **j** to state **k**:

$$P_{jk}\left(t\right) = P\left(X\left(t\right) = k \middle| X\left(0\right) = j;\, j,k \in S, t > 0\right) \tag{5}$$

It is defined the following possible states in which we can found PT system in function by deteriorating degree; we define:

- OK : S state in which PT not degraded;
- D_1 : S state in which PT are in slowly degradation state; depth limit of defect is 0.15mm;
- D_2 : S state in which PT are degradation in relatively major degree; depth limit of defect is 0.5mm;
- F_1 : S state in which PT system can be in critical degradation state; depth limit of defect is 1.6mm;

The system states D are included in two categories:

- states with defects detected at control effected D_{1d} and D_{2d};
- states with defects undetected at control effected D_{1n} and D_{2n};

If we start in one of the states OK, D_{1n} or D_{2n} at the beginning of an inspection interval, we get a time continuous Markov chain. This will be valid for the complete inspection interval of length, *T*. However, if we during the inspection detect that the line is in the state D_1, then the next inspection interval will start in state D_{1d}, and then the more general diagram of Figure 1 applies.

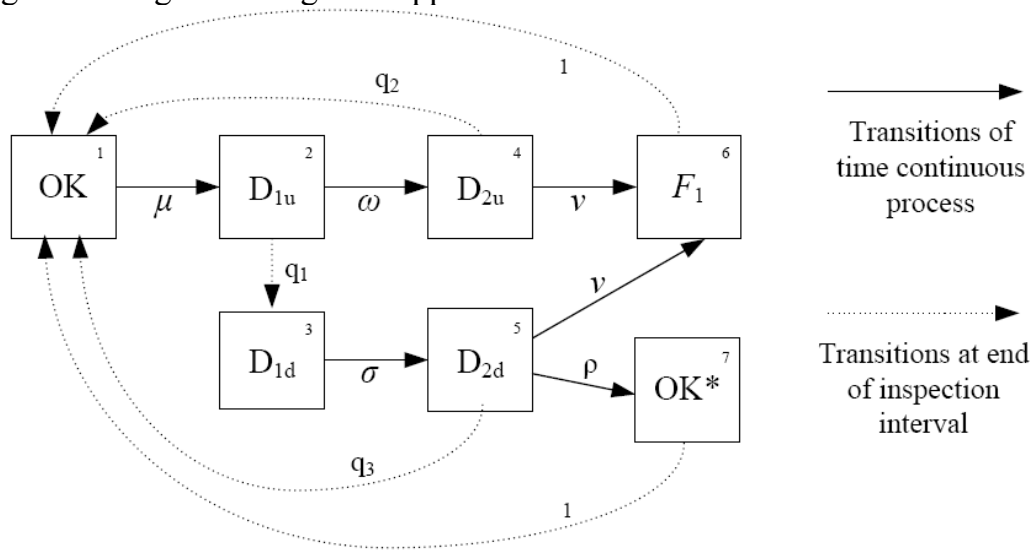

Figure 1. Overall failure/maintenance model, (state F2 not included)

The states $X_n(0)$ and $X_n(T)$ are of particular interest, where *T* is the length of the inspections interval. Now, we consider the transitions of state that may occur at the following of the inspection (occurring at times *T*, 2*T*, ….). In order to be able to fit the model to the failure/inspection data, we now introduce the variables U_n and V_n. U_n tells the true state for PT immediately before inspection, and V_n tells the true state immediately after inspection, i.e. at the start of the next inspection interval. Thus, we have:

$$\begin{aligned} U_n &= X_n(T) \\ V_n &= X_{n+1}(0) \end{aligned} \qquad n = 1, 2, \tag{6}$$

Now, introducing the asymptotic distributions of *Un* and *Vn*

$$\begin{aligned} a_k &= P\left(U_k = k\right) \\ b_k &= P\left(V_k = k\right) \end{aligned} \quad \text{k = 1, 2, . . . , 7} \tag{7}$$

we can then introduce the matrix R for the transitions at the inspections, transitions from U_n to V_n.

$$R = \begin{bmatrix} OK & D_{1n} & D_{1d} & D_{2n} & D_{2d} & F_1 & OK^* \\ 1 & 0 & 0 & 0 & 0 & 0 & 0 \\ 0 & 1-q_1 & q_1 & 0 & 0 & 0 & 0 \\ 0 & 0 & 1 & 0 & 0 & 0 & 0 \\ q_2 & 0 & 0 & 1-q_2 & 0 & 0 & 0 \\ q_3 & 0 & 0 & 0 & 1-q_3 & 0 & 0 \\ 1 & 0 & 0 & 0 & 0 & 0 & 0 \\ 1 & 0 & 0 & 0 & 0 & 0 & 0 \end{bmatrix} \tag{8}$$

Further, we introduce probabilities that degraded states are detected by inspection:

q_1 – probability that state D_1 of the system is detected;

q_2 – probability that a degraded failure D_2 is detected by the inspection; it is not know in advance that the state D_1 was reached;

q_3 – probability that a degraded failure D_2 is detected by the inspection; it is known in advance that the state D_1 was reached.

The dotted lines of Figure 1 indicate transitions at the end of the test interval.

The state vectors $\vec{a}$ and $\vec{b}$, which correspond to the system states before and after inspection, are calculated with relations:

$$\begin{aligned} \vec{b} &= \vec{a} \cdot R \\ \vec{a} &= \vec{b} P\left(T\right) \end{aligned} \tag{9}$$

or

$$\begin{aligned} \vec{a} &= \vec{a} \cdot R \cdot P\left(T\right) \\ \vec{b} &= \vec{b} \cdot P\left(T\right) \cdot R \end{aligned} \tag{10}$$

The probability of moving from the state j in state k is calculate with relation:

$$p_k\left(t\right) = \sum_{j=1}^{7} b_j p_{jk}^*\left(t\right) \tag{11}$$

where p_{jk}^* is means probability on a give range.

The input parameters for the estimation of model parameters are listed in Table 1. The statistical data was made on 10.000 pressure tubes in range time 10-12 years at IAEA Viena.

Table 1: Inputs to parameter estimation

Parameter definition	Parameter	Value
Number sets	N	10 000
Length of rail	L	62 000
Number of tests/inspections 1989-2002	n_{TF}	11.3
Number of tests/inspections 1991-2002	n_{TD}	9

Number of days, 1989-2002	N_1	4661
Number of days, 1991-2002	N_2	3909
Length of test/inspection interval	T	360
Number of observations in state D1, (i.e. transitions from D1u to D1d)	N_{D1}	187
Number of observations in D2 when it was not known that state was degraded, (i.e. transitions from D2u)	N_{D2a}	238
Number of observations in D2 when it was known that state was degraded, (i.e. transitions from D1d)	N_{D2b}	20
Number of observations in F1	N_{F1}	83
Probability of detecting D1 failure for coefficient of 95%	q_1	0.48
Probability of detecting D2 failure at test (state D1n not detected previously) for coefficient of 95%	q_2	0.70
Probability of detecting D2 failure at test (state D1 already detected)	q_3	0.98
Rate of detecting D2 in additional inspections; (assuming on the average two additional inspections within each interval *T*)	ρ	(2/T)* q_3

3. Experimental results

The system states before inspection to determinate by NDT tests by which show states a_2 , a_4 , a_5 and a_6 with detection probabilities q_1,q_2, q_3, and (2/T)*q_3 respectively.

State a_3 assume that system or to be in state 2 by which moving from state 3 with transition probability q_1, or state to be direct in state 3 in which are not possible ulterior transitions, i.e. in state 5:

$$\vec{a}_3 = \left(\vec{a}_2 \cdot q_1 + \vec{a}_3\right)\left(1 - e^{-\sigma T}\right) \tag{12}$$

The system transitions from state 3 (D_{1d}) to state 5 (D_{2d}) can be made with rate of transitions σ. Going with initial value for σ_i , we obtain a distribution for states q_i with state vectors $\vec{a}$.

For the new value σ_{i+1} we obtain a new state vector $a_{(i+1)}$:

$$a_{(i+1)} = a(i)R \cdot P(T) \tag{13}$$

The system states after inspection can be obtained by the relation:

$$\vec{b} = \vec{a} \cdot R \tag{14}$$

where R is matrix detection probabilities at effectuated control, respectively:

$$\begin{aligned} b_1 &= a_1 + a_4 \cdot q_2 + a_5 \cdot q_3 + a_6 + a_7 \\ b_2 &= a_2\left(1 - q_1\right) \\ b_3 &= a_2 \cdot q_1 + a_3 \\ b_4 &= a_4\left(1 - q_2\right) \\ b_5 &= a_5\left(1 - q_3\right) \end{aligned} \tag{15}$$

The probability as system is in state k at time t is taking by relation:

$$p_k(t) = \sum_j b_j p_{jk}(t) \tag{16}$$

(a) Determination of the detection probabilities for small discontinuities with depth of cca 0.125mm.

In this scope it was used the sample ARG 1 from Argentina in frame of Contract No. 11164/R between NIRDTP Iasi and IAEA Vienna [5].

The inspection defects are noted with #1, #2, #3 and #4 with dimensions and orientations given bellow.

Table 2: Flaw details in ARG 1 sample

Flaw #	Location and Orientation	Length (mm)	Width (mm)	Depth (mm)	Characteristics
1	ID, axial	6.1	0.3	0.136	calibration slot
2	OD, axial	6.15	0.4	0.14	calibration slot
3	ID, circumferential	6.2	0.3	0.152	calibration slot
4	OD, circumferential	6.6	0.4	0.16	calibration slot

The distribution for the estimated defect severity with depth 0.125 mm is present in figure 2 using a original method to resolve inversion problem for EC [1]. Considering the probability distribution for defects of log normal type (continue curve by figure 5) and integrating in range 0.1 – 0.3 it was a detected probability of 46% with reliability coefficient 95%.

(b) Determination of the detection probabilities for small discontinuities with depth of cca 0.47mm.

The inspection defects are noted with #1 and #4 with dimensions and orientations given of KOR 1 sample.

Table 3 Flaw details in KOR 1 sample

Flaw #	Location and Orientation	Length (mm)	Width (mm)	Depth (mm)	Characteristics
1	OD, axial	6.0	0.3	0.47	Short notch deeper than calibration slot
4	OD, circumferential	6.0	0.3	0.41	Short notch deeper than calibration slot

The histogram and log normal distribution for estimations concerning the defect with 0.47 mm depth is present in figure 3. It was made 30 measurements and 30 estimations for defect severities. In two cases the defect was estimate as having depth 0.4 mm, in 4 cases the signal was estimate as being from defect with depth 0.4 mm, in 8 cases the defect was estimate as having depth 0.5 mm, in 9 cases the signal was estimate as being from defect with depth 0.6 mm and in 7 cases the signal as being from defect with depth 0.7 mm. It was a detected probability of 70% with reliability coefficient 95%.

(c) determination of the detection probabilities for small discontinuities with depth of cca 1.63mm. It was a detected probability of 98% with reliability coefficient 95%.

The figures 4 and 5 show the probability to detect a pressure tube to be found in the degradation state (D_{1n} or D_{2n}) but not put in evidence by eddy currents procedure in function of time range between the inspections.

We can see that in time range between 300-400 days is minimum time up at the inspection following. Hence, it results that in this range the chance as a flaw is undetected is minim.

Upper 600 days in the range time between two inspections to undetected probability of the flaws which can be dangerous for reactor running.

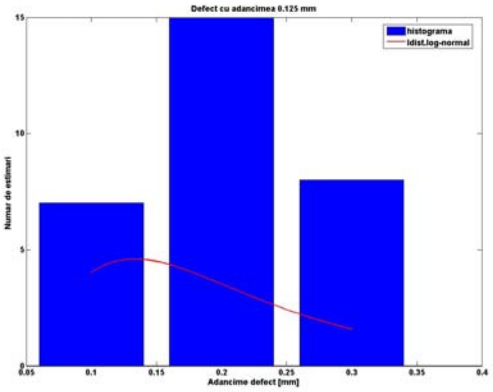

Figure2 To estimated distribution for flaw with depth 0.125mm

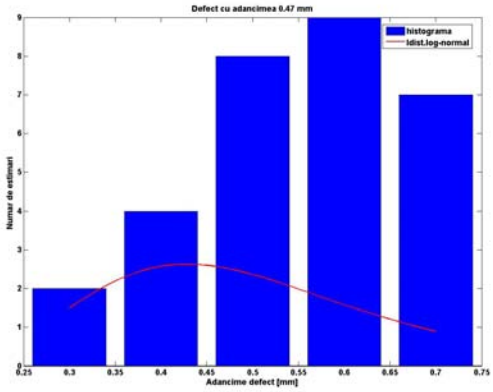

Figure 3 To estimated distribution for flaw with depth 0.47mm

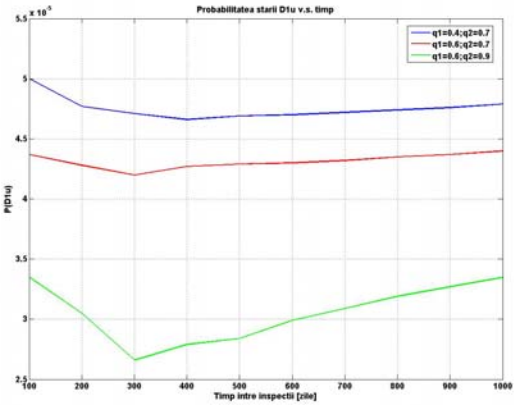

Figure 4 The probability for state D_{1n}

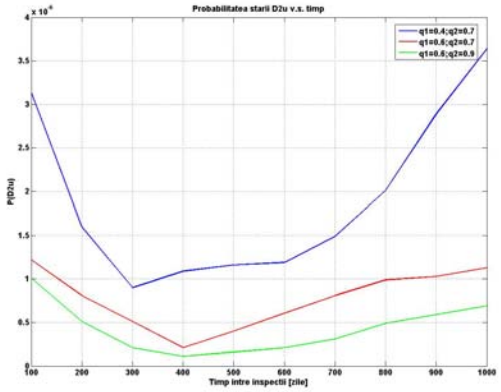

Figure 5 The probability for state D_{2n}

]

4. Conclusions

It was elaborate a Markov model for life time prediction for pressure tubes. The initial values with which we have to work are given in table 1.

We developed a soft using MATLAB 7.0 programmer which uses a series of apriority knowledge which appear as accumulated experience in the exploitation of nuclear reactors PHWR type. Other results are obtained by nondestructive testing for pressure tubes at annual outage.

This model has more simplifications for interpretation light the results and to use for maintenance optimization.

Acknowledgements

This paper is supported by Romanian Ministry of Education and Research, Research of excellence Program, under Contract no. 6110/2005, acronym SINERMAT and Nucleus Program PN 06 - 38 01 03.

Received March 1st , 2007

**National Institute of Research and Development*
for Technical Physics Iasi
47 D.Mangeron Blvd, 700050, Iasi, Romania
*** Al.I.Cuza University*
11 Carol I Blvd, Iasi, 700506, Romania

REFERENCES

[1] Raimond Grimberg et al. Emerging Technologies in Non-destructive Testing, ETNDN Fourth International Conference, April 2 – 4, 2007, Stuttgart, Germany;
[2] Dan M. Frangopol, Maarten-Jan Kallen and Jan M van Noortwijk, Probabilistic models for life-cycle performance of deteriorating structures: review and future directions, Prog. Struct. Engng Mater. 2004; 6 : 197-212;
[3] Christophe Blain, Taking into Account Uncertainties of Non-Destructive Tests in the Estimation of Stochastic Degradation Processes, ECNDT 2006 – Tu. 3.7.2;
[4] Per Hokstad, Helge Langseth, Bo H. Lindqvist, Failure modeling and maintenance optimization for a railway line, International Journal of Performability Engineering Volume 1, Number 2, October 2005.
[5] IAEA TECDOC 2005 , Report for CRP Meeting Chalk River Canada - October 2005

MODELAREA COMPORTAMENTULUI TUBURILOR D EPRESIUNE REALIZATE DIN ZR 2.5%NB DIN REACTOARELE PHWR TIP CANDU

Rezumat: In aceasta lucrare s-a elaborat un model Markov pentru predictia timpului de viata a tuburilor de presiune din inspectia reactoarelor nucleare de tip PHWR si s-a dezvoltat un soft utilizand programul MATLAB 7.0 care utilizeaza o serie de cunostinte apriori.

BULETINUL INSTITUTULUI POLITEHNIC DIN IAŞI
Tomul LIII (LVII), Fasc. 2, 2007
Secția
ŞTIINȚA ŞI INGINERIA MATERIALELOR

THE METALS IN THE BIBLICAL WORLD OF THE OLD TESTAMENT

STRUL MOISA and DAVID ITZHAK

Abstract*: Modern historians divide the roughly 3,000 year-period beginning approximately 3200 B.C. into two major segments—the Bronze Age and the Iron Age. The Bronze Age extends from about 3200 B.C. to 1200 B.C. Thereafter it is the Iron Age. These periods are parallel and contemporary to the events presented in the Old Testament. The periods are actually related to the most commonly used metals. Six metals are mentioned in the Bible: gold, silver, copper, iron, lead, and tin. There are numerous intriguing evidence references to the metals and metals working in the Old Testament as they came in use in the Near and Middle East. Although the Bible is a religious text, it represents an authentic written source of information.*

The article presents 3 aspects: (a) references regarding the way the metals are mentioned "for the first time" in the Bible; (b) references which due to incorrect translations of the Bible, create the false impression that brass might have existed in the Biblical antiquity; and (c) a micro-journey through the existing names in the list regarding metals and the ancient metallurgical art.

Keywords: *metal, copper, iron, bronze, brass, Bronze Age, Iron Age, ancient metallurgy, biblical world, Old Testament.*

A. Historical survey of the ancient biblical metallurgy

The technological civilian progress is appropriately evaluated by the stage at which its pyrotechnology has reached. For example, the Neolithic age of civilization is marked by the use of fire that was of major impotence in food processing, light and heat formation. The designations Chalcolytic, Bronze, and Iron Ages are simply reflections of the stage of pyrotechnic at which a particular culture has arrived. The earliest stage in which metallurgy has started to be developed is considered to be around 5000 B.C when the first known metallic objects – tools and jewels - were made in the Middle East and Afghanistan; the raw material used, was pieces of basic natural metal, all related to the noble elements group: gold, silver and copper. Men discovered the noble metals in rivers and mountains being attracted by their glittering. Still, the shape of these objects was pretty much like the stone tools. But sophisticated metal use requires smelting process, using special furnaces in order to extract metal from ores. The second stage of development the early metallurgy began the moment men realized that metal can be processed in different shapes when heated. The first objects produced by melting and forging looked like authentic metal tools with no resemblance with the stone tools. Nearby the natural metals, men often found colorful minerals such malachite, chalcopyrite, etc. The next important logic metallurgic discovery has started by heating the minerals on vegetal coal based fire. Copper has been obtained by this type of process and this was the beginning of the copper age. The copper minerals, such as malachite, were easily

found in nature as compared to the basic natural metals. This method of copper extraction was widely used and provided large amount of copper during a very long period. The Bronze Age, started around 3200 B.C. It was the first time in human history to demonstrate how technology of metals revolutionized society. It was the most important result of the early experiments to increase the resistance of copper by alloying it with other metals – initially 90 percent Cu and 10 percent Sn. Copper was the first metal to be smelted and used in abundance, but the real metallurgical innovation was the discovery of copper alloys. This also enabled an easier molding into shapes. The fact that the earliest metalworking period is called the Bronze Age is testimony to the importance of bronze. The earliest copper alloy, *arsenic bronze*, was developed in the Middle East. This alloy usually contained few percent of arsenic. It was probably obtained as a by-product of smelting copper from copper sulfide mineral. This was a product which was quite comparable to bronze in hardness and utility. The extraction was dangerous due to the hazard of arsenic fumes released during the smelting process.

The use of iron became popular around the year 1200 B.C., almost 2000 years after discovery of bronze. The reason is very simple: the melting point of copper (1084°C) is much lower than the melting point of iron (1538°C). Iron processing requires high temperatures technology was used in the old word for the first time by the Hittite in northern Anatolia. The Black Sea coast has self-fluxing iron sand, contains eighty percent of magnetite and other elements promote the fusing of the heated metal. The real reason why iron swept the ancient world was very simple. It was cheaper and much more abundant as compared to copper and tin. The iron's alloying – *carburized iron* - and the quench hardening became known soon after the beginning of the Iron Age. The properties of the new carburized iron products were superior to the similarly bronze products. Through most of history iron was extracted by smelting ore to obtain "bloom", a mixture of iron and slag. To shape it, the iron was heated red hot and pounded into shape. The progress in the iron technologies affected the development of society through the history. Society skilled in the iron and carburized iron technologies had a crucial advantage over the others in terms of war strategy and dominating far territories with a small and powerful army. To establish the historical context of the events presented in the Old Testament, is wanted taking into consideration the historical events and the chronological evolutions which are parallel with the ones in the Old Testament.

B. Metals in biblical "première"

Next, the verses in the Bible that mention for the first time the 6 metals will be presented: *gold, silver, copper, iron, lead, and tin.* The chemical symbols for these elements (*Au, Ag, Cu, Fe, Pb,* and *Sn*, respectively) come from their Latin names, a testament to their antiquity.

Gold - Latin *aureum*, Greek *chrysos* - is the first metal named in the Bible, in the Paradise/Eden Garden description context, ***Genesis 2:11***: "*The name of the first is Pishon; that is it which compasseth the whole land of Havilah, where there is* ***gold***".

The first biblical reference on **copper** and **iron** is in ***Genesis 4:22:*** *"Zillah also had a son, Tubal-Cain, who forged all kinds of tools out of* ***copper*** *and* ***iron***". As presented in Bible, Tubalcain is also the first biblical metalworking of copper and iron; this reference is the first biblical recorded reference to the profession of blacksmith.

The first biblical reference related to **silver** (Latin *argentums*, Greek *arguros*) is in ***Genesis 13:2***: "*And Abram was very rich in cattle, in* ***silver****, and in gold"****.***

The first biblical reference on ***lead*** is located in the second book of the Pentateuch, ***Exodus 15:10***: *Thou didst blow with thy wind, the sea covered them: They sank as* ***lead*** *in the mighty waters*.

The first biblical reference on **tin** is located in ***Numbers 31:22***: *howbeit the gold, and the silver, the brass, the iron, the tin, and the lead*. Although tin is mentioned tangential in the Old Testament – statistic, only 4 references - the tin is a very important metal: the alloying between copper and tin leaded to produce the alloy known under the name bronze. Certainly, without the existence of the tin, the age of bronze wouldn't have existed.

C. Is the existance of brass and steel in the biblical antiquity a fact? Consequences of an incorrect translation of some metallurgical terms.

Brass is the term used for alloys of copper and zinc, the amount of zinc varying from 5-45 % to create a range of brasses, each with unique properties. The idea of dealing with this subject comes after reading the American version of the Old Testament, *American Standard Version* (ASV). For example ***Genesis 4:22***: *And Zillah, she also bare Tubal-cain, the forger of every cutting instrument of **brass** and iron: and the sister of Tubal-cain was Naamah*. The question in the title is asked again: was brass known in the age of the Old Testament? The reader interested in a comparative reading will have a few surprises. Therefore we will go back to the former example from ***Genesis 4:22*** while comparing the translation of 2 versions in English – *American Standard Version* (ASV) and *Modern King James Version* (MKJV) - with one version in Romanian - *Romanian Ortodox Bible* (ROB).

- (ASV) *And Zillah, she also bare Tubal-cain, the forger of every cutting instrument of **brass** and iron: and the sister of Tubal-cain was Naamah.*
- (MKJV) *And Zillah also bore Tubalcain, the hammerer of every engraving tool of **bronze** and iron. And the sister of Tubalcain was Naamah*.
- (ROB) *Sela a născut şi ea pe Tubalcain, care a fost făurar de unelte de **aramă** şi de fier. Şi sora lui se chema Noema*.

In order to find an answer to the title question, a further example is brought, this time from ***Deuteronomy 8:9***. The example is also presented through the four versions mentioned above:

- (ASV) *a land wherein thou shalt eat bread without scarceness, thou shalt not lack anything in it; a land whose stones are iron, and out of whose hills thou mayest dig **copper***.
- (MKJV) *a land in which you shall eat bread without want. You shall not lack any thing in it. It is a land whose stones are iron, and out of whose hills you may dig **brass***.
- (ROB) *Într-o ţară unde sunt măslini, untdelemn şi miere, în care fără lipsă vei mânca pâinea ta şi nu vei duce lipsă de nimic; în care pietrele au fier şi din munţii căreia vei scoate **aramă***.

The question in the title comes back again and again especially for the metal expert: was brass known during the age of the Old Testament? Can it be free-brass found in nature? Answer: **free-brass cannot be found in nature;** brass is an alloy, an artificial engineering composite material. For the ordinary reader the question may seem unimportant. Inconsistancies in the translation of the Old Testament from Hebrew into other languages, as well as various translations in English, may cause confusions for a reader less initiated into the history of metals science. We talk about the inconsistency regarding the unanimous consensus of the chronology of the historical ages of metals (and alloys): Chalcolytic time/Copper Age, Bronze Age and Iron Age. This confusion can become clearer and stronger for the reader who is anchored in the field of metal science. In fact, the reference to inconsistancy refers to the premature appearance on the history stage of the technical alloy known as **brass**. We talk about the period in the Old Testament which includes events between centuries 13-2 BC. The contradiction results from the translation of the Hebrew word **copper** / **נחשת** – as it appears in the Old Testament – both into **brass** and into **bronze**.

Mention must be made that both brass and bronze are binary technical alloys based on copper, but they are two completely different materials: brass is an alloy based on copper and zinc, while bronze is an alloy based on copper and tin. Therefore the two notions - brass and bronze – are two completely different notions.

The events presented in the Old Testament cover the period between Genesis and the birth of Jesus Christ. In order to clarify the period when the events presented in the two previous examples – ***Genesis 4:22*** and ***Deuteronomy 8:9*** – took place, mention must be made that both verses refer to events previous to year 1400 BC. According to these 2 verses brass existed during the period of the Old Testament. Still, the answer to the generic question – whether brass was known during the Old Testament – is very clear: brass was not known during the Old Testament. This will be discussed on the basis of various translation related to the SEPTUAGINTA. This was the first translation of the Old Testament from Hebrew into Greek and it was made in the first half of the third century B.C. A few references to metals and metallurgy are problematic; the difficulty is somewhat tempered by the fact that the Hebrew word **nechoshet** is translated into English as either bronze or copper (also Greek *Chalkkos* can indicate either copper or bronze), although the proper - antique and modern - translation is copper. The original Hebrew version of the Old Testament does not use the term **bronze**; only the term **copper** appears. The metallurgical process to obtain the technical alloy known as brass (melting copper and zinc) was not known during the period of the Old Testament, while the melting of bronze (binary alloy of copper and tin) was widely used since 3000 BC. This is why the whole period is called the Bronze Age.

Only six metals are mentioned in the Old Testament – gold, silver, copper, iron, lead and tin – zinc does not appear.

Progressing in time, towards the period described in the Old Testament which was written in the first century CE, it looks like the antics discovered the ore of Calamine, a mixture of zinc carbonate ($ZnCO_3$) and zinc silicate [$Zn_4Si_2O_7(OH)_2 \cdot H_2O$]. Around the years 20 BC – 20 CE, the metal workers were able to use the calamine mixed with copper obtaining the brass known as *Calamine Brass*. The ancient Greeks called this brass "*oreichalcos*" (*orei* meaning gold in Greek). The Romans used brass to make helmets, jewelers, coins and to decorate armors. In ancient Rome, the brass alloy made of 75% copper, 20% zinc, 5% tin was called "*aurichalcum*" because it looked like gold (*aurum* is the latin for gold). Of course, the value of the *aurichalcum* coin was inferior to the silver coin although they had the same weight.

How was the Calamine Brass obtained? Three parameters had to be considered: two parameters regarding zinc – the melting point and the boiling point of zinc being 420ºC and 910ºC respectively. The third parameter was the melting point of copper, 1083ºC. It can be seen that the melting point of copper is higher than the melting and boiling temperatures of zinc. The manufacturing process for obtaining the calamine brass consisted in heating a mixture of copper and calamine to a high temperature for several hours. This temperature was higher than the boiling temperature of zinc, but lower than the melting point of copper. At this temperature zinc vapors were obtained. Maintaining the mixture at this temperature allowed zinc vapors to distill from the ores and permeate the metallic copper. In fact, it was obtained a surface coating of copper with zinc. The homogenizing of the chemical composition in the whole bulk was obtained through a later melting. Using calamine – instead of metallic zinc- to obtain calamine brass, had two disadvantages: (a) contained a significant amount of slag material resulting from the non-zinc components of calamine, and (b) the process did not permit to accurately produce the desired final proportion of copper to zinc. These disadvantages contributed to a limited use of brass.

It can be concluded:

- Brass is a binary alloy obtained by melting two distinct metallic materials: metallic copper and metallic zinc. Even if calamine brass is accepted as what we call brass today, it

appeared only during the confluence of the events presented in the Old Testament with the events in the New Testament.

- Before 1700 CE metallic zinc didn't have a birth certificate, in other words pure zinc couldn't have been produced. Only in 1738 William Champion granted the patent of producing metalic zinc by cracking calamine with coal. In 1746 pure metalic zinc was obtained by Andreas Marggrag who also established its properties. In 1781 James Emerson granted the method of obtaining brass from metalic zinc and copper. Therefore, we can conclude that brass appeared on the history stage – as a technical alloy and according to a well defined technology – in the middle of the 18th century, moment when the industrial process of obtaining metalic zinc was defined.

Consequently, the "extension" of the term copper or bronze towards brass for the period of the Old Testament does not have scientific archeo-metallurgic support (archeological traces, typified technology etc.) Moreover, the substitution generates confusions.

Remark: The reference version of the Bible in Romanian follows the Hebrew version, the translation being *arama*. Today, in Modern Hebrew, the confusions for the copper alloys are totally excluded because the word ***arad*** is used for bronze and the word ***pliz*** is used for brass.

Moving on to the period of reference of the New Testament – in the ancient Rome period – the existence of brass can be accepted. But even now the various translations cause hesitations. As an example, two verses from the first two books of the New Testament are presented. **The Gospel of Matthew,** ***Matt 10:9*** and **The Gospel of Mark,** ***Mark 7:4***. For the parallel translation of the verses the International Standard Version (ISV) was also used.

Matt 10:9:

- (ASV) *Get you no gold, nor silver, nor* ***brass*** *in your purses*;
- (ISV) *Don't take any gold, silver, or* ***copper*** *in your moneybags*,
- (MKJV) *Do not provide gold or silver, or* ***copper*** *in your purses*,
- (ROB) *Să nu aveţi nici aur, nici arginţi, nici* ***bani*** *de arama în cingătorile voastre*;

Mark 7:4:

- (ASV) *and when they come from the market-place, except they bathe themselves, they eat not; and many other things there are, which they have received to hold, washings of cups, and pots, and* ***brass*** *vessels*.
- (ISV) *They don't eat anything from the marketplace unless they dip it in water. They also observe many other traditions, such as the washing of cups, jars,* ***brass*** *pots, and dinner tables*.
- (MKJV) *And coming from the market, they do not eat without immersing, and there are many other things which they have received to hold, the dipping of cups and pots, and of* ***copper*** *vessels, and of tables*.
- (ROB) *Şi când vin din piaţă, dacă nu se spală, nu mănâncă; şi alte multe sunt pe care au primit să le ţină: spălarea paharelor şi a urcioarelor şi a vaselor de* ***aramă*** *şi a paturilor*.

In some other versions of the translations of the Old Testament in English, the confusion is even more striking: for the Hebrew word **copper** the word **steel** is used in addition to brass and bronze. To illustrate the explanation above, three comparatively translated verses are presented from ***2 Samuel 22:35***, ***Job 20:24***, ***Psalms 18:34*** and **Jeremiah 15:12.** For this illustration it was also used the King James Version (KJV+):

2 Samuel 22:35:

- (ASV) *He teaches my hands to war, So that mine arms do bend a bow of* ***brass***.
- (KJV+) *He teaches my hands to war; so that a bow of* ***steel*** *is broken by mine arms*.

- (MKJV) *He teaches my hands to war, so that my hands may bend a bow of **bronze***.
- (ROB) *Care-mi deprinde mâinile mele la război Şi braţele mele să întindă arcul de **aramă***.

Job 20:24:

- (ASV) *He shall flee from the iron weapon, and the bow of **brass** shall strike him through*.
- (KJV+) *He shall flee from the iron weapon, and the bow of **steel** shall strike him through*.
- (MKJV) *He shall flee from the iron weapon, a bow of **bronze** shall pierce him*.
- (ROB) *Dacă va scăpa de platoşa de fier, îl va străpunge arcul de **aramă***.

Jeremiah 15:12:

- (ASV) *Can one break iron, even iron from the north, and **brass**?*
- (KJV+) *Shall iron break the northern iron and the **steel**?*
- (MKJV) *Can one break iron, iron or **bronze** from the north?*
- (ROB) *Poate cineva să rupă fierul, fierul de la miazănoapte şi **arama**?*

Psalms 18:34:

- (ASV) *He teacheth my hands to war; So that mine arms do bend a bow of **brass***.
- (KJV+) *He teacheth my hands to war, so that a bow of **steel** is broken by mine arms*.
- (MKJV) *He teaches my hands to war, so that a bow of **bronze** is bent by my arms*.
- (ROB) *Cel ce întăreşti mâinile mele în vreme de război, şi ai pus arc de **aramă** în braţele mele*.

To conclude, the three very distinctive terms – iron, carburized iron, steel - should be included into the progressive historical context. Iron was used long time before it could be melted. The scientific world agrees today that the meteoric iron was used by the ancient civilizations. The melting point of iron is at about 1538°C, but this high temperature could not have been reached with the pyrotechnical methods existing at that time. After the beginning of the Iron Age, around 1200 BC, concurrent with the transition from bronze to iron age was the discovery of *carburization of iron*, which was the process of adding until 0.8 % carbon to the irons of the time. Iron was recovered as sponge iron, a mix of iron and slag with some carbon and/or carbide, which was then repeatedly hammered and folded over to free the mass of slag and oxidize out carbon content, so creating the product wrought iron. Wrought iron was very low in carbon content, usually less than 0.035%C, and was not easily hardened by quenching. The people of the Middle East found that a much harder product could be created by the long term heating, 920 – 950 ^{0}C, of a wrought iron object in a bed of charcoal, which was then quenched in water (or oil). The resulting product, *carburized iron*, was harder and less brittle than the bronze it began to replace. Hittites knew *carburized iron* since the VIII century BC and by the end of the same century, because of migrations, the process of the carburized iron was spread over Middle East. This aspect represented a remarkable qualitative lap because the use properties of the carbonized iron were definetely superior to those of bronze – even if the new empiric technology was not simple for that period.

Steel is a metalic alloy, in which iron is the major component and carbon represents 0.02 – 1.8% of its weight. Steel has higher proprieties compared to iron and at the same time represents a higher level of pyrotechnology and metallurgical technology. However, the steel metallurgy was developed much later than the events presented in the Bible. Steel is also to be distinguished from wrought iron with little or no carbon. It is common today to talk about

'the iron and steel industry' as if it were a single thing; it is today, but historically they were separate products. Consequently, if the substitution of the term bronze with brass in the Old Testament was attributed to translations, the "evolutionist" extension of the term brass with steel is totally inappropriate and discordant with the historic evolution of the metallurgical science. It is important to underline that the Romanian translation of the Bible is faithful to the original text.

D. A micro-incursion in the world of the existing names in the list of names regarding metals and the ancient metallurgical art.

The Old Testament reflects - among other things - the intimacy of the ancient biblical peoples with the metals and the metallurgic arts; throughout the subsequent two millennia of Judaic existence as a nation and as a Diaspora culture, Jews were closely associated with metallurgy. Metallurgical industries revived in Judah with the return of artisans from the Babylonian exile (586-538 BC) and continued to flourish into the Greek and Roman periods. The Jewish artisans continued to practice their metallurgic trades in the most populous Jewish center in the Diaspora. It was the practice to assume a surname either of the town or region from which they stemmed, or of the trade with which they made a livelihood. Onomastic studies prove the existence of a large scale in this direction.

The fact that names such as *Gold, Goldsmith, Goldberg, Goldstein, Goldman, Golda, Aura, Aurica,* etc. from gold, *Silver, Silberstein, Silberberg, Silversmith,* etc. from silver, *Ferro, Ferrere, Ferriere Hierierro, Eisen, Eisenstein, Eisensmith,* etc. from iron, *Cupersmith, Coppersmith, Cuperstein, Copperman, Cupermann, Kupfermann,* etc. from cooper, became generically names and remain so to the present day bespeaks the seminal role of artisans in these trades through the centuries. Many examples of names originated in the profession practiced can be given even from Russian: from **gold** – золото (zoloto): *Золотов (Zolotov), Золотой (Zalatoi), Золотников (Zolotnikov), Золотых (Zalatăh),* etc., from **silver** – серебро (serebro): *Серебров (Serebrov), Серебровский (Serebrovski), Серебрянский (Serebrianski), Серебряный (Serebrianâi), Серебреников (Serebrenikov)*, *Серебряков (Serebriakov)*, etc., from **copper** – медь (med'): *Медник (Mednik), Медников (Mednikov), Медяков (Mediakov), Медяник (Medianik), Медянников (Medianikov), Медяницков (Medianscikov), Медянкин* (*Mediankin*), etc., from **tin** – олово (olovo): *Оловянишников (Oloviani*ş*nikov), Оловянников (Olovianikov), Оловяношников (Olovianoşnikov), Оловенников (Olovenikov),* etc., from **iron** – железо (jelezo): *Железников (Jeleznikov), Железнов (Jeleznov), Железняк (Jelezniak), Железняка (Jelezniaka), Железняков (Jelezniakov), Железный (Jeleznâi),* etc.

All the names were likewise distinctly surnames that identified gold-, silver-, iron- and respectively cooper-smiths, who carried on their trade in an Italian, French, Spanish, Romanian, Russian or German environment through the ages. In Italian, a typical name, *Orrefici*, or *Auraru* in Romanian, translates to gold-worker. Likewise, *Argintaru*, *Cupraru*, *Aramaru, Fieraru,* in Romanian, translates to silver- copper- iron-worker respectively. Similarly the names *Blecher* (Yiddish, tin- or plate-worker) and *Klempner* (German, metal-folder) are recognizable names that translate literally to tin- or plate-smith. The names *Messing, Messinger,* (brass-worker) and *Prager* (minter) likewise derive from German, and remained characteristically names for centuries.

Received March 15, 2007

Department of Materials Engineering, Ben-Gurion University of Negev, Israel.

BULETINUL INSTITUTULUI POLITEHNIC DIN IAŞI
Tomul LIII (LVII), Fasc. 2, 2007
Secția
ŞTIINȚA ŞI INGINERIA MATERIALELOR

INVESTIGATION ON THE Cr(III) SORPTION PROPERTIES OF AN ACRYLIC RESIN WITH FUNCTIONAL GROUPS OF HYDROXAMIC ACID AND AMIDOXIME

R. WENKERT, I. SARGHIE, S. MOISA, V. NEAGU, I. BUNIA

Abstract: *The sorption of Cr(III) ions on an acrylic ion exchange resin with functional groups of hidroxamic acid and amidoxime has been studied. In order to establish the proper conditions of sorption, the effect of some experimental factors (pH, initial concentration, amount of exchanger, contact time) on the retention process has been investigated. It was shown that the equilibrium distribution of Cr(III) between sorbent phase and solution is well described by the Langmuir model with two parameters. The bifunctional resin under study exhibits favorable kinetic properties, indicating the flexibility of applications in environmental management.*

Keywords*: hidroxamic acid, amidoxime, acrylic resin, Langmuir model.*

1. Introduction

Today, with the rapid increasing urban population and water resources becoming more and scarcer, there is a strong need to reconsider our consumption patterns and the way we use our water resources. Developing countries suffer from water pollution; the high cost of contents and treatments make the major problems in these countries. A perspective method for water treatment is the sorption. Using this method the sorbents have to answer to a number of requirements to be active, stable, selective, accessible, cheap and easy to regenerate, [1].

In order to find new materials fulfilling these requirements, a study concerning the sorption of Cr(III) ions from aqueous solutions on an acrylic ion exchange resin with hydroxamic acid and amidoxime functional groups has been performed. The experimental results are very promising for removal of Cr(III) ions from aqueous effluents. It can be mentioned that in previous studies the acrylic bifunctional resin with functional groups of hydroxamic acid and amidoxime has been tested for Cu(II) and Co(II) ions[2-5].

1. Experimental

- Acrylic bifunctional ion exchange of type A, with features recorded in Table 1.
- Stock solution of Cr(III) with $5x10^{-2}$M concentration,
- Working solutions, obtained by appropriate dilutions of the stock solution
- Buffer solutions of pH (CH_3COOH-CH_3COONa; NH_4Cl-NH_4OH)

Table 1, The features of acrylic bifunctional resin under study

Functional groups*	Weak acid exchange capacity		Diameter of particles (mm)
	mEq/mL	mEq/g	
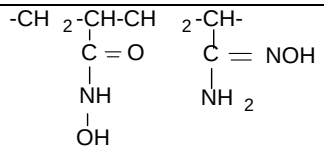	1.38	4.06	0.3 – 0.8

* The ion exchanger has been performed with a crosslinked degree of 10 % DVB in the presence of benzene, as diluent at dilution D = 0.25 (D = mL diluent/ mL diluent + mL monomers).

The study of Cr(III) retention on the acrylic bifunctional resin has been carried out by the batch method. Samples of about 0.05g exchanger were equilibrated with volumes of 25 mL solution containing known amounts of Cr(III). The phases were separated by filtration, after a determined time of contact (24 hours, intermittent stirring) The Cr(III) amount in filtrate was determined spectrophotometrically with complexon III (concentration range: 10-40μg/mL; λ= 550nm).

2. Results and Discussion

In order to establish the optimum conditions of Cr(III) retention, the influences of pH, initial concentration, amount of exchanger and contact time on sorption efficiency have been studied.

Influence of solution pH

Due to acid-base character of the both functional groups, the retention process of Cr(III) on acrylic bifunctional resin depends on the solution pH. Figure 1 presents the sorption percentage change as function of medium pH, adjusted by buffer solution addition.

As can be seen from Figure 1, the sorption process has high values in the pH range of 4-6. Until the value of pH= 3, the metallic ion retention is very low, due to amidoxime group protonation resulting in the decrease of the weakly acid functional group toward H^+ ions. It can be mentioned that the pH value corresponds to the solution obtained by a simple dilution of the initial solution, without use of buffer solution. From this reason, the subsequent determinations were performed in unbuffered solution.

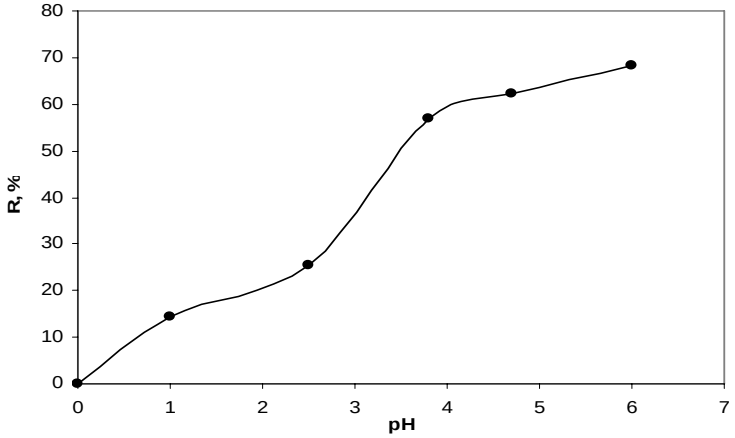

Fig.1, The Cr(III) sorption percentage as function of solution pH.
(initial concentration C_0=156mg/L; equilibration time= 24h)

Influence of Cr(III) concentration in initial solution

The effect of solution initial concentration on Cr(III) sorption by bifunctional acrylic resin is shown in Figure 2.

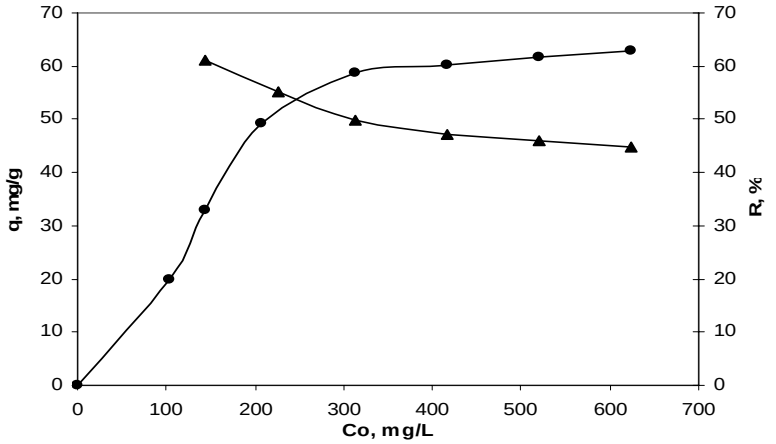

Fig, 2, The influence of Cr(III) concentration in initial solution on its sorption process by ion exchange resin with functional groups of hidroxamic acid and amidoxime

In solutions with pH=4 the amount of Cr(III) retained on acrylic bifunctional resin with functional groups of hidroxamic acid and amidoxime increases to metallic ion initial concentration increasing until to saturation of resin. On the other hand, the increase of Cr(III) results in the decrease of the sorption percentage. This behavior of the solid support suggests that the bifunctional resin could be efficient in quantitative recovery of Cr(III) from diluted solutions.

Influence of contact time of phases

To point out the effect of phases contact time on Cr(III) retention process by acrylic bifunctional resin the experimental determinations were performed at two metallic ion initial concentrations: 156mg/L and 312mg/L respectively (figure 3).

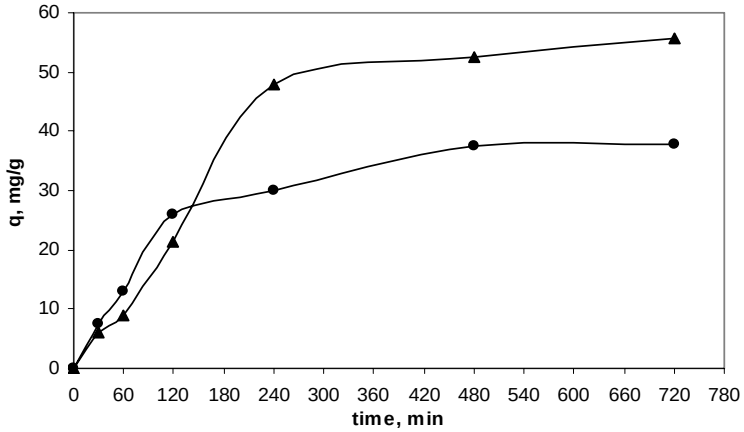

Fig. 3, The effect of contact time in Cr(III)- acrylic bifunctional resin sorption systems

It is obvious from figure 3 that to Cr(III) concentration of 156 mg/L almost entire amount of metallic ion is retained after about 2 hours. For higher concentration of Cr(III), the equilibrium is attained harder; the sorbent needs four hours to retain the most part of Cr(III) amount. To determine the value of rate constant K' (min^{-1}) the kinetic experimental data were processed according to Lagergren equation:

$$\lg (q_0 - q) = \lg q_0 - K't /2.303$$ where

q_0 is the Cr(III) amount taken up per 1 gram of acrylic bifunctional resin at equilibrium, mg/g, q is the amount of Cr(III) taken up per gram of sorbent at time t, mg/g, and K' is the sorption rate constant, min^{-1}. The values of these constants determined from the linear Lagergren plots are recorded in table 2. The kinetic data recorded in table 2 lead to the conclusion that the retention of Cr(III) on acrylic ion exchange resin with hydroxamic acid and amidoxime group is a process of mass transfer, determined by diffusion of Cr(III) ions on exchanger bead. Furthermore the kinetic data confirm to the assumption that the resin under study can be used to concentration of Cr(III) ions from diluted aqueous solutions.

Table 2, Processing of experimental data according to Lagergren equation

	t, min	lg (q_0- q)	Equation of regression	R^2
156mg/L	30 60 120 240 480 720	1,48 1,47 1,26 0,99 0,31 -0,52	y = -0,003x + 1,76 q_0 = 38,48 K'= 6,9x$10^{-3}min^{-1}$	0,9977
	t, min	lg (q_0- q)	Equation of regression	R^2
312mg/L	30 60 120 240 480 720	1,71 1,69 1,57 1,34 0,98 0,43	y = -0,0018x + 1,7903 q_0= 58,87 K'= 4,14x$10^{-3}min^{-1}$	0,9963

Influence of acrylic resin amount

Another parameter under study is the variation of acrylic resin amount taken up per a determination the experiments were carried out by contacting different amounts of sorbent with volumes of 25 mL solution containing 316 mg Cr(III)/L at pH=4.

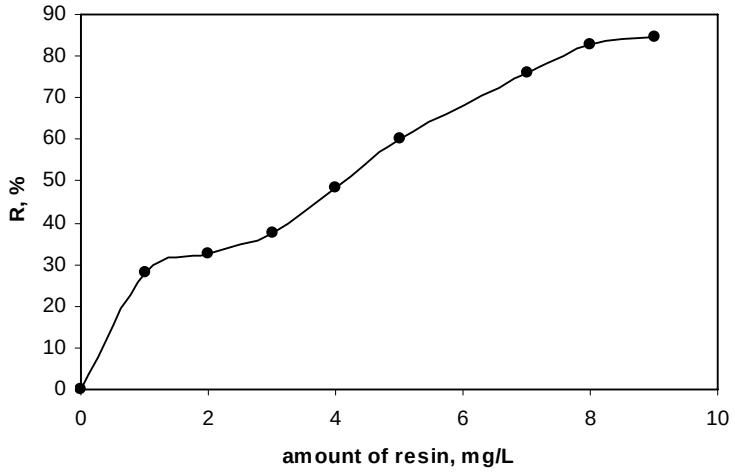

Fig. 4, The influence of the sorbent amount in the sorption systems under study

The dependence in figure 4 shows a percentage of Cr(III) retention (R≈90%) increase to ratio of phases increasing.

The characterization of sorbent process

The equilibrium distribution of Cr(III) between the ion exchange resin and aqueous solutions of pH=4 and variable initial concentration has been described by means of Langmuir and Freundlich isotherm models (Figures 5 and 6)

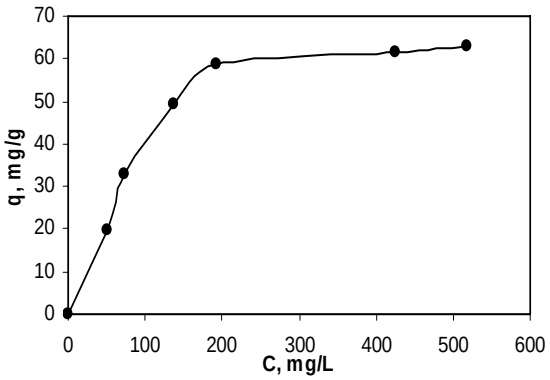

Fig,5, The Langmuir isotherm of Cr(III) sorption on acrylic bifunctional resin of type A

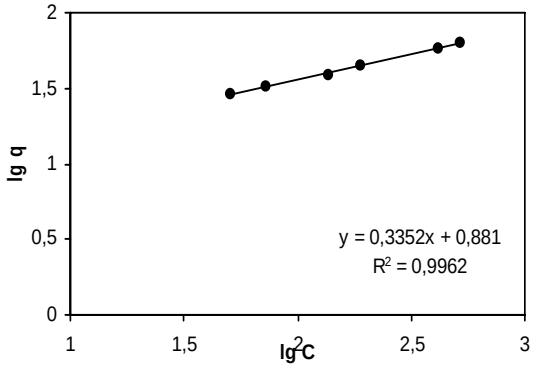

Fig,6, Freundlich plots of Cr(III) sorption on acrylic bifunctional resin of type A

Langmuir isotherm

The linear form of the Langmuir isotherm in figure 5 is described by equation:

$$q = K_L.q_0.c/(1+K_L.c)$$ where:

q = the amount of sorbed Cr(III) on acrylic resin (mmol/g); c = equilibrium concentration of Cr(III) in solution (mmol/mL); q_0 = maximum capacity of sorption (mmol/g); K_L = affinity parameter that represents the power of the bond between the metal retained and sorbent, (L/mol).

A plot of 1/q versus 1/c is linear with the intercept equal to $1/q_0$ and the slope equal to $1/K_L.q_0$. The q_0 and K_L values derived from the linear Langmuir plot in the studied system are given in Table 3.

Freundlich isotherm

The Freundlich isotherm is represented in this study by the following equation:

$$\lg q = \lg K_F + (1/n) \lg c \qquad \text{where:}$$

q is the amount of Cr(III) taken up per 1 gram of sorbent (mg/g); c is the equilibrium concentration of Cr(III) in solution (mmol/mL); K_F and n are the Freundlich constant relating to all factors affecting the retention process. The condition for a favorable sorption is: $1< n < 10$.

Table 3 records the K_F and n values derived from the Freundlich plot given in Figure 6. To compare the Langmuir and Freundlich isotherm models, the experimental data were statistically processed by linear regression. The regression equations of y=ax+b type and the obtained values of the coefficient of correlation R^2, are given in table 3, too. The results in table 3 indicate that by introducing hydroxamic acid and amidoxime groups into the acrylic resin of type A favorable conditions for selective retention of Cr(III) were created.

Table 3, Quantitative description of the Cr(III)-acrylic bifunctional resin sorption system on the basis of the Langmuir and Freundlich models

Langmuir model	Langmuir constants		Statistical analysis	
	q_0(mg/g)	K_L(L/mol)	Equation regression	R^2
	1.3842	699	y = 0.7224x+1.033	0.9994
Freundlich model	Freundlich constants		Equation regression	R^2
	K_F	n	y = 0.3352x + 0.881	0.9962
	7.868	3.0175		

In addition, from table 3 it may be noticed that the obtained data fit better the Langmuir model (higher value for R^2). The values of the Langmuir constants, q_0 and K_L indicate the existence of a complexing mechanism between the metallic ions and the functional groups of the resin under study. On the basis of Langmuir sorption constant K_L, the Gibbs free energy change has been calculated using the usual relation ($\Delta G = -RT\ln K_L$). The obtained value is negative, ΔG = -15,948kJ/mol, and reflects the high affinity and accessibility of functional groups toward Cr(III) ions.

3. Conclusions

On the basis of these experimental results the following conclusions may be drawn:

- The percentage of Cr(III) retention on acrylic ion exchange resin with functional groups of hydroxamic acid and amidoxime depends on solution pH, being very high in the pH range of 4-6.
- Due to decrease of retention percentage to initial concentration increasing, the Cr(III) preconcentration by sorption on bifunctional resin can be efficiently for diluted solution.

- The study of contact time influence reveled the fact that Cr(III) retention from diluted solutions requires a contact time of minimum 2.5 hour, with for more concentrated solutions was necessary a time of 3.5 hours.
- The equilibrium distribution of Cr(III) between sorbent and solution phases has been described on basis of the Langmuir and Freundlich models. The obtained results point out that the Cr(III) sorption process conforms better to Langmuir model of monolayer adsorption.
- The values of Langmuir sorption constants and Gibbs free energy suggest a high affinity of resin bifunctional groups toward Cr(III) ions and are characteristic to a spontaneous process taking plan by a complexing mechanism.

References

[1] D. Bilba, D. Bejan, L. Tofan, *Croatica Chemica Acta*, **71**(1), 155, (1998)
[2] V. Neagu, I. Bunia, I. Pleşca, M. Popa, J. Appl. Polym. Sci., 88 (2003) 2956
[3]] R. Wenkert; I. Sârghie, V. Neagu, I. Bunia, Annals of the Suceava University, 13 (nr.1-2006)
[4] M.B. Colella , S. Siggia, R.M. Barnes, Anal. Chem., 52 (1980) 967
[5] E.S. A. Hegazy, H. Kamal, N. A. Khalifa, G. A. Mahmoud, J. Appl. Polym. Sci. 81 (2001) 849

Received March 15, 2007

R. WENKERT, Soroka University Medical Center, Beer-Sheva, Israel, rodicawe@clalit.org.il
I. SARGHIE, "Gh. Asachi" Technical University, Faculty of Chemical Engineering, Department of Environmental Engineering and Management, 71 D.Mangeron Bd., 700050 Iasi, Romania
S. MOISA, Ben-Gurion University of the Negev, Department of Materials Engineering, POB 653, Beer-Sheva 84105, Israel, smoisa@bgu.ac.il
V. NEAGU, **I. BUNIA**, "P. Poni" Institute of Macromolecular Chemistry, Aleea Grigore Ghica Voda 41A, Iasi, Romania

BULETINUL INSTITUTULUI POLITEHNIC DIN IAŞI
Tomul LIII (LVII), Fasc. 2, 2007
Secţia
ŞTIINŢA ŞI INGINERIA MATERIALELOR

NANOSTRUCTURES AND FRACTAL SPACE-TIME (I)

M. AGOP, P. VIZUREANU, D.G. GALUSCA, I. IONITA

Abstract: *A theoretical approach of the transport mechanisms in nanostructures, considering that the motion of the micro-particles takes place on continuous but non-differentiable curves, i.e. on the fractals, is established. Then, by means of a scale covariance form of the Newton's equation, the Scrödinger's type equation, as an irrotational motion of the fluid in the topological dimension $D_T=2$, results. The interface dynamics between two nanostructures as an application of the model is given.*

I. Introduction

Acording to [1-3], the transport of charged particles in electronic devices is generally described by kinetic models such as Boltzmann-like equations or macroscopic models of hydrodynamic or diffusion type. Due to the ongoing miniaturization of these devices, reaching the nanometric scale, the reliability of these classical models becomes doubtful as quantum effects become important. Since, at an intermediate scale, collision phenomena remain significant, one of the most challenging areas of investigation in semiconductor modeling deals with the setting-up of quantum transport models which take into account scattering effects. Though many works are concerned with the numerical simulation of ballistic quantum transport models for semiconductors (see *e.g.* [4, 5]), a quantum theory of collisions is still under development (among other works on the quantum theory of scattering, see *e.g.* [6, 7]. Furthermore, several attempts were made to adapt existing classical macroscopic models to quantum mechanics [8, 9] but, generally, the link between the so-obtained models and a microscopic quantum description of the particle transport is to a large extent phenomenological.

New ideas concerning the physical basis of self-organizing phenomena observed in the so called intelligent materials miniaturized at micrometer and nanometer sizes gained substantial interest because of the wide range of their technological purpose. Thus, miniaturization makes possible the implementation of better computer architecture but the presence of physical limits imposed by quantum and thermal fluctuation phenomena makes such systems less and less reliable. The recognition of these ultimate limits has lead computer scientists to seek inspiration from biology. This is because living organisms operate with functional elements that are of mesoscopic scale dimensions and actually exploit collective quantum effects and thermal energy for ensuring its "living" state. The hope to break the barrier of miniaturization seems to lie in the knowledge of the self-organization mechanism able

to explain the self-assemblage and the working regime of the simplest organisms created by nature.

In solid-state physics and electronics, a large variety of different nonequilibrum phenomena accompany the spontaneous self-assemblage of spatial and spatio-temporal patterns [10]. Thus, attention has been paid to thyristor-like semiconductor structures with large active area, as these nonlinear systems with bistable properties show several spatial and spatio-temporal current density patterns. Such semiconductors could potentially be used as multi-stable elements for integrated circuits, self-organizing devices for image recognition and image processing. It is remarkable that the instability mechanism observed in such samples exhibits some features very similar to those studied in biological or chemical media.

Self-organization phenomena can be revealed also in non-crystalline materials in which metastable configuration of atoms at nanometer scale gives to the material the possibility to choose one among various pathways to change free energy [10]. This occurs when, by providing some energy, the system is pushed to modify the quasi-equilibrium phenomenon ensures the reversibility of the atomic state during energy exchange with the surrounding medium.

All these results requires the development of a new "scale" physical theories, *i.e.* of fractal space-time type (for details see Refs [11, 12]), in which the macroscopic scale specific to the classical quantities coexist and it is compatible, simultaneously, with the microscopic "scale" specific to the quantum quantities. Then i) the semi-quantum physical theories, *e.g.* Wigner-Boltzmann model [8], must not be imposed, but are generated as transitions between the interaction scales; ii) the topological dimension and implicitly, the fractal one (for details see Ref. [13]) induces the transport mechanisms; iii) the so-called anomalies, *e.g.* the increases of the thermal conductivity in nanostructures [14], appear as natural phenomenon in the context of material structures self-organization by means of the spontaneous symmetry breaking (for details see Refs. [8-10, 15]). In the present paper, a fractal space-time theory will be established to explain the transport mechanisms in nanostructures.

This paper is organized as follows: Section II, discusses the fractal function and dilatation operator. Section III provides the fractal variables and the genesis of scales. In the Section IV, by means of a scale covariance form of the Newton's equation, the Scrödinger's type equation, as an irrotational motion of the fluid in the topological dimension D_T=2, is established. The dynamics of interface as an application of the model is given in the Section V. In Section VI the conclusions are given.

II. Fractal functions. Dilatation Operator

Let us build a curve $f(x)$ between the points A and B which has to be continuous, yet nowhere differentiable. If we start from the segment $\overline{AB}$, it is differentiable in every point, thus there will be an x, where $F(x_1)$ doesn't situate itself on this segment and let us denote by C this point. Now we have the crooked line ACB.

By continuing the procedure, we get to the crooked line $ADCEB$ (see Fig. 1). If we continue the reasoning limitless, a fractal curve is obtained everywhere between A and B.

Such a curve has an infinite length. This differentiable is a direct consequence of a Lebesque theorem, which states that a finite length curve is almost everywhere (i.e. except a set of points with null dimension).

Another important feature of the curve built is that between any two points of the curve, we can get a curve with the same properties as the initial curve, i.e. it is continuous, nowhere differentiable and therefore of infinite length. We state for such a curve that it is **almost selfsimilar everywhere**.

A possibility of approximating such a curve is to divide the interval $\lfloor x_0, x_f \rfloor$ into parts of length ε, i.e. to consider the absices $x_0, x_1, ..., x_n, ..., x_f$ with

$$x_n - x_{n-1} = \varepsilon, \quad n \in N \tag{1}$$

and to obtain a crooked line in the points

$$f(x_1), ..., f(x_n), ..., f(x_f) \tag{2}$$

Let $f(x,\varepsilon)$ be the function which describes this crooked line and we say that it is the ε **scale approximation** of the fractal function $f(x)$.

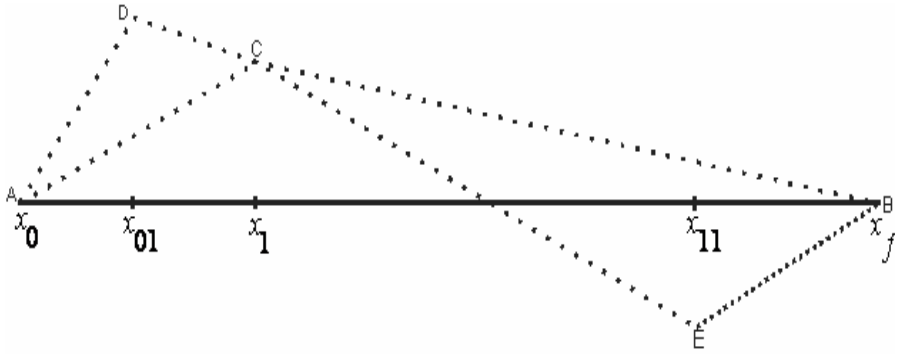

Fig. 1 The fractal curve construction

A change of scale from ε to $\varepsilon + d\varepsilon$ must keep the fractal properties of $f(x)$. Moreover, since the fractal is almost selfsimilar, if we take a certain multiple of this scale, the situation has to be the same. What remains unchanged after this scale inflation, as can be seen from Fig. 2, is the ratio

$$\frac{d\varepsilon}{\varepsilon} = d\rho \tag{3}$$

Therefore, in explicitating the properties of **scale invariance,** the ratio (3) plays an important part.

The function $f(x,\varepsilon)$ is differentiable in the interval $\lfloor x_0, x_f \rfloor$ except for a finite number of points with the abscisa $x_0 + n\varepsilon$, yet on a finite metric set, i.e. $f(x,\varepsilon)$ is almost everywhere differentiable.

Now we can make an infinitesimal scale transformation (see (3))

$$\varepsilon' = \varepsilon + d\varepsilon = \varepsilon + \varepsilon d\rho \tag{4}$$

and after that, the fractal function $f(\varepsilon)$ (we have omitted the variable *x*, which remains unchanged according to the considerations below) becomes

$$f(\varepsilon') = f(\varepsilon + \varepsilon \cdot d\rho) = f(\varepsilon) + \frac{\partial f}{\partial \varepsilon} \varepsilon d\rho \tag{5}$$

and

$$f(\varepsilon')=\left(1+\varepsilon\frac{\partial}{\partial\varepsilon}d\rho\right)f \tag{6}$$

respectively. Yet

$$\frac{\partial}{\partial\varepsilon}=\frac{\partial(\ln\varepsilon)}{\partial\varepsilon}\frac{\partial}{\partial\ln\varepsilon}=\frac{1}{\varepsilon}\frac{\partial}{\partial\ln\varepsilon} \tag{7}$$

and thus (6) becomes

$$f(\varepsilon')=\left(1+\tilde{D}d\rho\right)f(\varepsilon),\qquad \text{with}\quad \tilde{D}=\frac{\partial}{\partial\ln\varepsilon} \tag{8}$$

where $\tilde{D}$ is the **dilatation operator**.

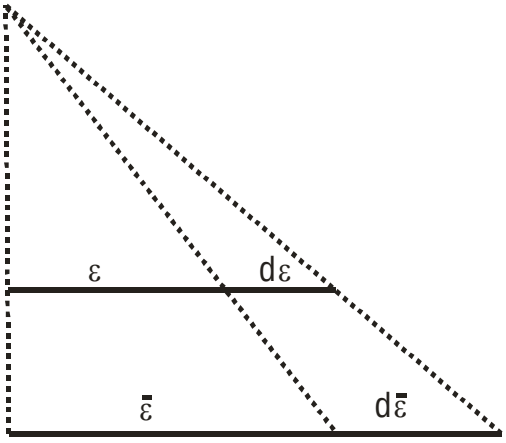

Fig. 2 The dilatation of the scale

From the above it is obvious that the intrinsic variable of resolution isn't ε, but $\ln\varepsilon$. This claim has yet another important consequence. **Since both the argument of the logarithm and the exponent of the exponential function must be non-dimensional, the same feature must have the variables of the fractal functions (in the above case ε).**

III. Fractal variables. The genesis of the scales

Even if the fractal functions are not differentiable, taking into account the experience of centuries of the theoretical physics, we will be forced to discover a way to find a link to the differential calculus. There are continuous curves which are not fractals but have points where they are not differentiable, in these points we find the left and right derivative. We try now to make a link to these concepts.

Let $P(x^1,x^2)$ be a point of the fractal curve and let us consider a line which starts from this point and let Q be the first intersection of this line with the fractal curve.

We denote by x^1+dX^1, x^2+dX^2 the coordinates of Q, thus ***PQ*** is a vector of components dX^1, dX^2. We denote by dX^i the components of the vector ***PQ*** for which $dX^1>0$, hence they are at the right of the line (d) and by dX^i the case when $dX^1<0$,

such as is the case for the vector ***PQ'*** – see Fig. 3. Considering all the lines (segments) which start from *P*, we denote the average of these vectors by $dx_{\pm}^{i}$ i.e.

$$\left\langle dX_{\pm}^{i} \right\rangle = dx_{\pm}^{i} \quad (i = 1,2) \tag{9}$$

Therefore we can write

$$dX_{\pm}^{i} = dx_{\pm}^{i} + d\xi_{\pm}^{i}, \tag{10}$$

where

$$\left\langle d\xi_{\pm}^{i} \right\rangle = 0 \tag{11}$$

Here $dx_{\pm}^{i}$ are the left and right differentials of the classical variables, and $d\xi_{\pm}^{i}$ describe the fractal characteristic.

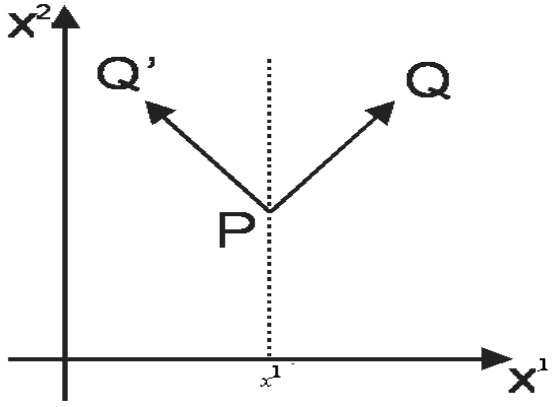

Fig. 3 The continuous curves which are not fractals but have points where they are not differentiable

If a point like body along the fractal curve moves, the parameter *t* of the time could establish the place where the moving object is at a given moment. Since $d\xi_{\pm}^{i}$ describes the fractal properties of the considered curve which has the fractal dimension D_T, it is natural to impose $\left(d\xi_{\pm}^{i}\right)^{D_T}$ to be proportional to dt, *i.e.*

$$\left(d\xi_{\pm}^{i}\right)^{D_T} = D_o dt \tag{12}$$

where D_0 is a coefficient of proportionality.

Let us suppose that the motion of physical objects takes place on continuous but non-differentiable curves, *i.e.* on fractals. The "non-differentiable" nature of space-time implies a breaking of differential time reflection invariance. In such a context the usual definitions of the derivative of a given function with respect to time

$$\frac{df}{dt} = \lim_{\Delta t \to +0} \frac{f(t+\Delta t) - f(t)}{\Delta t} = \lim_{\Delta t \to +0} \frac{f(t) - f(t-\Delta t)}{\Delta t} \tag{13}$$

are equivalent in the differentiable case. One passes from one to the other by the transformation $\Delta t \to -\Delta t$ (time reflection invariance at the infinitesimal level). In the non-differentiable case two functions (df_{+}/dt) and (df_{-}/dt) are defined as explicit functions of t and of dt

$$\frac{df_{+}}{dt} = \lim_{\Delta t \to +0} \frac{f(t+\Delta t, \Delta t) - f(t, \Delta t)}{\Delta t}, \quad \frac{df_{-}}{dt} = \lim_{\Delta t \to +0} \frac{f(t, \Delta t) - f(t-\Delta t, \Delta t)}{\Delta t} \tag{14a, b}$$

The sign (+) corresponds to the forward process and (-) to the backward process.

From (10) we obtain the speed field:

$$\frac{d\boldsymbol{X}_{\pm}}{dt}=\frac{d\boldsymbol{x}_{\pm}}{dt}+\frac{d\boldsymbol{\xi}_{\pm}}{dt} \tag{15}$$

We denoted by $(d\boldsymbol{x}_{+}/dt)=\boldsymbol{v}_{+}$ the "forward" speed and by $(d\boldsymbol{x}_{-}/dt)=\boldsymbol{v}_{-}$ the "backward" speed. If $(\boldsymbol{v}_{+}+\boldsymbol{v}_{-})/2$ may be considered as classical speed, the difference between them, i.e. $(\boldsymbol{v}_{+}-\boldsymbol{v}_{-})/2$ is the fractal speed, so that we can introduce the complex speed:

$$\boldsymbol{V}=\frac{\boldsymbol{v}_{+}+\boldsymbol{v}_{-}}{2}-i\frac{\boldsymbol{v}_{+}-\boldsymbol{v}_{-}}{2}=\frac{d\boldsymbol{x}_{+}+d\boldsymbol{x}_{-}}{2dt}-i\frac{d\boldsymbol{x}_{+}-d\boldsymbol{x}_{-}}{2dt} \tag{16}$$

Using the notations $d\mathbf{x}_{\pm}=d_{\pm}\mathbf{x}$, (16) becomes:

$$\boldsymbol{V}=\left(\frac{d_{+}+d_{-}}{2dt}-i\frac{d_{+}-d_{-}}{2dt}\right)\boldsymbol{x} \tag{17}$$

that allows defining the operator:

$$\delta=\frac{d_{+}+d_{-}}{2dt}-i\frac{d_{+}-d_{-}}{2dt} \tag{18}$$

To summarize, while the concept of velocity was classically a single concept, if space-time is non-differentiable, we must introduce two speeds instead of one, even when going back to the classical domain. Such a two-valuedness of the speed vector is a new, specific consequence of non-differentiability that has no standard counterpart (in the sense of differential physics), since it finds its origin in a breaking of the symmetry ($dt\rightarrow -dt$). Such a symmetry was considered self-evident up to now in physics (since the differential element *dt* disappears when passing to the limit), so that it has not been analyzed on the same footing as the other well-known symmetries. Note that it is actually different from the time reflection symmetry *T*, even though infinitesimal irreversibility implies global irreversibility.

Now, at the level of our description, we have no way to favor $\boldsymbol{v}_{+}$ rather than $\boldsymbol{v}_{-}$. Both choices are equally qualified for the description of the laws on nature. The only solution to this problem is to consider both the forward ($dt>0$) and backward ($dt<0$) processes together. The number of degrees of freedom is double with respect to the classical, differentiable description (6 velocity components instead of 3, see (16)). Thus, **the two interaction scales are obtained, the non-fractal by means of the classical variables $dx_{\pm}^{i}$, and the fractal one through the variables $d\xi_{\pm}^{i}$, the transition between them being given by the proportionality coefficient D_0.**

IV. Special consideration in the topological dimension D_T=2

Let us assume now that the fractal curve is immersed in a 3-dimensional space, and $\boldsymbol{X}$ of components X^i (i=$\overline{1,3}$) is the position vector of a point on the curve. Let us consider also a function $f(X,t)$ and the following Taylor series expansion up to the second order:

$$df=f(X^i+dX^i,t+dt)-f(X^i,dt)=\left(\frac{\partial}{\partial X^i}dX^i+\frac{\partial}{\partial t}dt\right)f(X^i,t)+\frac{1}{2}\left(\frac{\partial}{\partial X^i}dX^i+\frac{\partial}{\partial t}dt\right)^2 f(X^i,t) \tag{19}$$

From here, the forward and backward average values of this relation using notations $dX_{\pm}^{\ i} = d_{\pm}X^{i}$ take the form:

$$\langle d_{\pm}f\rangle = \left\langle \frac{\partial f}{\partial t}dt\right\rangle + \langle \nabla f \cdot d_{\pm}\mathbf{X}\rangle + \frac{1}{2}\left\langle \frac{\partial^2 f}{\partial t^2}(dt)^2\right\rangle + \left\langle \frac{\partial^2 f}{\partial X^i \partial t}d_{\pm}X^i dt\right\rangle + \frac{1}{2}\left\langle \frac{\partial^2 f}{\partial X^i \partial X^l}d_{\pm}X^i d_{\pm}X^l\right\rangle \tag{20}$$

We make the following stipulations: the mean values of the function *f* and its derivates coincide with themselves, and the differentials $d_{\pm}X^i$ and *dt* are independent, therefore the averages of their products coincide with the product of average. Then (20) becomes:

$$d_{\pm}f = \frac{\partial f}{\partial t}dt + \nabla f\langle d_{\pm}\boldsymbol{X}\rangle + \frac{1}{2}\frac{\partial^2 f}{\partial t^2}\langle (dt)^2\rangle + \frac{\partial^2 f}{\partial X^i \partial t}\langle d_{\pm}X^i dt\rangle + \frac{1}{2}\frac{\partial^2 f}{\partial X^i \partial X^l}\langle d_{\pm}X^i d_{\pm}X^l\rangle \tag{21}$$

so that, using (10) in the form (9),

$$d_{\pm}f = \frac{\partial f}{\partial t}dt + \nabla f d_{\pm}\boldsymbol{x} + \frac{1}{2}\frac{\partial^2 f}{\partial t^2}(dt)^2 + \frac{\partial^2 f}{\partial X^i \partial t}d_{\pm}x^i dt + \frac{1}{2}\frac{\partial^2 f}{\partial X^i \partial X^l}\left(d_{\pm}x^i d_{\pm}x^l + \langle d\xi_{\pm}^i d\xi_{\pm}^l\rangle\right) \tag{22}$$

Let us focus now on the mean $\langle d\xi_{\pm}^i d\xi_{\pm}^l\rangle$. If $i \neq l$ this average is zero due the independence of $d\xi^i$ and $d\xi^l$. So, using (14) we can write:

$$\langle d\xi_{\pm}^i d\xi_{\pm}^l\rangle = \delta^{il}(D_0 dt)^{2/D_T} \tag{23}$$

with

$$\delta^{il} = \begin{cases} 1, & if \quad i = l \\ 0, & if \quad i \neq l \end{cases}$$

Through of a Peano type curves which covers a two-dimensional surface, i.e. D_T=2, (23) becomes:

$$\langle d\xi_{\pm}^i d\xi_{\pm}^l\rangle = \pm\delta^{il}(D_0 dt) \tag{24}$$

where we had considered that:

$$\begin{cases} \langle d\xi_{+}^i d\xi_{+}^l\rangle > 0 \ and \ dt > 0 \\ \langle d\xi_{-}^i d\xi_{-}^l\rangle > 0 \ and \ dt < 0 \end{cases}$$

Then (22) may be written under the form:

$$d_{\pm}f = \frac{\partial f}{\partial t}dt + \nabla f d_{\pm}\boldsymbol{x} + \frac{1}{2}\frac{\partial^2 f}{\partial t^2}(dt)^2 + \frac{\partial^2 f}{\partial X^i \partial t}d_{\pm}x^i dt + \frac{1}{2}\frac{\partial^2 f}{\partial X^i \partial X^l}d_{\pm}x^i d_{\pm}x^l + \frac{1}{2}\frac{\partial^2 f}{\partial X^i \partial X^l}\delta^{il}D_0 dt \tag{25}$$

If we divide by d*t* and neglect the terms which contain differential factors, (25) is reduced to:

$$\frac{d_{\pm}f}{dt} = \frac{\partial f}{\partial t} + \boldsymbol{v}_{\pm}\nabla f_{\pm} \pm \frac{D_0}{2}\Delta f \tag{26}$$

Let us calculate, under the circumstances *(δf/dt)*. Taking into account (26), we have:

$$\frac{\delta f}{dt}=\frac{1}{2}\left[\frac{d_+f}{dt}+\frac{d_-f}{dt}-i\left(\frac{d_+f}{dt}-\frac{d_-f}{dt}\right)\right]=\frac{1}{2}\left(\frac{\partial f}{\partial t}+\boldsymbol{v}_+\nabla f+\frac{D_0}{2}\Delta f\right)+\frac{1}{2}\left(\frac{\partial f}{\partial t}+\boldsymbol{v}_-\nabla f-\frac{D_0}{2}\Delta f\right)-$$

$$-\frac{i}{2}\left[\left(\frac{\partial f}{\partial t}+\boldsymbol{v}_+\nabla f+\frac{D_0}{2}\Delta f\right)-\left(\frac{\partial f}{\partial t}+\boldsymbol{v}_-\nabla f-\frac{D_0}{2}\Delta f\right)\right]=\frac{\partial f}{\partial t}+\left(\frac{\boldsymbol{v}_++\boldsymbol{v}_-}{2}-i\frac{\boldsymbol{v}_+-\boldsymbol{v}_-}{2}\right)\nabla f-i\frac{D_0}{2}\Delta f \tag{27}$$

or using (17):

$$\frac{\delta f}{dt}=\frac{\partial f}{\partial t}+\boldsymbol{V}\cdot\nabla f-iD\Delta f\,,\qquad 2D=D_0 \tag{28a, b}$$

with D a scale coefficient.

This relation also allows us to give the definition of the fractal operator:

$$\frac{\delta}{dt}=\frac{\partial}{\partial t}+\boldsymbol{V}\cdot\nabla-iD\Delta \tag{29}$$

We now apply the principle of scale covariance, and postulate that the passage from classical (differentiable) mechanics to the new non-differentiable mechanics that is considered here can be implemented by replacing the standard time derivative $d/\delta t$ by the new complex operator δ/dt. As a consequence, we are now able to write the Newton's equation in covariant form:

$$\frac{\delta\boldsymbol{V}}{dt}=\frac{\partial\boldsymbol{V}}{\partial t}+\boldsymbol{V}\cdot\nabla\boldsymbol{V}-\eta\Delta\boldsymbol{V}=\frac{\boldsymbol{F}}{m}=-\nabla\left(\frac{U}{m}\right) \tag{30}$$

with U scalar potential of the external field and m the rest mass of the test particle.

The equation (30) is a generalized Navier-Stokes type equation with a imaginary viscosity coefficient $\eta=iD$ and contains, simultaneously, the macroscopic scale and microscopic one by means of the complex speed field $\boldsymbol{V}$.

From here and from the operational relation

$$\boldsymbol{V}\cdot\nabla\boldsymbol{V}=\nabla\left(\frac{\boldsymbol{V}^2}{2}\right)-\boldsymbol{V}\times(\nabla\times\boldsymbol{V}) \tag{31}$$

we obtain the equation

$$\frac{\delta\boldsymbol{V}}{dt}=\frac{\partial\boldsymbol{V}}{\partial t}+\nabla\left(\frac{\boldsymbol{V}^2}{2}\right)-\boldsymbol{V}\times(\nabla\times\boldsymbol{V})-\eta\Delta\boldsymbol{V}=-\nabla\left(\frac{U}{m}\right), \tag{32}$$

Moreover, applying of the curl operator to (32) and denoting

$$\boldsymbol{\Omega}=\nabla\times\mathbf{V} \tag{33}$$

the vortex equation results

$$\frac{\delta\boldsymbol{\Omega}}{dt}=\frac{\partial\boldsymbol{\Omega}}{\partial t}+\nabla\times\left(\boldsymbol{\Omega}\times\mathbf{V}\right)=0 \tag{34}$$

If the "fluid" is irrotational, *i.e.*

$$\boldsymbol{\Omega}=\nabla\times\boldsymbol{V}=0 \tag{35}$$

we can choose $\boldsymbol{V}$ of the form:

$$\mathbf{V}=\nabla\phi \tag{36}$$

with ϕ the complex speed potential. Then, equation (32) becomes

$$\frac{\delta\boldsymbol{V}}{dt}=\frac{\partial\boldsymbol{V}}{\partial t}+\nabla\left(\frac{\boldsymbol{V}^2}{2}\right)-\eta\Delta\boldsymbol{V}=-\nabla\left(\frac{U}{m}\right) \tag{37}$$

and more, by substituting Eq. (36) in Eq. (37) and integrating,

$$\frac{\partial \phi}{\partial t} + \frac{1}{2}(\nabla \phi)^2 - \eta \Delta \phi + \frac{U}{m} = F(t) \tag{38}$$

with $F(t)$ a time dependent arbitrary function. Therefore, the equations (37) are reduced to a solely scalar equation (38) in which the complex speed field $\boldsymbol{V}$ was substituted by complex scalar field ϕ namely the complex speed potential.

Particularly, for a function ϕ of the form

$$\phi = -2iD \ln \psi \tag{39}$$

the relation (38), with the identity

$$(\nabla \ln f)^2 + \Delta \ln f = \frac{\Delta f}{f}, \tag{40}$$

takes the form

$$D^2 \Delta \psi + iD \frac{\partial \psi}{\partial t} + \left[\frac{F(t)}{2} - \frac{U}{2m} \right] \psi = 0 \tag{41}$$

where D is a constant. From here, up to an arbitrary phase factor which may be set to zero by a suitable choice of the phase of ψ, i.e. $F(t) \equiv 0$, a Schrödinger type equation is obtained

$$D^2 \Delta \psi + iD \frac{\partial \psi}{\partial t} - \frac{U}{2m} \psi = 0 \tag{42}$$

Therefore, **the Schrödinger type equation is obtained as an irrotational movement of fluids and contains the macroscopic scale and the microscopic one by means of the complex speed potential (39)**. Then: i) ψ becomes simultaneously wave-function and complex speed potential; ii) D defines the fractal/nonfractal transition, i.e. the transition from the explicit scale dependence to scale independence. In the Nottale's model of the scale relativity theory, D has the form [11, 12, 16].

$$D = \frac{\lambda \cdot c}{2}$$

with λ a length scale and c the speed of light in the vacuum. This length scale is to be understood as a structure of scale space not of standard space (for example see the definition of the Compton length [11, 12]); iii) for $2mD = \hbar$ (see the Refs. [11, 12]), Eq. (42) takes the standard form,

$$\frac{\hbar^2}{2m} \Delta \psi + i\hbar \partial_t \psi - U\psi = 0$$

V. The dynamics interface by means of the fractal space-time theories

Using the results given in the previous section, the interface dynamics is described by the coupled equations set,

$$\begin{aligned} 2imD\partial_t \Psi_1 &= T_1 \Psi_1 + \Gamma \Psi_2 \\ 2imD\partial_t \Psi_2 &= T_2 \Psi_2 + \Gamma \Psi_1 \end{aligned}, \tag{43a, b}$$

with Ψ_1, Ψ_2 the wave functions of two nanostructures, T_1, T_2 the associated "Hamiltonians", Γ a coupling constant which describes the interface, D the fractal/nonfractal coefficient and *m* the effective mass of the charged particles.

Expliciting the wave functions by the following relations:

$$\psi_1 = \sqrt{\rho_1} e^{i\theta_1}, \ \psi_2 = \sqrt{\rho_2} e^{i\theta_2} \tag{44a, b}$$

and separating in (43a, b) the real parts from the imaginary ones, we obtain:

$$\partial_t \rho_1 = -\partial_t \rho_2 = \frac{\Gamma}{mD}\sqrt{\rho_1 \rho_2}\sin(\theta_2 - \theta_1)$$

$$\partial_t \theta_1 = -\frac{T_1}{2mD} - \frac{\Gamma}{2mD}\sqrt{\frac{\rho_2}{\rho_1}}\cos(\theta_2 - \theta_1) \tag{45a-c}$$

$$\partial_t \theta_2 = -\frac{T_2}{2mD} - \frac{\Gamma}{2mD}\sqrt{\frac{\rho_1}{\rho_2}}\cos(\theta_2 - \theta_1)$$

From here, with:

$$T_1 = qV\,,\ T_2 = -qV\,,\ \rho_1 = \rho_2 = \rho\,,\ \theta = \theta_2 - \theta_1 \tag{46a-d}$$

it results the current:

$$I = q(\partial_t \rho_1 - \partial_t \rho_2) = I_M \sin\theta \tag{47}$$

of amplitude I_M

$$I_M = \frac{2q\rho\Gamma}{mD} \tag{48}$$

and phase difference θ

$$\theta = \theta_0 + \frac{q}{mD}\int V dt\,,\ \theta_0 = const. \tag{49a, b}$$

with q the effective charge and V the potential.

The relations(47)-(49a, b) reproduces a d.c. Josephson type effect if $V=0$, and an a.c. Josephson type effect if $V \neq 0$, i.e. oscillations of current with the pulsation:

$$\omega = \frac{qV}{mD} \tag{50}$$

Let us consider the dependency $V = V(t)$ of the form

$$V = V_0 + v_0 \cos(\Omega t + \varphi_0)\,,\ \varphi_0 = const. \tag{51a, b}$$

Substituting the (51a, b) relation into (49a, b) and integrating it, we obtain the time dependence of the phase difference:

$$\theta = \theta_0 + \frac{qV_0}{mD}t + \frac{qv_0}{mD\Omega}\sin(\Omega t + \varphi_0) \tag{52}$$

With (52) relation the (47) expression of the current becomes

$$\begin{aligned} I &= I_M \sin\left[\theta_0 + \frac{qV_0}{mD}t + \frac{qv_0}{mD\Omega}\sin(\Omega t + \varphi_0)\right] = \\ &= I_M \sum_{n=-\infty}^{+\infty} J_n\left(\frac{qv_0}{mD\Omega}\right)\sin\left[\left(n\Omega + \frac{qV_0}{mD}\right)t + n\varphi_0 + \theta_0\right] \end{aligned} \tag{53}$$

where J_n is the n-order Bessel function [17].

When the pulsation $\Omega_0 = qV_0/mD$ satisfies the relation

$$\Omega_0 = n\Omega, \tag{54}$$

the temporal average of *I(t)* differs from zero, i.e. there is a continuous component of the current of the form:

$$I_c = (-1)^n I_M J_n\left(\frac{qV_0}{mD\Omega}\right)\sin(n\varphi_0 + \theta_0) \tag{55}$$

From (53) relation it results peaks of the continuous current for

$$V_n = n\frac{mD\Omega}{q}, \quad n = 1,2,..... \tag{56a, b}$$

and consequently a negative differential resistance. So, the negative differential resistance is a self-organizing condition of the two nanostructure as an interface. This result is in good agreement with the observations from [9, 18, 19].

We notice that any time-dependent signal admits locally a Fourier discrete decomposition [17]. This means that the previous results are of maximum generality.

VI. Conclusions.

A mathematical model of the transport mechanisms in nanostructures, considering that the motion of the micro-particles takes place on continuous but non-differentiable curves, *i.e.* on the fractals, is established. Then:
i) The fractal functions and the dilatation operator are introduced;
ii) While the concept of velocity was classically a single concept, if space-time is non-differentiable, we must introduce two speeds (forward and backward speeds) instead of one, even when going back to the classical domain;
iii) At the level of our description, we have no way to favor the forward speed rather than backward one. Both choices are equally qualified for the description of the laws on nature. The only solution to this problem is to consider both the forward and backward processes together, so that a complex speed and a time covariant derivative are introduced;
iv) Two interaction scales are obtained, the macroscopic scale by means of the classical variables and the microscopic one through the fractal variables, the transition between them being given by the proportionality coefficient D_0;
v) Appling the principle of scale covariance, and postulating that the passage from classical (differentiable) mechanics to the non-differentiable mechanics can be implemented by replacing the standard time derivative by time covariant derivative, a generalized Navier-Stokes type equation is established;
vi) For an irrotational motion, the correspondence with a Scrödinger's type equation resulted. Then, the wave-function simultaneously becomes a complex speed potential;
vi) The interface dinamics of two nanostructures using this mathematical model is given. It results that the interface works through of a d.c. Josephson type effect for zero potential or an a.c. Josephson type effect for nonzero potential. For $2mD = \hbar$, the standard Josephson effect results.

Acknowledgements
The present work was supported by the contract CEEX no. 76-5/2006 MATNANTECH.

Received March 15, 2007

Technical "Gh. Asachi" University

References:

[1] J. P. Bourgade, *On Spherical Harmonics Expansion type models for electron-phonon collisions,* Math. Methods Appl. Sci. **26** (2003), no. 3, 247-271

[2] P. Degond, V. Latocha, L. Guarrigues, J. P. Boeuf, *Electron Transport in Stationary Plasma Thrusters*, Transp. Theory and Stat. Phys., **27** (1998), 203-221

[3] P. Degond, F. Méhats, C. Ringhofer, *On Quantum Energy Transport and Quantum Drift-Diffusion Models*, J. Stat. Phys. **118** (2005), no. 3-4, 625-665.

[4] N. C. Kluksdahl, A. M. Kriman, D. J. Ferry, C. Ringhofer, *Self-consistent study of the resonant-tunelling diode*, Phys. Rev. B **39** (1989) 7720

[5] P. Mounaix, O. Vanbésien, D. Lippens, *Effect of cathode spacer layer on the current voltage characteristics of resonant tunneling diodes*, Appl. Phys. Lett., **57** (1990), 1517.

[6] P. N. Argyres, *Quantum kinetic equations for electrons in high electric and phonon fields*, Physics Lett. A **171** (1992), 373

[7] F. A. Buot, K. L. Jensen, *Lattice Weyl-Wigner formulation of exact manybody quantum-transport theory and applications to novel solid-state quantum-based devices*, Phys. Rev. B **42** (1990), 9492.

[8] I. Gasser, P. Markowich, C. Ringhofer, *Closure conditions for classical and quantum moment hierarchies in small temperature limit*, Tranp. Th. Stat. Phys. **25** (1996), no. 3-5, 409-423.

[9] I. Gasser, A. Jüngel, *The quantum hydrodynamic model for semiconductors in thermal equilibrium*, Z. Angew. Math. Phys. **48** (1997), no. 1, 45-49

[10] M. Sanduloviciu, D. G. Dimitriu, L. M. Ivan, M. Aflori, C. Furtuna, S. Popescu, E. Lozneanu, *Self-organization scenario relevant for nanoscale science and technology*, Journal of Optoelectronics and Advanced Materials, **7**(2005), no. 2, 845-851

[11] L. Nottale, Fractal Space-Time and Microphysics: Towards a Theory of Scale Relativity (World Scientific, Singapore) (1993);

[12] M.S. El Naschie, O.E. Rösler and I. Prigogine, Quantum Mechanics, Diffusion and Chaotic Fractals (Elsevier, Oxford), (1995);

[13] B. Madelbrot, The fractal geometry of nature, (Freeman, San Francisco) (1982);

[14] S.H.Mohoreanu, M. Agop, *A theoretical approach of the heat transfer in nanofluids,* Jurnal of Optoelectronics and Advanced Materials, Vol. 8, No. 5, Oct. 2006, p. 1741-1743;

[15] M. Agop, P. D. Ioannou, P. Nica, *Superconductivity by means of the subquantum medium coherence*, Journal of Mathematical Physics **46**, 1 (2005);

[16] M. Agop, C. Murgulet, *El Naschie* $\varepsilon^{(\infty)}$ *space-time and scale relativity theory in the topological dimension D=4,* Chaos, Solitons and Fractals **32** (2007), 1231-1240;

[17] Jackson, E. A., Perspectives in nonlinear dynamics vols. I and II, *Cambridge, Cambridge University Press*, 1991;

[18] P. Degond, C. Ringhofer, *Quantum moment hydrodynamics and the entropy principle*, J. Stat. Phys. **112** (2003), 587-628

[19] S. Gallego, F. Méhats, *Numerical approximation of a quantum drift-diffusion model*, C. R. Acad. Sci. Paris, Ser. 1 **39** (2004), 519-524.

BULETINUL INSTITUTULUI POLITEHNIC DIN IAŞI
Tomul LIII (LVII), Fasc. 2, 2007
Secția
ŞTIINȚA ŞI INGINERIA MATERIALELOR

NANOSTRUCTURES AND FRACTAL SPACE-TIME (II)

P. VIZUREANU, M. AGOP, D.G. GALUSCA, I. IONITA

Abstract: *Using the fractal space-time theories in the topological dimension $D_T=2$, a hydrodynamic approach of transport phenomena in nanostructures is established. In such a context, the expression of the current density and the quantization of the conductance are established.*

I. Introduction

In Part I of this paper, a fractal space-time theory on the transport phenomena in nanostructures, considering that the motion of the micro-particles takes place on continuous but non-differentiable curves, *i.e.* on the fractals, is established. Then, by means of a scale covariance form of the Newton's equation,

$$\frac{\delta \boldsymbol{V}}{dt}=\frac{\partial \boldsymbol{V}}{\partial t}+\nabla\left(\frac{\boldsymbol{V}^2}{2}\right)-\boldsymbol{V}\times(\nabla\times\boldsymbol{V})-iD\Delta\boldsymbol{V}=\frac{\boldsymbol{F}}{m}=-\nabla\left(\frac{U}{m}\right) \tag{1}$$

where $\boldsymbol{V}$ is the complex speed field, U is the scalar potential of an external field, m the effective mass of a particle fluid and D a coefficient which defines the fractal/non-fractal transition, i.e. the transition from the explicit scale dependence to scale independence [1,2], the Scrödinger's type equation:

$$D^2\Delta\psi+iD\frac{\partial\psi}{\partial t}-\frac{U}{2m}\psi=0 \tag{2}$$

as an irrotational motion of the fluid

$$\boldsymbol{\Omega}=\nabla\times\boldsymbol{V}=0\ ,\mathbf{V}=\nabla\phi,\phi=-2iD\ln\psi \tag{3a-c}$$

in the topological dimension D_T=2, results. Then, ψ becomes simultaneously wave-function and complex speed potential.

In the present paper, a hydrodynamic model and some implications of this approach in nanotechnology are given.

II. Hydrodynamic Model

Let us consider the wave function $\psi=\sqrt{\rho}e^{iS}$, with $\sqrt{\rho}$ the amplitude and S the phase of ψ. Then the complex speed field (3b, c) becomes:

$$\boldsymbol{V}=\boldsymbol{v}-i\boldsymbol{u},\boldsymbol{v}=2D\nabla S,\ \boldsymbol{u}=D\nabla\ln\rho \tag{4a-c}$$

Introducing (4a-c) in (1) with the restriction (3a) and separating the real and imaginary parts (for details on the method see [3,4]), we obtain:

$$\frac{\partial \boldsymbol{v}}{\partial t}+\nabla\left(\frac{\boldsymbol{v}^2-\boldsymbol{u}^2}{2}-D\nabla\cdot\boldsymbol{u}\right)=-\nabla\left(\frac{U}{m}\right)$$
$$\frac{\partial \boldsymbol{u}}{\partial t}+\nabla\left(\boldsymbol{v}\cdot\boldsymbol{u}+D\nabla\cdot\boldsymbol{v}\right)=0 \qquad (5a, b)$$

or, up to an arbitrary phase factor which may be set to zero by a suitable choice of the phase of ψ,

$$(m\partial_t\boldsymbol{v}+m(\boldsymbol{v}\cdot\nabla)\boldsymbol{v})=-\nabla(Q^{(2)}+U)$$
$$\partial_t\rho+\nabla\cdot(\rho\boldsymbol{v})=0 \qquad (6a, b)$$

with $Q^{(2)}$ the fractal potential in the topological dimension D_T=2

$$Q^{(2)}=-2mD^2\frac{\Delta\sqrt{\rho}}{\sqrt{\rho}}=-\frac{m\boldsymbol{u}^2}{2}-mD\nabla\cdot\boldsymbol{u} \qquad (7)$$

The fractal potential depends only on the imaginary part, $\boldsymbol{u}$, of the complex speed field $\boldsymbol{V}$. Since $\boldsymbol{u}$ arises from non-differentiability according to the non-differentiable space model of "mechanics", it might be stressed out that the fractal potential comes from the non-differentiability of the fractal space-time.

The wave function of $\psi(\boldsymbol{r},t)$ is invariant when its phase changes by an integer multiple of 2π. Indeed, equation (4b) gives:

$$\oint m\boldsymbol{v}d\boldsymbol{r}=2mD\oint dS=4\pi mD,\quad n=0,\pm1,\pm2,... \qquad (8)$$

a condition of compatibility between the fractal scale and the non-fractal one.

For $D=\hbar/2m^*$ with $m^*=2m_e$ the mass of the Cooper type pair [5, 6] and $\hbar$ the reduced Planck's constant, the relation (8) becomes

$$\oint \boldsymbol{p}\cdot d\boldsymbol{r}=nh$$

This result can be identified with the quantification law of the magnetic flux [4]

$$\phi_e=n\phi_{0e},\ \phi_{0e}=h/2e$$

with ϕ_{0e} the magnetic fluxoid and $2e$ the charge of the Cooper pair. Indeed, the generalized momentum of the Cooper pair in the magnetic field $\boldsymbol{B}_e=\nabla\times\boldsymbol{A}_e$ with $\boldsymbol{A}_e$ the potential vector of the magnetic field, $\boldsymbol{P}_e=2m_e\boldsymbol{v}+2e\boldsymbol{A}_e$, is null [5, 6], i.e. $\boldsymbol{P}_e\equiv0$. Through integration, we obtain

$$\oint \boldsymbol{p}\cdot d\boldsymbol{r}=2e\oint \boldsymbol{A}_e\cdot d\boldsymbol{r}=2e\iint_{\partial\Sigma}\boldsymbol{B}_e\cdot d\boldsymbol{\Sigma}=2e\phi_e=\pm nh$$

i.e. the quantization of the magnetic field.

The set of equations (6a, b) represents a complete system of differential equations for the fields $\rho(\boldsymbol{r},t)$ and $\boldsymbol{v}(\boldsymbol{r},t)$; relation (8) relates each solution $(\rho,\boldsymbol{v})_n$ with the wave solution ψ in a unique way.

The field $\rho(\boldsymbol{r},t)$ is a probability distribution, namely the probability of finding the particle in the vicinity $d\boldsymbol{r}$ of the point $\boldsymbol{r}$ at time t,

$$dP=\rho\,\mathrm{d}\boldsymbol{r},\quad \iiint\rho\,\mathrm{d}\boldsymbol{r}=1, \qquad (9a, b)$$

the space integral being extended over the entire area of the system. Any time variation of the probability density $\rho(\boldsymbol{r},t)$ is accompanied by a probability current $\rho\boldsymbol{v}$ pointing towards or outwards, the corresponding field point $\boldsymbol{r}$ (equation (6b)). Therefore, the equation (6b) by means of equation (9a, b) corresponds to the Born's postulate.

The position probability of the real velocity field $\boldsymbol{v}(\boldsymbol{r},t)$ (equation (6a)), varies with space and time similar to a hydrodynamic fluid placed in the fractal potential (7). The fluid (in the sense of a statistical particles ensemble) exhibits, however, an essential difference compared to an ordinary fluid: in a rotation motion $\boldsymbol{v}(\boldsymbol{r},t)$ increases (decreases) with the decreasing (increasing) distance $\boldsymbol{r}$ from the center (equation (8)).

The expectation values for the real velocity field and the velocity operator $\hat{\boldsymbol{v}} = -2iD\nabla$ of the fractal mechanics are equal

$$\langle \boldsymbol{v} \rangle = \iiint \rho \boldsymbol{v} d\boldsymbol{r} = \iiint \Psi^* \hat{\boldsymbol{v}} \Psi d\boldsymbol{r} = \langle \hat{\boldsymbol{v}} \rangle_{WM} \tag{10}$$

but in the higher-order, $|n|>2$, similar identities are invalid, namely $\langle \boldsymbol{v}^n \rangle \neq \langle \boldsymbol{v}^n \rangle_{WM}$. The expectation for the 'fractal force' vanishes at all times (theorem of Ehrenfest [5]), i.e.,

$$\left\langle -\nabla Q^{(2)} \right\rangle = \iiint \rho \left(-\nabla Q^{(2)} \right) d\boldsymbol{r} = 0 \tag{11}$$

or explicitly

$$2mD^2 \iiint \rho \nabla \left(\frac{\nabla^2 \sqrt{\rho}}{\sqrt{\rho}} \right) d\boldsymbol{r} = mD^2 \oint \left(\rho \nabla \nabla \ln \rho \right) \cdot d\boldsymbol{\sigma} = 0 \tag{12}$$

Two types of stationary states are to be distinguished:

i) Dynamic states. For $\partial/\partial t = 0$ and $\boldsymbol{v} \neq 0$, equations (6a, b) give

$$\nabla \left(\frac{1}{2} m\boldsymbol{v}^2 - \frac{m\boldsymbol{u}^2}{2} - mD\nabla \cdot \boldsymbol{u} + U \right) = 0, \quad \nabla(\rho \boldsymbol{v}) = 0 \tag{13a, b}$$

namely

$$\frac{1}{2} m\boldsymbol{v}^2 - \frac{m\boldsymbol{u}^2}{2} - mD\nabla \cdot \boldsymbol{u} + U = E, \quad \rho \boldsymbol{v} = \nabla \times \boldsymbol{F} \tag{14a, b}$$

Consequently, non-fractal inertia, $m\boldsymbol{v} \cdot \nabla \boldsymbol{v}$, fractal force, $-\nabla Q^{(2)}$, and external force, $-\nabla U$, are in balance at every field point (equation (13a)). The sum of the non-fractal kinetic energy, $m\boldsymbol{v}^2/2$, fractal potential, $Q^{(2)}$, and external potential, U, is invariant, *i.e.* equal to the integration constant $E \neq E(\boldsymbol{r})$ (equation (14a)). $E \equiv \langle E \rangle$ represents the total energy of the dynamic system. The probability flow density $\rho\boldsymbol{v}$ has no sources (equation (13b)), *i.e.* its streamlines are closed (equation (14b)).

ii) Static states. For $\partial/\partial t = 0$ and $\boldsymbol{v} = 0$, equations (6a, b) give

$$\nabla \left(-\frac{m\boldsymbol{u}^2}{2} - mD\nabla \cdot \boldsymbol{u} + U \right) = 0, \tag{15}$$

i.e.

$$-\frac{m\boldsymbol{u}^2}{2} - mD\nabla \cdot \boldsymbol{u} + U = E \tag{16}$$

The fractal force, $-\nabla Q^{(2)}$, and external force, $-\nabla U$, at any field point has the same value (equation (15)). The sum of the fractal potential, $Q^{(2)}$, with the external

potential, U, is invariant, *i.e.* equal to the integration constant $E \neq E(\boldsymbol{r})$ (equation (16)). $E \equiv \langle E \rangle$ represents the total energy of the static system.

III. The current density in the topological dimension $D_T=2$.

Using the standard method from references [7, 8], the current density has the form,

$$\boldsymbol{j}^{(l)} = -qD_{diff}^{(l)} \nabla n - \mu^{(l)} n^{(l)} \nabla \left(U + Q^{(2)} + k_B T \right) \tag{17}$$

or, substituting (7) in (17)

$$\begin{aligned} \boldsymbol{j}^{(l)} &= -qD_{diff}^{(l)} \nabla n^{(l)} - \mu^{(l)} n^{(l)} \nabla \left(U - 2mD^2 \frac{\Delta\sqrt{\rho}}{\sqrt{\rho}} + k_B T \right) = \\ &= -qD_{diff}^{(l)} \nabla n^{(l)} - \mu^{(l)} n^{(l)} \nabla \left(U - \frac{m\boldsymbol{u}^2}{2} - mD\nabla \cdot \boldsymbol{u} + k_B T \right) \end{aligned} \tag{18}$$

In the relations (17) and (18), D_{diff} is the diffusion coefficient, μ is the mobility, q the electric charge, and the superscript l=e, p specifies the charge type. Therefore, the equation (18) depends not only on the classical quantities, i.e. $qD_{diff}^{(l)} \nabla n^{(l)}$, $\mu^{(l)} n^{(l)} \nabla (U + k_B T)$, but also on the fractal ones $\mu^{(l)} n^{(l)} \nabla \left[m\left(\boldsymbol{u}^2/2\right) + mD\nabla \cdot \boldsymbol{u} \right]$ and on the scales transition by means of the D coefficient.

For $2mD = \hbar$ the equation (18) becomes:

$$\boldsymbol{j}^{(l)} = -qD_{diff}^{(l)} \nabla n^{(l)} - \mu^{(l)} n^{(l)} \nabla \left(U - \frac{\hbar^2}{2m} \frac{\Delta\sqrt{\rho}}{\sqrt{\rho}} + k_B T \right) \tag{19}$$

a result in agreement with the one from references [9-14].

IV. The quantization of the conductance by means of the fractal potential

Let us show that we can derive from (14a) the quantized conductance of an ideal quasi-1D liquid. We consider the electron liquid adiabatically connected to two reservoirs, and we call $v_{L(R)}$ and $\mu_{L(R)}$ the velocity and the chemical potential, respectively, in the left (right) reservoir, with μ_L - μ_R=eV_{bias}. Then, taking zero external potential, U=0, and chemical potential identical with fractal potential (for details see [3-5, 8]), (14a) becomes,

$$\frac{v_L^2}{2} + \frac{\mu_L}{m} = \frac{v_R^2}{2} + \frac{\mu_R}{m} \tag{20}$$

By denoting the flow velocity, $v = (v_L + v_R)/2$, and the co-moving Fermi velocity [15], $v_F = (v_L - v_R)/2$, we get from (19) the relation $2mvv_F = eV_{bias}$. By definition, the current is given by $I = env$ so that, by using the 1D density of states and $2mD = \hbar$, $I = emvv_F / \pi\hbar = e^2 V_{bias} / h$, which, in the linear regime, gives the quantized conductance (per spin) $G_0 = I / V_{bias} = e^2 / h$. If we assume that only a fraction α of electrons is transmitted due to the presence of a barrier in the liquid, we can argue that, in linear

response, the current is an equal fraction of the current in the absence of the barrier, i.e. $I = env\alpha$. The conductance is thus $G = \alpha \cdot e^2 / h$ in accordance with references [16].

The same quantized conductance relation could be obtained from the equation (8) using the method described in the references [1, 2].

6. Conclusions.

The main conclusions of the present paper are as follows:
i) By means of a scale covariance form of the Newton's equation, a hydrodynamic model is given. It results the law of conservation of the probability density and the law of conservation of the momentum;
ii) The compatibility between the macroscopic scale and microscopic one leads to a quantification condition;
iii) The expressions of the current density and the quantization of the conductance in nanostructures are established.

Acknowledgements

The present work was supported by the contract CEEX no. 76-5/2006 MATNANTECH.

Received March 15, 2007

Technical "Gh. Asachi" University

References:

[1] L. Nottale, Fractal Space-Time and Microphysics: Towards a Theory of Scale Relativity (World Scientific, Singapore) (1993);
[2] M.S. El Naschie, O.E. Rösler and I. Prigogine, Quantum Mechanics, Diffusion and Chaotic Fractals (Elsevier, Oxford), (1995);
[3] M. Agop, P. D. Ioannou, and P. Nica, Journal of Mathematical Physics **46**, 1 (2005).
[4] M. Agop, and C. Murgulet, Chaos, Solitons and Fractals **32**, 1231 (2007).
[5] Ş. Ţiţeica, Quantum mechanics, (Ed. Acad. Bucharest) 1984;
[6] G. Burns, High-Temperature superconductivity. An introduction, (Academic Press: San Diego), (1992)
[7] P. Degond, V. Latocha, L. Guarrigues, J. P. Boeuf, *Electron Transport in Stationary Plasma Thrusters*, Transp. Theory and Stat. Phys., **27** (1998), 203-221
[8] P. Degond, F. Méhats, C. Ringhofer, *On Quantum Energy Transport and Quantum Drift-Diffusion Models*, J. Stat. Phys. **118** (2005), no. 3-4, 625-665.
[9] N. C. Kluksdahl, A. M. Kriman, D. J. Ferry, C. Ringhofer, *Self-consistent study of the resonant-tunelling diode*, Phys. Rev. B **39** (1989) 7720
[10] P. Mounaix, O. Vanbésien, D. Lippens, *Effect of cathode spacer layer on the current voltage characteristics of resonant tunneling diodes*, Appl. Phys. Lett., **57** (1990), 1517.
[11] P. N. Argyres, *Quantum kinetic equations for electrons in high electric and phonon fields*, Physics Lett. A **171** (1992), 373
[12] I. Gasser, A. Jüngel, *The quantum hydrodynamic model for semiconductors in thermal equilibrium*, Z. Angew. Math. Phys. **48** (1997), no. 1, 45-49

[13] P. Degond, C. Ringhofer, *Quantum moment hydrodynamics and the entropy principle*, J. Stat. Phys. **112** (2003), 587-628
[14] S. Gallego, F. Méhats, *Numerical approximation of a quantum drift-diffusion model*, C. R. Acad. Sci. Paris, Ser. 1 **39** (2004), 519-524.
[15] Giuliani G. F., and Vignale G., *Quantum theory of the Electron Liquid*, Cambridge University Press, 2005;
[16] R. D'Agosta, and M. Di Ventra, *Hydrodynamic approach to transport and turbulence in nanoscale conductors*, J. Phys.: Condens. Matter **18**, 11059 (2006)

BULETINUL INSTITUTULUI POLITEHNIC DIN IAŞI
Tomul LIII (LVII), Fasc. 2, 2007
Secția
ŞTIINȚA ŞI INGINERIA MATERIALELOR

SIMULATION OF HEAT TREATMENT STRESS AND DISTORSION

RADU CRISTIAN IVĂNUŞ

Abstract: *This paper gives an overview of the problem of heat treatment stress and distortion. Simulations are presented for a quenched cylinder to demonstrate the capabilities of software available for predicting heat treatment stress and distortion. The software package ANSYS was identified as one of the most advanced tools for solving heat treat distortion problems.*

Key words: *simulation,heat treatment, stress, distorsion, quenching*

1. Introduction

The modeling of heat treatment and its effects on the stress state of a casting is not easy. It involves not just modeling the heat transfer and stresses in the casting, but also modeling the microstructural changes in the steel throughout processing. Changes in the steel microstructure are very important since they produce changes in mechanical properties (density and thermal expansion coefficient). Other technical obstacles to computer modeling include complex heat transfer (i.e. boiling regimes during quenching), quenchant properties, variable mechanical properties with temperature and microstructure, and non-uniform heat transfer conditions over the casting surface.

An excellent overview of the mathematical modeling of heat treatment distortion is presented by Fletcher [1]. Here the reader will find important background on the elastic-plastic and finite element modeling used to compute thermal stresses, as well as background on the relationship between microstructure and thermal stress. Fletcher [1] also provides an overview of thermo-mechanical material properties dependent on temperature and microstructural phase. Even though this reference reflects the state of capabilities in the 1980's, and presents only two-dimensional modeling results for cylinders and plates, it presents the fundamentals of the models and issues that do not change. A recent literature review on the topic is given by Rohde and Jeppsson [2], where they present Figure 1. This figure is repeated here because it is an excellent graphical representation of the problem. Starting with the three main model components required to simulate heat treatment distortion (heat transfer analysis, phase transformations and mechanical response), Figure 1 gives their important factors, issues to be addressed, and the most critical results from heat treatment simulation: distortion, residual stress and microstructure. Using Figure 1 as a visual aid representing the complexity of the problem, it is easy to understand why the problem has been attacked in a piece by piece fashion over the years.

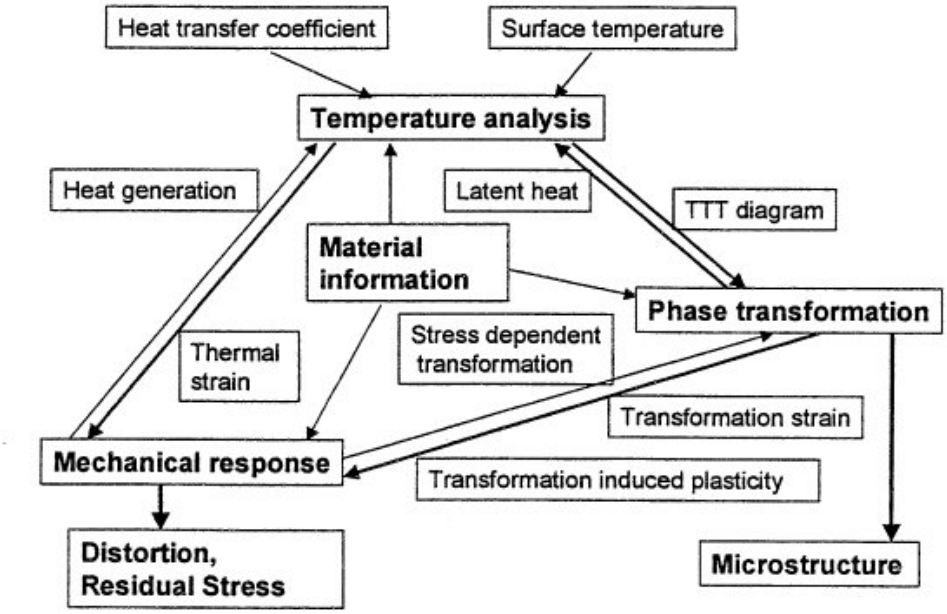

Fig. 1. Diagram of the three coupled parts to simulating heat treatment distorsion and their important factors [2]

The phase transformation and material constitutive models must be combined with a thermal stress computation. Commercial finite element software packages are readily capable of predicting un-coupled and coupled heat transfer with stress and displacement (ABAQUS, ANSYS, NASTRAN and many others).

ANSYS was chosen as the simulation software used in the present work. The primary goal here is to investigate and demonstrate its abilities to predict heat treatment distortions and residual stresses in steel castings. A classic test problem, the heat treatment of a cylinder, will first be solved to demonstrate the fundamental issues arising during heat treatment, due to thermally induced plastic deformation and multiple phases present.

2. Heat Treatment Stress and Distortion with Software Demonstration

A classic problem commonly used to visualize the formation of residual stresses is the cooling (or quenching) of a cylinder. Consider longitudinal stress and deformation in a section taken from a cylinder as cooling proceeds from steps “A” through “D” shown in Figure 2 a) and b), taken from [3]. At step “B”, rapid cooling at the surface results in longitudinal tension near the surface, and compressive stress forms at the center. If plastic deformation occurs, the center contracts, and the surface expands relieving the stress – a final residual stress distribution shown at “D” results as shown in Figure 2 c). This process occurs simply due to thermal stresses forming as a result of temperature dependent material properties, without the consideration of phase changes. Commercial finite element software, such as ANSYS used here, is readily capable of predicting these thermal stresses.

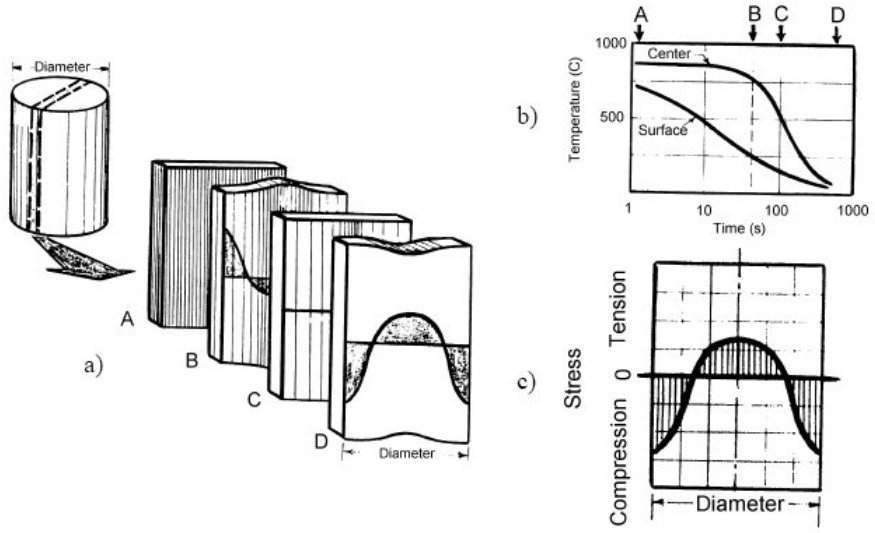

Fig. 2. Illustration of residual stress formation in quenching [3]

Additional stress and deformation occurs in the presence of phase change due to differences in material properties (thermal expansion coefficient for example) of the phases present. The complexities associated with residual stress formation in the presence of phase changes are discussed in detail by Dulămiță and Florian [3]. Here we follow an example presented by Dulămiță and Florian to illustrate the nature of the stresses that form due to phase transformations and the final microstructural variations in a part. Consider a cylinder cooling, but now overlay the cooling curves for the surface and center of the cylinder onto a continuous cooling transformation diagram as shown in Figure 3 [3]. For the steel under consideration, the rapid cooling at the surface forms martensite, beginning at the martensite start temperature M_s indicated by point S1 in Figure 3. The surface continues cooling until the end of the martensitic reaction at point S2. The center cooling curve indicates that the austenite will decompose into pearlite beginning at point C1 until C2 when all the austenite has decomposed into pearlite.

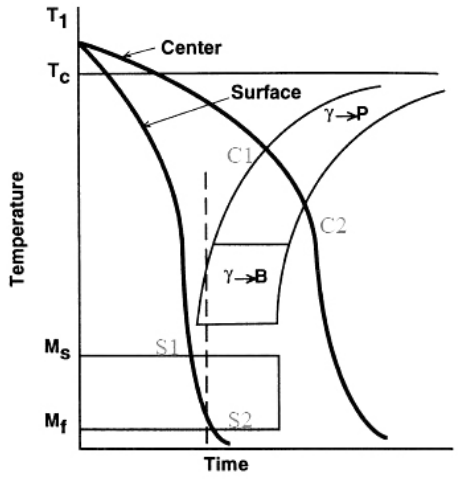

Fig. 3. Example cooling curves for the surface and center of a cooled steel cylinder overlaid on a schematic CCT diagram [3].

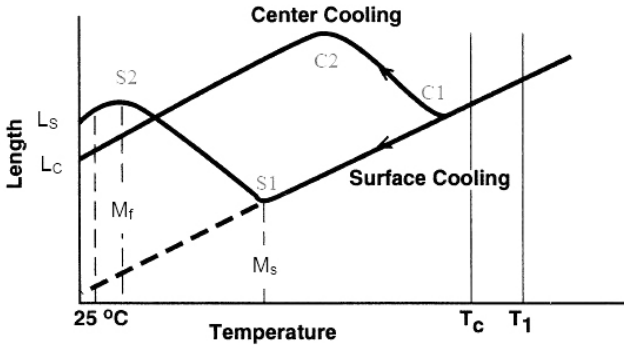

Fig. 4. Variation in length for steel cooled at the surface and center as given in Figure 3 [3]. Points S1, S2, C1, and C2 correspond to those given in Figure 3.

Consider now the volumetric changes that occur in the metal when it changes phase. Martensite has about 5% greater specific volume than the austenite from which it forms. Even though the austenite from which the martensite is forming continues to contract on cooling, the formation of the martensite results in a net expansion of the steel. This can be visualized by imagining an entire cylinder being cooled under the conditions of the surface shown in Figure 4 from point S1 to S2. Point S1 indicates the start of expansion due to the beginning of martensite formation. Eventually, at point S2, the martensite is finished forming, and there is no further expansion due to the phase transformation. At this point, our imaginary cylinder undergoing the "surface" cooling conditions will continue to contract according to the thermal expansion coefficient of martensite until it reaches a final length L_S as indicated in Figure 4. Visualize another imaginary cylinder being cooled under the conditions at the center. For the center cooling curve, pearlite begins to form at C1 shown in Figure 4. Since the specific volume of pearlite is larger than austenite (like martensite), it expands until the completion of the austenite decomposition to pearlite at C2. After C2, the pearlite will contract according to its thermal expansion coefficient to a final length of L_C. Next imagine that we can join the material in the two imaginary cylinders (cooled at surface and center conditions) into one cylinder. Without restriction, the length of the surface of this cylinder would be L_S and the center would be L_C. However, they are restricted now by being joined together and since $L_C < L_S$, the surface pulls on the center section placing it in tension, while the center also resists being pulled placing the surface in compression. The resulting length of the joined-cylinder (having a center made of pearlite and a surface of martensite) will be between L_C and L_S and the longitudinal stress state will be compressive at the surface and in tension at the center.

In Figures 5 through 9 results of ANSYS calculations user subroutines are made for a OLC 45 STAS 791-88 steel cylinder quench from 900^{o}C to 65^{o}C in an oil bath. The cylinder is 25 mm diameter by 100 mm long. As an added demonstration, the surface of the cylinder has been carburized using that feature of the software package. Three simulations were run the achieve these results:

- a carburization (diffusion) calculation to establish the carbon distribution in the part from the carburization process.
- a heat transfer simulation of the quenching process that accurately predicts the phase transformations occurring in the cylinder in the presence of the non-uniform carbon distribution from carburization along with the thermal field. The increase in carbon due to the carburization process is incorporated by transferring the carbon field resulting from step 1) above while the cylinder is at the carburization temperature.
- a thermal-stress calculation is made using the temperature, and phase dependent material model that includes the effect of the carbon distribution in the part.

An additional feature demonstrated in this example is ANSYS's ability to simulate the immersion process of the part into the quenchant. This can be quite important for long parts or longer immersion times where substantial thermal gradients are induced in parts during the immersion process. In this case, immersion was set to take place over 5 seconds which is rather long for a cylinder this size, but this serves to demonstrate that a noticeable temperature gradient is developed.

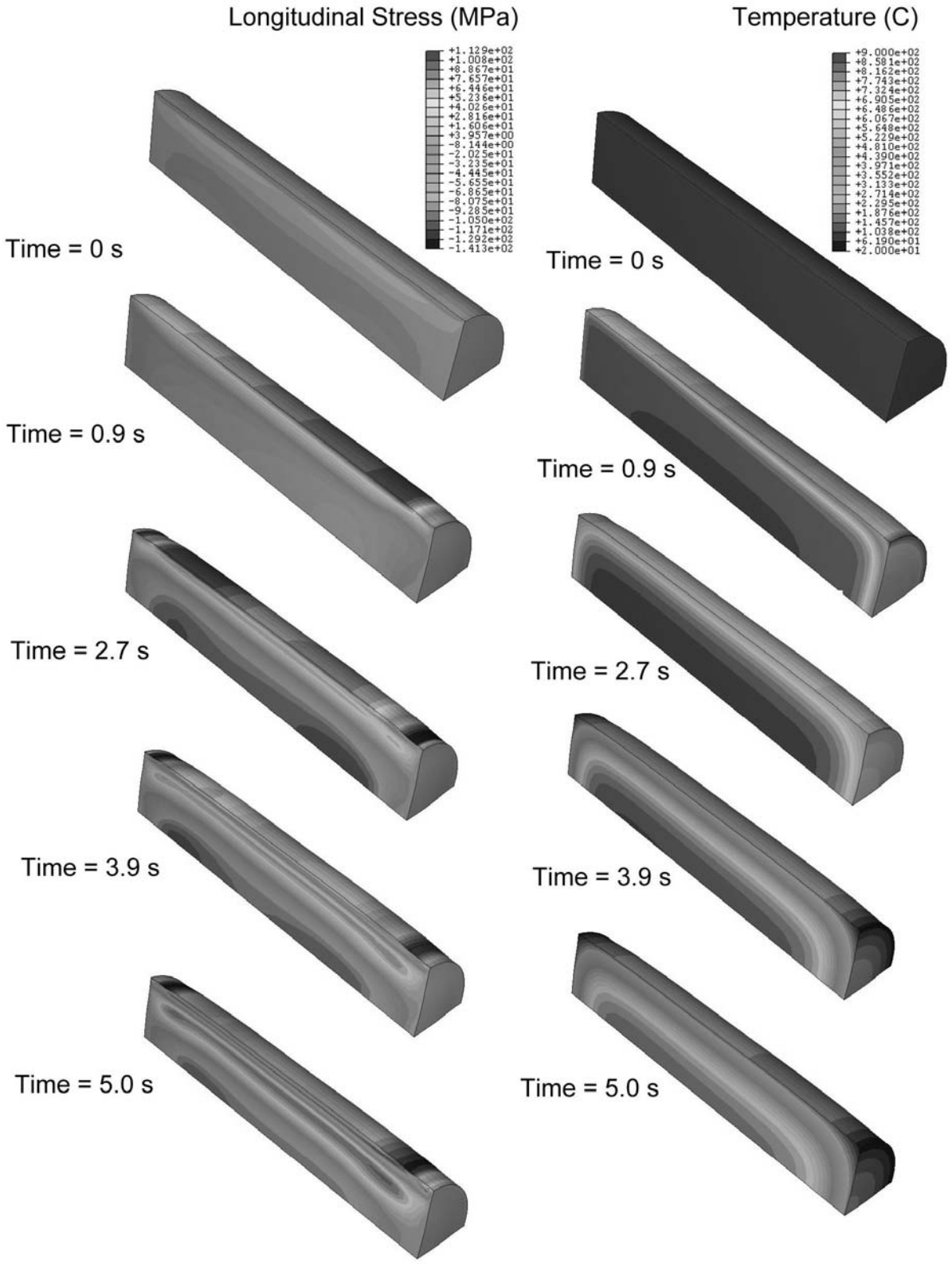

Fig. 5. Results of ANSYS thermal-stress calculation for a steel cylinder immersed into an oil bath at 65^{o}C over a period of 5 seconds. The cylinder was removed from furnace at 900^{o}C. Longitudinal stresses are shown on the left hand side and temperatures on the right hand side. Deformation is 30 x

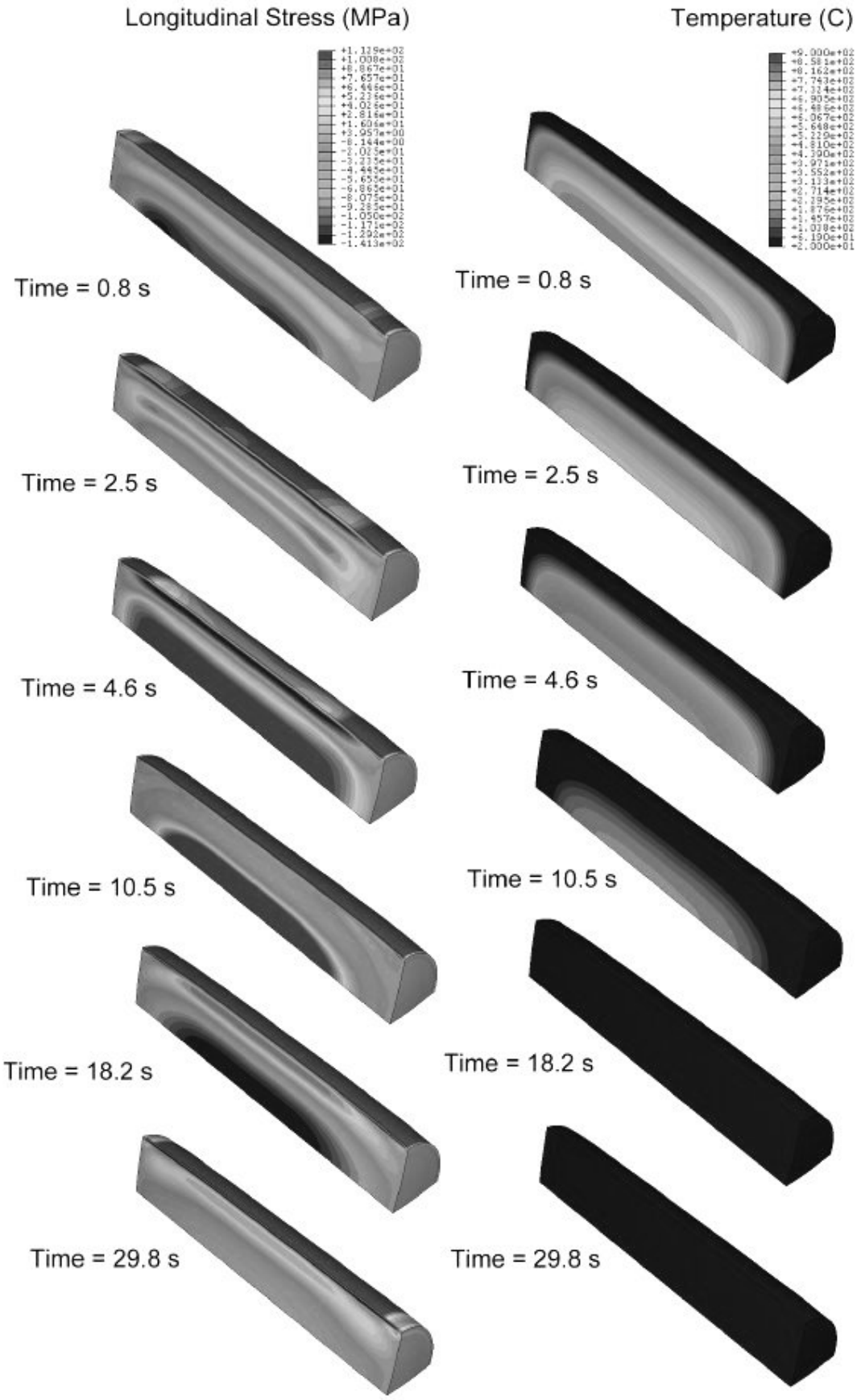

Fig. 6. Results of ANSYS thermal-stress calculation for a steel cylinder after immersion into an oil bath at 65^{o}C over a period of 30 seconds. Longitudinal stresses are shown on the left hand side and temperatures on the right hand side. Deformation is 30 x.

In Figure 5 the longitudinal stress and temperature fields at 0, 0.9, 2.7, 3.9 and 5.0 seconds into the immersion process are shown. The direction of the advance quenchant surface is shown also. The greatest temperature and stress field gradients along the length appear at 0.9 and 2.7 seconds. After immersion, the surface appears to be slightly in tension and the center in compression.

Figure 6 shows the stress field development after the immersion process, up to about 30 seconds after immersion is complete. Note the initial stress field at 0.8 seconds after immersion has a large tensile stress at the surface and compressive stresses at the center. As the rapid cooling proceeds, the stress field very nearly reverses itself at 4.6 seconds to high tension at the center and a region of compressive stress developing near (but still under) the surface; in this region austenite is decomposing to bainite resulting in phase transformation induced stresses such as those discussed in Figures 3 and 4. The surface has not yet begun to undergo transformation to martensite and remains in tension. At 29.8 seconds the surface appears to begin to show the development of compressive stresses due to the onset of martensite formation as shown in Figure 7. Beginning around 29.8 seconds, the martensite start temperature is reached for the carburized region near the surface and it proceeds to form as shown at 41.8 seconds until achieving its final distribution. As the martensite forms, a large compressive stress develops at the surface. There is not a great difference between the stress field at 41.8 seconds and the final stress field shown in Figure 8. The final microstructural phases resulting from the heat treatment process are shown in Figure 10. Martensite forms in amounts greater than 90% near the surface and to a smaller degree at the corner/ends of the cylinder, a 10% to 50% amount of primary ferrite (increasing towards the center), and a substantial amount of bainite forms through the cylinder except at the carburized surface.

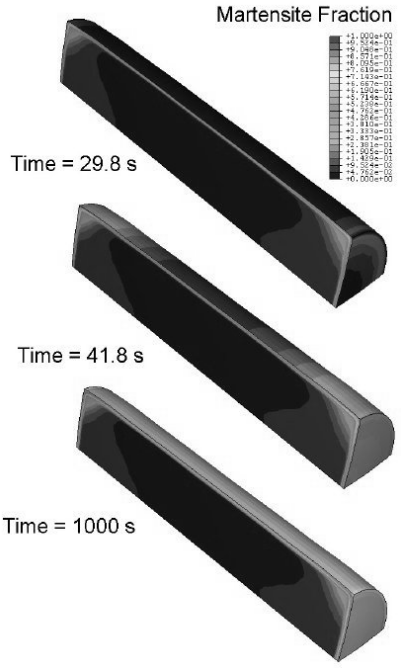

Fig. 7. Results of martensite fraction formation from ANSYS for a steel cylinder after immersion into an oil bath at 65°C

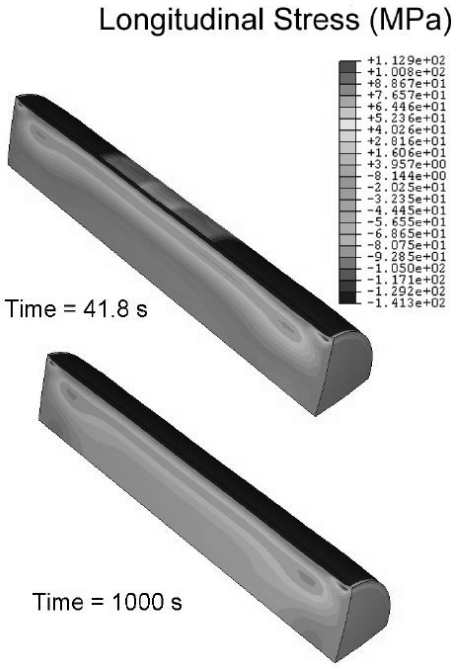

Fig. 8. Results of longitudinal stress field from ANSYS calculation for a steel cylinder after immersion into an oil bath at 65°C. Deformation is 30 x

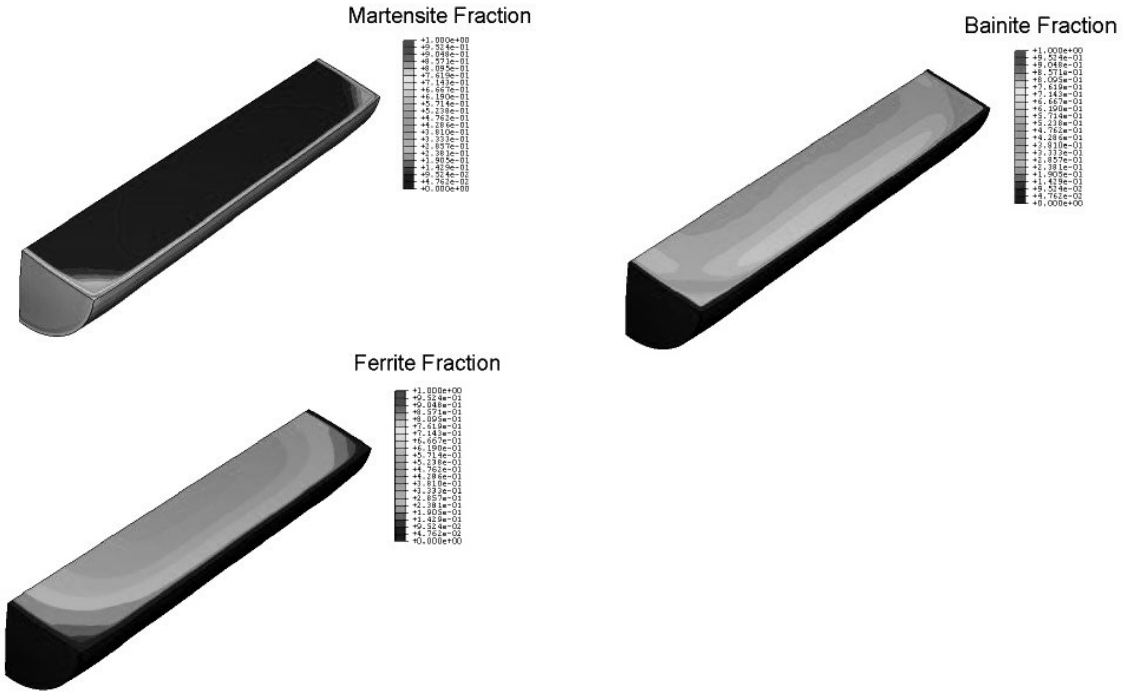

Fig. 9. Final microstructural fields from ANSYS calculation for a steel cylinder after immersion into an oil bath at 65^{o}C for 1000 s

3. Conclusions

The work presented here gives an overview of the problem of heat treatment stress and distortion and software that has been developed to model it. Simulations were performed and are presented here to demonstrate the software available for predicting heat treatment stress and distortion. The software package ANSYS was identified as one of the most advanced tools for solving heat treat distortion problems.

References

1. A.J. Fletcher, *Thermal Stress and Strain Generation in Heat Treatment*, Elsevier Science, London, 1989.
2. J. Rohde, A. Jeppsson, "Literature Review of Heat Treatment Simulations with Respect to Phase Transformation, Residual Stresses and Distortion," *Scandinavian Journal of Metallurgy,* 2000, **29(2)**, pp. 47-62.
3. T. Dulămiță, E. Dulămiță, *Tratamente termice şi termochimice*, Editura Didactică şi Pedagogică, Bucureşti, 1982.

University of Craiova, Faculty of Mechanics, Dept. of Technology and Materials

SIMULAREA TENSIUNILOR ŞI DEFORMAȚIILOR PROVOCATE DE TRATAMENTUL TERMIC

Rezumat: Lucrarea prezintă o vedere de ansamblu asupra tensiunilor şi deformațiilor provocate de tratamentul termic. Simulările au fost efectuate folosind un cilindru călit pentru a demonstra capacitățile software-lui de a anticipa tensiunile şi deformațiile provocate de tratamentul termic. Software-ul ANSYS a fost considerat una din cele mai avansate metode utilizate pentru a rezolva problemele cauzate de tensiuni şi deformații.

BULETINUL INSTITUTULUI POLITEHNIC DIN IAŞI
Tomul LIII (LVII), Fasc. 2, 2007
Secția
ŞTIINȚA ŞI INGINERIA MATERIALELOR

MODELLING AND SIMULATION FOR HEAP BIOLEACHING OF COPPER WASTES

RADU CRISTIAN IVĂNUŞ, MARIUS STĂNESCU

Abstract: *A computational model for heap bioleaching of spent catalysts, which include forced aeration is investigated to identify and understand aspects of bacteria in bioleaching applications. A parameter analysis is performed which shows that the factors important to copper leaching are liquid and air flow rates, and permeability. The ability to control which parts of the bed received the highest extraction as a function of the liquid and air flow rates was established. Forced aeration is found to increase the oxygen concentration throughout the heap compared to the circumstance with natural convection, and consequently improves the copper extraction significantly.*

Key words: *copper, Thiobacillus ferrooxidans, spent catalysts, modelling, simulation*

1. Introduction

Heap bioleaching is an important hydrometallurgical process used in industry for the removal of metals such as copper and gold from low grade ores [1] and industrial wastes [2]. The process is favoured because of the low maintenance and large volume in processing, only requiring the control of acid application, inoculation of bacteria and provisions for supplying sufficient oxygen throughout the heap. The leaching process occurs as a result of infiltration of sulphuric acid into the heap, which forms a film over the particles. Oxygen in the air phase reacts chemically with the ferric ions in the acid and copper sulphide in the ore or waste, to produce ferrous ions and copper in solution which flows out of the heap with the liquid. The process occurs in the presence of bacteria, such as *Thiobacillus ferrooxidans,* which convert ferrous ions back into ferric ions. In addition to the infiltration of acid, the ore particles during heap construction are coated with liquid (acid), which is inoculated with bacteria.

There are a number of factors to be accounted for in heap bioleaching modelling, including the liquid and air flow, bacterial action and copper extraction. The chemical reactions of these components (oxygen, liquid, bacteria, copper) are reasonably well known, however reaction rate depends on mass transfer processes, specifically oxygen supply in many cases. In this work we assume the liquid flow behaviour in the heap is uniform, and look at the effect on copper extraction of air flow in the heap under forced aeration, for various assumed bacterial concentrations. Without the use of forced aeration, oxygen supply to the heap depends on natural convection which occurs when temperatures inside the heap are greater than outside.

The onset of such effects has been studied by Lu and Zhang [3]. For large heaps like those used in industry, this does not provide enough oxygen deep within the heap for copper extraction [4]. In addition, Casas *et al.* [5] found that heaps with height and width larger than 10 by 20 metres, respectively, were ineffective in terms of copper recovery due to lack of air flow.

2. Model description

Consider a two dimensional uniform porous medium of trapezoidal shape (Figure 1) with a given permeability and porosity. In practice the particle size distribution can be widely varying, with regions of different permeability and porosity through the bed. Figure 1 shows the heap in bold, and the computational domain used.

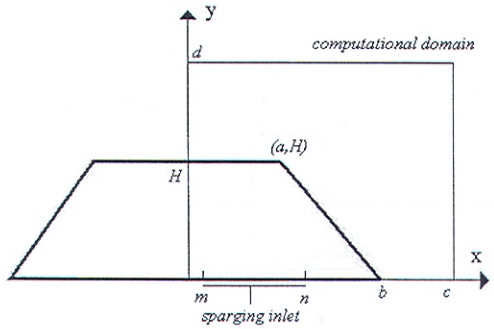

Fig. 1. Schematic heap

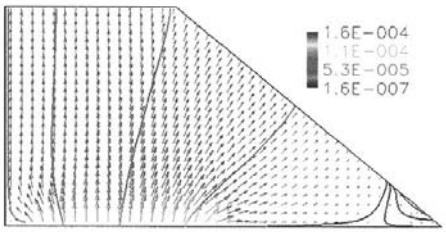

Fig. 2. Streamlines with vector plot and coloured by speed, $V_{in}=1.0\times10^{-4}$, $q_l=0.5q_{L,0}$, $K=5\times10^{-10}$

Acid solution is assumed to feed uniformly downward under the influence of gravity, though in practice the solution flow can take tortuous flow paths, with both channelling and liquid stagnant regions, due to heterogeneities and properties of the unsaturated liquid flow [1]. The liquid is assumed to coat the grains of the heap such that its affect on the pore space available to the gas can be ignored. Due to the large grain size, capillary pressure is neglected in this work and the gas flow is determined ftom a single-phase, rather than a two-phase calculation. It can be shown that it is a good approximation to assume that the temperature of the air is in local thermodynamic equilibrium with the liquid and ore bed. Consequently, it is sufficient to solve for the heat transport of air, taking into account the heat advected by the liquid.

The bacterial concentration would vary in time and space in practice, but is kept constant in this work for simplicity.

The acidophilic mesophile iron oxidiser used in the study was *Thiobacillus ferrooxidans* (originally isolated from Cavnic Mine water, Romania). For the cultivation of *Thiobacillus ferrooxidans*, the 9K media (0,15 g KCl; 0,15 g $(NH_4)_2SO_4$; 0,5 g $MgSO_4$; 0,5 g K_2HPO_4; 0,1 g $Ca(NO_3)_2$; 5 g $FeSO_4$; 1000 ml distilled water) with a reduced iron content (4 g $FeSO_4 \cdot 7H_2O$/l) was utilised; the pH was adjusted to 2 with concentrated H_2SO_4. *Thiobacillus ferrooxidans* cultures were shaken at 150 rpm on an orbital shaker at room temperature (19-22°C). Subcultures were carried out every 4–5 days to keep the bacteria in the logarithmic phase of growth.

The copper waste was collected by S.N.P. Petrom – Doljchim chemical combine platform. The specific mesh size was prepared by crushing in a jaw crusher.

The reaction of a metal sulphide (MS) in the heap is a two stage reaction. The solution contains ferric ions (Fe^{3+}) that reacts with copper sulphide to produce ferrous ions (Fe^{2+}) as

$$MS + 2Fe^{3+} \rightarrow 7M^{2+} + 2Fe^{2+} + S$$

Ferrous ions are re-oxidized to ferric ions in the presence of bacteria (only *Thiobacillus ferrooxidans* is considered as

$$2Fe^{2+} + 0.5O_2 + 2H^{+} \xrightarrow{bacteria} 2Fe^{3+} + H_2O$$

where M is the metal copper or iron.

The overall reactions for chalcocite Cu_2S and pyrite FeS_2 have the stoichiometries

$$FeS_2 + 3.5O_2 + H_2O \rightarrow FeSO_4 + H_2SO_4$$

$$Cu_2S + 2.5O_2 + H_2SO_4 \rightarrow 2CuSO_4 + H_2O$$

3. Numerical method

The system of partial differential equations were discretized and solved using a computational fluid dynamics solver *ANSYS CFX* [6] and the simulations required an orthogonal grid (250 by 250 cells) to avoid instability. The grid used was rectangular and a staircase of computational cells represents the slanted top of the heap. The results for a grid with 125 by 125 cells was found to be insignificantly different to that of 250 by 250 cells. Liquid was applied evenly across entire exposed boundary of the heap with a given flow velocity q_L.

4. Results and discussion

The concentration of bacteria in the heap, in particular *T. ferrooxidans,* is largely unknown, and it is appropriate to look at the effect of such levels on the temperature, oxygen and copper extraction. Hence, the results are split into two parts for low and high bacterial concentrations, with values of $X=5\times10^{13}$ bacteria/m^3 and $X=5\times10^{12}$ bacteria/m^3 respective!y. We have not investigated the effect of variation of the *FPY* factor, unlike Casas *et al.* [5], due to space constraints. For the parameters in Table 1 we present the results at several times.

Low Bacterial Levels. The results found for relatively low bacterial levels are described in this section, with the constant value $X=5\times10^{12}$ *bacteria/m*^{3}. In Figures 2-5 we see (in order) the 2-D plots with streamlines of vectors coloured by speed, and flooded contours of % oxygen mass fraction normalized by atmospheric oxygen mass fraction ($100\times W_0/0.22$*),* temperature and % copper extracted ($\alpha\times100$, after l year) for a sparging velocity $V_{in}=1\times10^{-4}$ m/s.

Table 1. Parameters for all results

Parameter	Value
Bed porosity, ε [m^3/m^3]	0.25
Bed height, H [m]	1.0
Top, a and bottom, b length [m]	1.0; 2.5
Upper computational domain, c; d [m]	1.25; 3.0
Air density, ρ_a [kg/m^3]	1.208
Air viscosity, μ_a [kg/m/s]	1.812×10^{-5}
Air diffusion coefficient, D_a [m^2/s]	1.44×10^{-5}
Air thermal conductivity, λ [W/m/K]	2.88×10^{-2}
Air thermal expansion coefficient, γ [1/K]	3.43×10^{-3}
Liquid specific heat, $C_{P,L}$ [J/kg/K]	4000
Relative liquid flow rate, $q_{L,0}$ [m/s]	1.4×10^{-6}
Monod half growth rate constant, K_m [kg/m^3]	1.0×10^{-3}
Heat of reaction, ΔH [J/kg]	-1.26×10^{7}
Stoichiometric factor, β [m/s]	0.193370
Copper grade, G_0 [% wt]	0.5
FPY	5
Atmospheric oxygen mass fraction, W_0 *(atmospheric)* [% wt]	25.0

In Figure 5, the copper extracted after 1 year is calculated by extrapolating linearly from the initial reaction rate. This corresponds to a typical air flow rate used in practice [1]. The figures show that some natural convection occurs, whilst sparging dominates the air flow. The oxygen mass fraction stays relatively high through out the heap, showing that the process of sparging avoids low oxygen levels that inhibit copper extraction.

In Figure 3, the minimum oxygen level occurs near the bottom right hand corner of the heap, which is caused by the low flow rates (Figure 2) in that area. This low oxygenated area occurs in spite of the fact there is some natural convection in that area. In Figure 4 and 5 the temperature and copper extraction (after l year) are shown revealing the strong dependence of the copper extraction upon the temperature.

In Figures 6 and 7 a comparison is made between cases with and without forced aeration, for fixed liquid flow rate, bacterial concentration and permeability. Figure 7 shows that oxygen becomes depleted without the use of sparging, limiting copper extraction with a characteristic extraction time of 13,258 days, compared to 8,013 days when sparging at $V_{in}=1\times10^{-4}$ (Figure 6).

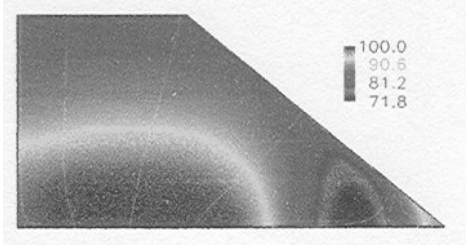

Fig. 3. Streamlines with contours of normalised mass fraction oxygen % ($100\times W_0/0.22$), $V_{in}=1.0\times10^{-4}$, $q_l=0.5q_{L,0}$, $K=5\times10^{-10}$

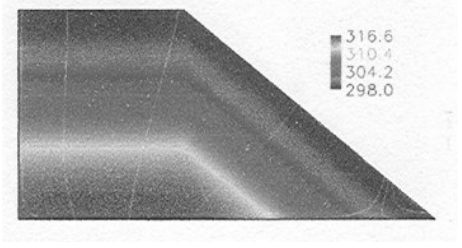

Fig. 4. Streamlines with contours of T, $V_{in}=1.0\times10^{-4}$, $q_l=0.5q_{L,0}$, $K=5\times10^{-10}$

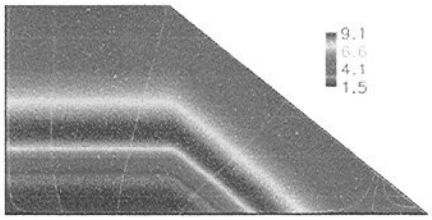

Fig. 5. Streamlines with contours of $100\times\alpha$ (1 year), $V_{in}=1.0\times10^{-4}$, $q_l=0.5q_{L,0}$, $K=5\times10^{-10}$

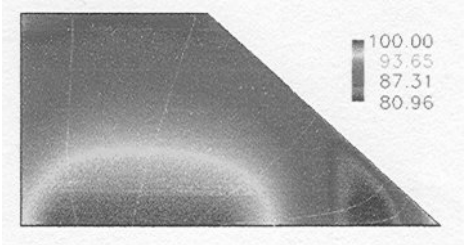

Fig. 6. Streamlines with contours of normalised oxygen mass fraction oxygen % $(100\times W_0/0.22)$, $V_{in}=1.0\times10^{-4}$, $q_l=0.5q_{L,0}$, $K=5\times10^{-10}$

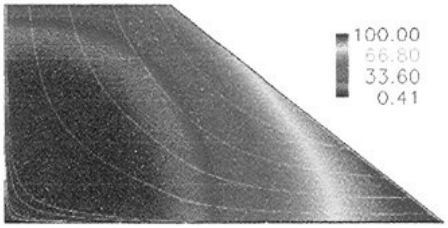

Fig. 7. Streamlines with contours of normalised oxygen mass fraction oxygen % $(100\times W_0/0.22)$, no forced aeration, $q_l=0.5q_{L,0}$, $K=5\times10^{-10}$

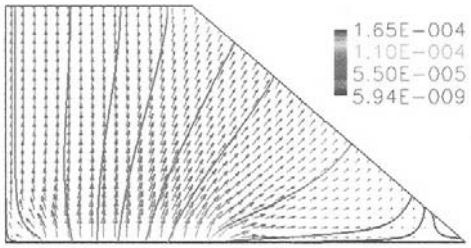

Fig. 8. Streamlines with vector plot and coloured by speed, $V_{in}=1.0\times10^{-4}$, $q_l=0.5q_{L,0}$, $K=5\times10^{-10}$

In Table 2 a comparison of the characteristic copper extraction time $t*\equiv1/(d\alpha/dt)$ is made for different flow rates, showing that $t*$ is highly dependent on the liquid flow rate, with a minimum occurring around $0.5q_{L,0}$ where $q_{L,0}=1.4\times10^{-6}$. This dependence occurs due to the cooling effect the liquid has on the air. Thus liquid flow rate may be used to control the temperature distribution to ensure that it remains as close as possible to the optimal value of around 311K.

Table 2. $t*$ versus liquid flow rate q_L ($\times$ $q_{L,0}$), $V_{in}=1.0\times10^{-4}$, $K=5\times10^{-10}$

$q_L(\times q_{L,0})$	0.125	0.25	0.5	1	1.5	2	3
t* (days)	17857	10371	6667	7042	8013	8264	8333

In Table 3 the effect of the permeability is shown on the characteristic copper extraction time $t*$. It is only dependent on the permeability to a small extent for an air sparging velocity $V_{in}=1.0\times10^{-4}$ and $V_{in}=1.0\times10^{-5}$, as explained by the $t*$ ratio in Table 3. The relative difference is negligible in terms oflong term extraction.

High Bacterial Levels. In this section we look at the results in the case of a higher constant bacterial concentration, $X=5\times10^{13}$ bacteria/m^3, compared to the last section where $X=5\times10^{12}$. One of the most significant changes was the decrease in characteristic copper extraction time $t*$ (compare Table 2 and Table 4). Again, the liquid flow rate has a substantial effect on the copper extraction (Table 4), due to the ability of the liquid to cool the heap, and push the temperature closer to the optimal

temperature *(~311K)*. Table 4 shows the best liquid flow rate occurs around $5q_{L,0}$, and such estimates could be useful in practice.

Table 3. $t*$ versus K for $q_L = 1.5q_{L,0}$ and associated t∗ ratio of $V_{in}=1.0\times10^{-5}$ to $V_{in}=1.0\times10^{-4}$

K	*t∗ (days)*		*t∗ ratio*
	$V_{in}=1.0\times10^{-4}$	$V_{in}=1.0\times10^{-5}$	
5×10^{-9}	8065	8170	0.9871
5×10^{-10}	8013	8621	0.9295
5×10^{-11}	8091	8681	0.9320

The computed results for this "optimal" liquid flow rate are shown in Figures 8-11. Figure 8 shows some entrainment of air occurs into the heap, whilst in Figure 9 we see the oxygen mass fraction becomes depleted well before air leaves the heap, suggesting that a higher inlet velocity should be used (Figures 12-14). Figure 10 shows that the temperature is distributed around the optimal temperature of *311K* for a large area, leading to extraction in some areas as high as 92% after one year.

Table 4. $t*$ versus liquid flow rate q_L ($\times q_{L,0}$), $V_{in}=1.0\times10^{-4}$, $K=5\times10^{-10}$

$q_L(\times q_{L,0})$	1	2	3	4	5	6
t∗ (days)	2274	1409	1140	1122	1119	1125

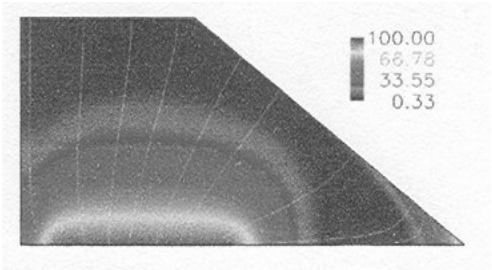

Fig. 9. Streamlines with contours of normalised oxygen mass fraction % *(100×W_0/0.22)*, $V_{in}=1.0\times10^{-4}$, $q_l=5q_{L,0}$, $K=5\times10^{-10}$

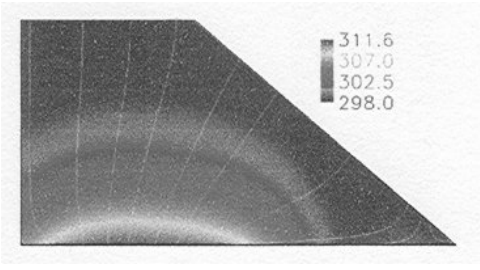

Fig. 10. Streamlines with contours of T, $V_{in}=1.0\times10^{-4}$, $q_l=5q_{L,0}$, $K=5\times10^{-10}$

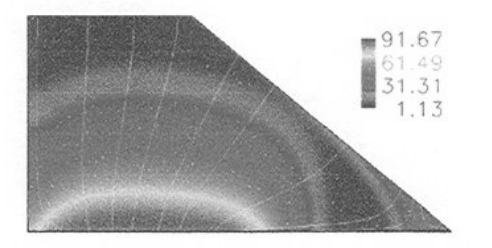

Fig. 11. Streamlines with contours of *100×α* (1 year), $V_{in}=1.0\times10^{-4}$, $q_l=5q_{L,0}$, $K=5\times10^{-10}$

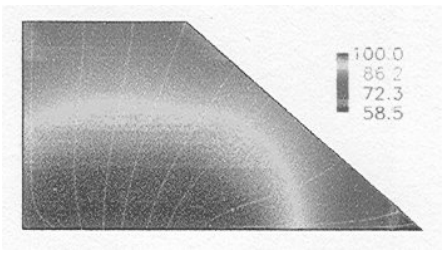

Fig. 12. Streamlines with contours of normalised mass fraction oxygen % *(100×W_0/0.22)*, $V_{in}=1.0\times10^{-4}$, $q_l=5q_{L,0}$, $K=5\times10^{-10}$

This estimate does not represent an extraction value obtainable in practice,

since we have not accounted for variation in *FPY* as discussed earlier. Overall the predicted characteristic extraction time $t*$ is 1119 days (Table 4).

Figure 14 shows that for a higher inlet velocity of $V_{in} = 1.0\times10^{-3}$, a completely different copper extraction profile is obtained, with most of the extraction occurring in the middle of the bed. This suggests the possibility of controlling copper extraction through different regions of the bed, by using certain combinations of liquid and air flow rates. This higher air velocity pushes the characteristic copper extraction time down to 676 days (Table 5), since more oxygen is present in the heap (Figure 12) and the temperature distribution is closer to the optimal value of *311K* (Figure 13). An even higher sparging velocity of $V_{in} = 1\times10^{-2}$ does not provide any better copper extraction (Table 5), because the temperature becomes higher than optimal over a large region.

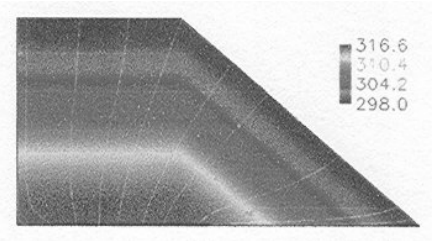

Fig. 13. Streamlines with contours of T, $V_{in}=1.0\times10^{-4}$, $q_l=5q_{L,0}$, $K=5\times10^{-10}$

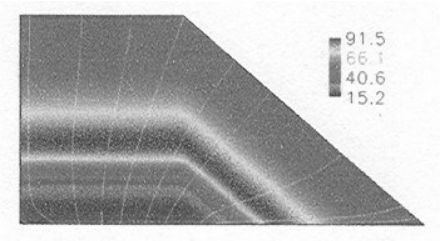

Fig. 14. Streamlines with contours of copper extracted $100\times\alpha$ (1 year), $V_{in}=1.0\times10^{-4}$, $q_l=5q_{L,0}$, $K=5\times10^{-10}$

Table 5. $t*$ versus V_{in} for K for $q_L = 5q_{L,0}$

V_{in}	1×10^{-2}	1×10^{-3}	1×10^{-4}
$t*$ *(days)*	694	676	1119

For the permeability $K = 5\times10^{-10}$, the characteristic copper extraction time ratio (Table 6) depends in the inlet velocity, but the dependence is less for $K = 5\times10^{-9}$. This comparison shows that if the heap permeability can be increased to $K = 5\times10^{-9}$, a lower sparging rate can be used to obtain similar copper extraction. In fact, a characteristic copper extraction time without sparging and $K = 5\times10^{-9}$ has been found to be 2,212 days, indicating that for the size of heap studied here, there is essentially no benefit to be gained from sparging with such high permeabilities. This analysis shows the benefits of creating high permeability, to reduce costs of sparging.

Table 6. $t*$ for $q_L = 1q_{L,0}$ and associated t* ratio of $V_{in}=1.0\times10^{-5}$ to $V_{in}=1.0\times10^{-4}$

K	$t*$ *(days)*		$t*$ *ratio*
	$V_{in}=1.0\times10^{-4}$	$V_{in}=1.0\times10^{-5}$	
5×10^{-9}	2217	2212	1.002
5×10^{-10}	2274	3155	0.7208

3. Conclusions

The model simulation presented in this work has shown that forced aeration has a critical effect on the heap leaching process, in addition to the effect of the liquid flow rate. This is the first time this effect has been simulated in a numerical model. Copper extraction has been shown to increase greatly with the use of forced aeration, in comparison to relying on natural convection.

References

1. R. Bartlett, *Solution Mining: Leaching and fluid recovery of materials,* 2nd edition, The Netherlands: Gordon and Breach Science Publishers, 1998.
2. R. Ivănuş, *Solubilizarea bacteriană*, Craiova, Editura Universitaria, 2005.
3. N. Lu, Y. Zhang, Onset of thermally induced air convection in mine wastes, *Int. J. Heat Mass Transfer, 40* (11), 1997, 2621-2636.
4. R. Bartlett, K.A. Prisbrey, Convection and diffusion limitation aeration during biooxidation of shallow ore heaps, *Int. J. Miner. Process.,* 47, 1996, 75-91.
5. J.M. Casas, J. Martinez, L. Moreno, T. Vargos, Bioleaching model of a coppersulphide ore bed in heap and dump configurations, *Met. Mat. Trans., 29B,* 1998*,* 899-909.
6. ***, ANSYS CFX 5.0 Solver On-line documentation, AEA Technology, Harwell Laboratory, Oxfordshire, UK, 2004

Received March 15, 2007

University of Craiova, Faculty of Mechanics, Dept. of Technology and Materials
STĂNESCU MARIUS, University of Craiova, Dept. of Applied Mathematics

MODELAREA ŞI SIMULAREA BIOSOLUBILIZĂRII ÎN VRAC A DEŞEURILOR DE CUPRU

Rezumat: Modelul matematic elaborat pentru biosolubilizarea în vrac a cuprului din de]eurile de catalizator uzat, cu aerare forţată, este cercetat pentru a identifica şi înţelege rolul bacteriilor în astfel de aplicaţii industriale. O analiză a parametrilor evidenţiază factorii importanţi pentru biosolubilizarea cuprului: ratele de curgere a lichidului şi aerului, permeabilitatea. S-a stabilit deasemeni şi capacitatea de a controla care părţi ale stratului au primit cea mai mare extracţie ca funcţie a ratelor de curgere a lichidului şi aerului. Aerarea forţată a mărit concentraţia de oxigen în vrac, spre deosebire de convecţia naturală. Prin urmare, extracţia cuprului s-a îmbunătăţit în mod semnificativ.

BULETINUL INSTITUTULUI POLITEHNIC DIN IAŞI
Tomul LIII (LVII), Fasc. 2, 2007
Secția
ŞTIINȚA ŞI INGINERIA MATERIALELOR

THEORETICAL CONTRIBUTIONS ABOUT THE TRANSITORY WORKING CONDITIONS BEHAVIOUR OF THE ELECTRIC RESISTANCE FURNACE

ELENA CHIRILĂ

Abstract: *The paper presents a mathematical model of oscillations of slag-melting interface which take place between slag and melting in electric arc furnace. This model permits to reduce the energetic consumption.*

Keywords*: mathematical model, electric resistance furnace, slag-melting interface*

1. General considerations

There are differences between geometrical interface and physical interface. The geometrical interface is the separation surface between two mediums having different nature. It can be a plane, a spherical calotte, a surface limited by a Möbius curve, etc. The physical interface is a volume but not a surface. Because the two different mediums are not distinct limited, the physical interface is structured in two geometrical interfaces. This is the case of the slag-melting interface in electric arc furnace, two. When the electrodes alternative potential is missing, this interface (influenced by a uniform gradient) is a plane composed in two parallel geometrical planes. The distances between these planes are molecular (10^{-9}-10^{-8}m). In this are there is not slag of melting (fusion) but a mixture between them. For this reason the interface is a complex one having slag characteristics but melting, too. Applying a special kind of excitation in interface, a special kind of thermal waves appears in interface. A modification of the excitation goes to a modification of the thermal wave.
When the electric arc take place in the electric arc furnace function, it induces perturbations in slag-melting interface. So, different kind of waves begin to propagate to the walls of furnace where they are reflected or absorbed. If the reflexion is a total one, a stationary thermal waves system appears in the furnace. This system presents high temperatures areas and low temperatures areas in the same time. So, this means that the thermal gradient of the interface is not a uniform one now, so the interface is not a plane anymore. When the oscillation surface of the interface is increased (by applying of a supplementary potential on the electrodes), the process of the absorption of the oxygen is higher, the quantity of slag is lower and so are the electric consumptions, too.

Knowing that the reaction of the slag-melting interface is different when the excitations are different, we must chose that kind of excitation which produce a maximum oscillation of the interface. This is unknown by now and so are the mathematical model of phenomenons in interface and of the characteristics of the

wave, too. So, it is imperious necessary to find a mathematical model of that interface wave which produces a maximum surface for the interface.

This model must characterize the excitation of the electrodes which produced that kind of wave, too.

2. Paper contents

When we begin to study for a mathematical model of the phenomenons which take place in slag-melting interface of the electric arc furnace, we based on the machineries of the gaseous oxygen in melting, the electrochemical character of the interaction between the slag and the melting, the activity and the solubility of the oxygen in pure liquid iron, etc.), on the superficial tension and on the electrocapillarity phenomenons.

For our researches we have used the function of an electric arc furnace having three vertical electrodes in the bottom of furnace. Knowing that the instantaneous electric potential of the three electrodes was in a 120° phase difference, we presumed that the undulations of the surface of the interface for each electrode don't become zero during the interferences but they will propagate to the walls of the furnace. So, in the separation surface between slag and melting, a complex oscillator phenomenon takes place (fig. 1).

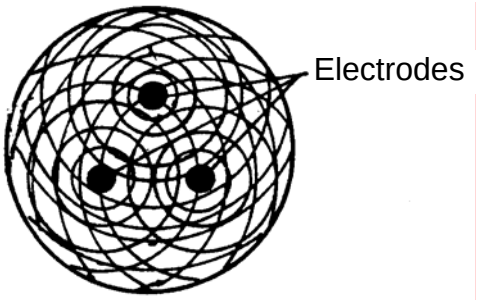

Figure 1. The assuming and the propagation of the undulations in the surface of the slag-melting interface, for the electric arc furnace

So, we noticed that, when the steel is produced in electric arc furnace, the furnace of the slag-melting interface is three times bigger then the surface when the furnace is inactive.

The undulation phenomenons are continuously in the separation surface, so the surface between slag and melting are changeable all the time. This phenomenon goes to the acceleration of the metallurgical processes in melting (desulphuration, dezoxidation, dephosphoration, etc.).

Using the Lippman equation:

$$\frac{d\sigma_{m-z}}{d\varphi} = -\varepsilon , \tag{1}$$

with: φ - the electric potential, [V]; ε - the density of the charges on the melting surface, [C/m^2]; $\sigma_{m\text{-}z}$ – the superficial tension, [J/m^2], and using an integration constant with zero value:

$$\sigma = -\varepsilon\varphi , \tag{2}$$

Using the law of the potential energy conserving for the superficial surface:

$$\frac{dE}{dt}=\frac{d(\varepsilon\varphi)}{dt}=\frac{d\sigma}{dt}, \tag{3}$$

with: E – the electrostatic potential energy.

Using the adimensional co-ordinates for (3):

$$\frac{\partial u}{\partial\tau}+c(u)\frac{\partial u}{\partial\xi}-\mu\frac{\partial^2 u}{\partial\xi^2}-\alpha\frac{\partial^3 u}{\partial\xi^3}=0, \tag{4}$$

with: u – the adimensional superficial tension; τ - the adimensional time; ξ - the adimensional co-ordinate; μ - the dissipation adimensioanal coefficient; α- the dispersion adimensional coefficient.

The first phase in interface engendering is dominated by nonlinear and dissipative effects, so (4) becomes:

$$\frac{\partial u}{\partial\tau}+c(u)\frac{\partial u}{\partial\xi}-\mu\frac{\partial^2 u}{\partial\xi^2}=0, \tag{5}$$

If c is a constant (the linear case), the equation (5) has the following solution:

$$u=u_0 e^{-\mu k^2\tau}e^{ik(\xi-c\tau)}, \tag{6}$$

This solution describes low damp down waves for the interphasic field which has the dispersion equation:

$$\omega=ck-i\mu k^2, \tag{7}$$

with: k – the vector of the adimensional wave; i=-$\sqrt{-1}$ - it indicates the absorption in interface.

If c(u) ≡ u (a nonlinear approximation) the equation (5) becomes:

$$\partial_\tau u+u\partial_\xi u-\mu\partial_{\xi\xi}u=0, \tag{8}$$

The solution of this equation for the initial conditions is:

$$u=-2\mu\partial_\xi \ln\varphi(\xi,\tau), \tag{9}$$

We continue our researches developing an initial perturbation. This perturbation disappears when $\xi\to\pm\infty$. So, the equation (8) has a solution with an asymptomatic aspect (when $\xi\to\infty$):

$$u(\xi,\tau)\approx-2\mu\partial_\xi \ln F\left(\frac{\xi}{\sqrt{2\mu\tau}}\right), \tag{10}$$

knowing that:

$$F(x)=\frac{1}{\sqrt{\pi}}\left[e^{-\frac{M}{4\mu}}\int_{-\infty}^{x}e^{-\eta^2}d\eta+e^{\frac{M}{4\mu}}\int_{x}^{\infty}e^{-\eta^2}d\eta\right], \tag{11}$$

$$M=\int_{-\infty}^{+\infty}u(\xi,\tau)d\xi=\int_{-\infty}^{+\infty}u_0(\xi)d\xi, \tag{12}$$

η - the adimensional integration parameter.

The obtained results prove that $u(\xi,\tau)$ has an asymptotic profile when τ has big values (fig. 2).

If $\mu\to 0$, the function "*u*" describes an triangle profile having the shock wave in front or behind of the profile (if "M" sign is "+" or "-").

The value of the shock wave discontinuity $\sqrt{2 \cdot M / \tau}$ is in a proportional relation with $\tau^{-1/2}$ but the surface is unchanged.

So, the shock is:

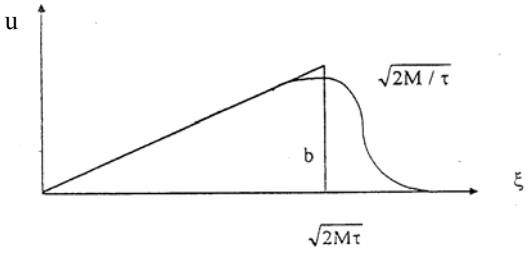

Figure 2. $u = f(\xi)$ variation when τ has big values

$$u(\theta) = w - A \tanh\left(\frac{A\theta}{2\mu}\right), \tag{13}$$

with: θ - the adimensional integration parameter; w – the adimensional speed of the wave; $A = \left(a + w^2\right)^{1/2}$ - the amplitude of the wave; a – the integration constant.

If $2\mu/A = \delta$ is the thickness of the passing area, it can be notice that the bigger "A" is, the lower "δ" is (fig. 3).

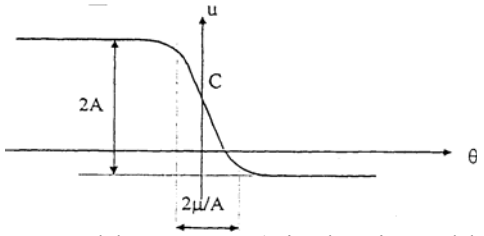

Figure 3. The graphic representation for the (13) solution

The final phase (the transition of the interface to a stable structure) is dominated by nonlinear and dissipative effects. So, equation (4) becomes:

$$\frac{\partial u}{\partial \tau} + c(u)\frac{\partial u}{\partial \xi} - \alpha \frac{\partial^3 u}{\partial \xi^3} = 0, \tag{14}$$

If "c" is a constant and $\frac{\partial u}{\partial \tau} = 0$ (the linear and stationary case) and using the substitution:

$$\frac{c}{\alpha} = \frac{1}{\lambda^2}, \ \frac{\partial u}{\partial \xi} = G, \tag{15}$$

equation (14) becomes:

$$\frac{d^2 G}{d\xi^2} - \frac{1}{\lambda^2} G = 0, \tag{16}$$

It can be observed that the gradient of the tension field is expelled out from the interface. We called this effect – "the interphasic Meissner effect" – making a similitude with the phenomenons which take place in the supraconductors. Similarly, "λ" represents the penetrating thickness. So, the consequences are:

- this effect is similarly with subcooling phenomenons; this are the solidification conditions;
- the slag-melting interface is like a generalized supraconductor;
- the solution of the equation (10) is:

$$G = G_0 e^{-\frac{\xi}{\lambda}}, \tag{17}$$

with: G_0 – the gradient of the tension field on the surface of the interface; it shows that a particle is acted by a specific force:

$$\frac{d^2\xi}{d\tau^2} = -A_0 e^{-\frac{\xi}{\lambda}},\ A_0 = \frac{3}{2}\frac{K_B K_0 T_0 G_0}{m\omega_0^2}, \tag{18}$$

with: K_B – the Boltzman constant, j/K; K_0 – the adimensional speed of the wave; T_0 – the absolute temperature, T_0= 273K; m – the mass of a particle of the interface, kg.

The equation (18) when $\xi \to 1$, after two integration operations, using the necessary substitutions and after the inversion of the first species elliptical integral has the solution:

$$\xi = e_2 - 2Acn^2\left[\gamma(\tau - \tau_0) : k\right], \tag{19}$$

with: $e_1<e_2<e_3$; e_1, e_2, e_3 the solutions of the polynomial equation:

$$P(\xi) = \xi^3 - 3\xi^2 + 6\xi + 6C = (\xi - e_1)(\xi - e_2)(\xi - e_3),\ C = const., \tag{20}$$

and cn – the normal cosinus elliptical function having a k Jacobi modulus:

$$\xi = e_1 + (e_2 - e_1)y^2,\ A = \frac{e_2 - e_1}{2},\ K^2 = \frac{e_2 - e_1}{e_3 - e_1},\ \gamma^2 = \frac{A_0(e_3 - e_1)}{12\lambda}, \tag{21}$$

So, the oscillations of the slag-melting interface are cnoidals.

When c(u)≡u (the nonlinear case) equation (4) becomes:

$$\frac{\partial u}{\partial \tau} + u\frac{\partial u}{\partial \xi} - \alpha\frac{\partial^3 u}{\partial \xi^3} = 0, \tag{22}$$

Using the same method as in (18) equation case, the solution is:

$$u(z) = e_2 - Acn^2(z,s), \tag{23}$$

with:

$$A = e_2 - e_1,\ s^2 = \frac{e_2 - e_1}{e_3 - e_1},\ z = \left(\frac{A}{12\alpha}\right)^{1/2}\frac{\theta}{s},\ \theta = \xi - \omega\tau, \tag{24}$$

So, this means that the oscillations of the slag-melting interface are cnoidal (fig. 4).

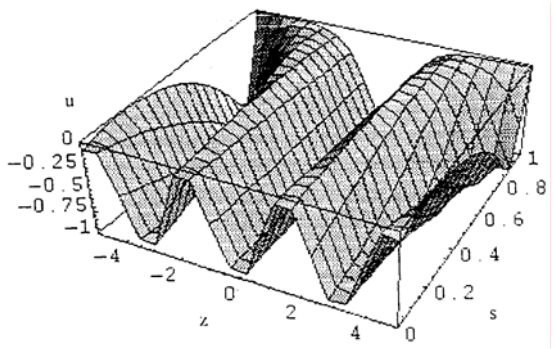

Figure 4. The way of oscillation for the slag-melting interface.

So, we noticed the following degenerations:

a) if the dispersion phenomenons take place before the nonlinears one (S→0), then solution (23) means a packet of "dark waves":

$$u(\theta) = \bar{u} - \frac{A}{2}\left[\cos k\theta + \frac{1}{8}s^2\cos 2k\theta + \theta(s^4)\right], \tag{25}$$

So, the dispersion equation is:

$$\omega(k) = \bar{u}k + \alpha k^3, \tag{26}$$

with k=2π/λ, having a graphical variation (fig. 5):

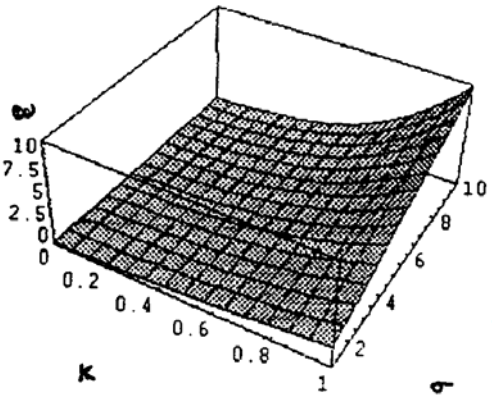

Figure 5. The graphic for the dispersion relation (26).

b) if the nonlinear effects appear before the dispersive one (S→1), then the solution (23) means a packet of "dark solitons", A – constant.

c) if the linear and dispersive effects are comparable (S=1), then the solution (23) means a "dark soliton":

$$u(\theta) = \bar{u} - A\sec h^2\left[\left(\frac{A}{12\alpha}\right)^{1/2}\theta\right], \tag{27}$$

This oscillation is represented in fig. 6 for A, amplitude, and $D = \left(\frac{12\alpha}{A}\right)^{1/2}$ - thickness.

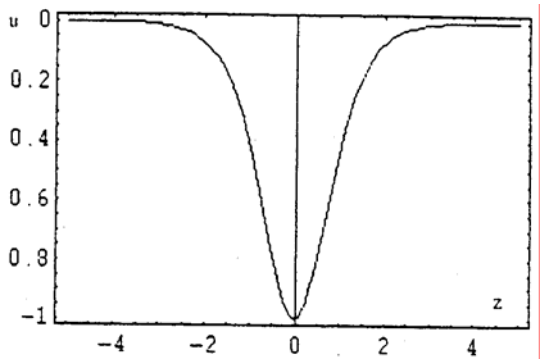

Figure 6. The graphic for the "dark soliton".

As a conclusion:

- the solidification is similarity with dark oscillations of the slag-melting interface;
- the degenerations - packet of dark waves, packet of dark solitons, dark soliton – are sleps of the action of the process.

If the nonlinear and dispersive effects are prevalent, equation (4) becomes:

$$\frac{\partial u}{\partial \tau} + c(u)\frac{\partial u}{\partial \xi} + \alpha\frac{\partial^3 u}{\partial \xi^3} = 0, \tag{28}$$

If c – constant, $\frac{\partial u}{\partial \tau}=0$ (the linear and stationary case) and using the substitution $-\frac{c}{\alpha}=\frac{1}{\lambda^2}$ and $\frac{\partial u}{\partial \xi}=G$, equation (28) becomes:

$$\frac{d^2G}{d\xi^2} + \frac{1}{\lambda^2}G = 0, \tag{29}$$

So, this means that in slag-melting interface, the Meissner effect in tensions is absent (λ - the fundamental thermic length). This absence is similarly with a supraheating phenomenon; this are the conditions for the melting of the interface.

If c(u)≡u (the nonlinear case), equation (28) becomes:

$$\frac{\partial u}{\partial \tau} + u\frac{\partial u}{\partial \xi} + \alpha\frac{\partial^3 u}{\partial \xi^3} = 0, \tag{30}$$

Its solution is:

$$u(z) = e_2 + A\,cn^2(z,s), \tag{31}$$

This solution represents the way of "bright" cnoidal oscillation (fig. 7).

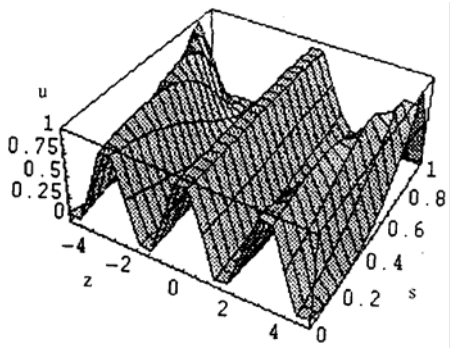

Figure 7. The bright cnoidal oscillation.

We noticed the following degenerations:

a) if $S \to 0$, the solution (31) represents a packet of bright waves:

$$u(\theta) = \bar{u} + \frac{A}{2}\left[\cos k\theta + \frac{1}{8}s^2\cos 2k\theta + \theta(s^4)\right], \tag{32}$$

having a relation of dispersion:

$$\omega(k) = \bar{u}k - \alpha k^3, \tag{33}$$

with a graphic variation (fig. 8):

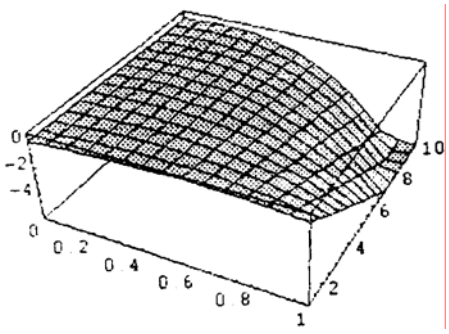

Figure 8. The graphic for the dispersion relation.

b) if $S \to 1$, equation (30) means a "packet of bright solitons", having $A = e_1 - e_2$ = constant;

c) if S = 1, solution (31) means a "bright soliton":

$$u(\theta) = \bar{u} + A\,\mathrm{sech}^2\left[\left(\frac{A}{12\alpha}\right)^{1/2}\theta\right], \tag{34}$$

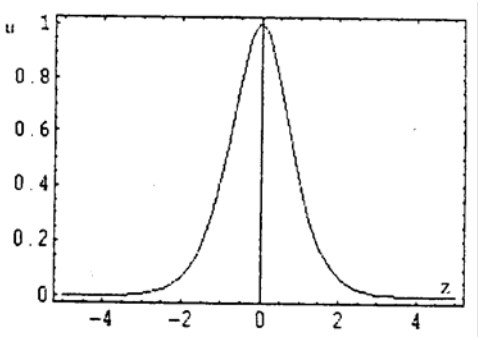

Figure 9. The bright soliton.

So:

- the melting is similarly with bright oscillations of the slag-melting interface;
- the anterior degenerations are steps of the melting.

3. Conclusions

Our researches and theoretical contributions prove that the oscillations of the slag-melting interface are very complex. So, the reduction of the oxidation produces of the interface is the same time with the increase of the quantity of slag are similarly with dark cnoidal oscillation, dark linear waves, the packet of dark waves and the train of dark solitons are steps of this process. The increase of the oxygen absorption in interface (the increase of the melting) means bright cnoidal oscillation, bright linear waves, the packet of bright waves and the train of bright solitons are steps of the process.

In conclusion, wishing a short time for the melting process (the reduction of the energetic consumptions) it is necessary to stimulate the components of bright cnoidal solitons and trains of bright solitons.

Only these components cause a maximum surface of the slag-melting interface and minimum energetic consumption.

Received March 20, 2007 *The "Gh.Asachi" Technical University Iaşi*

REFERENCES

1. Elena Chirilă – *Contribuţii privind îmbunătăţirea constructiv-funcţională a cuptoarelor electrice cu arc în vederea reducerii consumurilor energetice,* Teză de doctorat, Iaşi, 2001.

CONTRIBUŢII TEORETICE PRIVIND MODELAREA MATEMATICĂ A FENOMENELOR FIZICE LA INTERFAŢA ZGURĂ-BAIE METALICĂ LA TOPIREA ÎN CUPTORUL ELECTRIC CU ARC

Lucrarea prezintă un model matematic al oscilaţiilor la nivelul interfeţei zgură-baie metalică la topirea în cuptorul electric cu arc pentru reducerea consumurilor energetice.

BULETINUL INSTITUTULUI POLITEHNIC DIN IAŞI
Tomul LIII (LVII) , Fasc. 2, 2007
Secția
ŞTIINȚA ŞI INGINERIA MATERIALELOR

NEW MODEL BASED ON ANN FOR DESIGN AND CHARACTERISATION OF FERROMAGNETIC ALLOYS

BY

SERGIU MOHORIANU and MIHAI LOZOVAN

Abstract: We introduce here as tools, the Artificial Neural Network (ANN). A neural network is an adaptable system that can learn relationships through repeated presentation of data and is capable of generalizing to new, previously unseen data. Neural networks are used for both regression and classification. Since ANN's learn from the data, the data must be valid for the results to be meaningful. A successful neural network simulation requires the specification of many parameters. The performance is highly dependent on the choice of these parameters. By adapting its weights, the neural network works towards an optimal solution based on a measurement of its performance. In our model we intend to use for the input data the following: the chemical composition, the thermal treatments and possibly some structure data. As output data Hall Effect, magnetoresistance effect of this alloys.

Keywords: Nanocrystalline and amorphous alloys, ANN, MLP, PE

1. Introduction

In our everyday life we are assault with situations so complex that we do not have analytical ways to solve them. Once we have a crisp definition, the next step is to select the input variables and the desired responses. So, we introduce here the Artificial Neural Network (ANN) [1]. We always use common sense to select the variables that are relevant for the problem. One should seek variables and conditions that appear relevant to the problem being analyzed. One should also seek data that cover a wide spectrum of cases. If the ANN does not see an equilibrated set of cases, its output will be 'biased' [2]. The designing and performing of the new nanocrystalline and amorphous alloys with targeted properties is an actual problem for the ferromagnetic materials. Our model is intented to enhance some new properties of these materials.

a) The current stage

We propose to obtain for the beginning a new model for the characterization of some materials in the class: FeCrSiBMo and CoFeSiB alloys. In the present days are studied with other methods some interesting properties like: Hall Effect, magnetoresistance effect and the influence of the composition and of the thermal treatments on the properties of this alloys [3-6].

b) What are ANN, and how it works?

A neural network is an adaptable system that can learn relationships through repeated presentation of data and is capable of generalizing to new, previously unseen data. Some networks are supervised, in that a human determines what the network should learn from the data. In this case, you give the network a set of inputs and

corresponding desired outputs, and the network tries to learn the input-output relationship by adapting its free parameters [7-10].

Neural networks are used for both regression and classification. In regression, the outputs represent some desired, continuously valued transformation of the input patterns. In classification, the objective is to assign the input patterns to one of several categories or classes, usually represented by outputs restricted to lie in the range from 0 to 1, so that they represent the probability of class membership. For regression, it can be shown that a single hidden layer Multilayer Perceptron (MLP) can learn any desired continuous input-output mapping if there are sufficient numbers of axons in the hidden layer(s). For classification, Multilayer Perceptrons can learn the Bayesian posterior probability of correct classification. This means that the neural network takes into account the relative frequency of occurrence of the classes, giving more weight to frequently occurring classes. Neural networks have been trained to perform complex functions in various fields of application including pattern recognition, identification, classification, speech, and vision and control systems. The field of neural networks has a history of some five decades but has found solid application only in the past fifteen years, and the field is still developing rapidly. Today neural networks can be trained to solve problems that are difficult for conventional computers or human beings [11,12].

c) What we expect from our new Model

Since Ann's learn from the data, the data must be valid for the results to be meaningful. Sometimes the desired response is unknown. Our model implements and use the basic building blocks of neural computation, such as multi-layer perceptrons, Jordan and Elman networks, radial basis function, also called probabilistic networks, principal component analysis networks, self-organizing feature map networks, and time-lagged recurrent networks. In our work we usually use NeuroSolutions, a Neuro Dimension Inc. product. A successful neural network simulation requires the specification of many parameters. The performance is highly dependent on the choice of these parameters. A productive way to assess the adequacy of the chosen parameters is to observe the signals that flow inside the network. One can observe signals flowing in the network, weights changing, errors being propagated, and most importantly the cost, all while the network is working. This means that we do not need to wait until the end of training to find out that the learning rate was set too high. All probes within NeuroSolutions belong to one of two categories -- static probes and temporal probes. The big difference is that the first kind access instantaneous data, while the second access the data over a window in time. By generating the code for the network, we can compile this code on a high-end workstation and train the network there [13,14]. The resulting weights can then be saved to a file and imported back into your breadboard within NeuroSolutions.

2. A short New Model presentation

At the core of neural computation are the concepts of distributed, adaptive and nonlinear computing. Neural networks perform computation in a very different way than conventional computers, where a single central processing unit sequentially dictates every piece of the action. Neural networks are built from a large number of very simple processing elements that individually deal with pieces of a big problem. A

processing element (PE) simply multiplies an input by a set of weights, and nonlinearly transforms the result into an output value. The principles of computation at the PE level are deceptively simple. The power of neural computation comes from the massive interconnection among the PEs, which share the load of the overall processing task, and from the adaptive nature of the parameters – weights, that interconnect the PEs. Normally, a neural network will have several layers of PEs. The most basic feed forward architecture is the multilayer perceptron (MLP). By adapting its weights, the neural network works towards an optimal solution based on a measurement of its performance. For supervised learning, the performance is explicitly measured in terms of a desired signal and an error criterion.

Data Structures. How the format of input data structures affects the simulation of networks. For concurrent vectors, the order is not important, and if we had a number of networks running in parallel, we could present one input vector to each of the networks. For sequential vectors, the order in which the vectors appear is important.

In our model we intend to use for the input data the following: the chemical composition, the thermal treatments and possibly some structure data. As output data Hall Effect, magnetoresistance effect of this alloys.

Training Styles. We can use two different styles of training. In incremental training the weights and biases of the network are updated each time an input is presented to the network. In batch training the weights and biases are only updated after all of the inputs are presented.

Learning Rules. We define a learning rule as a procedure for modifying the weights and biases of a network. This procedure may also be referred to as a training algorithm. The learning rule is applied to train the network to perform some particular task. As the inputs are applied to the network, the network outputs are compared to the targets. The learning rule is then used to adjust the weights and biases of the network in order to move the network outputs closer to the targets. The perceptron learning rule falls in this supervised learning category. In unsupervised learning, the weights and biases are modified in response to network inputs only. Most of these algorithms perform clustering operations. They categorize the input patterns into a finite number of classes. This is especially useful in such applications as vector quantization.

3. What are the Model connections

The simulation of a neural network requires the orchestration of many pieces [15]. When we run the simulation we should start by checking if the data is being correctly fed into the network by placing probes on the input sources. Another important aspect is to check if the learning rates are sufficiently low to avoid divergence. Divergence will usually occur during the beginning of training. We might place a matrix viewer on the first synapse to see if the weights are changing. Observing a steady decrease of the cost is the best overall indicator that everything is progressing well. We now have to decide if the learning was successful or not. Most of the time, the first check is to see if the cost is within what we think is appropriate for the application. All the information gathered by the network from the input data is contained in the weights. So we should save the weights, along with the topology. The weights are saved by default.

4. Conclusions

Neural networks have been applied very successfully in the identification and control of dynamic systems, for locate common characteristics in large amounts of data. The universal approximation capabilities of the multilayer perceptron make it a useful choice for modelling nonlinear systems and for implementing general-purpose controllers and magnetic characteristics extractor from wide data amount.

This model will permit the finding of new materials with enhanced Hall and magnetoresistive properties.

Received March 31, 2007 *National Institute of R & D for Technical Physics Iaşi*

REFERENCES

1. Caudill, M., and C. Butler, Understanding Neural Networks: Computer Explorations, Vols. 1 and 2, Cambridge, MA: the MIT Press, 1992
2. Charalambous, C.,"Conjugate gradient algorithm for efficient training of artificial neural networks," IEEE Proceedings, vol. 139, no. 3, pp. 301-310, 1992
3. G. Bordin, G. Buttino, A. Cecchetti and M. Poppi, J. Magn. Magn. Mater., vol. 172, (1997), 291-300,
4. H. Chiriac, M. Lozovan, Maria Neagu and Cornelia Hison, J. Magn. Magn. Mater. 215-216, (2000), 378,
5. H. K. Lachowicz, R. Zuberek, M. Kuzminski, A. Slawska-Waniewska, J. Magn. Magn. Mater., vol. 196-197, (1999), 151-153,
6. J. Gonzalez, N. Murillo, J. M. Blanco, P. Quintana, E. Amano and R. Velenzuela, IEEE Trans. Magn., vol. 30, (1994), 4812-4814,
7. Chen, S., C. F. N. Cowan, and P. M. Grant, "Orthogonal least squares learning algorithm for radial basis function networks," IEEE Transactions on Neural Networks, vol. 2, no. 2, pp. 302-309, 1991
8. DARPA Neural Network Study, Lexington, MA: M.I.T. Lincoln Laboratory, 1988
9. Hagan, M. T., H. B. Demuth, and M. H. Beale, Neural Network Design, Boston, MA: PWS Publishing, 1996
10. Hebb, D. O., The Organization of Behavior, New York: Wiley, 1949
11. Kohonen, T., Self-Organization and Associative Memory, 2nd Edition, Berlin: Springer-Verlag, 1987
12. Kohonen, T., Self-Organizing Maps, Second Edition, Berlin: Springer-Verlag, 1997
13. Lippman, R. P., "An introduction to computing with neural nets," IEEE ASSP Magazine, pp. 4-22, 1987
14. Nguyen, D., and B. Widrow, "Improving the learning speed of 2-layer neural networks by choosing initial values of the adaptive weights," Proceedings of the International Joint Conference on Neural Networks, vol 3, pp. 21-26, 1990
15. Wasserman, P. D., Advanced Methods in Neural Computing, New York: Van Nostrand Reinhold, 1993

NOU MODEL CU RETELE NEURONALE PENTRU PROIECTAREA SI CARACTERIZAREA UNOR ALIAJE FEROMAGNETICE

Rezumat: In lucrare propunem un nou model cu metode ale inteligentei artificiale in vederea rezolvarii problemei obtinerii de noi aliaje feromagnetice nanocristaline si amorfe cu proprietati Hall si magnetorezistive superioare. O simulare de suces cu retele neuronale artificiale solicita specificarea mai multor parametrii. Obinerea performantei este dependenta de buna alegere a acestor paramtri. Prin adaptarea ponderilor retelei neuronale, aceasta permite obtinerea solutiei optime, bazata fiind pe masuratori ale performaței sale.

BULETINUL INSTITUTULUI POLITEHNIC DIN IAŞI
Tomul LIII (LVII), Fasc. 2, 2007
Secția
ŞTIINȚA ŞI INGINERIA MATERIALELOR

(Mn,X)S COMPOUNDS - MAJOR SITES FOR GRAPHITE NUCLEATION IN GREY CAST IRON

MIHAI CHISAMERA, IULIAN RIPOSAN, STELIAN STAN, DOUG WHITE

Abstract: *Despite the cubic system, the ability of sulphides to nucleate graphite can be enhanced by inoculating elements which transform them in complex compounds with a better lattice matching to graphite, a low coagulation capacity, good stability and adequate interfacial energy. (Mn,X)S compounds, usually less than 5.0μm in size, with an average 0.4-2.0μm well defined core (nucleus), were found to be important sites for graphite nucleation in grey irons. A three-stage model for the nucleation of graphite in grey irons is proposed: 1) very small micro-inclusions based on strong deoxidizing elements (Mn, Si, Al, Ti, Zr) are formed in the melt; 2) nucleation of complex (Mn,X)S compounds at these previously formed micro-inclusions; 3) graphite nucleates on the sides of the (Mn,X)S compounds with lower crystallographic misfit with graphite. Aluminium appears to have a key role in this process, as aluminium contributes to the formation of oxides in the first stage and favors the presence of Sr and Ca in the sulphides, in the second stage. 0.005-0.010% Al range was found to be beneficial for lower undercooling solidification, type-A graphite formation and carbides avoidance.*

Keywords*: Grey Iron; Graphite Nucleants; (Mn,X)S; Aluminium Key Role; Graphite Nucleation Model.*

Introduction

High performance grey irons, especially those used in the automotive and mechanical engineering field, may be obtained primarily by structure control: graphite morphology and distribution, metal matrix composition and control of possible defects. Hypoeutectic and near eutectic range (carbon equivalent CE=3.35-4.30%) characterizes high performance grey irons. Graphite morphology control is known to be a key factor in high strength grey iron production. The morphology of the eutectic graphite is primarily determined by the temperature at which the austenite-lamellar graphite cell is nucleated. The graphite morphology is controlled by the difference between the stable grey eutectic temperature, which is mainly a function of the silicon content, and the effective eutectic temperature (degree of eutectic undercooling).

At the highest temperature close to the stable eutectic temperature, and consequently a lower degree of eutectic undercooling, the eutectic solidifies with randomly oriented, uniformly distributed graphite flakes (ASTM type A). Moderate undercooling prior to eutectic nucleation results in the initial growth of graphite particles as a cell wherein the graphite flakes are more closely spaced. The resultant cell with fine flake graphite at the centre, surrounded by coarser flake graphite appears as a rosette (ASTM type B). Considerable undercooling results in a generally fine spacing of graphite flakes within austenite flake graphite; randomly oriented graphite within interdendritic regions devoid of graphite (ASTM type D). Type E-graphite is an extreme form of type D and is promoted by very low carbon equivalent or rapid solidification of thin section. Type

C graphite is formed as a pro-eutectic graphite phase (primary graphite). Types A, B, D and E are typically for hypoeutectic and eutectic irons, while type C is typically for hyper-eutectic grey cast irons.

Potential Graphite Nucleation Sites in Grey Irons

The initiation of graphite nucleation during the solidification of all commercial cast irons generally requires a nucleation site with specific peculiarities in each case. Several conditions for heterogeneous graphite nucleation on the existing/creating particles in the iron melt were evaluated, as follows: a) particles must be solid: b) good crystallographic compatibility; c) lowest lattice disregistry (no more than 3%); d) interfacial energy (substrate/graphite) barrier overcoming; e) fine dispersion in the melt (1-3 μm); f) lower capacity to coagulate in the iron melt; g) higher stability at higher temperature; h) sufficient content of molten iron element(s) and inoculant active element(s), respectively; i) easy of access inoculating elements [1-5] .

Residual graphite should be an ideal nucleant for the formation of graphite during solidification, but some microinclusions, formed in the molten iron, are also possible sites for the heterogeneous nucleation of graphite, depending on the melting practice and later inoculation treatment (Table 1).

Metallic charge materials usually used in the production of cast iron are very different as measured by the amount and size of graphite they contain. In foundry pig iron more than 15% (surface) graphite at more than 500 μm size particles is typical of Kish-graphite characterizing this important charge component at 0.01-0.07%S. Cast iron scrap, as returns and purchased cast iron will represent a large range of materials, with 0-20% graphite and graphite particles sized 1…500μm and sulphur content between 0.002-0.2%. Steel scrap without any graphite, also has lower sulphur content (less than 0.05%S). Amorphous or graphitic carbon materials play an important role in raising and controlling carbon in the final cast irons. Graphite added to molten iron for increasing carbon levels disperses without dissolving for a while, so residual graphite particles when they become critically sized may act as nuclei for graphite crystallization in cast irons. Sulphur suppresses dissolution of graphite and prolongs the period of graphite particles in suspension. All metallic and non-metallic charge materials in the iron melt contribute a large quantity of different types (chemistry) of non-metallic inclusions that also vary in size and association.

After melting, the resulted metallic liquid may be considered to be a colloidal solution which includes: Fe-C-Si (X_i) base solution (1-2%C); Residual (remnant) graphite particles (0.1…10μm); Non-metallic inclusions. The colloidal solution aspect is especially descriptive of the remnant graphite particles that stay suspended for a long time. The dissolution rate of the residual graphite particles is very slow immediately after melting due to the high stability of the C-C atoms bond and the presence of the minor active elements (S, O) on the surface of the residual graphite particles (dissolution is impaired). Si in the melt will decrease the C - dissolution capacity. Other elements, such as Mg, will accelerate dissolution of remnant graphite.

Ongoing heating of the iron melt in the furnace will bring about important changes on the iron characteristics: elements diffusion and solution homogenization; remnant graphite dissolution; non-metallic inclusions flotation, at least for the larger particles.

Table 1. Standard Enthalpy (ΔH^0_{298}) and Free Energy (ΔG^0_{1723}) of different compounds

Oxides	$-\Delta H^0_{298}$	KJ/mole oxide	La > Ce > Al > Zr > Ti > Si >Ca >Mg >Sr >Ba >Mn 1842 1806 1677 1090 930 880 635 604 592 558 386
		KJ/ mole O_2	Ca > La > Mg ≥ Ce > Sr > Al ≥ Ba > Zr > Ti >Si >Mn 1270 1228 1208 1204 1185 1118 1116 1090 930 880 772
	$-\Delta G^0_{1723}$	KJ/mole oxide	Ce > Al > Zr >Ti > Si >Ca > Sr > Ba = Mg >Mn 1246 1124 774 621 578 456 416 383 383 256
		KJ/ mole O_2	Ca > Ce = Sr > Zr >Ba = Mg > Al >Ti > Si > Mn 911 831 831 774 767 766 749 621 578 512
Sulphides	$-\Delta H^0_{298}$	KJ/mole sulphide	Ce > La > Al > Zr > Ca > Sr > Ba > Ti > Mg > Mn 1258 1237 723 699 484 464 451 380 349 226
		KJ/ mole S_2	Ce > La > Ca > Sr > Ba > Ti > Zr = Mg >Al > Mn 1064 1053 969 927 902 760 699 698 482 452
	$-\Delta G^0_{1723}$	KJ/mole sulphide	La >Ce > Zr >Ca > Sr > Ba >Mg >Ti > Mn 925 402 392 368 353 331 224 181 149
		KJ/ mole S_2	Ce > Ca > Sr > La > Ba > Mg > Zr > Ti > Mn 804 736 706 694 662 447 392 362 299
Nitrides	$-\Delta H^0_{298}$	KJ/mole nitride	Si > Mg >Ca > Sr > Ba > Zr > Ti >Ce = Al >La >Mn 755 470 438 387 368 364 336 324 320 298 128
		KJ/ mole N_2	Zr > Ti > Ce ~Al > La > Mg > Ca > Sr > Si > Ba >Mn 729 673 649 640 597 470 438 387 377 369 256
	$-\Delta G^0_{1723}$	KJ/mole nitride	Zr > Ti > La > Si > Ce > Al > Ca > Sr = Mg > Ba 204 175 163 156 146 131 72 +5 +5 97
		KJ/ mole N_2	Zr > Ti > La > Ce > Al > Si ~ Ca > Sr = Mg > Ba 408 351 325 292 261 78 72 +5 +5 97
Carbides	$-\Delta H^0_{298}$	KJ/mole carbide	Al > Zr > Ti > Ce >Ba ~ Sr >Mn ~La ~ Si >Ca >Mg 296 198 185 97 89 85 80 80 78 60 25
		KJ/mole C	Zr > Ti > Si > Al >Ce >Ba ~Sr > La >Ca >Mn >Mg 192 185 78 72 49 45 43 40 30 27 8
	$-\Delta G^0_{1723}$	KJ/mole carbide	Zr > Ti > Mn > Ce > La > Al ~ Ca > Ba > Si 181 163 158 132 111 101 100 86 70
		KJ/mole C	Zr > Ti > Si > Ce > La > Mn > Ca > Ba > Al 181 163 70 66 56 53 51 43 34

The iron melt will evolve, due to the heating effect, from a colloidal solution stage (just after melting) to a quasi-homogeneous solution [Fe-C-Si-X_i solution and C-atoms as groups or clusters] up to quasi-ideal solution at the highest superheating level. Remnant graphite particles will gradually disappear, while non-metallic inclusions will change and quantity and size will be drastically reduced. The first transition temperature range (T_I), is usually about 1400-1450^{o}C while the second (T_{II}) is mainly at the 1500-1550^{o}C level. Higher amounts of foundry pig iron in the charge, higher silicon, sulphur and oxygen content in the melt appear to be the most important favorable factors for higher levels of both transition temperatures.

A higher superheating temperature or holding time leads to more complete dissolution of the residual graphite particles, floatation of coarse inclusions and de-activation of microinclusions in terms of their ability to act as "un-controlled" nucleants for graphite, especially in grey irons. These conditions can be exploited to eliminate un-desirable heredity effect from the charge materials. In many cases, the "natural nucleants" of graphite such as coarse remnant graphite or microinclusions could be detrimental for the final casting structure, which could be non-homogeneous,

with occurrence of free carbides. For this reason high performance grey iron production requires two steps of iron melt treatment be completed: a) enough superheating time at temperature (according to the heredity intensity) and b) inoculation, as a mandatory treatment after superheating, to compensate for the increased undercooling behavior of the base iron. Generally, a higher degree of undercooling of the base iron requires a higher inoculation potency to avoid undercooled graphite morphologies and chill tendency, including inverse chill. Appropriate superheating on the one hand and a balance of inoculation on the other appear to be an ideal solution in grey cast iron production.

A number of inclusions have been evaluated as possible formation in molten grey iron. Two types of particles were mainly considered namely sulphides and oxides/silicates. Both of these types of particles may according to the thermodynamics be formed in industrial grey iron melts as simple or complex compounds during melting, holding or handling (see Table 1).

Experimental Procedure

Extensive research laboratory programs were conducted to evaluate the response of different grey cast iron melts to different FeSi based inoculants, especially with Ca and Sr as the active elements. Iron melts, obtained in an acid lined induction furnace, were designed having different contents of carbon (3.0-3.7%), silicon (1.0-2.2%), manganese (0.2-0.7%), sulphur (0.005-0.12%), oxygen (25-100 ppm) and aluminium (0.001-0.05%) at different specific ratios, covering the most representative foundry situations. A very low level of other elements was ensured for all irons.

Experimental grey irons with typical Si concentration (1.2%) were conventionally or excessively inoculated (0.2% and 1.0% inoculant, respectively). In addition, other irons with low Si level (0.4-0.5%) were over-inoculated by the addition of 2.0%wt inoculant in order to facilitate the detection of the inoculating elements (Ca, Sr) in the possible graphite nucleants. High Purity (HP)-FeSi and Sr-FeSi or Ca-FeSi were used for ladle inoculation. The last two materials contain lower (0.01%), normal (0.5-1.0%) and intentionally higher (2%) Al content, at representative inoculating element levels (0.7-1.0% Ca or Sr). Up to 40ppm Ca or 30ppm Sr were ensured in the inoculated irons. Major experiments were the analysis of cooling curves, chill tendency, graphite size and morphology, carbides occurrence, pearlite/ferrite ratio, eutectic cell count and the characterization of microinclusions as possible graphite nucleation sites [4-11].

The main objective of the present paper concerns a thorough analysis of a large number of inclusions that may act as possible nucleation sites for graphite. The analyses includes using state-of-the-art electron microscopy including both SEM and TEM analyses as well as electron probe micro analyses for the detailed characterization of the graphite nucleants (microinclusions).

Results and Discussion

In the inoculated grey irons it was found a good connection between eutectic undercooling degree, chilling sensitivity and structure features, according to inoculant type and sulphur/oxygen levels of the irons. It was evidently that the base iron and HP-

FeSi treated iron have a lower graphite nucleation capacity, especially at higher cooling rate and lower levels of sulphur and oxygen. The negligible contribution in active elements (Ca, Sr) of the HP-FeSi iron melt over treatment cannot be compensated by its high silicon contribution in the melt. In the same conditions, Ca and Sr-FeSi inoculated irons present a good graphite nucleation capacity.

Four relative positions of microinclusions in the structure were recorded: a) no visible contact with graphite (embedded in matrix); b) superficial contact between inclusion and graphite; c) partially and d) totally encapsulated by graphite.

The most of the microinclusions, assumed to play a role in the nucleation of graphite, present some specific characteristics: 1) size between 1 and 8 μm, but is usually less than 5.0μm in diameter; 2) the size of microinclusions depends mainly on the cooling rate, as lower size at higher cooling rate; 3) these microinclusions have mainly an oval shape in Ca-FeSi treated irons, a regular polygonal shape in Sr-FeSi treated iron and mostly an irregular polygonal shape in HP-FeSi treated iron; 4) the majority of these microinclusions posses a well-defined core (nucleus), measuring 0.1-2.7μm in diameter but most often 0.4-2.0μm; 5) it appears that the type of inoculant affects the size of the cores of the graphite nucleants: there is a decrease in core size from un-inoculated (2.0μm) to HP-FeSi and Sr-FeSi treated irons and to Ca-FeSi treated irons, at last having the lowest core size (< 0.5μm); 6) a visible dependence of the nucleus shape on the inoculant type was not observed.

The chemical composition in different regions of the inclusions, such as the nucleus (n), compound body/shell (Cm), compound/graphite interface (i_{c-g}) and compound matrix interface (i_{c-m}) was found by the use of EDXA (Energy Dispersive X-ray Analysis). Complex (Mn,X)S compounds were identified as major nucleation sites for graphite in all tested grey irons, un-inoculated and inoculated irons, independent of iron melt chemistry and inoculant type and/or addition rate (Fig. 1). The core and body parts of these compounds can be separated in terms of chemical composition.

Strong deoxidizers such as Al and Si, were found to be important parts of the first formed, very small microinclusions in the iron melt, which was believed to be nucleation sites for precipitation of (Mn,X)S particles. At very low levels of aluminium in the iron melt (<0.002wt.% Al), the Al and Si contents in these early formed small microinclusions are similar (up to 2.0wt.%). At more than 0.005wt.% residual aluminium in the iron, the Al content in the cores of (Mn,X)S compounds is more than ten times higher that of Si. It can be concluded that Si-Al-O containing microinclusions are the bases of the cores (nuclei) of (Mn,X)S compounds for low residual al content (< 0.004wt.% Al), while Al-O containing microinclusions are typically nuclei for (Mn,X)S compounds for more than 0.004wt.% Al residual in the iron melt. In specific conditions the first formed microinclusions were found to include also zirconium or/and titanium, known as strong deoxidizers in the ferrous melt, too.

The Mn/S ratio of the inclusions is mainly affected by their position (compound placed on matrix or on graphite) and inoculant type. In addition the Mn/S ratio changes with position within the inclusion, such as compound mass (Cm) and compound/graphite interface (i_{c-g}) (Fig. 2). The highest values of the Mn/S ratio was found in the compound body of particles embedded in matrix (no nucleants for graphite) while the lowest Mn/S ratio was found on the compound/graphite interface. The particles which are associated with graphite have a lower Mn/S ratio than the

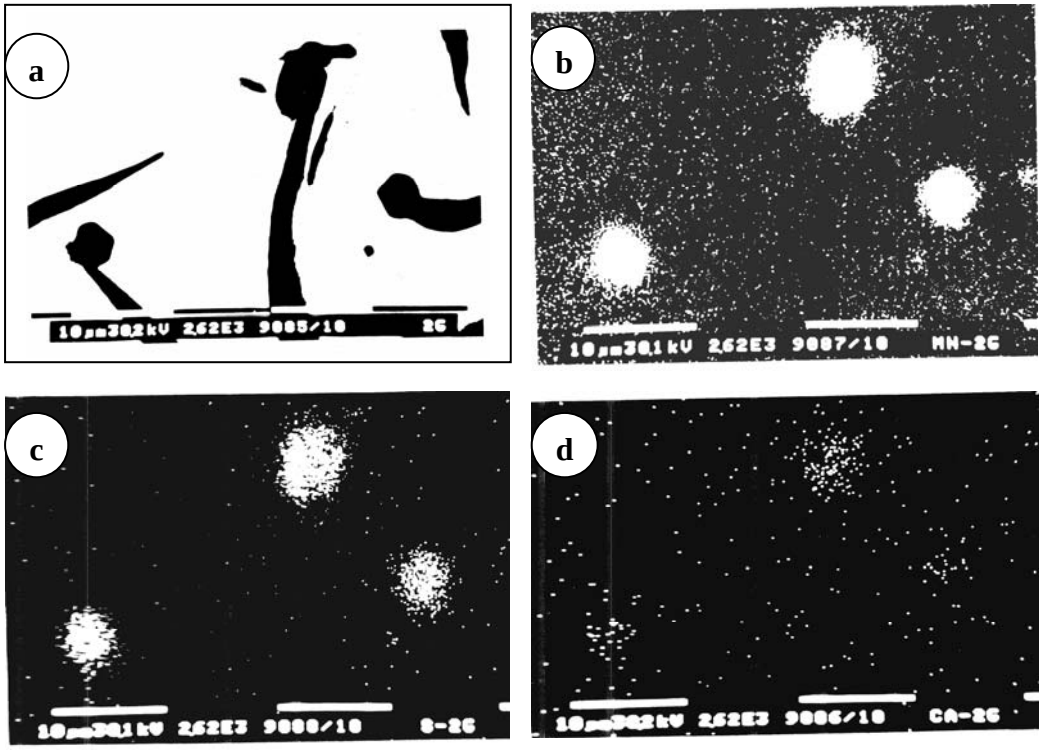

Fig.1 Typical example of graphite nucleants in Ca-FeSi inoculated iron:
a) compo image; b) MnKα; c) SKα; d) CaKα

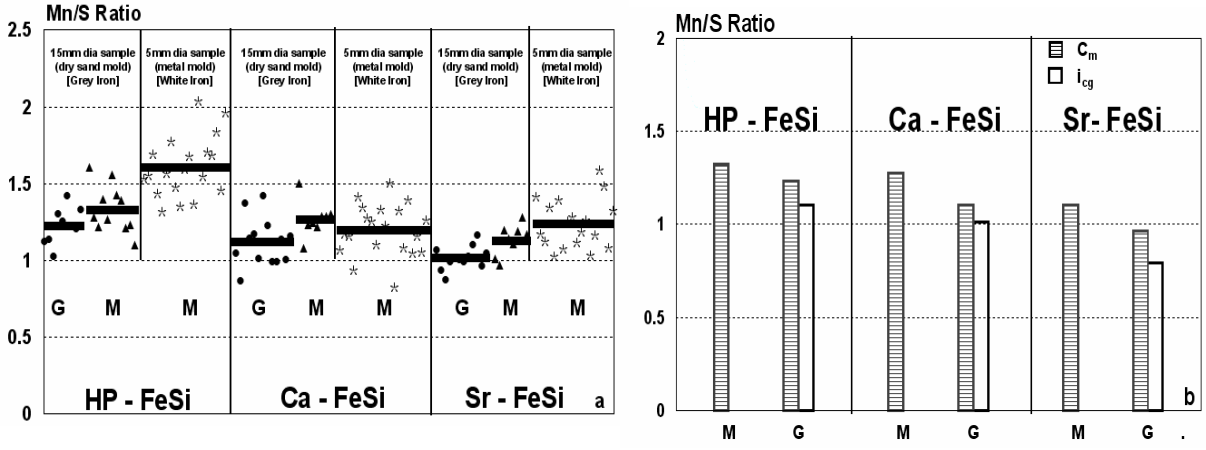

Fig.2 Mn/S ratio in (Mn,X)S Compounds associated with graphite (G) or embedded in the matrix (M)
[C_m – compound mass; i_{cg} – interface compound/graphite, as average level]

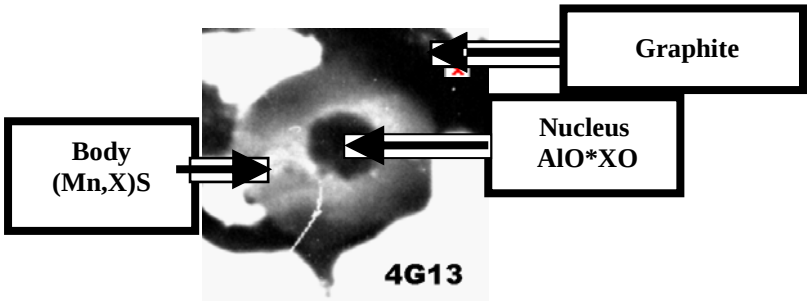

Fig.3 Three stage model for the nucleation of graphite in grey iron

embedded particles in all examined specimens. Ca-FeSi inoculated irons had a lower Mn/S ratio than the HP-FeSi treated iron, the lowest value, however, was found for the Sr-FeSi inoculated iron, at the same ranking as inoculating efficiency increasing:
HP-FeSi < Ca-FeSi < Sr-FeSi.

As inoculating elements, Ca is present in most (Mn,X)S compounds, including Sr-FeSi and HP-FeSi treated irons, while Sr has a detectable presence only in the Sr-FeSi inoculated irons. Increasing the residual Al level in the iron melt appears to favor higher concentrations of Sr or Ca in the (Mn,X)S compounds.

It is generally considered that Al has virtually no inoculating effects as such and it is not included in the inoculating elements group. However, this research pointed out a key role that Al plays in the graphite nucleation process. It forms Al_2O_3-based sites, which act as nucleants for (Mn,X)S compounds. In addition Al appears to favor the presence of Ca or Sr in the shell of these compounds, which lowers the crystallographic misfit between the compound and the graphite. Higher Al levels in the iron result in higher concentrations of Al in the nuclei of these compounds, and at a lesser extent also in their shells (bodies). Increasing the residual Al level in iron melt is useful to initiate the graphite nucleation process. A 0.005…0.01wt.%Al range appears to be beneficial for graphite formation in grey irons (type A-graphite formation, no carbides, higher eutectic cell count etc.), without the detrimental effect on pinhole occurrence (under specific conditions, up to 0.015wt%Al is necessary).

Conclusions

*Residual graphite should be an ideal nucleant for the formation of graphite during solidification, but sulphide and/or oxide/silicate microinclusions, formed in the commercial molten iron, are more probable sites for the heterogeneous nucleation, depending on the melting practice and later inoculation treatment.

*(Mn,X)S compounds (X=Fe, Al, O, Si, Ca, Sr, Ti etc.) with different morphologies (regular/irregular polygonal or ovoid shape) are major sites for graphite nucleation in grey irons. These compounds are usually less than 5.0μm in size and have a well defined core (nucleus), mainly measuring no more than 2.0μm, at different chemistry.

*In un-inoculated iron the (Mn,X)S compound is simple and the crystallographic misfit graphite/compound is relative large. In inoculated iron the (Mn,X)S compound is more complex and the crystallographic misfit is lower, so the nucleation capacity is higher, especially as inoculating elements (Ca, Sr etc.) contribute.

*A three-stage model for the nucleation of graphite in grey iron is proposed: 1) very small micro-inclusions based on strong deoxidizing elements such as Mn, Si, Al, Ti, Zr are formed in the melt; 2) nucleation of complex (Mn,X)S compounds at these micro-inclusions; 3) graphite nucleates on the sides of the (Mn,X)S compounds with lower crystallographic misfit with graphite (Fig. 3).

*It was found that Al has the ability to contribute to the formation of Al_2O_3-based sites suitable for the nucleation of (Mn,X)S compounds and to favor the presence of Sr or Ca in the shell of these compounds, to obtain better graphite nucleation capacity. A 0.005-0.010%Al range appears to be usually beneficial for low eutectic undercooling solidification.

References

1. C.R. Loper and R.B. Gundlach, "Inoculation what is it and how does Inoculation Work?", AFS International Inoculation Conference, Chicago, 1998, Paper No.1.
2. T. Skaland, O. Grong and T. Grong, "A Model for the Graphite Formation in Ductile Cast Iron", Metallurgical Transactions, 1993, **24A**, 2321.
3. D.M. Stefanescu, "Inoculation of Thin-Wall Castings", AFS International Inoculation Conference, Chicago, 1998, paper No.16.
4. M. Chisamera, I. Riposan and M. Barstow, "The Importance of Sulphur to Control Graphite Nucleation in Cast Iron", AFS Intern. Inoculation Conference, Chicago, 1998, Paper no.3.
5. M. Chisamera, I. Riposan, S. Stan and T. Skaland, "Undercooling - Chill Size - Structure Relationship in the Ca/Sr Inoculated Grey Irons under Sulphur/Oxygen Influence", 64th World Foundry Congress, Paris, 2000, paper RO 62.
6. I. Riposan, M. Chisamera, S. Stan, T. Skaland and M.I. Onsoien, "Analyses of Possible Nucleation Sites in Ca/Sr Over-inoculated Gray Irons", AFS Transactions, 2001, **109**, 1151-1162.
7. M. Chisamera, I. Riposan, S. Stan and T. Skaland, "Cooling Curve Analysis of the Ca/Sr Over-Inoculated Gray Iron, at Lower Initial Silicon Content", International Conference on the Science of Casting and Solidification, Brasov, 2001, pp. 330-335.
8. M. Chisamera, I. Riposan, S. Stan and T. Skaland, "Effects of Residual Aluminium on Solidification Characteristics of Un-inoculated and Ca/Sr Inoculated Gray Irons", AFS Transactions 2004, **112**, pp. 867-877.
9. I. Riposan, M. Chisamera S. Stan and T. Skaland, "Graphite Nucleants (Microinclusions) Characterization in Ca/Sr Inoculated Irons", International Journal of Cast Metals Research, **16**, no.1-3, 2003, pp. 105-111.
10. I. Riposan, M. Chisamera, S. Stan, C. Gadarauteanu and T. Skaland, "The Key Role of Residual Aluminium in Chill Tendency and Structure Characteristics of Un-inoculated and Ca/Sr Inoculated Gray Irons", Proceedings of 66th World Foundry Congress, 2004, Istanbul, 775-789.
11. I. Riposan, M. Chisamera, S. Stan and T. Skaland, "A New Approach to Graphite Nucleation Mechanism in Gray Irons", AFS Cast Iron Inoculation Conf., 2005, Schaumburg, USA, pp.31-41.

MIHAI CHISAMERA*, IULIAN RIPOSAN*, STELIAN STAN*, DOUG WHITE**

*POLITEHNICA University of Bucharest, Romania; **ELKEM Metals Inc, Pittsburg, USA

COMPUSII (Mn,X)S – PRINCIPALII GERMENI DE GRAFITIZARE IN FONTELE CENUSII

Desi au un sistem de cristalizare cubic, capacitatea sulfurilor de a germina grafitul poate fi imbunatatita de catre elementele modificatoare, care le transforma in compusi complecsi, cu o compatibilitate structurala mai mare cu grafitul, o capacitate mai mica de coagulare, o buna stabilitate si o energie interfaciala adecvata. A fost gasit faptul ca sulfurile de tipul (Mn,X)S, de regula sub 5 um, cu un nucleu (miez) bine definit de ordinul a 0.4-2.0 um, constitue principalii germeni de grafitizare in fontele cenusii. A fost propus un model de grafitizare, in trei etape: 1) microincluziuni foarte mici pe baza de oxizi se formeaza in topitura, sub actiunea unor dezoxidanti puternici (Mn, Si, Al, Ti, Zr); 2) sulfurile complexe (Mn,X)S germineaza pe acesti primi compusi; 3) lamelele de grafit germineaza pe una sau mai multe fete ale sulfurilor, cele mai apropiate de conditiile formarii grafitului. Aluminiul pare sa joace un rol important in acest proces, contribuind la formarea primilor compusi oxidici si la cresterea cantitatii de elemente modificatoare (Ca, Sr) dizolvate in sulfuri. Domeniul 0.005-0.01% Al rezidual apare ca benefic solidificarii cu un grad de subracire eutectica mai mic, favorizand formarea grafitului tip A si limitand formarea carburilor.

BULETINUL INSTITUTULUI POLITEHNIC DIN IAŞI
Tomul LIII (LVII), Fasc. 2, 2007
Secţia
ŞTIINŢA ŞI INGINERIA MATERIALELOR

THE ANALYSIS OF ACCUMULATIVE ROLL-BONDING

LUCHIAN ZAHARIA and ADRIAN MOCANU

Abstract. *In Accumulative Roll-Bonding (ARB) process, the cohesion between the laminated layers is very important. In this paper an analysis of the influence of initial stacking number on the engineering and effective (von Mises) strain is made. The experimental results show an increasing of bonding, with the initial number of stacking strips.*

Keywords*. Accumulative Roll-Bonding (ARB), Severe Plastic Deformation (SPD), engineer strain, effective (von Mises) strain, stacking strips, bonding zone*

1. The description of accumulative roll-bonding (ARB) process

The accumulative roll-bonding (ARB) process was proposed like Severe Plastic Deformation (SPD) technique by Saito et al. [1], [2] to obtain ultra high strains in metallic materials, in order to refine the grain.

Fig.1 schematically represents the principle of ARB process, from which it can be seen that this technique is in fact a succession of conventional rolling applied to some sheets or strips initially stacked (before rolling).

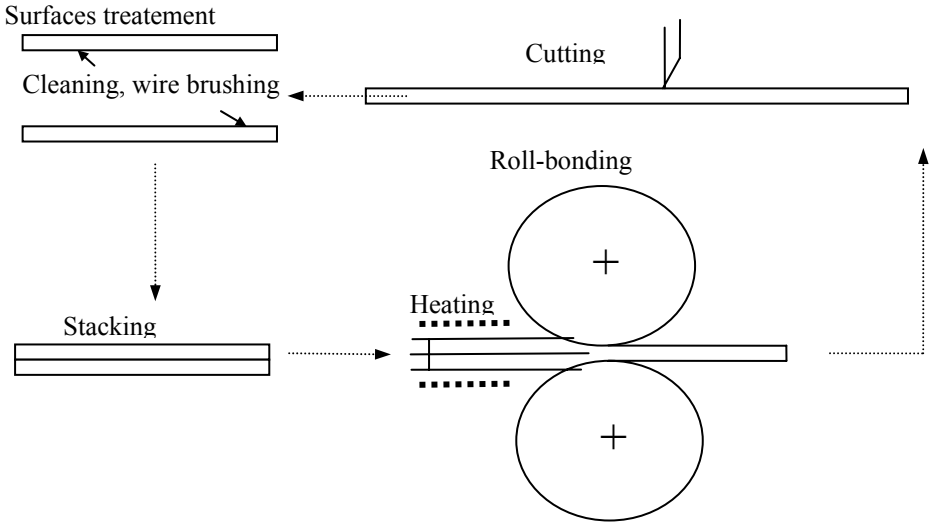

Fig.1: The principle of accumulative roll-bonding (ARB).

Before rolling the two surfaces are treated (oxides cleaning, degreasing) in order to achieve a good bond. After stacking each other they are being laminated with 50% strain. During the rolling process an acceptable bond between the surfaces in contact is obtained, so, a new strip results, having the length almost double (if the width growing

is negligible). The new strip is being cut in two; the interfaces are again prepared, stacked, and roll-bonded.

By repeating this procedure several times, it is possible to obtain extremely high (over 99,95%) cumulative strains; the effect is the grain refinement at nano-metric values and the increasing of mechanical characteristics [3]. It was found that the microstructure is lamellar and the boundary spacing decreases with the increasing of rolling strain [4]. Moreover, the studies have shown significant differences in the evolution of the micro-structural parameters in conventional rolling and ARB respectively [5], [6].

2. The necessary conditions to achieve bonding

To achieve a good bond between the contact surfaces in ARB, it is recommended the heating below the re-crystallization temperature, because recrystallization cancels the accumulated strain. A low temperature can lead to a smaller ductility and pour bonding.

There is a minimum limit in the thickness reduction to achieve sufficient bonding, named *threshold deformation*. The threshold deformation decreases with the temperature so a good bonding can be obtained by using thickness strains > 50%.

3. The evaluation of deformation

SPD by ARB achieve ultra high strain without any geometrical change when the strain is 50%. The process is repetitive, and in principle endless, the strain is unlimited at least from the theoretical point of view.

Let's analyse the evolution of engineering strain as a function of the number of strips initially stacked. Speciality literature presents only the case with two strips. We proposed the analysis of ARB process when the number of strips initially stacked is ≥ 2 and the initial thickness of each strip before rolling is equal with the thickness of the laminated strip, i.e. the thickness of the initial strip is a multiple of the thickness resulting from rolling. It is obvious that in the case of rolling using the multilayer initial stacking, in the condition described above, each layer will be deformed with a strain bigger than 50%. Subsequently, the bond will be achieved easier, at smaller working temperatures and the grain refinement will be achieved by a smaller number of passes.

When one wants to stake more than two strips before rolling, the ARB follows the same steps and stages as described in fig.1. The only difference is the fact that the strip is being cut in more pieces not only in two but 3, 4, 5…as the needed number of layers we want to roll.

a) The analysis of ARB with 2 strips initially stacked

When one stakes two strips for the rolling process and the reduction applyied is 50%/cycle, the thickness g, of a strip (from the multilayer strip formed by adhesive rolling) will be:

- after the *first* pass: $\left(\frac{g}{g_0}\right)_1 = \frac{1}{2}$ (1)

- after the *second* pass: $\left(\frac{g}{g_0}\right)_2 = \frac{\frac{1}{2}}{2} = \frac{1}{4} = \frac{1}{2^2}$ (2)

- after the *third* pass: $\left(\frac{g}{g_0}\right)_3 = \frac{\frac{1}{4}}{2} = \frac{1}{16} = \frac{1}{2^3}$ (3)

.....

- - after the n^{th} pass: $\left(\frac{g}{g_0}\right)_n = \frac{1}{2^n}$ (4)

where g_0 is the initial thickness.

The total strain, after n cycles is:

$$\varepsilon = \frac{g_0 - g}{g_0} = 1 - \frac{1}{2^n} \quad (5)$$

By using von Mises criterion for the plane strain state (because spreading ≈ 0), the equivalent plastic strain for the rolling strip can be computed using the known expression:

$$\varphi_{ef} = \sqrt{\frac{2}{3}}\sqrt{2\left(\ln\frac{g_0}{g}\right)^2} = \frac{2}{\sqrt{3}}\ln\frac{g_0}{g} \quad (6)$$

Replacing g_0/g, one obtains:

$$\varphi_{ef} = \left[\frac{2}{\sqrt{3}}\ln\left(\frac{1}{2}\right)\right]n = 0,8n \quad (7)$$

b) The analysis of ARB with 3 strips initial stacked

In this case $g=g_0/3$, and the schematically representation of rolling looks like in Fig.2.

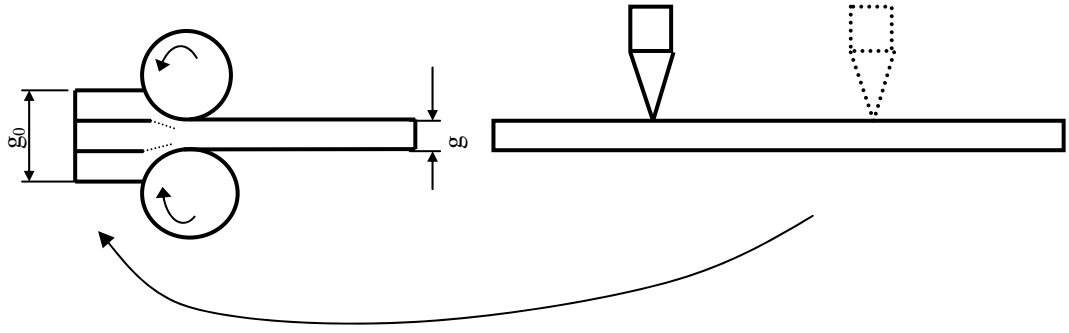

Fig. 2. Schematically representation of ARB when 3 strips are being stacked

The thickness of a layer from the laminated strip is:

- after the *first* pass: $\left(\frac{g}{g_0}\right)_1 = \frac{1}{3}$ (8)

- after the *second* pass: $\left(\frac{g}{g_0}\right)_2 = \frac{\frac{1}{3}}{3} = \frac{1}{9} = \frac{1}{3^2}$ (9)

- after the third pass : $\left(\frac{g}{g_0}\right)_3 = \frac{\frac{1}{9}}{3} = \frac{1}{27} = \frac{1}{3^3}$ (10)

.....

- after the n^{th} pass: $\left(\frac{g}{g_0}\right)_n = \frac{1}{3^n}$ (11)

The strain at the first pass is:

$$\varepsilon = \left(\frac{g_0 - g_1}{g_0}\right) x100 = \left(1 - \frac{g_1}{g_0}\right) x100 = \left(1 - \frac{1}{3}\right) x100 = 66\% \quad (12)$$

The total strain (after *n* passes) will be:

$$\varepsilon_t == \left(1 - \frac{g}{g_0}\right) x100 = \left(1 - \frac{1}{3^n}\right) x100 \quad (13)$$

The equivalent strain (von Mises) will be:

$$\varphi_{ef} = \left[\frac{2}{\sqrt{3}} \ln\left(\frac{1}{3}\right)\right] n = 1,28\, n \quad (14)$$

If the initial thickness is 1 mm and the process is repeated 5 times, the thickness after rolling will be $1/3^5$ = 0,004 mm = 4 μm and the total strain will be $\varepsilon_t = \left(1 - \frac{1}{3^5}\right) x100 = 99,6\%$

In the previous case (when only 2 strips were stacked), the thickness of a layer from laminated strip after 5 passes was 30 μm and the value of the strain was 97%.

c***) The analysis of ARB with 4 strips initial stacked***

If $g=g_0/4$, the diagrammatic representation of ARB shows like in Fig. 3.

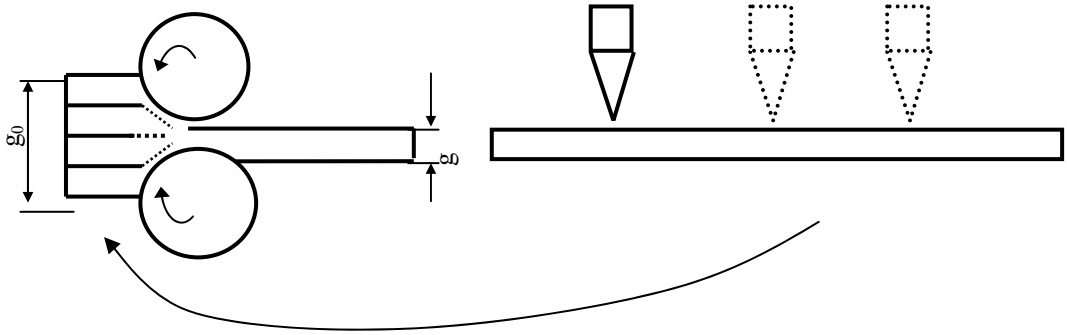

Fig. 3: Schematically representation of ARB with 4 strips initially stacked

Following a similar reasoning like this described above, it results that in this case the ratio g/g_0 after n passes will be:

$$\left(\frac{g}{g_0}\right)_n = \frac{1}{4^n}. \quad (15)$$

The strain at the first pass is:

$$\varepsilon = \left(\frac{g_0 - g_1}{g_0}\right) x100 = \left(1 - \frac{g_1}{g_0}\right) x100 = \left(1 - \frac{1}{4}\right) x100 = 75\% \quad (16)$$

The total strain (after *n* passes) will be:

$$\varepsilon_t == \left(1 - \frac{g}{g_0}\right) x100 = \left(1 - \frac{1}{4^n}\right) x100 \quad (17)$$

The equivalent strain (von Mises) will be:

$$\varphi_{ef} = \left[\frac{2}{\sqrt{3}} \ln\left(\frac{1}{4}\right)\right] n = 1,6\,n \quad (18)$$

The number of strips/sheets initial stacked from theoretical point of view can be endless. However, in practical situations this number is limited in function of the real rolling conditions (the diameter of rolls, excessive spreading).

A synthesis of data regarding the thickness of layers from laminated strips and the total strains for the 3 cases previously described, in function of passes number is shown in Tab.1

Tab.1. The thickness of layers after ARB[mm]/Total strain[%]

Pass nr.		0	1	2	3	4	5	6	7	8	9	10	11
No. of strips initially stacked	2	1	0,5 50%	0,25 75%	0,12 88%	0,06 94%	0,03 97%	0,015 98,5%	0,008 99,2%	0,004 99,6%	0,002 99,8%	0,001 99,9%	0,0005 99,95 %
	3	1	0,33 66%	0,11 89%	0,037 96%	0,012 98,8%	0,004 99,6%	0,0013 99,9%	0,0004 99,95%	0,00013 99,98%	-	-	-
	4	1	0,25 75%	0,06 94%	0,015 98,5%	0,004 99,6%	0,001 99,9%	0,00025 99,97%	-	-	-	-	-

To have a visual image for the variation of thickness of layers from a laminated strip by ARB with the pass number, in Fig. 4 are presented the curves drawn with the data from Tab.1, for 2, 3 and 4 strips initially stacked.

From this analysis it results clearly that by increasing the number of strips, initially stacked, the total strain increases and the thickness of layers from the laminated strip achieves sub-micronic values after a smaller pass number.

It can be shown that sub-micronic thickness of layers from laminated strips by ARB are obtained after 11 passes when 2 strips are initially stacked, after 7 passes when 3 strips are initially stacked and after 6 passes when the strips number initially stacked is 4.

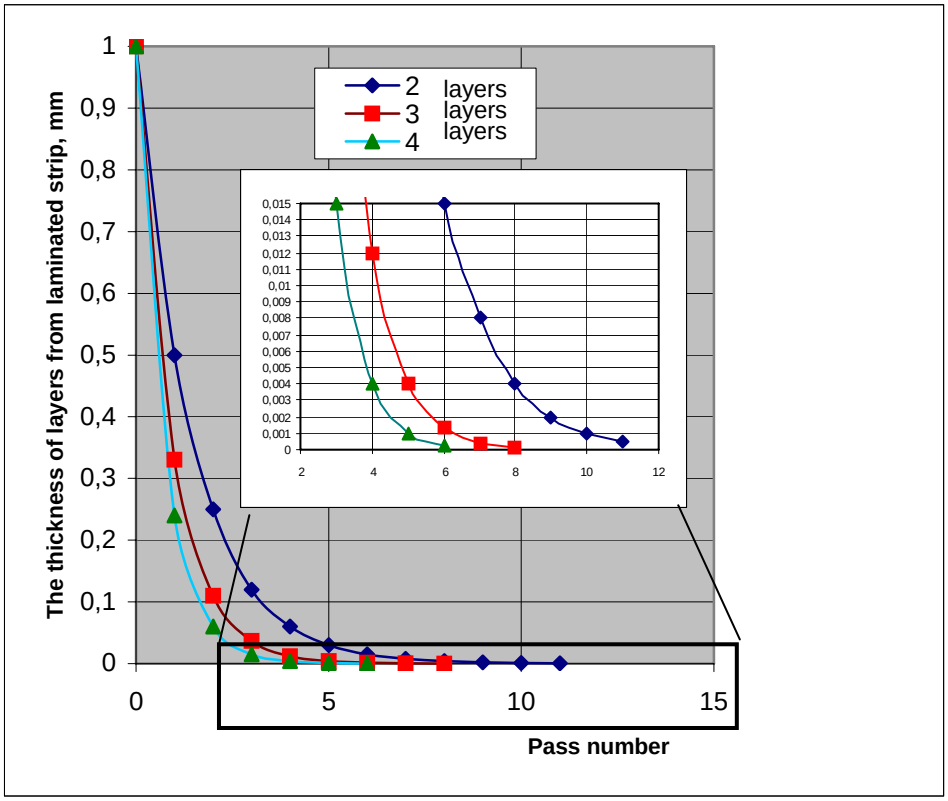

Fig.4: Theoretical decrease of thickness for a strip of 1 mm with the pass number at ARB.

4. Experimental procedure

4.1. The specimens

In experiments there were used specimens from commercial pure aluminium, laminated in strips with 1 mm initial thickness. After cutting, the specimens were recrystallized for 1 hour in an electric box furnace at 250^0C. Before rolling, the contact surfaces have been prepared in order to obtain o rough and degreased surface. To fix the samples in order to maintain the relative position they were assembled by nits in every corner. After assembling the staked strips have been introduced into a electric heating furnace and heated up to 200^0 C for 5 minutes. By ARB process the package of specimens was laminated down to 1 mm thickness.

After rolling the obtained strip was cut perpendicular on de rolling direction and the resulted surface was submitted to macro and microscopic investigations, following the evolution of the interference size zone resulting by ARB process.

4.2. Working equipment

The ARB was made on a duo rolling mill with flat rolls having the diameter 114 mm. Before rolling the rolls were degreased to achieve dry friction. The roll gap was fixed at 1 mm and maintained constant during all the tests.

The investigations concerning the sizes of the adherence zones were made on a Vickers type CV-400 DM hardness-meter at an enhancement power of 600x.

5. Results obtained

The images for the bonding zones for 3 specimens are shown in Fig.6, where:

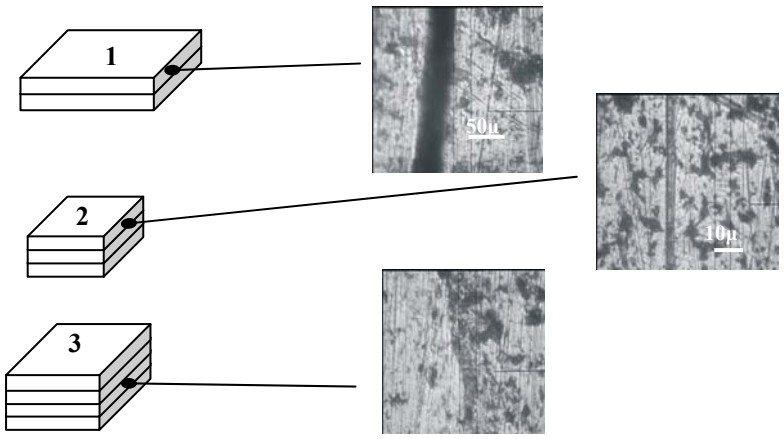

Fig. 6. Images of the adherence zones

sample 1 represents a sample with 2 layers initially staked (before rolling), sample 2 represents a sample with 3 layers initially staked and sample 3 is a sample with 4 layers initially staked.
The results of the measurements made are shown in Tab.2

Tab.2. Average width of interfaces

Sample No.	Average width of interfaces, µm
1	41,87
2	5,06
3	Un-identifiable

6. Discussions

Images from Fig.6 show clearly that the size of the adherence zones depends of the extent of the degree of reduction resulted by rolling, that at its turn is being linked to the number of initially staked layers and/or of the strip thickness of the layer before rolling. Thus:

- at the sample with two layers initially staked, the degree of deformation resulted by rolling was 50%, the adherence is satisfactory;
- at the sample with 3 layers initially staked, the degree of deformation resulted by rolling was 66%, the adherence is good;
- at the sample with 4 layers initially staked, the degree of deformation resulted by rolling was 75%, the adherence is very good; in this case, except the ends, the interface between strips can not be identified.

Even if the influence of the number of layers on the adherence is obvious, nevertheless it must be remarked that when one works with larger deformation degrees (a large number of layers initially staked), the margins cracking trend grows for the laminated material. One can see also that when rolling more than two strips initially staked, not all the strips deform with the same reduction degree; the strips in contact with the cylinders suffer larger deformations than the others, placed in the inner zones of the package.

7. Conclusions

The accumulative roll bonding is a SPD technique, through what one can achieve very high degrees of reduction as an effect of accumulation of the deformation by more passes. From the studies made, it results that the adherence is given both by a good preparation of specimens before rolling and by the degree of deformation achieved at a pass. We ascertained that by enhancing the number of initially staked strips it results a better adherence, because of the larger degree of deformation obtained. When there are being achieved degrees of deformation over 75%, the separation zone between the initially staked strips completely disappears, resulting a welding of strips.

References

1. Y. Saito, N. Tsuji, H. Utsunomiya, T. Sakai – Production method of ultrafine grained high strength metallic sheets by accumulative roll-bonding. Japan Patent nr. 2961263
2. Y. Saito, H. Utsunomiya, N. Tsuji, T. Sakai – Novel ultra-high straining process for bulk Materials-development of the accumulative roll-bonding (ARB) process. Acta materialia vol.47, no.2, 579-583,1999
3. Y. Saito, N. Tsuji, , H. Utsunomiya, T. Sakai, R.G. Hong – Ultra-fine grained bulk produced by accumulative roll-bonding (ARB) process. Scripta materialia vol.39, no.9, 1221-1227,1998
4. X.Huang, N. Tsuji, N. Hansen, Y Minamino - Microstructural evolution during accumulative roll-bonding of commercial purity aluminum. Materials Science and Engineering A 340 (2003), 265-271
5. Kusnierz J, Bogucka J. - Evolution of texture during ARB processing of Al 99.8%, MATERIALS SCIENCE FORUM, 495-497: 797-802 Part 1&2 2005,
6. Chowdhury, Sandip Ghosh; Srivastava, V.C.; Ravikumar, B.; Soren, S. - Evolution of texture during accumulative roll bonding (ARB) and its comparison with normal cold rolled aluminium–manganese alloy, Scripta Materialia Vol: 54, Issue: 9, May, 2006, pp. 1691-1696,

*Technical University "Gh. Asachi" Iaşi

ANALIZA LAMINĂRII ADEZIVE CUMULATIVE
(Rezumat)

In procesul de laminare adezivă cumulativă, coeziunea dintre straturile laminate este importantă atunci când se urmăreşte obţinerea unei table sau benzi compacte. Există mai mulţi parametri tehnologici care influenţează aderenţa (gradul de deformare, temperatura, presiunea de contact etc.). Lucrarea prezintă o analiză teoretică a influenţei numărului de straturi suprapuse iniţial asupra gradului de reducere pe grosime.

S-a ajuns la concluzia că un număr mai mare de benzi suprapuse iniţial are ca efect reducerea numărului de treceri necesar pentru a rafina granulaţia la valori nanometrice.

Rezultatele experimentale arată o creştere a adeziunii dintre straturi odată cu creşterea numărului de benzi suprapuse înainte de laminare. Aprecierea aderenţei dintre straturi s-a făcut prin măsurarea grosimii interfeţelor cu ajutorul unui microdurimetru digital. Pentru grade mari de reducere pe grosime (peste 66%) interfaţa dintre straturi este atât de mică încât se produce practic o sudare a benzilor multistrat.

BULETINUL INSTITUTULUI POLITEHNIC DIN IAŞI
Tomul LIII (LVII), Fasc. 2, 2007
Secția
ŞTIINȚA ŞI INGINERIA MATERIALELOR

THE GRAIN FRAGMENTATION BY SEVERE PLASTIC DEFORMATION

LUCHIAN ZAHARIA*, RADU COMANECI*, ADRIAN DINESCU**

Abstract. *The paper presents the main aspects of micro structural fragmentation by plastic deformation, starting from structural defects (dislocations, grain boundaries). It is analysed the formation of sub grains in the plastic deformation process, including severe plastic deformation. Aluminium specimens were processed by Equal Channel Angular Pressing (ECAP) die in 6 passes and analysed using a Scanning Electron Microscope (SEM) and Atomic Force Microscope (AFM) to put into evidence the grains refinement. The imagines obtained show clearly that the severe plastic deformation produces micro structural fragmentation and grains refinement down to nano metric sizes.*

Keywords: *grain boundaries, sub grains, micro structural fragmentation, grain refinement, severe plastic deformation, ECAP, SEM, AFM, nano crystalline structure.*

1. The role of structural defects in grain fragmentation

It is well known that between the *ideal* structure and the *real* structure of metallic materials there is a considerable difference.

The ideal structure is a theoretical one, characterised by the perfect arrangement of atoms in positions well-determined in space. An ideal metallic material is an edifice obtained by the stacking of cell-blocs, without any mistake. Such structures are not usual in practice, unless for the case of very small zones.

The real structures differ from the ideal ones by the fact they show a series of defects representing faults from the ideal spatial arrangement of atoms. The behaviour of metallic materials during plastic deformation is especially influenced mostly by structural defects including: *punctiform defects (*vacancies, connate atoms etc.), linear *defects (*dislocations), surface *defects (grain boundaries*, sub-grain boundaries (sub-boundaries)). From theses defects, the most important for plastic deformation generally, and for the grain fragmentation particularly, are the dislocations, the grain and sub grain boundaries.

2. The grain fragmentation during the plastic deformation

By plastic deformation the grains are fragmentised in *mosaic type blocks* with the size ranging between $10^{-1}...10^{-5}$ mm [1]. When the mosaic blocks have the dimensions ranging between $10^{-1}...10^{-3}$ mm, the grains are called sub-grains and at their turn can be divided in other smaller sub grains, by the mechanisms that will be analysed later. Together with the grain fragmentation it is produced a rotation, so the miss-orientation angle *(θ)* between the sub-grains increases.

An example of atomic arrangement between neighbouring grains is shown in Fig.1 [2].

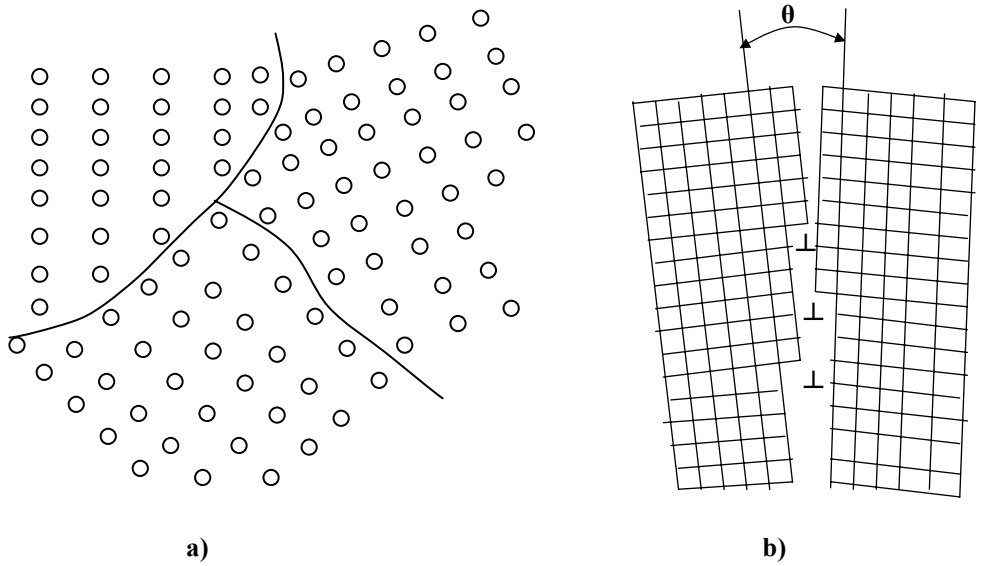

Fig. 1. Surface defects
a) Grain boundaries (high angle); b) Sub grains boundaries (low-angle)

Fig. 1.b presents a boundary between two sub grains. This boundary is achieved by a chain of dislocations occurred ones under others (wall of dislocations) in the deforming process, that produce a separation with a small angle **θ** in the interior of a grain.

In the plastic deformation process, reorientations and rearrangements of grains frequently occur both at the grain level and inside the grains. The reorientation of the crystalline lattice even inside the grain (with the mechanism described above in Fig 1.b) leads to the obtaining of a crystalline mosaic structure, made by sub grains and/or block-cells coming from the same grain, tilt each other with small angles and separated by walls of dislocations.

The aspect of a such a structure is suggested in Fig.2.

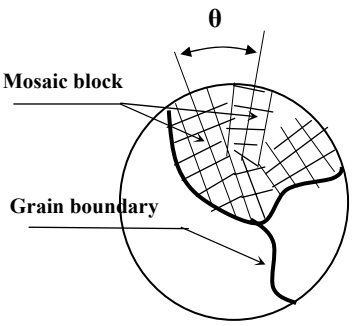

Fig. 2. Mosaic structure

After the values of the tilting angle between the two neighbouring grains/sub-grains, the surfaces defects are:

- high angle grain boundaries (HAGB)**;** these are grain boundaries;
- low angle grain boundaries (LAGB); these are generally boundaries between sub-grains.

LAGB is composed from an array of dislocations, and their properties and structure dependent on their miss-orientation. In contrast, the properties of HAGB are generally independent of the miss-orientation.

The transition between HAGB and LAGB is appreciated to be as $10\text{-}15^0$ but this is a value arbitrary chosen.

It was demonstrated that HAGB blocks the movement of dislocations in the interior of metallic materials.

The LAGB plays an important role in the grain fragmentation by Severe Plastic Deformation (SPD) and this is why, a more detailed analysis of them must by carried

out. The analysis of LAGB formation shows that they occur in two different modes, presented in Fig.3.

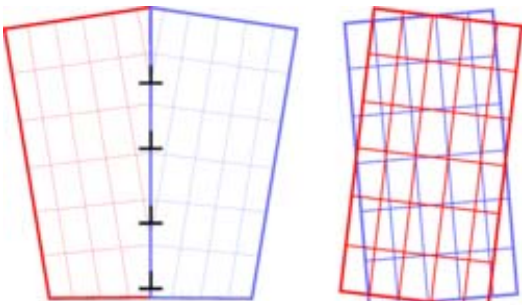

a) b)

Fig.3. Schematic reprezentation of LAGB formation
a - by tilting (with an array of edge dislocation);
b - by twisting (with an array of screw dislocations)

To explain the formation pattern of LAGB resulted by tilting, as suggested in Fig.3.a, one considers a grain that is gradually bent by internal stresses. The energy associated with the elastic bending of the lattice can be reduced by inserting a dislocation that is in fact a semi-plan of atoms that acts like a wedge. This wedge penetrates the lattice. If the grain is bent further, more and more dislocations penetrate into the lattice, enhancing the wedge effect and the occurring of a wall of dislocations leading to a LAGB. The initial grain can now be considered to have being split into two sub-grains, related crystallography but with different orientations. If the density of dislocations increases the ordered nature of the boundary will begin to breakdown so the boundary can be considered like a HAGB. In this moment the original grain is entirely separated in two new smaller grains.

Fig.3.b presents another possible pattern to fragmentise the grains, based on the twisting of the lattice. In this case the miss-orientation occurs around an axis that is perpendicular to the boundary. This type of new boundary incorporates two sets of screw dislocations. Generally, the mechanism for dividing the grain is similar with those described above.

Both the HAGB and the LAGB are in permanent moving during the plastic deformation process because the stress that acts in the material due the external forces. The movements of boundaries are strongly influenced by the presence of fine particles, dispersed into material, by the so called Zener effect. This effect is sometimes used in practice for commercial alloys to prevent the re-crystallisation and the growing of grains.

It is known that the plastic deformation process is governed by the formation, the movement and the storage of dislocations. Factors like grain orientation, strain and deformation pattern, initial size and shape of grains etc. can affect the grain refinement but the principle of micro-structural fragmentation is similar in all cases. It is also known that some conventional processes of plastic deformation like cold rolling or drawing are able to produce significant refinement of initial grain, which generally speaking is coarse (>10 μm). In these processes the sub-grains and the cell-blocks are made subsequently the strength and other properties of metallic materials can increase.

Additionally, during the cold plastic deformation processes, important structural changes occur. The shape, the dimensions and orientation of grains also change and

thus a metallic material processed using these technologies offer new properties and a large range of practical applications.

3. The grain fragmentation during Severe Plastic Deformation processes

Severe Plastic Deformation (SPD) is characterised by extremely large strains, obtained generally by repetitive plastic deformation processes, so the total strain resulted like a cumulus of partial strain of each stage. It is possible to achieve engineering strain over 99,95%, values impossible to be obtain by conventional plastic deformation processes.

The processing by SPD fragments more the granulation by introduction of a great number of dislocations in the interior of the grain, like low angle grain boundaries. When deformation increases, those arrangements of dislocations give birth to ultra-fine sub-grains and/or block-cells, separated by high angle grain boundaries, having big miss-orientation angles, similar with the grain boundaries. The continue increasing of dislocation density lead to a microstructure which significantly decrease in grain size as it can be seen in Fig.5 [3].

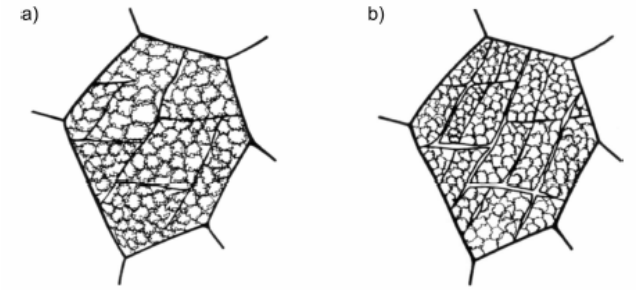

Fig.5. The mecanism of grain fragmentation by storeing of dislocations
a) A grain divided in subgrains and/or cell-blocks;
b) The formation of dislocation cells

The experiments have shown that very few dislocations can be seen inside the very small sizes sub-grains and inside the block-cells, while greater dislocation densities can be found in medium size grains and that sub-grains are present only in the big size grains.

4. Experimental procedure

In order to see the evolution of the micro-structure when a metallic material is processed by severe plastic deformation, it was used a die for Equal Channel Angular Pressing (ECAP) with the angle between channels having 120^0, shown in Fig.6.

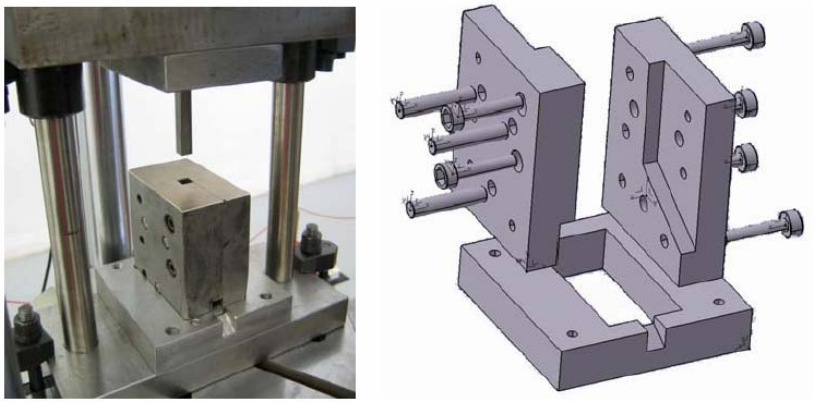

Fig.6. Die used for SPD by ECAP.

The specimens used in experiments have had the dimensions 10x10x60 millimetres and has been obtained from pure commercial aluminium, having the following chemical composition (Tab. 1).

Tab.1. Chemical composition of commercial pur aluminium, used in experiments

Al	Zn	Sn	Pb	Cu	Fe	Mn	Si	Ni	Ca	Cr
99,35	0,045	0,019	0,016	0,033	0,18	0,013	0,26	0,012	0,043	0,022

The specimens were deformed at room temperature by 6 passes using route B_C (90^0 rotation in the same direction after each pass). For lubrication zinc stearate was used.

For micro-structural analysis there has been retained the specimens after the 2nd, 4th and 6th pass. The specimens have been analysed with a Scanning Electron Microscope (SEM) type Tescan Vega 5136 with 3 nm resolution and an Atomic Force Microscope (AFM), using Noncontact Silicon Cantilevers type NSC21/50, with a radius less than 10 nm and the tip angle 20 centigrades, tapping mode scan in air, constant condition of temperature, pressure and humidity.

5. Experimental results concerning the grain fragmentation in SPD

An image of the initial microstructure (un-deformed specimen) is shown in Fig.7 while in Fig. 8 and Fig. 9 are shown the microstructures after the 4th and the 6th pass respectively.

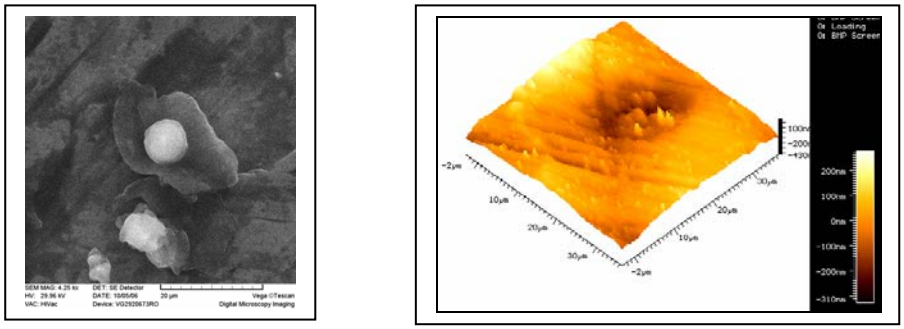

a) **b)**

Fig.7. The images of an un-deformed specimen (annealed material).
a) image obtained with SEM; b) image of a grain, obtained with AFM.

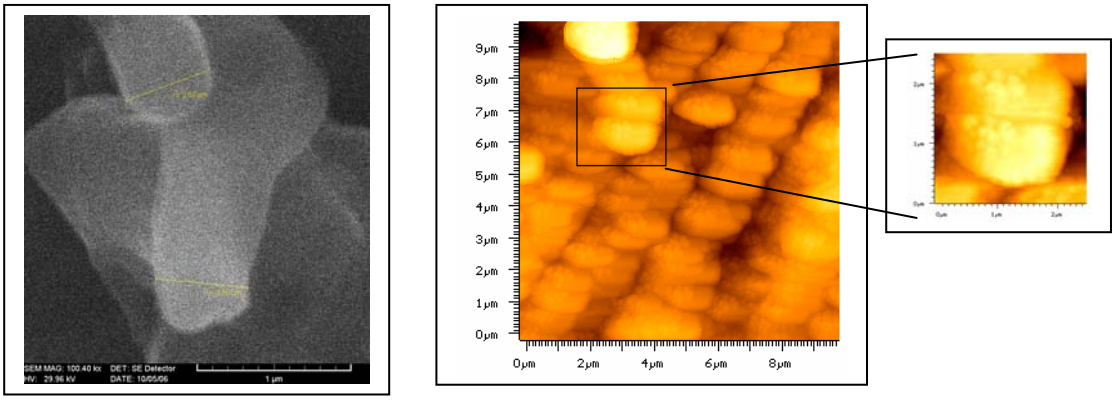

a) **b)**

Fig.8. Images of the specimen after 4 passes by ECAP.
a) image obtained with SEM; b) image obtained with AFM.

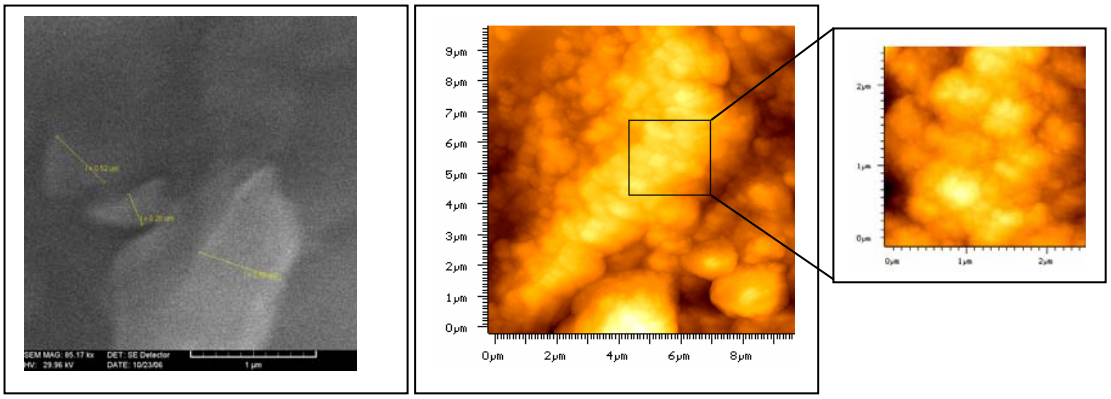

a) **b)**

Fig.9. Image of the specimen after 6 passes by ECAP.
a) image obtained with SEM; b) image of a grain, obtained with AFM.

6. Conclusions

SPD is a technique able to produce significant grain refinement, with spectacular effects on the structure and characteristics of metallic materials. ECAP is characterised by sharing of the material due to abrupt change of flow direction at the pass between the two channels. One can remark (Fig. 8) the positioning of the grains and sub-grains in parallel rows with the sharing direction and the significant reduction of grain/sub-grain size at the sixth pass, the sizes of those being in the nano-metric range.

REFERENCES

1 N.Geru – Metalurgie fizică. **Editura didactică şi pedagogică, Bucureşti 1981**
2. D.R. Askeland – The science and engineering of materials. **PWS-Kent Publishing Company,** USA 1984
3. A. Vorhauer – On the influence of temperature during sever plastic deformation and subsequent anneling. **Doctoral thesis. University of Leoben, march 2005**

Received March 15, 2007

[*]*Technical University "Gh. Asachi" Iaşi*
[**]*National Institute for Research and Development in Micro-technologies (IMT) – Bucharest*

FINISAREA GRANULAȚIEI PRIN DEFORMARE PLASTICĂ SEVERĂ
(Rezumat)

Lucrarea prezintă principalele aspecte ale fragmentării microstructurale prin deformare plastică, pe baza defectelor structurale (dislocații, limite dintre grăunți). Este analizată formarea subgrăunților prin deformare plastică, inclusiv prin deformarea plastică severă. Prin tehnica presării unghiulare în canale egale au fost procesate epruvete din aluminiu prin 6 treceri şi apoi analizate pe un microscop electronic cu scanare (MES) şi pe un microscop de forță atomică (MFA). Imaginile obținute arată cu claritate că deformarea plastică severă produce fragmentarea microstructurii şi rafinarea grăunților până la dimensiuni nanometrice.

BULETINUL INSTITUTULUI POLITEHNIC DIN IAŞI
Tomul LIII (LVII), Fasc. 2, 2007
Secția
ŞTIINȚA ŞI INGINERIA MATERIALELOR

MICRO-STRUCTURAL MODIFICATIONS PRODUCED IN THE IMPROVEMENT STEELS 40Cr10 AND OLC 55 BY THERMAL AND THERMO-CHEMICAL TREATMENTS IN ELECTROLYTIC PLASMA

MARIA BACIU, IOAN RUSU, OCTAVIAN LUPESCU

Summary
The paper presents the micro-structural modifications produced in the improvement steels 40Cr10 and OLC 55 nitrated and chilled or nitrated, chilled and tempered in electrolytic plasma

Keywords: electrolytic plasma, thermo-chemical treatment, microstructure

1. Introduction

The investigations on the micro-structural modifications produced in the improvement steels 40Cr10 and OLC 55 treated thermally and thermo-chemically in electrolytic plasma were conducted by analyses of optical microscopy in the transversal section of the test tubes (10 x 10 x 55 mm) at magnifications of 400:1.
Before being thermally processed in electrolytic plasma, the test tubes from the two steels were thermally treated by improvement.
The microstructures corresponding to the initial state for each steel considered are presented in figure 1.

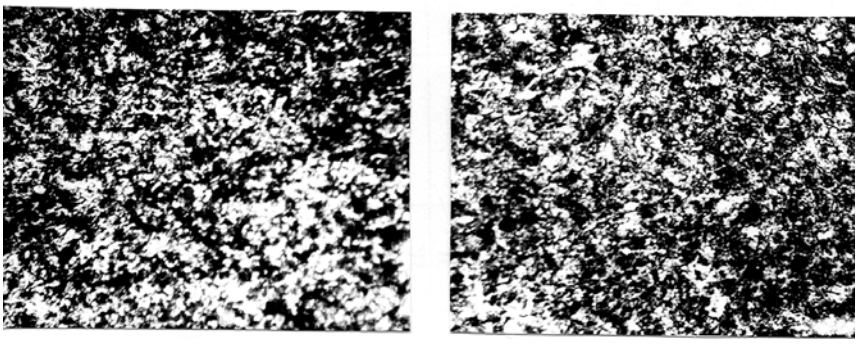

a) b)

Figure 1
a) Microstructure of steel 40Cr10 in initial state improved – S + carbides
b) Microstructure of steel OLC55 in initial state improved – S

2. Experimental procedure

The test tubes submitted to the metallographic analyses were processed thermally and thermo-chemically in electrolytic plasma with the work parameters presented in table [1] and figure 2.

Table 1. Thermal and thermo-chemical treatments in electrolytic plasma applied to the investigated steels

No. crt.	Type of steel	Thermo-chemical treatment	T_{dif}, [°C]	t_{dif}, [min]	Thermal in the diffusion treatment	T_{inc}, [°C]	T_{rev}, [°C]	Microstructure	
								in the core	layer
1	40Cr10	improvement (initial state)	-	-	-	-	-	S + carbides	
2	OLC 55							S	
3	40Cr10	nitriding	650	6	chilling	650	350	-	M_{rev}+nitrides+carbides
						750	-	-	M(N)+A_{rev}+ nitrides+carbides
			700			700	-	-	M(N)+A_{rev}+ nitrides+carbides
						750	350	-	M_{rev}+nitrides+carbides
			750			750	350	-	M_{rev}+nitrides+carbides
						800	-	-	M(N)+A_{rez}
4	OLC 55	nitriding			chilling				

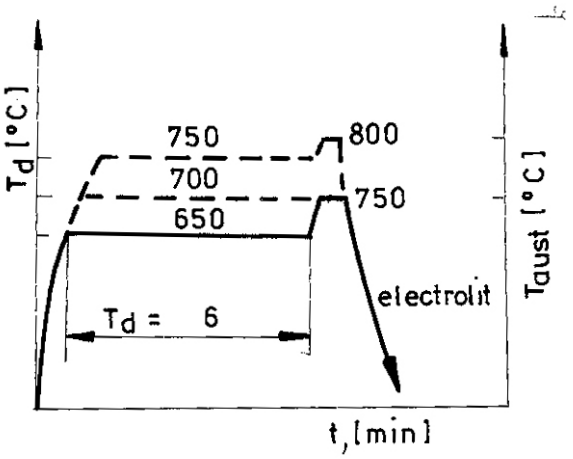

Figure 2. Variants of thermal treatments in electrolytic plasma – nitriding + chilling

3. Experimental results

The nitriding at 650°C for 6 minutes, followed by direct chilling and tempering (in the furnace) at 350°C (t_{rev} = 1h) did not modify the microstructure of the core of the test tubes from steel 40Cr10 (figure 3) only the structure of the superficial layer being slightly affected.

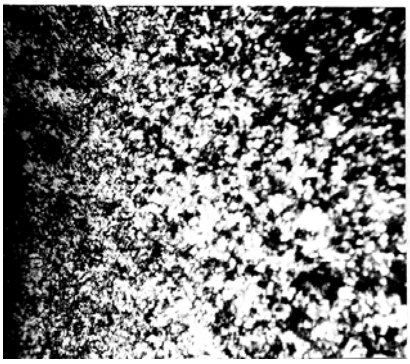

Figure 3. Microstructure of steel 40Cr10 nitrated (T_d = 650°C; t_d = 6 min) and chilled in electrolytic plasma, followed by tempering at 350°C (t = 1h) – the exterior layer of specimen 3B: $\underline{M}_{rev}$ + nitrides + carbides

The application, after the nitriding at 650°C, of a chilling at 750°C with cooling in electrolyte led to the obtaining of an exterior layer finely marked out and with a modified structure (figure 4).

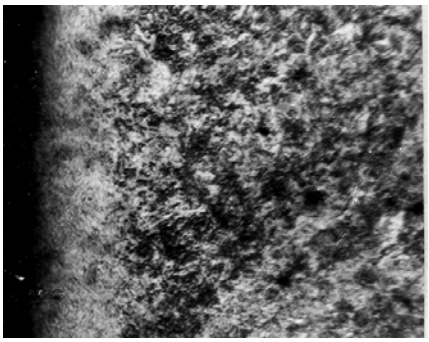

Figure 4. Microstructure of steel 40Cr10 nitrated (T_d = 650°C; t_d = 6 min) and chilled in electrolytic plasma ($\underline{T}_{aust}$= 750°C) - the exterior layer of specimen 3A: nitro martensite + $\underline{A}_{rez}$ + nitrides + carbides

The nitriding at 700°C for 6 minutes, followed by direct chilling in electrolyte led to the obtaining of an exterior layer slightly modified, having the structure formed of nitro martensite, residual austenite, nitrides and carbides (figure 5).

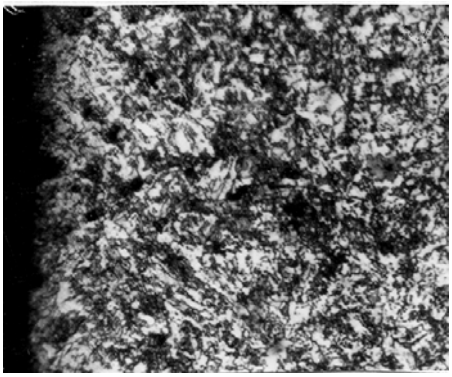

Figure 5. Microstructure of steel 40Cr10 nitrated (T_d = 700°C; t_d = 6 min) and chilled in electrolytic plasma - the exterior layer of specimen 3D: nitro martensite + $\underline{A}_{rez}$ + nitrides + carbides

The application of a chilling at 750°C followed by tempering at 350°C (t_{rev} = 1h), subsequent to the nitriding in electrolytic plasma at 700°C, had as effect the diffusion of the chemical elements from the layer into the core and the appearance of the structural transformations specific to tempering: secondary martensite, nitrides and carbides (figure 6).

Figure 6. Microstructure of steel 40Cr10 nitrated (T_d = 700°C; t_d = 6 min) and chilled from 750°C in electrolytic plasma, followed by tempering (T_{inc} = 550°C; t = 1h) – the exterior layer of specimen 3I: $\underline{M}_{rev}$ + nitrides + carbides

The nitriding at 750°C for 6 minutes, followed by direct chilling in electrolyte and tempering at 350°C led to the obtaining of an exterior layer finely outlined made of secondary martensite, nitrides and carbides (figure 7).

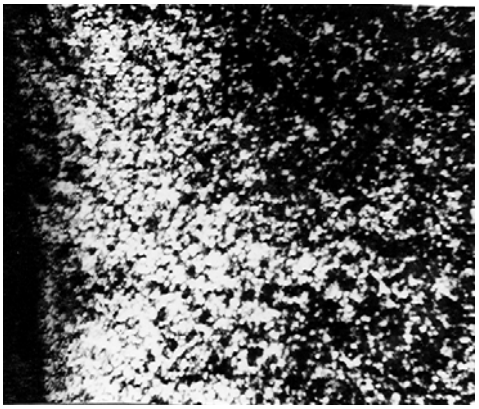

Figure 7. Microstructure of steel 40Cr10 nitrated (T_d = 750°C; t_d = 6 min) and chilled in electrolytic plasma, followed by tempering at 350°C (t = 1h) – specimen 3HH: $\underline{M}_{rev}$ + nitrides + carbides

If after the nitriding in electrolytic plasma at 750°C, we apply a short cooling at 600°C and then a chilling from 800°C, in electrolyte, we will obtain in the superficial layer a typical structure of chilling made of nitro martensite and residual austenite (figure 8).

Figure 8. Microstructure of steel 40Cr10 nitrated (T_d = 750°C; t_d = 6 min) cooled at 600°C and chilled at 800°C in electrolytic plasma ($\underline{T}_{aust}$= 750°C) - specimen J: nitro martensite + $\underline{A}_{rez}$

For the steel OLC 55, the application of nitriding at 650°C followed by cooling led to the obtaining of a white layer made of nitro martensite, residual austenite and nitrides (figure 9).

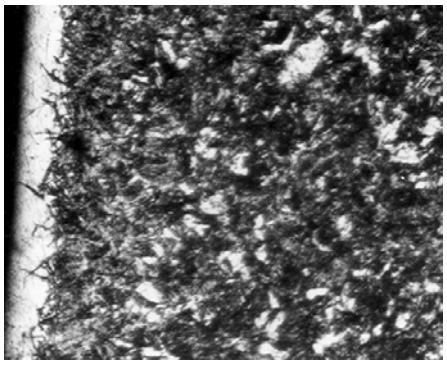

Figure 9. Microstructure of steel OLC55 nitrated (T_d = 650°C; t_d = 6 min) chilled in electrolytic plasma: nitro martensite + $\underline{A}_{rez}$ + nitrides

The application of a chilling from 750°C, after the nitriding at 650°C, determined the nitrogen diffusion in the superficial layer, resulting at its level a structure made of martensite and residual austenite (figure 10).

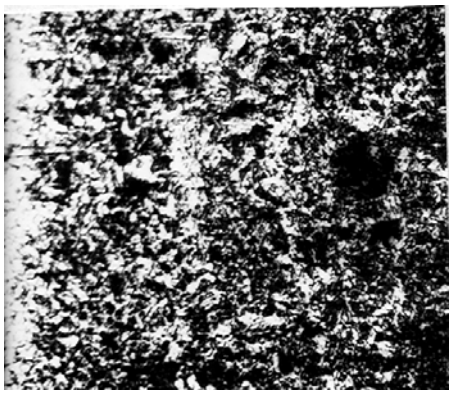

Figure 10. Microstructure of steel OLC55 nitrated (T_d = 650°C; t_d = 6 min) and chilled from 750°C in electrolytic plasma - the exterior layer of specimen 4T : $\underline{M}$ + $\underline{A}_{rez}$

The nitriding at 700°C, followed by direct chilling in electrolyte led to the obtaining of an exterior layer finely outlined made of nitro martensite, nitrides and residual austenite (figure 11).

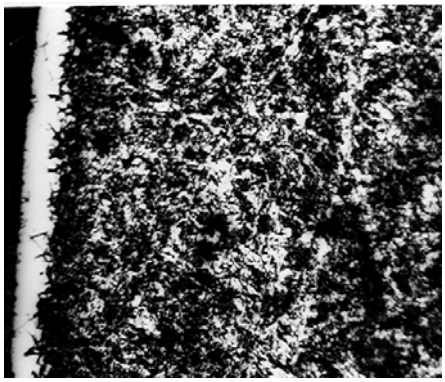

Figure 11. Microstructure of steel OLC55 nitrated (T_d = 700°C; t_d = 6 min) and chilled in electrolytic plasma - the exterior layer of specimen 4DD: nitro martensite + nitrides_+ $\underline{A}_{rez}$

The chilling from 750°C and the tempering at 350°C after the nitriding at 700°C for 6 minutes, led to the formation in the exterior layer of the secondary martensite (figure 12).

Figure 12. Microstructure of steel OLC55 nitrated (T_d = 700°C; t_d = 6 min) and chilled at 750°C in electrolytic plasma, followed by tempering at 350°C (t_{rev} = 1h) - the exterior layer of specimen 4U: $\underline{M}_{rev}$

The application of a direct chilling in electrolyte and of a tempering at 350°C (t_{rev} = 1h), after the nitriding at 750°C for 6 minutes, led to the obtaining of a layer made of secondary martensite (figure 13).

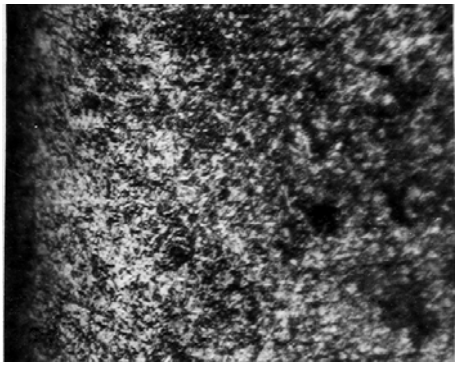

Figure 13. Microstructure of steel OLC55 nitrated (T_d = 750°C; t_d = 6 min) and chilled in electrolytic plasma, followed by tempering at 350°C (t_{rev} = 1h) - the exterior layer of specimen 4MM: $\underline{M}_{rev}$

The chilling in electrolyte from 800°C, after the nitriding at 750°C, followed by a short cooling at 600°C, determined the nitrogen diffusion from the superficial layer and the formation of a white layer made of nitro martensite and residual austenite (figure 14).

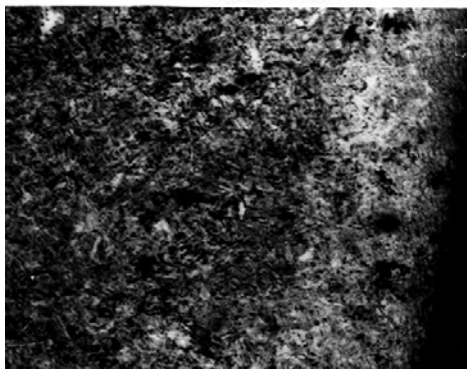

Figure 14. Microstructure of steel OLC55 nitrated (T_d = 750°C; t_d = 6 min) and chilled from 800°C in electrolytic plasma - the exterior layer of specimen 4Y: nitro martensite + $\underline{A}_{rez}$

Conclusions

The nitriding in electrolytic plasma, followed by direct chilling from high temperatures, of the improvement steels 40Cr10 and OLC 55 allowed the obtaining of a white layer finely outlined made of nitro martensite, carbides, nitrides and residual austenite.

The application of a tempering at 350°C (t_{rev} = 1h), after nitriding and chilling led to the disappearance of the white layer, due to the nitrogen diffusion and the transformations specific to tempering.

The structural modifications in the exterior layer of the steels 40Cr10 and OLC 55 produced by the thermal and thermo-chemical treatments in electrolytic plasma

represent the main cause of increase of the hardness and wearing resistance of these steels.

References

1. Baciu, Maria **– *Contributions in the structural and property modifications of the steels treated thermally and thermo-chemically in electrolytic plasma*,** doctoral thesis, Technical University, Iasi, 1999
2. Baciu, C.; Baciu, Maria – Incalzirea anodica a otelurilor in plasma electrolitica, Buletinul Sesiunii Academice Romane – filiala Iasi, pp. 42-45, Iasi, 1996
3. Structural changes in nitride steels in electrolytic plasma, Baciu, C., Baciu, Maria, Alexandru, Adrian – Conferinta internationala "Tehnologii si materiale avansate", Galati, 2003

Received March 15, 2007

Technical University Iasi

Modificări microstructurale produse în oţelurile de îmbunătăţire 40Cr10 şi OLC55 prin tratamente termice şi termochimice în plasmă electrolitică

Rezumat

Lucrarea prezintă modificările microstructurale produse în oţelurile 40Cr10 şi OLC55 nitrurate şi călite sau nitrurate,călite şi revenite în plasmă electrolitică.

BULETINUL INSTITUTULUI POLITEHNIC DIN IAŞI
Tomul LIII (LVII), Fasc. 2, 2007
Secția
ŞTIINȚA ŞI INGINERIA MATERIALELOR

NUMERICAL MODEL TO COMPUTE ULTRASONIC STRESS-RELIEF PROCESSES AT CARBON STEEL

BY

CONSTANTIN DUMITRACHE, CORNELIU COMANDAR, NICUŞOR AMARIEI, ADRIAN SABĂU

Abstract: *In the article [4] is published a mathematical model of optimization thermal stress-relief process which are conditioned by the plastic yield speed phenomenon. This new paper take in advance thermal stress-relief process and complete with overlapping ultrasonic stresses which is acting during cooling after welding process. In conformity with theory, Nevill and Brotzen [5] said that residual stresses are decreased because these overlapping stresses determined the altering of metallic yielding stress. In this article, using numerical method Runge-Kutta [1] is computed the overlapping ultrasonic stresses above welding residual stresses at OLC45 steel.*

Keywords: *Overlapping Ultrasonic Stresses, Ultrasonic Stress-Relief*

1. Mechanism of overlapping ultrasonic stress process

The principle of ultrasonic stress-relief consist in introducing of ultrasonic stress σ_A with magnetostrictive transducer at resonance frequency. The efficiency of this process deppends on the values of ultrasonic stresses σ_A introduced in thermal influence zone, which have to be comparable with the values of welding residual stresses. This overlapping ultrasonic stress performs the ultrasonic stress-relief process of tensile stresses in vicinity of weld bead, or pretension if there are compressive stresses in the same zone.

The acoustic wave is:

$$u = A \cdot \sin\left(\omega t - \frac{2\pi}{\lambda} x\right) \tag{1}$$

where $\omega = 2\pi \cdot f$ is pulsation, f - acoustic resonance frequency, $k = \frac{2\pi}{\lambda}$ is wave factor.

The metallic induced deformation is:

$$\varepsilon = \frac{du}{dx} = -\frac{2\pi}{\lambda} \cdot A \cdot \cos\left(\omega t - \frac{2\pi}{\lambda} x\right) \tag{2}$$

In conformity with Hooke' elasticity rule, ultraacoustic stress σ_A is:

$$\sigma_A = \varepsilon \cdot E = -\frac{2\pi}{\lambda} \cdot E \cdot A \cdot \cos\left(\omega t - \frac{2\lambda}{\lambda} x\right) \tag{3}$$

with λ wave length:

$$\lambda = \frac{c}{f} \tag{4}$$

c - ultrasonic speed propagation. The maximum value of ultraacoustic stress is obtained when:

$$\cos\left(\omega t - \frac{2\lambda}{\lambda}x\right) = 1 \quad ; \quad \omega t - \frac{2\lambda}{\lambda}x = 0 \tag{5}$$

Nevill and Brotzen [5] explained the decreasing of residual stresses with mechanism presented in figure 1. The overlapping of ultraacoustic stresses, with amplitude $\varepsilon = \frac{2\pi A}{\lambda}$ above the values of stresses σ, is performed in elasticity and plasticity areas. For example, every sample distorsioned under metallic yielding point (M area), during the half period of overlapping ultraacoustic oscilation, can get additional elastic distorsion. All periodical oscilations which are overlapped in elastic area between M_1 and M_2 don't affect the values of residual stresses.

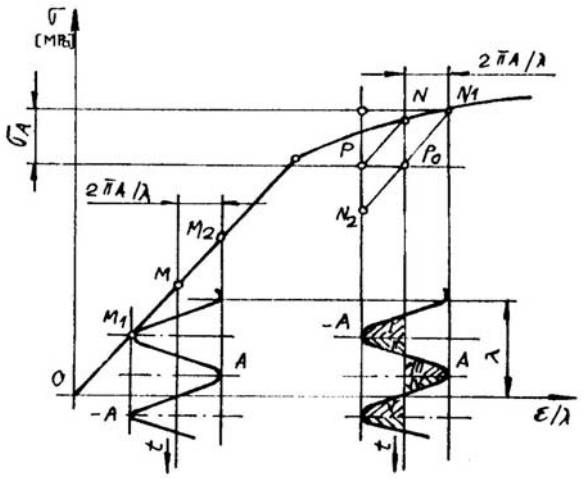

Fig. 1. The mechanism of overlapping stresses in elasticity and plasticity areas [1]

When overlapping process is acting in plastic area residual streses field are decreased:

- in the first quarter of oscilation period (I) the sample is "discharged" from N to P;
- in the second quarter of oscilation period (II) stress is returned to N;
- the additional distorsion determined by ultraacoustic stresses will be acting in the third quarter of oscilation period (III) with amplitude of distorsion $\varepsilon = \frac{2\pi A}{\lambda}$, from N to N_1;
- in the quarters (IV) and (V) the residual stresses decreasing from N_1 to N_2 passing to P_0.

Decreasing of residual stresses σ is represented by segment NP and the maximum values of ultraacoustic stress is determined with (3) and (5).

After all presented above, ultrasonic stress-relief process is acting if welding stress σ, produced during cooling welded joining is overlapped with ultraacoustic oscilation stress σ_A and total stresses $\sigma+\sigma_A$ have possibility to exceed metallic yielding stress σ_c. In fact, this action is essential for deacreasing of residual stresses.

2. Numerical method to compute ultrasonic stress-relief

If $\sigma+\sigma_A>\sigma_c$ welding residual stresses are decreasing and are produced during the first quarter of oscilation period T/4. This could be observed in figure 2 on the part of curve $\sigma+\sigma_A>\sigma_c$.

If $\sigma+\sigma_A<\sigma_c$ (fig.3) residual stress-relief process is determined as if on the material is acting ordinary mechanical stress.

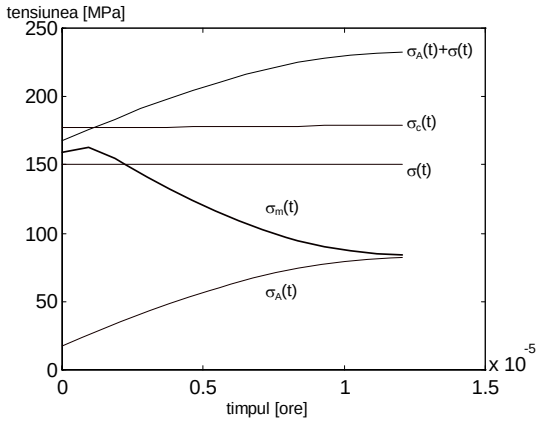

Fig. 2. Metallic yielding point variation and residual stresses during ultrasonic stress-relief for temperatures T=400°-393°C in time of 3.6 seconds ($\sigma+\sigma_A>\sigma_c$) [1]

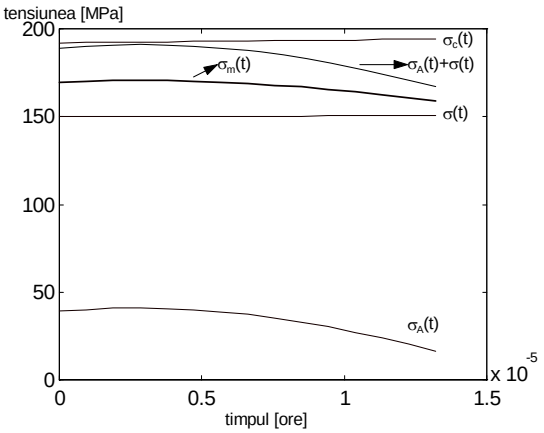

Fig. 3 Metallic yielding point variation and residual stresses during ultrasonic stress-relief for temperatures T=400°-393°C in time of 3.6 seconds ($\sigma+\sigma_A<\sigma_c$) [1]

Energy for ultrasonic stress-relief is wasted during the first quarter (T/4) of acoustic oscilation period when take place locally plastic distorsions. Stresses after ultrasonic stress-relief are determined with well known function:

$$\frac{d\varepsilon_p}{dt} = \frac{K \cdot \sigma}{\sigma_c - \sigma} \tag{6}$$

or stress-relief function [2] [3] where $\sigma=\sigma_m$ the values of residual stresses after ultrasonic stress-relief.

In this article, Young modulus E, metallic yielding point σ_c, residual stresses σ_m are altering with temperature and for them there is the same calculus model [3] as well as thermal stress-relief process for OLC45 steel. Before acting ultrasonic stress-relief, it was considered initial value of residual stresses, 150 [MPa]. Other values used to compute ultrasonic stress-relief process:

- ultrasonic speed propagation in steel c=5050000 [mm/s];
- ultrasonic oscilations frequency f=17500 [Hz];
- wave length λ=144.2857;
- ultrasonic oscilation amplitude in steel A=0.01 [mm]

3. Conclusions

This computational model presents the influence of acoustic frequency (fig. 4) in residual stresses field during cooling welded joining for temperature between 400-386°C. It were considered acoustic frequencies f=17.5 kHz and f=22.5 kHz; increasing of oscilation frequencies have determined an easier increasing of amplitude and residual stresses varies with phase difference of acoustic stresses induced in material. In steels, increasing of acoustic amplitude from A=0.01 mm from A=0.02 mm produces increasing quantity of induced acoustic energy in material (fig. 5).

If thermal residual stresses exceeds metallic yielding point $\sigma_c(t)$, appling of acoustic stresses in time-temperature interval produce elastic and plastic distorsions.

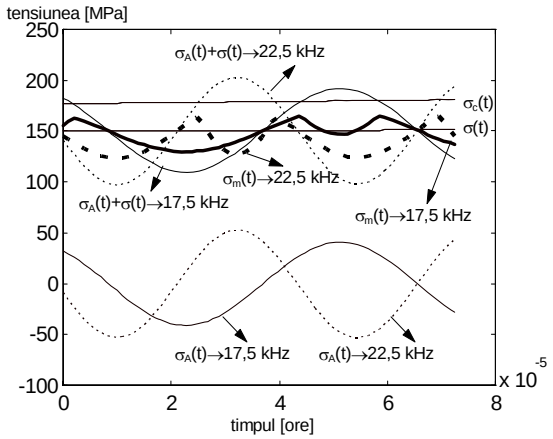

Fig. 4 Metallic yielding point variation and residual stresses during ultrasonic stress-relief for temperatures T=400°-386°C in time of 10.8 seconds when: a - f=17.5 kHz, b - f=22.5 kHz [1]

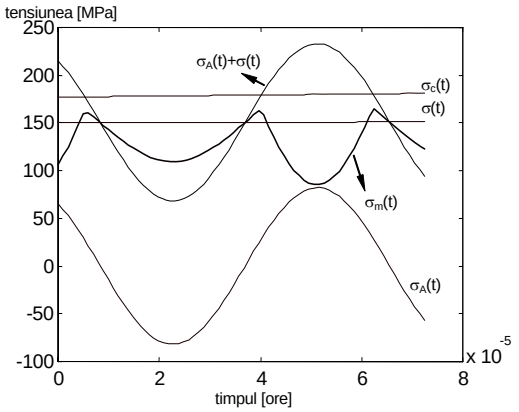

Fig. 5. Metallic yielding point variation and residual stresses during ultrasonic stress-relief for temperatures T=400°-386°C in time of 10.8 seconds when amplitude oscilation A=0.02 mm: [1]

This numerical model of ultrasonic stress-relief take in advance only elastic distorsions produced by ultrasounds.

Finally, performing utrasonic stress-relief depends by plastic yielding phenomenon near to metallic microvolumes produced by acoustic stresses which are exceeding metallic yielding point σ_c. Welding thermal residual stresses have essential influence because after these stresses are overlapping acoustic stresses induced by ultrasounds.

REFERENCES

[1]. Dumitrache C. - **Cercetări privind influența ultrasunetelor asupra elementelor de substructură şi tensiuni ale construcțiilor sudate**, Teză de doctorat, Iaşi, 2000;

[2]. Dumitrache C., Comandar C., Sabău Adrian Amariei N. - **Computational model of optimization thermal stress-relief processes at carbon steel,** 3rd International Conference "Research and development in mechanical industry" RaDMI 2003, 19-23 sept. 2003 Herceg Novi, Serbia and Montenegro;

[3]. Dumitrache C., Comandar C., Sabău A., Amariei N. - **Numerical model to compute thermal stress-relief processes at carbon steels,** The Fifth International Congress in Materials Science and Engineering May 26-28th, 2005 IASI - ROMANIA

[4]. Hopulele I., Leon D., Amariei N., Ştefan M. - **Un nou model matematic de analizare şi de optimizare a proceselor de detensionare termică**, Timişoara, 1993

[5]. Susan M., Dima A., Simionescu G., Catarschi V. - **Tragerea si trefilarea metalelor. Prelucrari cu ultrasunete**, Ed. Sedcom Libris, Iasi, 1997

METODĂ NUMERICĂ DE REZOLVARE A ECUAȚIEI DIFERENȚIALE A PROCESULUI DE DETENSIONARE CU ULTRASUNETE PENTRU UN OȚEL OLC45

REZUMAT: Această lucrare, continuarea articolelor [2] şi [3], pune in evidență rezolvarea numerică a procesului de detensionare cu ultrasunete. Modelarea acestuia s-a făcut conform "teoriei suprapunerii tensiunilor" [5]. Conform acestei teorii, efectele de volum (modificări în tensiunea de curgere a metalului) se datorează suprapunerii tensiunilor ultraacustice peste tensiunile remanente rezultate în urma regimului termic de la sudare. În final, detensionarea cu ultrasunete se produce dacă tensiunile ultraacustice au tendinta de a depăşi valoarea limitei de curgere a materialului. Acest proces este influentat de mărimile ultraacustice specifice ale undelor ultrasonice, dar şi de valorile tensiunilor interne obținute după regimul termic de la sudare.

BULETINUL INSTITUTULUI POLITEHNIC DIN IAŞI
Tomul LIII (LVII), Fasc. 2, 2007
Secția
ŞTIINȚA ŞI INGINERIA MATERIALELOR

STUDIES ABOUT THE GRAY CAST IRON HARDENING BY USING THE VIBRATING ELECTRODE METHOD BY MULTIPLE LAYER DEPOSITION USING W ELECTROD

CARMEN NEJNERU, DAN-GELU GALUSCA, MANUELA PERJU, TUDOR RAILEANU, DRAGOS ACHITEI

Abstract: *There have been tested samples of grey cast iron, the hardening being made through W coating through the vibrating electrode method with a layer, two layers and trough double layers combined with Ti, TiC. Besides double layers combined there were also made triple layers combined. Afterwards there made photographs of macro-hardness and HV50 micro-hardness into the material in into the layer, then in order to appreciate the internal stresses were made ring specimens type Naimov. On the exterior of these specimens were made coatings with the vibrating electrode.*

Keywords: *vibrating electrode, hardness, coating, combined layer.*

1. Introduction

The superficial heat treatments with material supply are domains which interest a lot. Some of these domains are: the surfaces processing with laser beam light, diffusion treatments in plasma, coatings through heat spraying, thin layers deposits through CVD and PVD proceedings.

The alternative methods of deposit on metallic surfaces can be divided according to the technological process:

- coatings through heat spraying which use arc flame, electric arc and plasma;
- PVD coatings (vapors physical deposition) that can be with ionic coating, electron bombing and laser alloying;
- Chemical deposition (CVD).

The vibrating electrode method belongs to the same class with the electric arc coatings. The principle of hardening through electric sparks of the metallic pieces consists in the fact that in case of sparking unloading under the pulsatory current take place the polar transport of the electrode material, which represents the anode, on the surface of the piece, which is the cathode.

This material alloys the layer of the piece and by chemically combining with the atomic dissociated azotes from the air, the carbon and the material of the piece it forms

a diffusion layer which is hardened and resistant to wear. In the superficial layer forms complex chemical reactions: azotizes, carbonitriding, very stable nitridings and quenching layers.

1. Experimental results

It was used for the experiment the ferrite-pearlite grey cast iron to which the chemical composition is given in the table.

Table 1

C	Si	Mn	P	S	Cr	Ni	Cu	Mo
3.97	2.87	0.25	0.06	0.07	0.28	0.126	0.17	0.03

We have chosen the grey cast iron because the study depends on the implementation of the method within the technological processes of the piston rings which are made of cast iron and have a powerful wear on the exterior. This made us think that we could prolong the life of the piston rings by making this micro alloying treatment.

There were made tests with layer deposition through sparking with W electrode, with a layer and two layers, but with double layer combined with Ti and TiC.

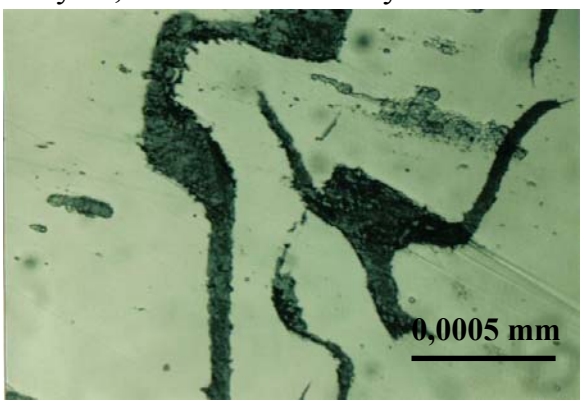

Fig.1. Base material: grey cast iron

Using W electrode we can observe that it is obtained a compact surface but with pronounced irregularities like in the figure 2. The coating had some difficulty degree because the W electrode realizes holes and jumps during the surface alloying. It was worked with high amplitude and average intensity (A_6, r_3). All the etchings were made with 5% Nital and the photos were made with a magnification power of x200 and x600.

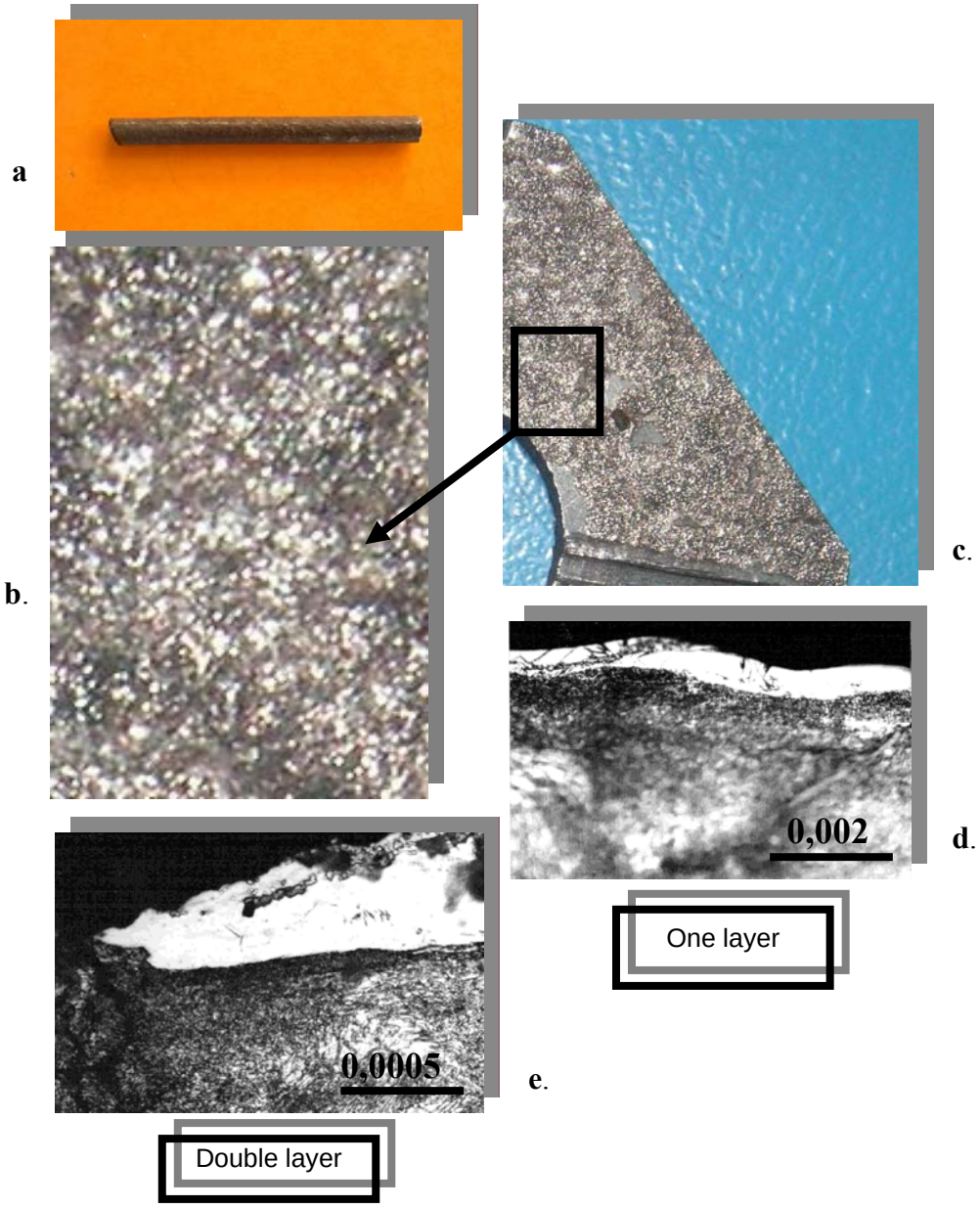

Fig.2. a. W electrode; b. Macrostructure surface with W deposition; c. Cast iron sample with W deposition by vibrating electrod; d. Microstructure of W deposition one layer; e. Microstructure of W deposition double layer

For the combined double layers I used as base Ti because it gave the layer a good compacting and anchor, the deposition was uniform and the WC was on the exterior because it gave hardness to the surface. The deposition with Ti base takes to the disparity of the defects like holes and oxides.

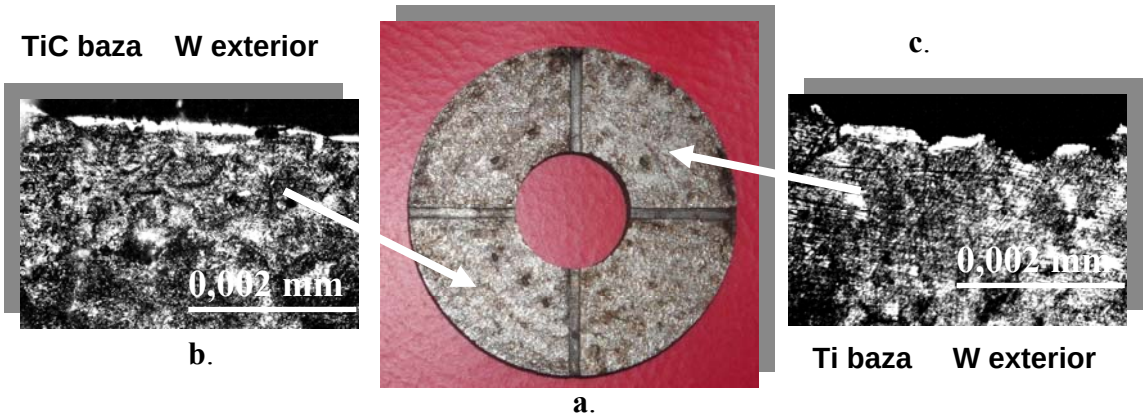

Fig.3. a. Cast iron sample with different kind of deposition-macrostructure; b. Microstructure double layer deposition, first layer TiC deposition and front layer W deposition;
c. Microstructure double layer deposition, first layer Ti deposition and front layer W

The tests were made on an apparatus type Elitron 22.

Fig.4. Elitron 22 –the installation for sputtering deposition
with different kind of electrodes

We used for the triple combined layers W as base because it has a good adherence on cast iron, Ti as an intermediate layer because it gives the combination a good toughness and on the exterior it was used a WC because it has high hardness. The second kind of sample was covered with triple combined layer having as base WC because it anchors on cast iron, TiC as an intermediate layer which leads to the

extinction of the defects like holes and oxides and on the exterior it was used W which leads to the appearance of a uniform layer.

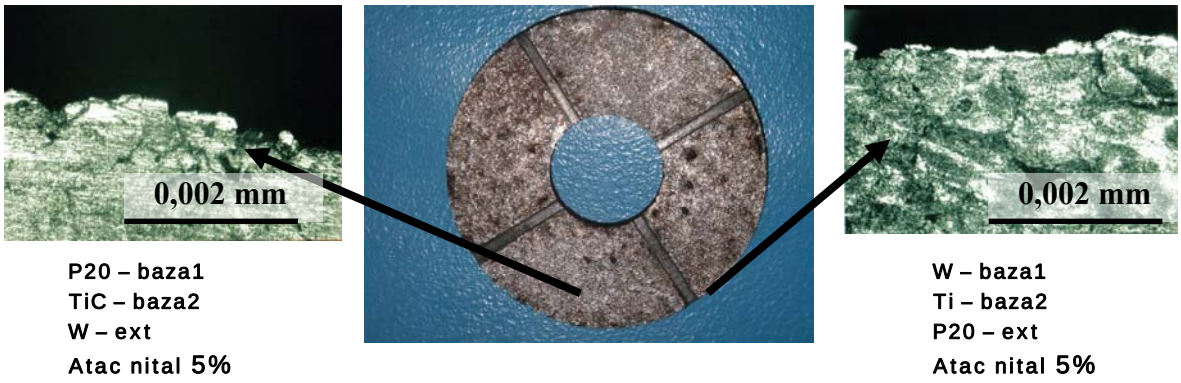

Fig.5. Cast iron sample with different kind of deposition-macrostructure; Microstructure triple layer deposition, first layer W, second layer Ti, WC exterior layer and WC first layer, TiC front layer, W exterior layer

Fig.6. Apparatus PMT3 for microhardness measurements

There were made the microhardness after the depositions by using the apparatus PMT3. It was used a weight of 50 g in order to press the diamond penetrator.

Making an average to the realized tests I noticed that we have the hardness much higher than the base material.

Table 2

Base material	W – one layer	W – double layer	Ti first layer, W front layer	TiC first layer, W front layer	W base, Ti second layer, WC front layer	WC base, TiC second layer, W front layer
400	754,42	818,32	566,89	689,31	979,42	867,29

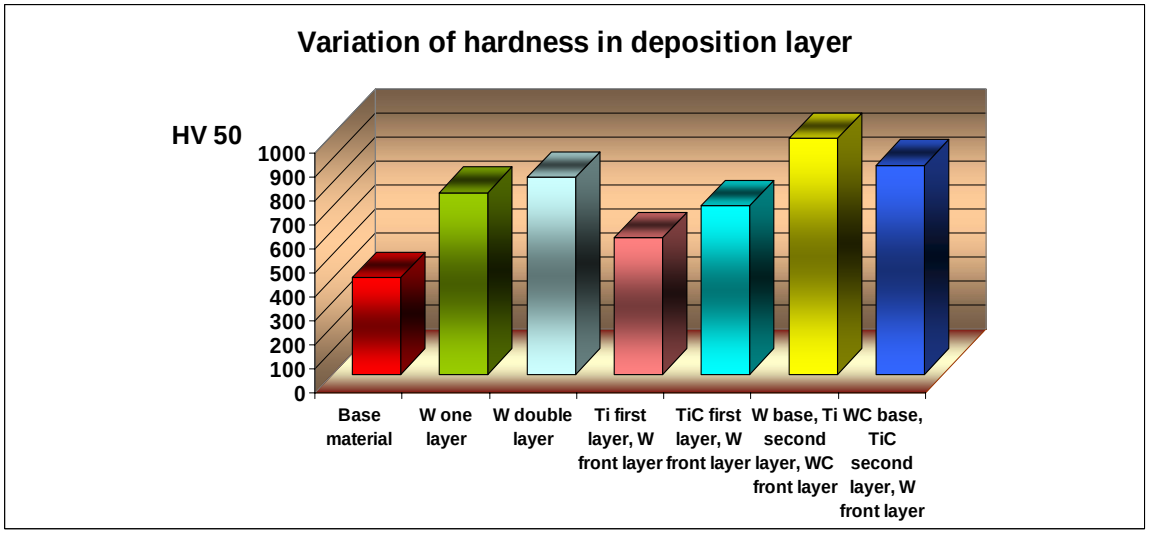

Fig.7. The graph of hardness in deposition layer

To determine the internal stresses there were used test bars type Naimov from grey cast iron.

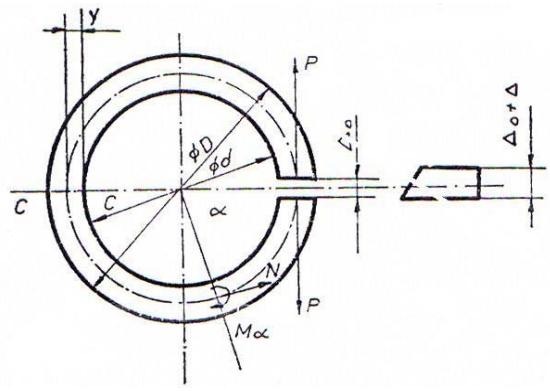

Fig.8. Test sample Naimov type

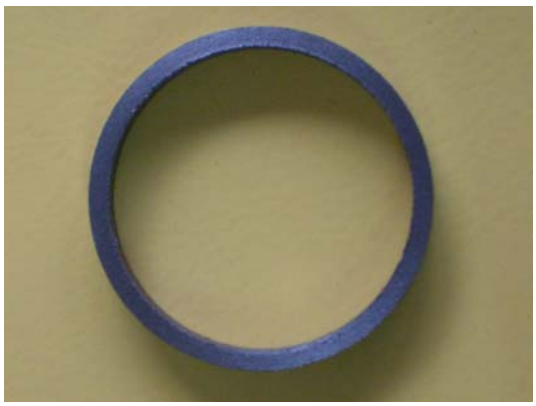

Fig.9. Test ring Naimov type

$$\sigma_f = \Delta_e \frac{Eh^2}{36\pi R^3}\left(\frac{2h}{K(2R-h)}-1\right) \qquad (1)$$

The rings were stress relieving treated to the temperature of 550°C, 3 hours maintaining and cooling with the furnace. On the rings there were traced two marks like a cross, the distance between them was measured before and after cutting. The

cutting was made after deposition so that the obtain opening is proportional with the size of the introduced internal stresses. We used the calculus from curve girders for the calculus of the stresses.

The introduced stresses are mainly forging drawing that adds on the value of the existent stresses from the piston rings prolonging their function period.

Table 3

Nr. inele	Tipul depunerii	Nr. straturi depuse	Δ_r [mm]	$\sigma_{rem.}$ [N/mm^2]
I	W	1	+0,225	17,9
II	W	2	-0,76	-60,45
III	Ti-b;W-e	1+1	+0,62	49,32
IV	TiC-b;W-e	1+1	+0,44	35,1
V	W-b1;Ti-b2;WC-e	1+1+1	+0,45	35,8
VI	WC-b1;TiC-b2;W-e	1+1+1	+0,41	32,61

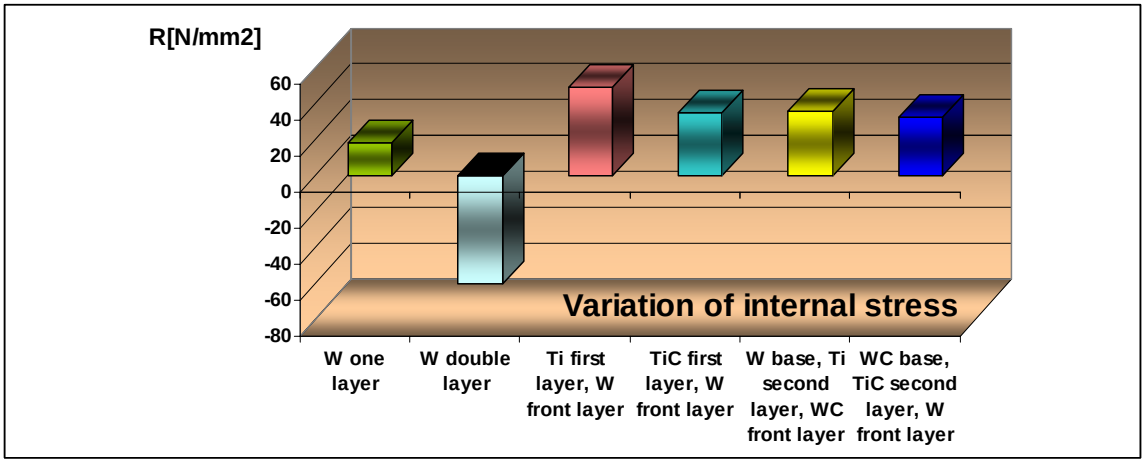

Fig.10. The graph of internal stress in different deposition layer

3.Conclusions

1.The method has practical applicability not only for restore but also for prolonging the function period of the cast iron pieces that work in intense regime like piston rings.

2.From technological point of view it works easier manually with electrodes of different dimensions: 3-6 mm diameter and the deposition are more uniform. The can also be automatic.

3.If we compare the results we can see from the graphs that the microhardness in deposition layer is almost double the microhardness of base material.

4.The most interesting thing is that the internal stress is compressions when the layer is W double layer and elongation strain at W one layer, Ti based layer and W front layer, TiC based layer and W front layer, W base, Ti second layer and WC front layer, WC base, TiC second layer and W front layer.

4. References

1. Raileanu, T.: Teza de doctorat, Contributia privind influienta unor tratamente termice din faza lichida asupra calitatii suprafetelor si rezistenta la uzare a unor repere din fonta, 2000.

2. Vermesan, G., Vermesan, E., Jichisan-Matiesan, D., Cretu, A., Negrea, G., Vermesan, H., Vlad, M.: Introducere in ingineria suprafetelor, Editura Dacia, 1999, ISBN 973-35-0922-1

Received March 15, 2007

Technical University Iasi

CERCETĂRI ASUPRA DURIFICĂRII FONTEI CENUŞII FOLOSIND METODA ELECTRODULUI VIBRATOR PRIN DEPUNERI DE STRATURI MULTIPLE FOLOSIND ELECTRODUL DE W

(Rezumat)

S-au folosit pentru testări epruvete din fontă cenuşie, iar durificările au fost realizate prin acoperiri, prin metoda electrodului vibrator, folosind electrodul de W, în strat simplu şi strat dublu, precum şi depuneri eterogene cu strat dublu şi triplu prin combinări cu electrod de TiC şi Ti. S-au realizat macrofotografii pentru aprecierea acurateții suprafeței şi microfotografii pentru evidențierea grosimii şi clarității stratului depus. S-au realizat măsurători de macroduritate HV50 şi s-au calculat tensiunile interne introduse de depuneri folosind epruvete tip Naimov.

BULETINUL INSTITUTULUI POLITEHNIC DIN IAŞI
Tomul LIII (LVII), Fasc. 2, 2007
Secţia
ŞTIINŢA ŞI INGINERIA MATERIALELOR

RESEARCHES CONCERNING VARIATION OF COOLING INTENSITY OF THE SYNTHETICAL MEDIUMS LIKE POLIALCHILENGLICOL (PAG) 5% SOLUTION IN WATER MODIFIED BY ADDING 16% Na_2SiO_4 AND $CaCO_3$ (5%, 10%, 15%)

CARMEN NEJNERU, DAN GELU GĂLUŞCĂ, ADRIAN GRECU, MANUELA PERJU, ION HOPULELE

Abstract

The paper presents the experimental researches on the cooling capacity on synthetical cooling mediums dissolved in water. The experiments were made by using a silver control cylinder and in its middle was introduced a cromel-alumel thermocouple connected to an y-t recording apparatus. The measurements were made on barbotaged with air(p=2atm) and non-barbotaged mediums by varying the initial temperature (20°C, 30°C, 40°C, 50°C) and the results were tabled. It was calculated the cooling variation intensity depending on the solution concentration and were made two spatial graphs.

Keywords: *hardening, cooling velocity, cooling curve, dynamic and cinematic viscosity.*

1.Introduction

If the cooling process in hardening is properly made, the success of the operation is guaranteed and we can obtain structures in the sectioned view of the pieces (hardening martensite structures) without producing hardening defects such as: cracks, deformations or big residual stresses.

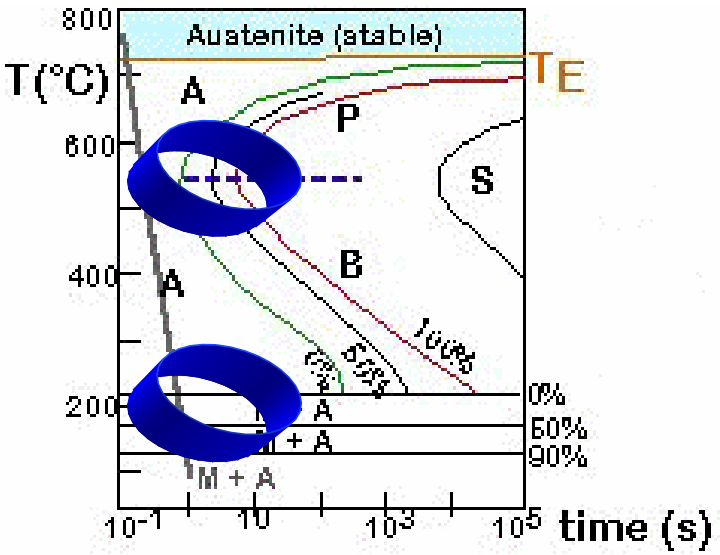

Figure 1. TTT diagrams with a theoretical cooling medium

We analyzed the cooling kinetic curves of the alloy (TRC diagram) and we also compared the cooling curves of the mediums in order to choose the right cooling medium.

The cooling mediums used until our days do not satisfy totally the demands required by the modern thermical treatments that must assure a wide-open spectrum of the physico-mecanical properties of the thermical treated pieces. They must have a low price and to maintain constant their cooling properties. In order to satisfy the demands there were used synthetical hardening mediums such as residual substances obtained from petroleum industry, the paper chemical processing industry.

2.Objectives

The oil has favorable cooling curve because it crosses quickly the minimum stability domain of the after cooled austenite and has a slow cooling velocity in the martensite domain when tensions caused by the structural transformations are very big and the thermical tensions are smaller caused by the cooling velocity. The oil has the great disadvantage that it can burn. It also is a non-ecological medium because during the process there are toxic gas emissions. This is the reason that synthetic mediums replaced the mineral oil. The synthetic mediums are non-toxic and it does not exist to the danger of ignition. Such medium is polialchilenglicol, still it does not have the same cooling properties in hardening as oil, and the tests make on different concentrations and different initial temperatures of the cooling medium in order to choose the optimum alternative.

P.A.G. has the following characteristics:

- great compatibleness in water;
- reverse solubility in water;
- instability at 50-100°C

The property of reverse solubility in water is interesting in cooling pieces because P.A.G. is soluble in cold water and insoluble in warm water meaning that when the hot piece immerse the glycol separates from water and surrounds the piece modifying cooling in high temperatures (also film boiling).

PAG solutions do not have the same good cooling properties as oil and in order to improve them it is added different modifiers.

5% PAG solutions in water have been modified by adding 16% Na_2SiO_4 and $CaCO_3$ (5%, 10%, 15%) to increase cooling rate on temperatures ranges 700-300^oC (as an effect of $CaCO_3$) and also to decrease the cooling rates on the temperature range 300-100^oC (as an effect of Na_2SiO_4).

It was chosen $CaCO_3$ as a modifier of the hardening compound because it has the following properties:

- it dissolves in H_2O and weakly reacts with organic substances without degrading them;
- it improves the heat conductance;
- it raises boiling temperature of water so that the film boiling produces to a lower temperature;

The second modifier Na_2SiO_4 has the following desirable properties:

- it worsens the heat transfer between the medium and piece, in temperatures smaller than 300°C, which removes the danger of cracks appearance;
- it raises the boiling temperature of the compound;
- it raises viscosity.

3.Results

It was used a silver control cylinder for determining the cooling capacity of a medium. Inside the control cylinder was assembled a chromel-alumel thermocouple which allows temperature measurement by a y-t recording apparatus. The test bar gets warm until the wanted temperature (800°C) and then cools in the analyzed medium. The silver test bar has the following sizes and characteristics:
Ø = 13 [mm], h = 28 [mm], S = 1408 [mm^2], m = 39.9 [g], ρ_{Ag} = 10.5 g/cm^3,
λ_{Ag} = 418.5 W/m-K

The installation used in experiments includes:

- electrical pipe; y-t recording apparatus; triangular signal generator; thermostat tube;

cooling tube; silver test bar with chromel-alumel thermocouple.

Figure 2. Experimental installation used for cooling curves determination

The test bar got warm in the pipe until 800°C and then conducted in P.A.G. barbotaged with air (p=2atm.) medium solution, the cooling curve recorded by "y-t recording apparatus".

The cooling intensity is a parameter which gives us information about the used area of the cooling mediums. It represents a global parameter.
For calculation it was used the global coefficient of heat transfer:

$$\alpha_g = \frac{\alpha_1 \cdot \Delta t_1 + ... + \alpha_8 \cdot \Delta t_8}{t_{total}} \quad (1)$$

$$\alpha_i = \frac{3600 \cdot m \cdot c}{\Delta t_u \cdot S} \cdot \ln \frac{T_i - T_0}{T_f - T_0} [W/m^2K] \quad (2)$$

Where :

m = 0.0399 [kg] test bar weight;
c = 0.056 [Kcal/kg·grad] heat capacity at silver;
S = 0.0014408 [m^2] test bar surface;

Δt[s] time ranger;
Ti, T_f [ºC] the initial and final temperature range;
T_0 the medium temperature;

Cooling intensity $H = \frac{\alpha_g}{2\lambda}[m^{-1}]$ (3)

Table 1

Cooling intensity variation H for solution PAG modified with Na_2SiO_4 16% and $CaCO_3$(0,5;10)% barbotaged with air (p=2atm.)		
Medium temperature	% $CaCO_3$	H
20,000	0,00	1,024
30,000	0,00	0,999
40,000	0,00	0,928
50,000	0,00	0,827
20,000	5,00	0,999
30,000	5,00	1,016
40,000	5,00	0,918
50,000	5,00	0,889
20,000	10,00	1,024
30,000	10,00	0,846
40,000	10,00	0,866
50,000	10,00	0,938

Table 2

Cooling intensity variation H for solution PAG modified with Na_2SiO_4 16% and $CaCO_3$(0,5;10)% non-barbotaged		
Medium temperature	% $CaCO_3$	H
20,000	0,00	0,941
30,000	0,00	0,796
40,000	0,00	0,838
50,000	0,00	0,701
20,000	5,00	0,955
30,000	5,00	0,777
40,000	5,00	0,866
50,000	5,00	0,782
20,000	10,00	0,905
30,000	10,00	0,843
40,000	10,00	0,889
50,000	10,00	0,772

The results were put in tables and then there were made spatial graphs.

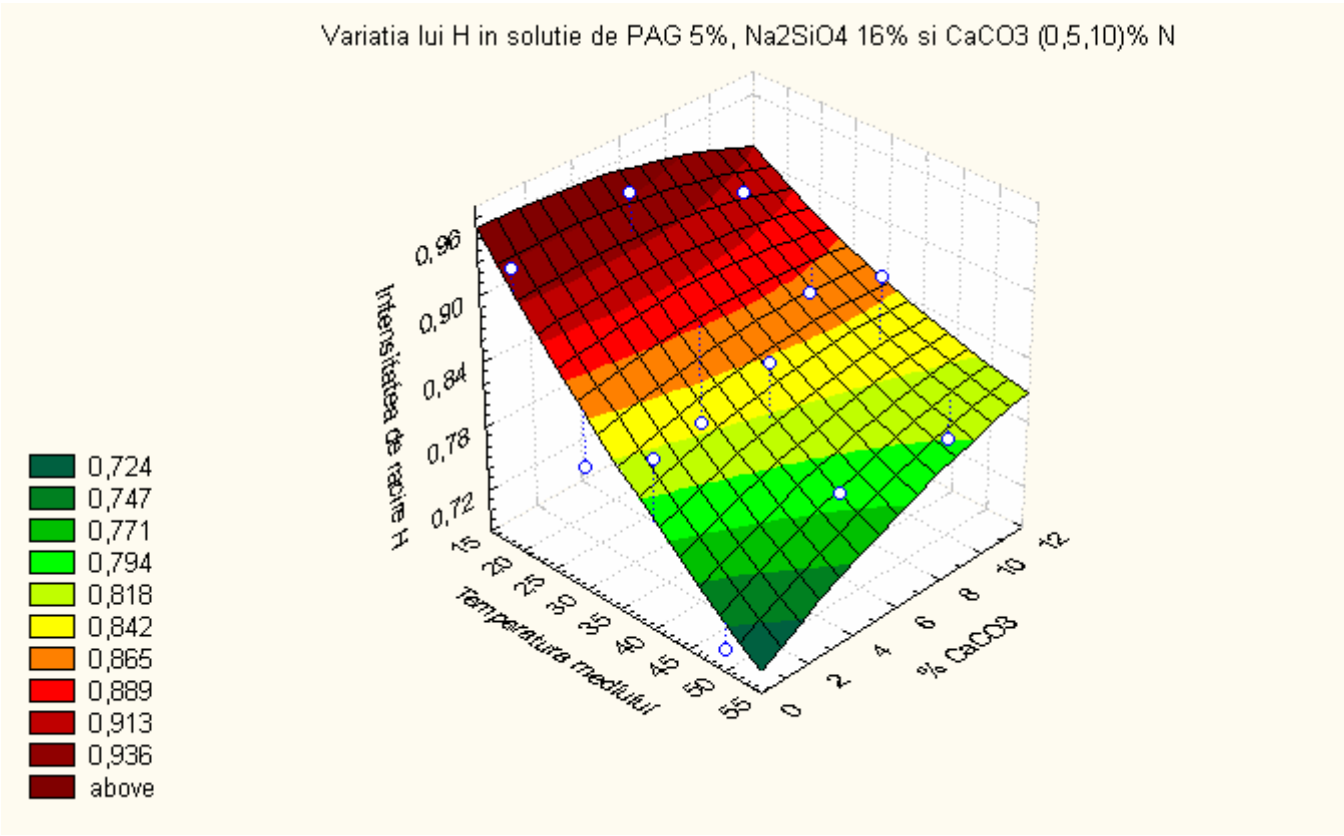

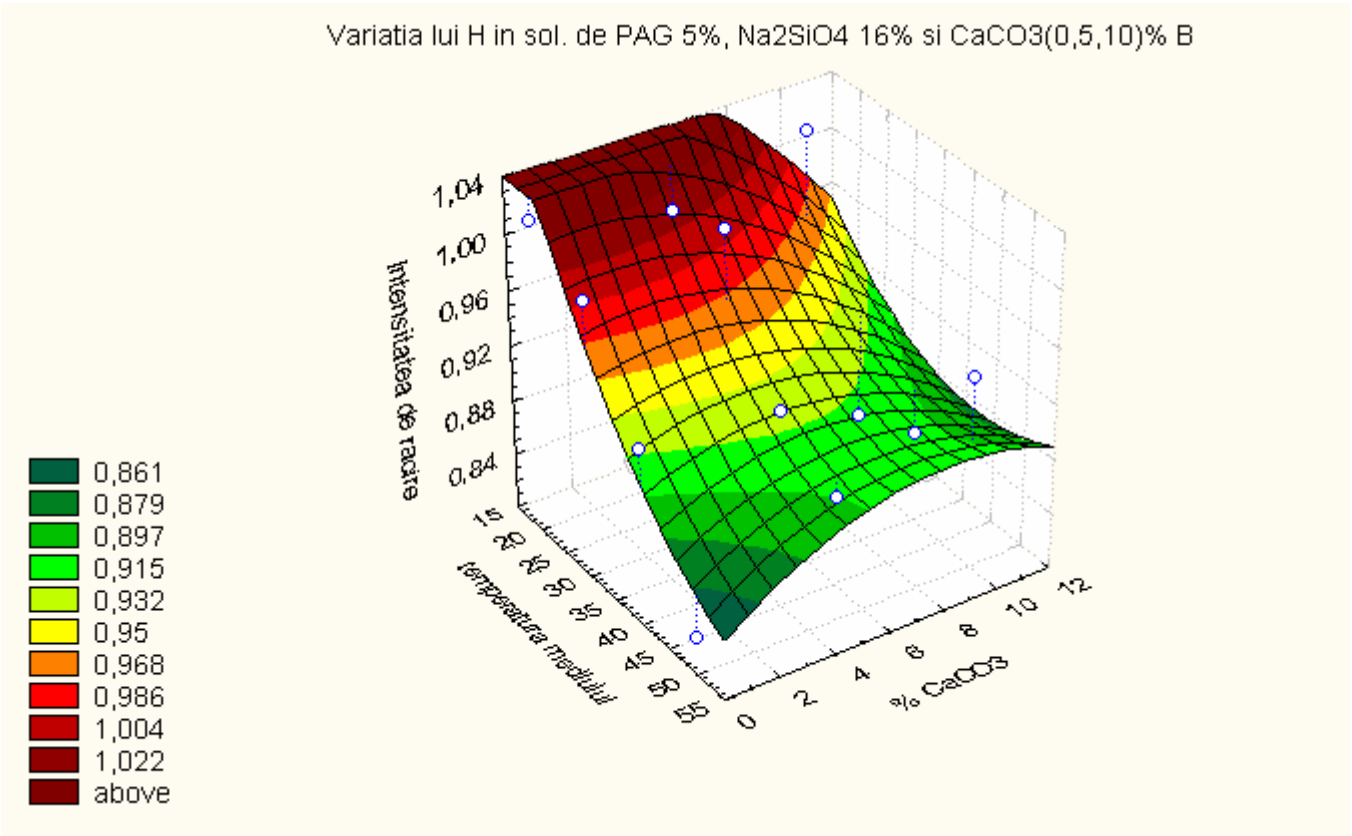

4.Conclusions

1.It can be noticed from the above tables that cooling intensity H is smaller at 50°C and bigger at 20°C both in calm and barbotaged medium.

2.It can be noticed by consulting graphs that PAG solution 5 % with modifiers has the cooling intensity bigger at barbotaged medium (1,024 [m^{-1}]) at 20°C and smaller at non-barbotaged mediums (0,7 [m^{-1}]) at 50°C.

5.References

1. I.Hopulele, G. D. Galuşcă, I. Alexandru - Tratamente termice şi termochimice, vol. I şi II, Rotaprint Iaşi, 1983

2. R. Dudau - Medii de răcire pentru călire, referat pentru pregătirea la doctorat

Received March 15, 2007

Technical University Iasi

CERCETĂRI PRIVIND VARIAȚIA INTENSITĂȚII DE RĂCIRE A MEDIILOR SINTETICE TIP POLIALCHILENGLICOL (PAG) 5% SOLUȚIE ÎN APĂ MODIFICATE PRIN ADĂUGAREA 16% Na_2SiO_4 AND $CaCO_3$ (5%, 10%, 15%)

(Rezumat)

Lucrarea prezintă cercetări experimentale asupra capacității de răcire a mediilor de răcire sintetice tip PAG 5% dizolvat în apă cu modificatori $CaCO_3$ (5%, 10%,15%) şi $NaSO_4$(16%). Experimentele au fost realizate folosind o epruvetă cilindrică din argint în centrul căreia a fost montat un termocuplu cromel-alumel conectat la un inscriptor y-t.

Măsurătorile s-au realizat pe medii barbotatecu aerla presiunea de 2 atmosfere şi nebarbotate variind temperatura inițială (20°C, 30°C, 40°C, 50°C) iar rezultatele au fost tabelate şi s-a calculat intensitatea de răcire în fiecare din cazuri. În final au fost trasate două grafice spațiale de variație a intensității de răcire funcție de temperatura inițială şi concentrația în $CaCO_3$ a soluției.

BULETINUL INSTITUTULUI POLITEHNIC DIN IAŞI
Tomul LIII (LVII), Fasc. 2, 2007
Secția
ŞTIINȚA ŞI INGINERIA MATERIALELOR

ON QUANTUM MECHANICS NAVIER – STOKES ANALOGUE AND SOME OF ITS APPLICATIONS

BY

VASILE BULANCEA AND MARCEL AGOP

Abstract: *By using the hydrodynamic model of the quantum mechanics, the Navier- Stokes analogue of this mechanics is developed. It has been found that, at a nanometer scale, there is as a datum, a tensor of the induced voltages of the quantum potential.*

Keywords*: Cryogenic treatment, Navier- Stokes analogue, mathematical model, tensions' tensor, conservation of energy****.***

1. Introduction

The Bohm formulation represents the probability distribution of a particle as a classic fluid (in the sense of an ensemble of particles) which moves both in the classical external field, and in its own field, Φ_B, known as the Bohm potential [1].

$$\Phi_B = -\frac{h^2}{4m}\left[\frac{\nabla^2\rho}{\rho} - \frac{1}{2}\left(\frac{\nabla\rho}{\rho}\right)^2\right] \tag{1}$$

where h is Plank's reduced constant, and m is the rest mass of the test particle.

Now, by means of the Schrödinger's equations, the equations of motions are:

$$\begin{cases} \left(\dot{\rho}\right) + \nabla\left(\frac{\rho\nabla S}{m}\right) = 0 \\ \frac{\partial S}{\partial t} + \frac{(\nabla S)^2}{2m} + \Phi_B + V(x) = 0 \end{cases} \tag{2}$$

or, for $\vec{\vee} = \frac{\nabla S}{m}$

$$\dot{\rho} + \nabla\left(\rho\vec{\vee}\right) = 0 \tag{3}$$

$$m\frac{d\vec{\vee}}{dt} = m\frac{\partial\vec{\vee}}{\partial t} + m(\vec{\vee}\cdot\nabla)\vec{\vee} = -\nabla(\Phi_B + V) \tag{4}$$

with V the classical external potential.

The parameter Φ_B appears as the kinetic energy of the Schrödinger's theory. By applying the "virial theorem" and of the statistic mechanics, the last ones suggest that Φ_B must be treated rather as a term of the kinetic equation than of the potential one. Our purpose is to show that this can be done by replacing Φ_B with a stress tensor due to viscosity (see the analogy with fluid mechanics, [2- 5]).

2. Mathematical model

We define a symmetrical tensor σ by:

$$\sigma_{ij} = \frac{h^2}{4m}\rho\nabla_{ij}\nabla_j \ln\rho = \frac{h^2}{4m}\left[\nabla_i\nabla_j\rho - (\nabla_i\rho)(\nabla_j\rho)/\rho\right] \tag{5}$$

The divergence of this tensor equals the force density associated with Φ_B,

$$\nabla\sigma = -\rho\nabla\Phi_B \tag{6}$$

Therefore σ identifies itself with the tensor of viscosity stress of the Navier- Stokes equation [2-5]:

$$m\frac{d\vec{\vee}}{dt} = \nabla\sigma - \rho\nabla V \tag{7}$$

The density of the momentum flux is:

$$\pi_{ij} = m\rho\vee_i\vee_j - \sigma_{ij} \tag{8}$$

and it satisfies the equation of the impulse current:

$$m\frac{\partial\left(\rho\vec{\vee}\right)}{\partial t} = -\nabla\pi - \rho\nabla V \tag{9}$$

In order to complete the analogy with the classical fluid mechanics [5], we introduce a "kinematical quasi-speed"

$$\vec{u} = \frac{h}{2m}\nabla\ln\rho \tag{10}$$

as well as the kinematical and dynamic viscosities [6]:

$$\vee = \frac{1}{4mh},\ \eta = \frac{1}{4}h\rho \tag{11}$$

The Reynold's number associated with $\vec{u}$ gives us a form of the uncertainty principle

$$R = \frac{\Delta x|u|}{\vee} = \frac{4m\Delta x|u|}{h}$$

because we do not expect analytical solutions for R≤2 (for details see [7]).
The tensions' tensor has now the well-known form:

$$\sigma_{ij} = \eta\left(\frac{\partial u_i}{\partial x_j} + \frac{\partial u_j}{\partial x_i}\right) \tag{12}$$

The kinematical quasi-speed $\vec{u}$ does not represent the real mechanical motion, but it contributes to the momentum transfer and energy concentration. This can be clearly seen from the absence of $\vec{u}$ in the continuity equation:

$$\dot{\rho} + \nabla\left(\rho\vec{\vee}\right) = 0$$

and from the role played by the variational principle, which can be written for the energy states as:

$$\frac{\partial E}{\partial S} = 0, \quad \frac{\partial E}{\partial \rho} = 0 \tag{13}$$

$$E = \int \rho\left(\frac{(\nabla S)^2}{2m} + \frac{h}{8m}\left(\frac{\nabla\rho}{\rho}\right)^2 + V\right)dx = \int \rho\left(\frac{m\vec{\vee}^{\,2}}{2} + \frac{m\vec{u}^{\,2}}{2} + V\right)dx = \int\left[\frac{1}{2}Tr\pi + \rho V\right]dx \tag{14}$$

3. Conclusions

Any interpretation of σ in hidden variables needs to take note of the "self" or internal nature of the momentum transfer. When stored in the form of mass motion and potential energy (like in the classical case), part of it has still another origin and only the total energy is conserved. Only the conservation of energy and momentum ensures the reversibility and existence of the proper states, but this denies a form of Brownian motion for the interaction with the external medium. Moreover, the existence of such a tensor implies at a nanometer scale, an additional tension (stress?) as compared to the usual ones (thermodynamic tensions etc), as in the case of cryogenic treatments applied to metals and metallic alloys [8, 9].

Received April 30, 2007

The "Gh. Asachi" Technical University of Iasi,

References

[1]. Ţiţeica, Şerban, Mecanica cuantică, Ed. Academiei, Bucureşti, 1983.
[2]. Amenzade, Yu.,A., Theory of Elasticity, Moscow, 1979.
[3]. Beju, I.,Soos,E., Teodorescu, P.,P., Tehnici de calcul apinorial şi tensorial neecludian cu aplicaţii. Ed. Tehnică, Bucureşti, 1979.
[4]. Teodorescu, P.,P., Ilie, V., Teoria elasticităţii şi introducere în mecanica solidelor deformabile, Ed. Dacia, Cluj-Napoca, 1976.
[5]. Landau, L.,D.,Lifshitz, E.,M., Mecanique des fluids, Moscou, 1967.
[6]. Harvey, R.,J., Physical Revue, vol.152, 1966, p.1115.
[7]. Keashaw, D., Physical Revue, vol.136, 1964, p. 1850.
[8]. Alexandru, I., Bulancea, V., Handbook of Residual Stresses and Deformation of Steel. *Effect of Cryogenic Cooling on Residual Stresses, Structure and Substructure* – Ed. by G. Totten, M. Howes, T. Inoue, ASM International®, March 2002.
[9]. Meng, F., Tagashira, K., Azuma, R., Sohma, H., Role of Eta-carbide Precipitations in the Wear Resistance Improvements of Fe-12Cr-Mo-V-1,4C Tool Steel by Cryogenic Treatment, ISIJ Intl., Vol.34, (1994), No.2, p.205-210.

ASUPRA ANALOGULUI NAVIER – STOKES AL MECANICII CUANTICE ŞI CÂTEVA DIN IMPLICAŢIILE SALE

(Rezumat)

Beneficiile obţinute de tratamentul criogenic la temperaturi până la -180^{0}C pot fi explicate şi prin apariţia unui tensor la scară nanometrică ca o tensiune suplimentară faţă de cele clasice. Utilizând modelul hidrodinamic al mecanicii cuantice se poate construi analogul Navier-Stokes acestei mecanici. Astfel s-a determinat că la scară nanometrică există, ca un datum, un tensor al tensiunilor indus de potenţialul cuantic.

BULETINUL INSTITUTULUI POLITEHNIC DIN IAŞI
Tomul LIII (LVII), Fasc. 2, 2007
Secția
ŞTIINȚA ŞI INGINERIA MATERIALELOR

DURABILITY EVALUATION FOR CRYOGENICALLY TREATED BEARINGS

BY

VASILE BULANCEA, DORIN CONDURACHE, OCTAVIAN LUPESCU, FLORIN TUDOSE-SANDU VILLE

Abstract. *The thermal treatment under 0^0C decreases the quantity of residual austenite and has a drastic influence on reliability of bearing elements too.*

Keywords*: Cryogenic treatment, reliability, durability test, Weibull's model.*

A. Bearings' reliability - basic aspects

The ball test of bearings is governed by the company standard SF 28103-2001 with the view to estimate the bearings' reliability.

For the most accurate estimation of the bearings' durability, the interactive influence of the parameters given in Figure 1 has to be taken into account.

By analyzing the interdependence of the parameters presented in Figure 1, one can notice the importance of the material on the bearing durability, as well as the multitude of factors that co-operate in the material quality.

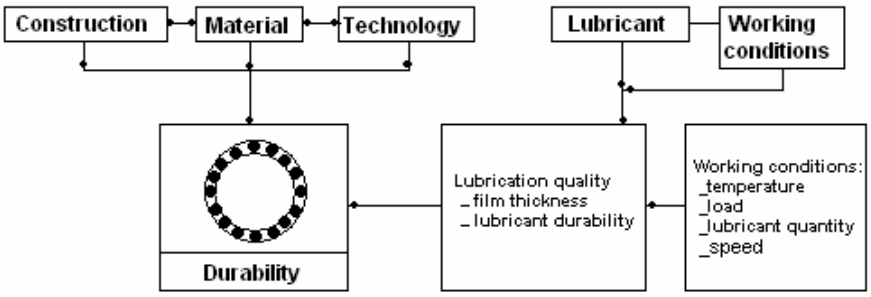

Figure 1. The parameters that influence the bearings durability.

The bearing reliability has a special importance in the intensive exploitation of the machines and installations. This aspect has led to the computation determination of the bearings estimative durability considering certain damaging probabilities.

A.1 The reliability function

It is quantitatively defined by the probability of faultless operation within the range of an imposed time period (t) and under given operating conditions.

The bearing reliability can be considered under the following specific aspects:

* the intrinsic reliability (F_i) – specific to bearing, is checked under laboratory conditions;

* the exploitation reliability (F_e) – determined for conditions specific to a given exploitation

* the operational reliability (F_o) – characterizes the ball utilization and its value is determined from the relationship:

$$F_0 = F_i \bigcap F_e$$

What is being determined (according to SF 28103-2001) is the intrinsic reliability (F_i), under laboratory conditions, on stands, at which the bearing operation duration is restricted by the contact fatigue endurance limit of one of its elements due to the occurrence of the pitting phenomenon.

Within the reliability studies applied to bearings, the following notations are consecrated for the parameters of the Weibull distribution function:

$$F(L, L_o, a, e) = 1 - \exp\left[-\left(\frac{L - L_0}{a}\right)^e\right] \text{ pentru } L \geq L, \quad (1)$$

where L denotes the durability expressed in millions of rotations or in working hours.

The durability indicators pursued while testing a lot of ball bearings on stands are the followings:

- L_{10} – the basic durability or the rated working duration for a 90% survival probability prior to the appearance of the material first contact fatigue signs (the pitting phenomenon) at one of the bearing elements.;

- L_{50} – the average durability or the survival probability of 50% of the bearings from the lot subjected to tests at a constant speed of rotation and load, prior to the appearance of the first signs of material contact fatigue signs at one of the bearing elements.

A.2 The durability test for bearings on the stand implies the existence of a mathematical model (Weibull's model, Lundberg's and Palmgren's model, ISO 77 model; SKF 83 model, SKF 89 model), the extraction volume (lot size) and the optimum test plan.

A.2.1 *The optimum mathematical model* for the study of the bearing reliability is *the Weibull's distribution function* (the theoretical distribution close to the empiric distribution obtained based on experimental data).

This distribution depends on three parameters, expressed as:

* Failure intensity
$$\lambda(t) = \frac{k}{\theta}\left(\frac{t-\gamma}{\theta}\right)^{k-1} \quad (2)$$

* Reliability function,
$$R_{(t)} = \exp\left[-\left(\frac{t-\gamma}{\theta}\right)^k\right]; \quad (3)$$

* Distribution function,
$$F_{(t)} = 1 - \exp\left[-\left(\frac{t-\gamma}{\theta}\right)^k\right]; \quad (4)$$

* Probability density,
$$F(t) = \frac{k}{t}\left(\frac{t-\gamma}{\theta}\right)^{k-1} \cdot \exp.\left[-\left(\frac{t-\gamma}{\theta}\right)^k\right] \quad (5)$$

where: t = bearing's working life (service life), (10^6 rots) or (hours)

k = the shape parameter in the Weibull distribution (Weibull slope);

θ = scale parameter in the Weibull distribution;

γ = localization parameter in the Weibull distribution,

and they satisfy the relationships: $k, \theta \in R^+$, $\gamma \in R$, $t \geq \gamma$, and $t < \gamma \Rightarrow F(t) = 0$.

The localization parameter γ has no influence on the dispersion condition, since it represents the minimum duration at which the failures may appear and permits the change or advance of the time origin.

By considering that $\gamma = 0$, the Weibull's distribution becomes bi-parametric.

In the reliability evaluation for bearings the both versions of the Weibull distribution (bi- and tri-parametric) are used, depending on the experimental values obtained in the corresponding test, as well as on the evolution in the corresponding sequence. The tri-parametric version is more exact.

A.2.2 *The volume n of the extraction* of elements subjected to experiments (the lot size). The optimum recommended extraction volume is n = 20 bearings.

One has considered r = the number of ball bearings deteriorated during the tests.

The bearings' tests may be complete and incomplete.

* Complete tests: $n = 20$; $r = 20$. $r/n = 20/20$- the tests are carried out until all the bearings fail.

* Incomplete (speedy) tests:

- *censored tests* at the level r, out of the n bearings subjected to tests

- *truncated tests*, at which the reliability tests stops after the lapse of a pre-established total duration t_r ;

- *sequential tests*, at which the decision to stop the tests may be taken at any moment, depending on the number of deteriorated bearings and the global tests duration.

The incomplete tests are also carried out at an initially pre-established regime.

A.2.3 *The test plan* recommended for the speedy tests is:

a**.** *r/n = 8/20,* or

b. r/n = 10/20.

A.3 *The composition of the bearings lot* for durability tests on stands is established as follows:

a. For the test plan 8/20, the lot size is of 30 bearings;

b. For the test plan 10/20, the lot size is 32 bearings;

c. For the test plan 20/20, the lot size is 42 bearings.

A.4 The methodology for bearings durability tests on a stand.

A.4.1 *Testing diagram*

The tests meant to evaluate the bearings durability uses the most common case of loading the rings with peripheral load on the inner ring and a local load on the outer ring.

The tests are carried out with the inner ring in rotation, and the load is applied on the outer steady one (Figure 2).

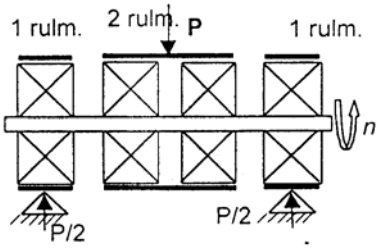

Figure 2. The loading diagram for durability measurements at radial ball/roller bearings.

A.4.2 *Test regimes*

In order to calculate the loads applied on the bearings subjected to reliability tests, the following value relationships are recommended:

a. radial ball bearings C/P= 3;

b. radial axial ball bearings and self-aligning bearings C/P= 5;

c. other ball and roller bearings: C/P= 4,

where C= the basic dynamic load, and P= the load applied on the bearing.

A.5 Reliability evaluation of the stand tested bearings lot

A.5.1 *Calculation of the real basic durability L_{10} and real median durability L_{50}*

In the case when the bi-parametric Weibull distribution is used:

$$L_{10} = \theta^{1/k}(0{,}10536)^{1/k}, \quad L_{50} = \theta^{1/k}(0{,}69315)^{1/k} \tag{6}$$

In the case of the tri-parametric Weibull distribution:

$$L_{10} = \theta^{1/k}(0{,}10536)^{1/k} + \gamma, \quad L_{10} = \theta^{1/k}(0{,}69315)^{1/k} + \gamma \tag{7}$$

The values of L_{h10} and L_{h50} expressed in hours, are calculated with the relations:

$$Lh_{10} = L_{10}\frac{10^6}{n \cdot 60}, \quad Lh_{50} = L_{50}\frac{10^6}{n \cdot 60}, \tag{8}$$

where n is the number of rotations per minute executed by the bearing.

A.5.2 *The calculation of L_{10} and L_{50} by the maximum verisimilitude method* is carried out starting from the results of bearing lot tests, which we arrange in an increasing order, taking into account only the first 8 worn out bearings: $t_1 \le t_2 \le \ldots..\le t_{r-8}\ldots..\le t_{n-20}$, or for tri-parametric form of Weibull function: $|t_1 - \gamma| \le |t_2 - \gamma| \le \ldots |t_{r=8} - \gamma| \le \ldots \le |t_{n=20} - \gamma|$ where we have:

t_1 = the time interval within which the i^{th} bearing is tested, since the test beginning till the appearance of the pitting phenomenon on one of the bearing parts; (i=1, 2, …r, …n).

n = the number of bearings at which the pitting phenomenon occurs while testing the n bearings of the lot. It is considered that r = 8.

γ = the localization parameter in the Weibull distribution.

With regard to the other 12 bearings of the lot that follow after the ordered sequence of the 8 bearings worn out due to the appearance of the contact fatigue phenomenon, we only know that they have realized durability of at least the value corresponding to the 8^{th} bearing; mathematically speaking, we know about the parameters t_i (i<r) that $t_i \ge t_r$ (t is generally the bearing operation life until the appearance of the pitting phenomenon).

Since the values of t_i ($\ge t_r$), therefore with i > r, were not considered in the calculus, we can consider them as being equal with the value of the 8^{th} ball and, as a rule, we are not aware of the reached value.

The Weibull distribution will be used in the bi/tri-parametric versions:

- if $t_s/t_1 \le 4.5$ the tri-parametric distribution is used;
- if $t_s/t_1 > 4.5$, the bi-parametric distribution is used.

B. Experimental evaluation of durability

The reliability (in the context of durability) of an individual bearing or a lot of apparently identical bearings that work under similar normal working conditions, represents the probability of its/their operation according to the pre-established parameters and specifications, such that the bearing/bearings reaches or exceeds the durability L_{calc} determined for the working conditions at which the bearing is subjected.

The durability tests are meant to determine the durability indicators necessary to establish the durability parameters distribution laws and to estimate the real values or the probable intervals which contain the real values.

The tests carried out by S.C. RULMENTI S.A. Barlad are of the laboratory type classified according to STAS R 12007/1-81.

B.1 The recommended test plan

Since at S.C. RULMENTI S.A. Barlad there is no free test stand, and the test intervals are very large, we chose the plan of incomplete (speedy) tests, *censored tests* respectively, at the level *r*, when the durability test is considered finished after the deterioration of a number *r*, out of the *n* elements subjected to tests.

The recommended plan for the speedy tests is: r/n = 8/20.

For the test plan r/n= 8/20, the lot size is of 30 bearings, such that each of the 8 bearings that get deteriorated by contact fatigue (revealing failure) could be replaced, at which 2 more bearings are added that might get out of service due to other independent causes of bearing operation (deviations from the technical execution conditions, disturbances/deviations in the stand operation, etc). These two bearings are excluded from the test results estimation.

B.2 Bearings preparation

The tests were carried out on two types of bearings produced at S.C. RULMENTI S.A. Barlad: annular ball bearings 6204 UG and cylindrical roller bearings NU 205 ES.

The 30 pieces lots for *r/n = 8/20* were constituted as follows:

A. Witness lots (classical thermal treatment): $\mathbf{A_1}$ – bearings 6205 UG; $\mathbf{A_2}$ – bearings NU205 ES.

B. Lots treated at -30^oC: $\mathbf{B_1}$ – bearings 6205UG; $\mathbf{B_2}$ – bearings NU205ES

C. Lots treated at -70^oC: $\mathbf{C_1}$ – bearings 6205UG; $\mathbf{C_2}$ – bearings NU205ES.

B.3 Bearing durability test stands

The test method is with the inner ring in rotation and the outer steady ring on which the load is applied.

B.4 Loading regimes

In order to calculate the loads applied to the bearings subjected to reliability tests, the following value relations are recommended:

a. annular ball bearings *C/P = 3*;
b. annular roller bearings *C/P = 10/3*.

where: **C** is the basic dynamic load, and **P** is the applied load.

During the durability stand test, the driving speed of the inner ring, i.e. of the roll carrying axle, should take values within the range $n = (0.4.....0.6)n_l$, where n_1 is the catalogue limit of the speed of rotation.

In the case when the indicated speeds of rotations can not be reached on the stand, one can adopt the maximum values permitted on the corresponding stand.

B.5 The calculus of theoretical durability

B.5.1 *Reference: bearing 6204 UG* (computation example)

Stand type: LBT 3000;

Beneficiary: URB- certification;

Computation basis: NIR 002- 77, RULMENTI S.A. Barlad
Project RELANSIN
Constructive diagram of the stand

Project data: C_r = 12.8 kN (dynamic capacity on a 6204 bearing)
n_{limit} = ball limit speed of rotation

Calculus of the necessary elements:

C_r = 12.8 daN
C_{rgroup} = Cr x i (i = 2 bearings r_n group)
C_{rgroup} = 1280 x 2 = 2560 daN

From the recommended C_r /P = 3, it follows that:

The necessary compression force (P from Figure 2):

P = C_r / 3 = 853 daN (drive is performed by direct transmission, with no lever, compression spring loading).

The speed of rotation n = (0.4...0.6) x n_{limit} = (0.4 …0.6) x 15000= (6000 …9000) rpm. One chooses n = 3100rpm (realizable on the stand).

Theoretical durability is: $L_{10} = 16666 \times (C/P)^3 / n$

$\underline{L_{10} = 16666 \times 3^3 / 3100 = 145 \text{ hours}}$

B.6 Computation card of real basic durability L_{10} and real durability L_{50} through the method of maximum verisimilitude (Simplified calculation method-calculus example).

6.1. **A1 lot** (bearing 6204 UG, classical thermal treatment)- witness lot.

After the stand tests of a lot of n= 20 bearings, 8 bearings resulted out of use due to the appearance of the pitting phenomenon, the following durability being realized:

$$T_i = (112, 145, 157, 177, 197, 266, 321, 358) \text{ hours.}$$

The parameters L_{10} and L_{50} of the Weibull distribution are calculated according to the following methodology:

1* . One calculate the ratio $t_8 / t_1 = 3.2 < 4.5$ therefore the tri-parametric Weibull distribution is used.

2* . The average durability value is calculated with the relation:

$$\hat{t} = \frac{\sum_{i=1}^{r} t_i + (n-r)t_8}{r} = 753{,}8.$$

3*. The value of the localization parameter $\hat{a}$ is calculated with the relation

$$\hat{a} = \frac{1}{n-1}\left(n \cdot t_1 - \hat{t}\right) = 78$$

4*. The Table 1 is drawn up for the computation of the specified relations:

Table 1

Nr.crt.	t_i	$t_i - \hat{a}$	$\lg(t_i - \hat{a})$	$(t_i - \hat{a})^{\hat{k}}$
1	112	34	1,53147	46,69
2	145	67	1,82607	97,81
3	158	80	1,90309	118,67
4	177	99	1,99563	149,70
5	197	119	2,07554	182,95
6	266	188	2,27415	301,18
7	321	243	2,38560	398,39
8	358	280	2,44715	464, 94
$\sum$	1734	-	16,4387	1760,33

5*. The form parameter $\hat{k}$ is calculated with the relation:

$$\hat{k} = \frac{0{,}428}{\lg\left(t_r - \hat{a}\right) - \frac{1}{r}\sum_{i=1}^{r}\lg\left(t_i - \hat{a}\right)} = 1{,}09;$$

6*. The form parameter $\hat{\theta}$ is calculated with the relation:

$$\hat{\theta} = \frac{1}{r}\left[\sum_{i=1}^{r}\left(t_i - \hat{a}\right)^{\hat{k}} + (n-r)\left(t_8 - \hat{a}\right)^{k}\right] = 917{,}4;$$

7*. The parameter $\hat{T}$ is calculated with the relation:

$$\hat{T} = \theta^{1/k} = 917{,}4^{1/1{,}09} = 522{,}3;$$

8* . The value of the real basic durability L_{10} is computed with the relation:

$$\hat{L}_{10} = \hat{a} + \hat{T}(-\ln 0{,}9)^{1/\hat{k}} = 144 \text{ hours;}$$

almost identical to the theoretical durability calculated based of the bearings dynamic capacity.

9* . The value of the median durability L_{50} is calculated with the relation:

$$\hat{L}_{50} = \hat{a} + \hat{T}(-\ln 0{,}5)^{1/\hat{k}} = 451 \text{ hours.}$$

Similarly, the values of the real basic durability L_{10} and median durability L_{50} are calculated for all the studied bearings lots (B1, C1, A2, B2, C2).

The durability values processed at item B.6 are concentrated in Table 2.

Table 2

Bearings	Thermal Treatment	Lot	L_{10}		L_{50}	
			[h]	[%]	[h]	[%]
6204 UG	TT- classical	A1- witness	144	100	451	100
	CT(- 30^{0}C)	B1	165	114,6	524	116,2
	CT(- 70^{0}C)	C1	193	134	608	134,8
NU205ES	TT- classical	A1- witness	3867	100	12528	100
	CT(- 30^{0}C)	B1	4478	115,8	14202	113,4
	CT(- 70^{0}C)	C1	5048	130,5	16243	129,6

*Note: TT- classical thermal treatment; CT- cryotreatment

By analyzing the Table 2 one can notice for the both bearings types, 6204 UG and NU205ES, that the durability of the bearings lots treated at negative temperatures of -30^{o}C and -70^{o}C, increases as follows:

* For the 6204 UG bearings:
- at the version B1 (-30^{o}C) L_{10} increases by 14.6%
  L_{50} increases by 16.2%
- at the version C1 (-70^{o}C) L_{10} increases by 34%
  L_{50} increases by 34.8%

* For the NU 205 ES bearings:
- at the version B2 (-30^{o}C) L_{10} increases by 15.8%
  L_{50} increases by 13.4%
- at the version C2 (-70^{o}C) L_{10} increases by 29.6%

The durability variation with the cooling temperature during quenching is presented in Figure 3.

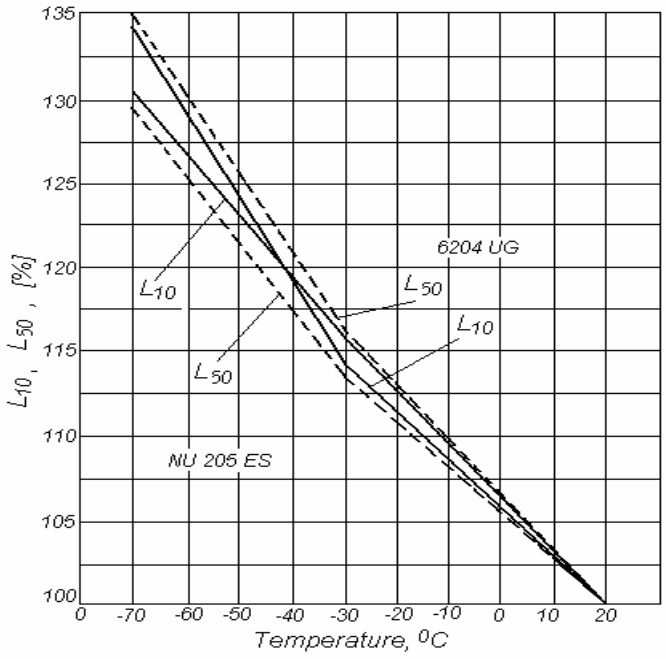

Figure 3. The durability variation with the cooling temperature.

C. Conclusions

For the durability analysis one has chosen as aleatory variable the time interval until the revealing bearing failure, with a Weibull type distribution.

The Weibull distribution parameters were determined taking into account the method of the estimates theory that permits to determine the parameters numerical value. For a good approximation the maximum verisimilitude method was used.

The contact fatigue resistance was considered as a deteriorating factor for wearing the bearings out.

The appearance of the contact fatigue by pitting is signaled by the modification of the bearings noise (heard with an amplifying rod or of the vibrations recorded at the speedometer).

The thermal treatment using the cooling within the negative temperature range increases the bearings durability.

The durability increase ranged between 14.6% and 34% for L_{10} and between 13.4% and 34.8% for L_{50}.

The durability increase minimum values were obtained after a cooling treatment down to -30^{o}C, while the maximum ones were obtained after a cooling treatment down to -70^{o}C.

The durability increases is accounted for by the decreasing residual austenite amount from 10…15% to 6…8% for the highest frequency of residual austenite appearance.

The decrease of the residual austenite amount has as an effect the dimensional stabilization of the bearings references and later the occurrence of the contact fatigue by pitting.

At the same time, the increase of the durability of the bearings treated at temperatures below 0^{o}C has to be due to the carbides finishing and the density increase of small sized carbides (< 1μm).

Received April 11, 2007

The "Gh. Asachi" Technical University of Iasi,

References

/1/. Ioan.Alexandru, Vasile.Bulancea, Handbook of Residual Stresses and Deformation of Steel. *Effect of Cryogenic Cooling on Residual Stresses, Structure and Substructure* – Ed. by G. Totten, M. Howes, T. Inoue, ASM International®, March 2002.

/2/ Jeff Gary, *A Review of Deep – Cryogenic Treatment of Steel*, University of Texas at Austin, Department of Mechanical Engineering, Spring, 1999.

/3/ Earl A. Carlson, *Cold Treating and Cryogenic Treatment of Steel*, ASM Handbook, vol.4, Heat Treating, 1991.

EVALUAREA DURABILITATII RULMENTILOR TRATATI TERMIC CRIOGENIC

(Rezumat)

În construcţia rulmenţilor un rol important îl are durabilitatea şi nivelul de zgomot. Aceste proprietăţi se pot obţine printr-o bună stabilitate dimensională. Diversele soluţii de tratament termic clasic şi criogenic aplicate elementelor de rulmenţi au scos în evidenţă oportunitatea aplicării tratamentelor criogenice la –90 ... –60^{0}C care realizează bune stabilităţi dimensionale cu efecte benefice în creşterea durabilităţii rulmenţilor.

BULETINUL INSTITUTULUI POLITEHNIC DIN IAŞI
Tomul LIII (LVII), Fasc. 2, 2007
Secţia
ŞTIINŢA ŞI INGINERIA MATERIALELOR

STUDY AND DETERMINATION OF THE ELECTRIC RESISTIVITY, OF THE COEFFICIENT OF VARIATION OF THE ELECTRIC RESISTIVITY AND OF THE ELASTIC MODULUS FOR THE BIMETALLIC BUSHINGS FOR AUTOMOBILES

CORĂBIERU ANIŞOARA, CORĂBIERU PETRICĂ, VELICU ŞTEFAN, VASILESCU DAN

Abstract

The electric resistivity of the bimetallic materials is a size influenced by the structural modifications that appear in the heating process. Into the framework of the experiments, determinations of the electric resistivity were effected, depending on the temperature for the interval of 20÷350 ^oC with a heating speed of 200 $^oC/h$. The variation of the electric resistivity with the temperature for the samples taken of the bimetallic bushings for automobiles made of steel-bronze have revealed the relation between this variation and the precipitation from the deposited bronze layer.

Keywords: *bimetallic bushings for automobiles*

1. Introduction

In general, the electric resistivity is a size influenced by the structural modifications that appear at heating. Into the framework of the experiments, determinations of the electric resistivity were effected, depending on the electric resistivity for the interval 20-350^{o}C with a heating speed of 200^{o}C/h. The determinations have been made on the device shown in the figure No.1, designed and manufactured in SC Presum Proiect SA Iaşi.

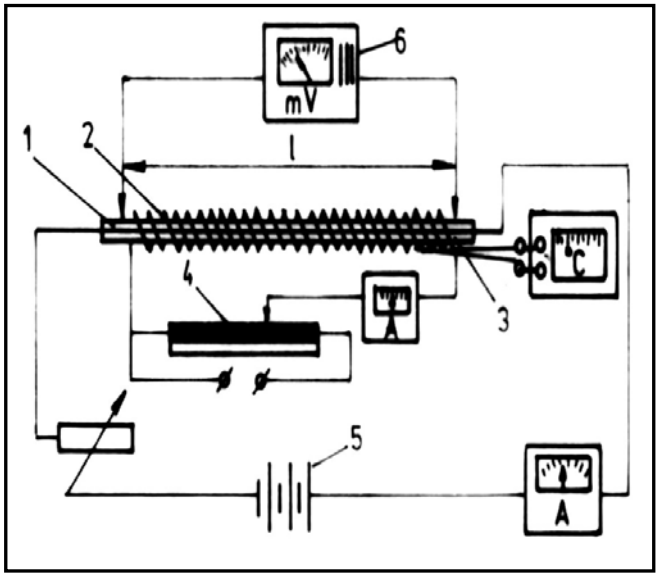

Fig.1 Sketch of the device for the study of the variation of the electric resistivity of the carbon steel -bronze bimetallic bushings for the cars, depending on the temperature
1 – carbon steel-bronze bimetallic sample (length = 100 mm; thickness = 3 mm; width b = 3,5 mm); 2 – electric resistance for heating in the air of the bimetallic sample; 3 – thermocouple NiCr-Ni; 4 – auto-transformer; 5 – direct current source (I = 0,5A, U = 9V); 6 – mili-voltmeter for the measurement of the electric tension on the bimetallic sample

2. Experiments in the laboratory

The specific resistivity has been calculated with the formula:

$$\rho = \frac{\Delta U}{I}\frac{S}{l} \qquad [\mu\Omega m] \qquad (1)$$

where: ρ – electric resistivity, μΩm; ΔU – electric tension indicated by the mili-voltmeter, mV; I – current intensity = 0,5A; S – cross section of the bimetallic sample = thick x b= 3x 3,5= 10,5 mm^2; l – length of the bimetallic sample = 100 mm.

Replacing the data in the formula (1), we obtain:

$$\rho = \frac{\Delta U}{0,5}\frac{10,5}{100} = 0,21 \cdot \Delta U \qquad [\mu\Omega m] \qquad (2)$$

In the table 1 and fig. 2 are shown the values of the determinations obtained in the experiments in the laboratory are shown.

Table 1. Electric resistivity ρ of the samples taken from the bimetallic bushings for automobiles, depending on the temperature

Crr Nr.	Type of the bimetallic bushings for automobile	Temperature, °C	Electric tension ΔU, MV	Electric resistivity $\rho = 0,21 \cdot \Delta U$, μΩm
1	OLT 35-CuSn10	20	1,2	0,25
		100	1,45	0,31
		200	1,75	0,37
		300	1,85	0,39
		350	1,55	0,33
2	OLT 35 CuAl9T	20	1,05	0,22
		100	1,30	0,27
		200	1,55	0,33
		300	1,35	0,28
		350	1,10	0,23
3	OLT 35 CuSn4Zn4Pb17	20	1,40	0,29
		100	1,55	0,33
		200	1,85	0,39
		300	1,95	0,41
		350	1,55	0,33

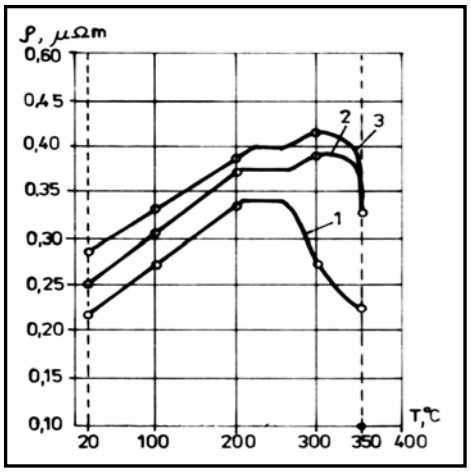

Fig.2. Variation of the electric resistivity with the temperature for the samples taken from the experimented bimetallic bushings for cars.
1 – OLT 35 –CuAl9T; 2 - OLT 35-CuSn10; 3 - OLT 35-CuSn4Zn4Pb17.

Studying the data presented in the table 1 and fig. 2, we can spotlight the following aspects:

- The variation of the electric resistivity is more marked in the case of the bimetallic bushings OLT35-CuSn10 and OLT 35-CuSn4Zn4Pb17 by respect to OLT 35 – CuAl9T, due to the higher contents of Sn and Pb (elements with higher resistivity than Al);
- The study of the resistivity of the car's bimetallic bushings with the temperature, has spotlighted the existence of 2 phenomenon:
  - the increase of the resistivity with the temperature: $\rho_T = \rho_o(1+ \alpha\Delta T)$;
  - the decrease of the resistivity on certain intervals of temperature due to the phenomenon of precipitation from the deposited layer;
- For the bimetal OLT35-CuAl9T the precipitation in the deposited bronze layer started at 200°C takes place with a constant intensity up to 250°C and after that the intensity increases up to 350°C (maximum intensity in the interval 250-350°C when a new compound precipitates with maximum intensity);
- For the bimetal OLT35-CuSn10 the precipitation phenomenon started at 200°C is continued up to 250°C, and after that it decreases and the resistivity increases again straight up to 300°C. After 300°C precipitation phenomenon appear again, producing the decrease of the resistivity;
- For the bimetal OLT35-CuSn4Zn4Pb17, the resistivity increases straight up to 200°C; between 200-250°C precipitation phenomenon appear, that maintain constant the resistivity; between 250-300°C, the resistivity increases straight again with the temperature, while after 300°C the precipitation with big intensity create a pronounced decrease of the resistivity;
- Up to 200°C the resistivity increases straight with the temperature for all studied bimetallic bushings, this way being possible to determine the coefficient of variation of the resistivity with the temperature:

$\rho_T = \rho_o(1+ \alpha\Delta T)$ and as per the data of the table 1 we have:

OLT35-CuAl9T $\rho_{20} = 0,22$ $\rho_{100} = \rho_{20}[1+\alpha(100-20)]$

$\rho_{100} = 0,27 \rightarrow \rho_{200} = \rho_{20}[1+\alpha(200-20)] \rightarrow$

$\rho_{200} = 0,33$

$0,27=0,22(1+80\alpha) \rightarrow \alpha = 2,84\cdot10^{-3}$

$0,33=0,22(1+180\alpha) \rightarrow \alpha = 2,77\cdot10^{-3}$

$\rightarrow \alpha = 2,8\cdot10^{-3}\ ^{o}C^{-1}$

3. Determination of the coefficient of variation of the electric resistivity with the temperature and of the elasticity modulus

In the table 2 the values determined experimentally of the coefficient of variation with the temperature of the electric resistivity for the interval 20-200^{o}C are presented.

Table 2. Coefficient of variation of the electric resistivity with the temperature determined into the framework of the laboratory experiments

Cr. Nr	Type of the bimetallic bushing	Electric resistivity ρ_{20}, Ωm	Electric resistivity ρ_{100}, μΩm	Electric resistivity ρ_{200}, Ωm	Average coefficient of variation of the electric resistivity with the temperature α, $^{o}C^{-1}$
1	OLT35-CuSn10	0,22	0,27	0,33	$2,85\cdot10^{-3}$
2	OLT35-CuAl9T	0,25	0,31	0,37	$2,8\cdot10^{-3}$
3	OLT35-CuSn4Zn4Pb17	0,29	0,33	0,39	$1,8\cdot10^{-3}$

Into the framework of the experiments, the elasticity modulus of the experimented bimetallic bushings was also determined, using the device of fig.3., designed and achieved in SC Presum Proiect SA Iaşi.

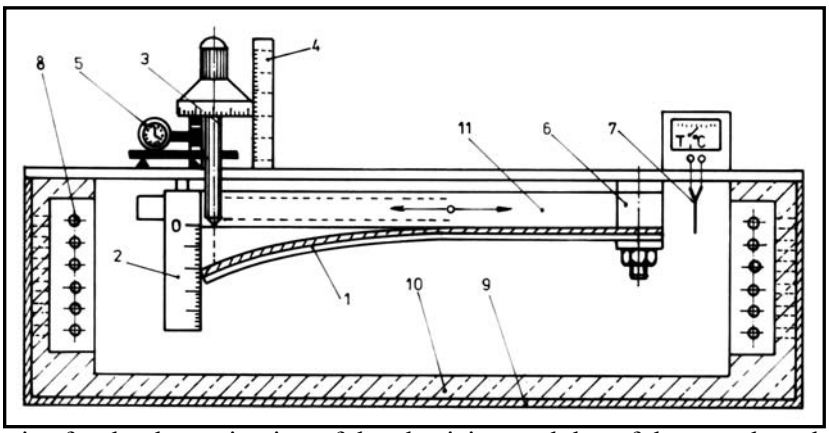

Fig.3. Device for the determination of the elasticity modulus of the samples taken from the bimetallic carbon steel -bronze bushings

1 – bimetallic sample; 2 – ruler; 3 – micrometric device with tightening screw; 4 – ruler with nomogram; 5 – portable compression dynamometer; 6 – building in device; 7 – thermocouple NiCr-Ni; 8 - electric resistances (silite bars); 9 – device precincts; 10 – thermo-insulating material; 11 – sliding rod of the building in device (depending on the length of the bimetallic sample).

Acting with the force F, through the device 3, on the free end of the built in metallic sample (Length=100mm, thickness =3mm =1,5 mm MB+1,5mm SD, width b=3,5 mm) the f arrow is measured, that is produced under the action of F force.

Elasticity modulus E will be given by the formula:

$$E = \frac{4l^3 \cdot F}{bg^3 f} \quad [\text{N/mm}^2] \quad (3)$$

where: E – elasticity modulus of the bimetallic sample, N/mm^2; F – the force applied at the free end = 10N; l – length of the bimetallic sample = 100 mm; b – width of the bimetallic sample = 3,5 mm; g – thickness of the bimetallic sample = 3 mm; f – arrow measured at the free end, mm.

$$E = \frac{4 \cdot 100^3 \cdot 10}{3{,}5 \cdot 3^3 f} = \frac{4{,}23}{f} \cdot 10^5 \quad \text{N/mm}^2$$

In the table 3 are presented the results obtained experimentally with a view to determination the elasticity modulus E for the samples taken from the bimetallic bushings that have shown a proper specific adherence.

Table 3. Elasticity modulus of the bimetallic samples determined into the framework of the experiments

Cr Nr	Type of the bimetallic bushing	Bimetallic sample taken					Action force F N	Free end arrow f mm	Elasticity modulus $E=\frac{4{,}23}{f}\cdot 10^5$ N/mm^2
		L mm	Thick .MB mm	Thick .SD mm	Thick. mm	Widt b mm			
1	OLT35-CuSn10	100	1,5	1,5	3	3,5	10	2,7	$1{,}56\cdot 10^5$
2	OLT35-CuAl9T	100	1,5	1,5	3	3,5	10	2,5	$1{,}69\cdot 10^5$
3	OLT35-CuSn4Zn4Pb17	100	1,5	1,5	3	3,5	10	2,7	$1{,}56\cdot 10^5$

In conformity with those presented in the table 3, the bimetal OLT35-CuAl9T had the highest elasticity modulus ($1{,}69\cdot 10^5$ N/mm^2).

4. Conclusions

- The variation of the electric resistivity is more pronounced in the case of bimetallic bushings whose deposited bronze layer contains chemical elements with high electric resistivity;
- The decrease of the electric resistivity on certain temperature intervals is due to the phenomenon of precipitation of the chemical compounds, which is more accentuated in the case of the bronzes based on aluminium;
- Up to 200^{o}C the electric resistivity increases linearly with the temperature independently on the chemical composition of the deposited bronze. Above this temperature, the differences are more accentuated due to the variation of the intensity of the precipitation phenomenon of the constitutive elements of the bronze grades, specially Al, Sn, Zn şi Pb.

REFERENCES

1.**Corăbieru A., Corăbieru P., Vrabie I., Toma D., Teodorescu V.** – Actual tendencies of the industry of cars metallic components – National Conference „Excellence Research – Favourable Premise for the development of the Romanian research space", Vol.II, pag. L3-12, Braşov 2006, ISBN (10) 973-718-552-8, ISBN (10) 973-718-554-4, ISBN (13) 978-973-718-552-5, ISBN (13) 978-973-718-554-9

2.**Corăbieru P., Predescu C., Velicu S., Corăbieru A., Vasilescu D.D.** – Researches concerning the influence of joining temperature on the bimetal layer – The 7th International Conference of Technology and Quality for Sustained Development, May 25-27, 2006, Bucharest, România – organised by Polytechnic University of Bucharest in co-operation with Politecnica di Milano, Italy and De Montfort University United Kingdom, Proceedings TQSD06, p. 139-144, ISBN 973-720-035-7, AGIR Publishing House.

3.**Corăbieru A., Corăbieru P**.,– Harmonisation of the manufacture technologies of the automobiles metallic parts with the environment European directive requirements, dir. 2000/53/CE– Machines Building Magazine – New Series Innovative Technology, 58/2006-nr.3-4, pag.23-25, Bucharest, ISSN 0573-7419

Received March 15, 2007

SC PRESUM PROIECT SA Iasi, Calea Chisinaului 32
Univ. Politehnica Bucuresti, Splaiul Independenței, nr. 313
SC Procom Iasi, Strada Canta 14

ANALIZA ŞI DETERMINAREA REZISTIVITĂȚII ELECTRICE, A COEFICIENTULUI DE VARIAȚIE A REZISTIVITĂȚII ELECTRICE ŞI A MODULULUI DE ELASTICITATE PENTRU BUCŞELE AUTO BIMETALICE

Abstract

Rezistivitatea electrică a materialelor bimetalice este o mărime influențată de modificările structurale care apar la încălzire. În cadrul experimentărilor s-au efectuat determinări ale rezistivității electrice în funcție de temperatură pentru intervalul 20÷350 ^{o}C cu o viteză de încălzire de 200 ^{o}C/h. Variația rezistivității electrice cu temperatura, pentru probele prelevate din bucşele auto bimetalice oțel-bronz au pus în evidență legătura dintre această variație şi precipitările din stratul de bronz depus.

BULETINUL INSTITUTULUI POLITEHNIC DIN IAŞI
Tomul LIII (LVII), Fasc. 2, 2007
Secţia
ŞTIINŢA ŞI INGINERIA MATERIALELOR

STUDY OF THE PROCESSING BY HEAT TREATMENTS OF BIMETALLIC BUSHINGS FOR AUTOMOBILES, OF HYPOEUTECTOIDE CARBON STEEL-BRONZE

CORĂBIERU ANIŞOARA, CORĂBIERU PETRICĂ, PREDESCU CRISTIAN, VASILESCU DAN

Abstract

The heat treatment of the bimetallic bushings of the automobiles must be seen as a compromise that satisfy the requirements both of the base material MB (hypoeutectoid carbon steel) and of the deposited layer SD (bronze with aluminium) regarding the framing in the temperatures range in which the phase transformations take place. Conforming to the phase equilibrium diagram, the bronze layers deposited present a variation of the solubility with the temperature, which involves the possibility of the modification of the physical-mechanical properties by heat treatments. The heat treatments applied to the bimetallic assembly hypoeutectoid carbon steel – bronze with aluminium can be the salt hardening, the aging and the homogenization annealing.

Keywords: *heat treatment of bimetallic bushings of automobiles*

1. Introduction

The improvement of the physical-mechanical properties of the bimetallic bushings of hypoeutectoid carbon steel – bronze with aluminium by heat treatments has to be achieved taking into consideration the following aspects:

- the heat treatment has to have favorable effects on the both metallic layers;
- if the improvement effect is preponderant for one of the layers, than at least not to present big disadvantages on the second one and not to affect negatively the specific adherence between layers;
- the heat treatment has to achieve a compromise that satisfy the requirements both of the base material MB and of the deposited layer SD. That's why the possibilities of thermal processing of the bimetallic components for automobiles are much reduced, only certain treatments and between certain limits can be applied with proper results.

2. The salt hardening of the bimetallic bushings for automobiles

The heat treatment of salt hardening has in view:

- conservation at ambient temperature, in a metastable supersaturated condition, of the solid solution existent at high temperature;
- the supersaturated solid solution is obtained by rash cooling from the temperature of meting in solution (the transformation by precipitation of certain components from the solid solution cannot take place), the deposited layer (bronze with aluminium) conserving its mono-phase structure of the high temperature;

- the technological parameters of the salt hardening have been established experimentally. The temperature and time of maintaining at salt hardening must ensure the dissolving of the inter-metallic components in solid solution, the homogeneity of the solid solution, the obtaining of a proper size of the crystalline grain.

Bimetal OLT35-CuAl9T: $T_{salt\ hard}$ = 850-900^{o}C, $t_{maintain}$ ~ 0,5h, water-cooling.

- the effect of this treatment on the base material MB hypoeutectoid carbon steel does not present big shortcomings because the cooling of the bimetallic bushing in water from 850^{o}C does not have the effect of a hardening in its self due to the low content of C of the base material MB- OLT35;
- the size of the heating speed is conditioned only by the capacity of the deposited layer SD of non-cracking at sudden temperature variations (for the bronzes with aluminium this variation of temperature can be maximum → the bushings can be introduced in the furnace directly at the treatment temperature);
- following the salt hardening, the deposited layer presents o mono-phase structure constituted of a metastable supersaturated solid solution α (alloying elements substitute the Cu atoms or penetrate in the net interstices) having low physical and mechanical properties.

3. Ageing

The ageing heat treatment has in view the following aspects:

- the heating of the metastable structure obtained by salt hardening in such a way that this one evolves towards the condition of physical-chemical equilibrium;
- if the metastable structure is supersaturated solid solution then the ageing hardens and if it is of martensite type then the ageing softens;
- this treatment supposes the heating under the curve of variation of the solubility with the temperature, maintaining and slow cooling;
- the supersaturated solid solution passes in equilibrium condition, separating from it by precipitation certain inter-metallic components depending on the nature of the alloying elements and the values of the treatment parameters;
- the technological parameters have been determined experimentally:

  Bimetal OLT35-CuAl9T: T_{temp} = 480-500^{o}C, $t_{maintain}$ ~ 1,5h, air-cooling.
- for the base material MB this treatment is equivalent with a high tempering
- having as effect the improvement of the rough ferrite-perlite structure and the diminishing of the acicular presence of the ferrite;
- the effect of the precipitation of the chemical compounds consists in the important increase of the mechanical characteristics due to the creation of the segregation areas, of the particles of precipitates metastable coherent and half-coherent to the matrix and of the fields of stresses existing around these ones; all these constitute obstacles in the way of displacement by sliding of the dislocations;
- in the case of the deposited layer SD – CuAl9T the most probably the following inter-metallic compounds precipitate : Cu_3Al, Al_2Cu, AlNi, Al_3Ni.

4. Homogenization annealing of the bimetallic components for cars

The heat treatment of homogenization annealing has in view the following aspects:

- elimination of the dendrite segregation (the chemical composition defects from the inside of the deposited layer SD crystals, that alters the properties creating phases out of equilibrium);
- re-heating at as higher temperature, maintaining a sufficient period of time for the proper distribution by diffusion of the components;
- the technological parameters of the annealing homogenization have been experimentally determined:

Bimetal OLT35-CuSn10: T_{ann} = 650-700^{o}C, $t_{maintain}$ = 5-8min/mm thick. wall ~0,5h, cooling in quiet air.

Bimetal OLT35-CuSn4Zn4Pb17: T_{ann} = 650^{o}C, $t_{maintain}$ = 0,5 h, cooling in quiet air.

- important modifications of the SD structure are produced (structure with dendrite segregations → homogeneous mono-phase or bi-phase structure);
- for MB this treatment is equivalent with a complete stress relieving annealing, the level of the remnant stresses decreasing at values under 5 daN/mm^2 concomitantly with hydrogen elimination.

In fig.1 the diagrams of the heat treatments experimented for the bimetallic hypoeutectoid carbon steel – bronze are shown.

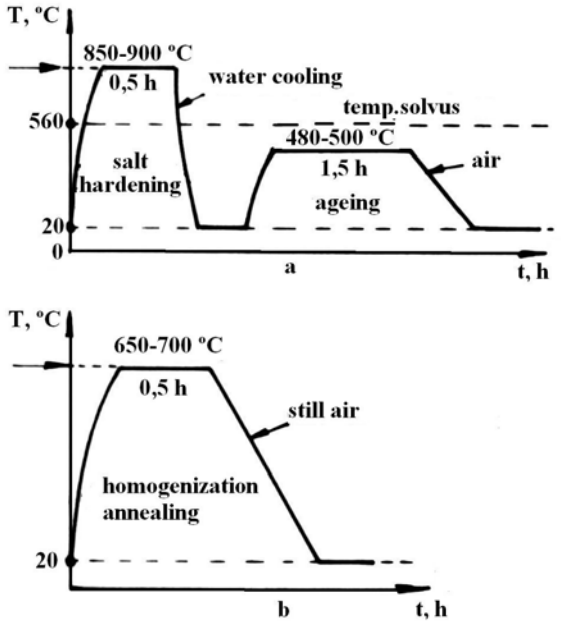

Fig.1. The heat treatment of the experimented bimetallic bushings for automobiles, made of hypoeutectoid carbon steel – bronze.

a. OLT35-CuAl9T → salt hardening + ageing;
b. OLT35- CuSn10, OLT 35-CuSn4Zn4Pb17 → homogenization annealing

5. Conclusions

The salt hardening induces in the bronze deposited layer a metastable mono-phase structure having low properties (the effect on the base material – hypoeutectoid carbon steel MB, does not present big disadvantages);

- Ageing leads to the evolution of metastable layers obtained by salt hardening to physical-chemical stability. If the metastable structure is of type supersaturated solid solution then the ageing hardens and if the metastable structure is of martensite type then the ageing softens the layers deposited on the base material;

- Homogenization annealing of the bimetallic components for automobiles has in view the elimination of the dendrite segregation that creates phases out of equilibrium leading to the reducing of the specific adherence between layers and to exfoliation.

References

1. **Corăbieru A., Corăbieru P**. – Objectives of alignment of the automobiles industry in Romania to the requirements of the environment European directives 2000/53/CE regarding out of use vehicles, Industrial Ecology Magazine, nr.5/2006, pag.32-37, ISSN 1224-3183 (works of the national symposium "Durable development and automobiles construction from concept to implementation", VI th edition- Bucharest, 16-17th of November 2006)
2. **Corăbieru A., Corăbieru P.,**–Alignment of the technologies of manufacture of the metallic components for automobiles to the requirements of the environment European directives 2000/53/CE 2000/53/CE– Automobiles Constructions - New series Innovative Technology, year 58/2006-nr.3-4, pag. 23-25, Bucharest, ISSN 0573-7419
3. **Corăbieru P, Corăbieru A., Velicu S., Predescu C**. – The new bronzes of replacement of the Cu-Be alloys for the increasing of the capacity of plastic deformation and cutting- Proceedings of the 15 th International Conference on Manufacturing Systems – ICMaS – Published by Editura Academiei Române, ISSN 1842-3183, pag. 383-386, 26-27.10.2006, Bucharest, Romania

Received March 15, 2007

SC PRESUM PROIECT SA Iasi, Calea Chisinaului 32
Univ. Politehnica Bucuresti, Splaiul Independenței, nr. 313
SC Procom Iasi, Strada Canta 14

ANALIZA PRELUCRĂRII BUCŞELOR AUTO BIMETALICE OȚEL CARBON HIPOEUTECTOID – BRONZ PRIN TRATAMENTE TERMICE

Abstract

Tratamentul termic al bucşelor auto bimetalice trebuie privit ca un compromis care să satisfacă cerințele atât ale materialului de bază MB (oțel carbon hipoeutectoid) cât şi al stratului depus SD (bronz cu aluminiu) din punct de vedere al încadrării în intervalul de temperaturi în care au loc transformările de fază. Conform diagramei de echilibru fazic, straturile depuse de bronz prezintă o variație a solubilității cu temperatura, ceea ce implică posibilitatea modificărilor proprietăților fizico-mecanice prin tratamente termice. Tratamentele termice aplicate ansamblului bimetalice oțel carbon hipoeutectoid-bronz cu aluminiu pot fi călirea de punere în soluție, îmbătrânirea şi recoacerea de omogenizare.

BULETINUL INSTITUTULUI POLITEHNIC DIN IAŞI
Tomul LIII (LVII), Fasc. 2, 2007
Secţia
ŞTIINŢA ŞI INGINERIA MATERIALELOR

INDUSTRIAL APPLICATIONS OF THE BIMETALLIC BUSHINGS. ECONOMIC ASPECTS

CORĂBIERU PETRICĂ, CORĂBIERU ANIŞOARA, SOHACIU MIRELA, VASILESCU DAN

Abstract

In the context of the integration of Romania in the EU the production increase and the utilization of the bimetallic products is expected in different fields due to the improvement of the electric, thermal, anti-friction properties, the improvement of the sticking, adherence possibilities, saving of the non-ferrous materials. The actual research in the field of bimetals hints at the gradual increase of the geometrical dimensions of the bimetallic bushings, the diversification of the assortments of the base materials and deposited layers in the direction of the increase of alloying degree, development of the automation and robot utilization for the deposition of the metallic layers. Savings of metals and critical alloys rich up to 90% in the case of the utilization of bimetallic half-products in the manufacture of apparatus with a high degree of incorporated intelligence.

Keywords: *industrial application of bimetallic bushings*

1. Introduction

In the context of the integration of Romania in the EU the production increase and the utilization of the bimetallic products is expected in fields like:

- electro-technique, electronics, energetic and nuclear industry;
- chemical, petrochemical, metallurgic and machines construction industry;
- food, textile, wood, cellulose and paper industry;
- air, naval transport and telecommunications;
- consumer goods of longtime utilization;
- manufacture of pharmaceutical and cosmetic products;
- vacuum, cooling and ventilation technique;
- manufacture of synthetic resins and plastics.

2. Industrial applications of bimetallic bushings

The use of the bimetals carbon steel-bronze has as main purposes the followings :

- the improvement of the electrical, thermal and anti-friction properties;
- the improvement of the sticking, adherence possibilities and surface appearance;
- bronze saving.

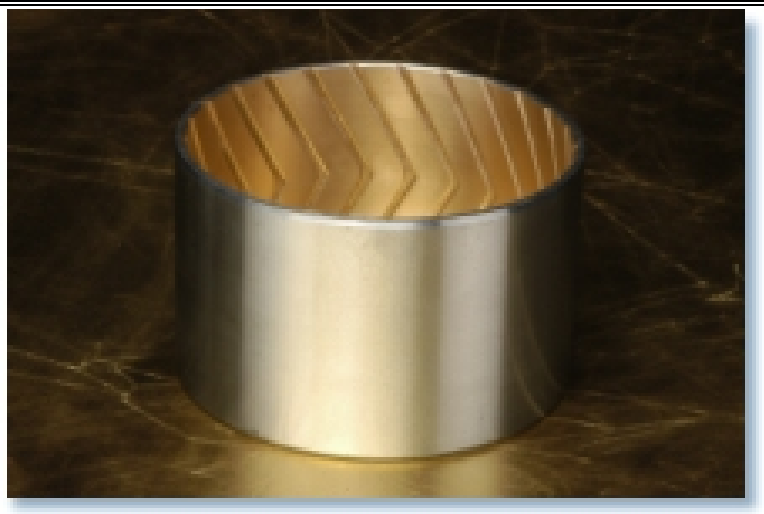

Fig.1. Bimetallic bushing of hypoeutectoid carbon steel low alloyed – bronze with tin

Bimetallic bushings carbon steel low alloyed – bronze obtained by special procedures of deposition are used especially for :

- connection bushings, connection couplings for feeding ducts;
- casings, contact points;
- motors sealing gaskets;
- connection bushings of the tanks for auto-vehicles radiators;
- tightening bushings for immersible boilers and heat changers;
- bushings and bearings for the containers under pressure and bearings for containers under pressure and condensers;
- the manufacture of the gearshifts, disks of the hydro-dynamic converters, disk brakes, synchronizing cones, clutches with multiple disks;
- bushings for crude oil refining installations;
- air-coolers at the converters with oxygen for the cooling of the blowing lances and converters hoods;
- half-bearings for tractor and truck motors;
- bearings at Diesel motors and tractors on caterpillars;
- bushings for the manufacture of big turning machines;
- bearings of the shake out machines compressors.

3. Economical aspects

By the utilization of the half-products and bushings with bimetallic layers the following aspects are had in view :

- saving of the expensive and critical materials and implicitly the imports reducing;
- obtaining a product that combine various properties, unreachable by using of a single metal:

a – the good thermal conductivity of the base steel with the corrosion-proof of the deposited steel;
b – high strength of the base steel with anti-friction good properties of the deposited alloy;
c – high mechanical properties and thermal dilatation coefficients different between component metals of the thermo-bimetal;

d – high technological properties of the base steel with distinct appearance of the deposited materials.

The thickness of the half-products and bimetallic bushings most utilized in the whole world is comprised between 0,5 – 5 mm, the proportion of the deposited layer SD being of 10 – 30%.

In fig.2. the variation of the ratio between the production cost of the monoblock massive half-product and the cost of the carbon steel – stainless high alloyed steel bimetallic half-product is presented, conforming to the economic studies effected in Germany and France.

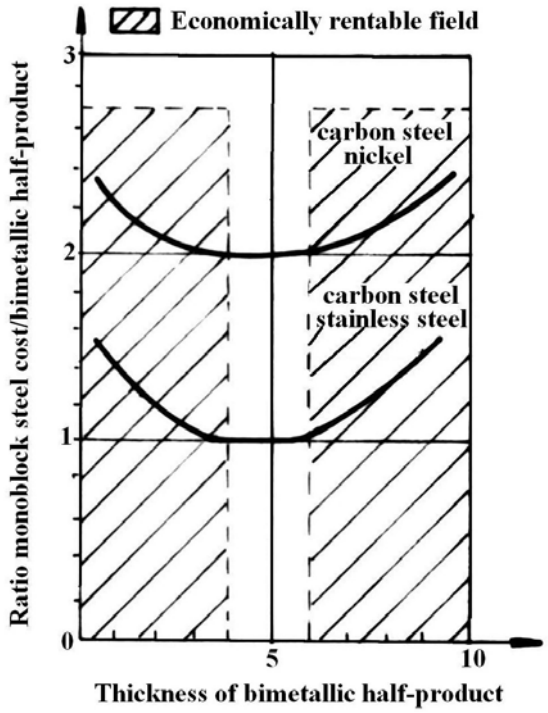

Fig.2. Variation of the ratio between the production cost of the half-products of monobloc metallic materials and the cost of the bimetallic half-products with deposited layer SD of these materials

Conforming to fig. 2 it is marked that for the thicknesses of the bimetal under 3-4 mm the economic advantage is increasing (the bimetals production is rentable), as well as for thicknesses over 5 mm.

Using the half-products and the bimetallic bushings low alloyed carbon steel – bronze, the percentage savings presented in table 1 are obtained.

Table 1. Average savings achieved by the obtaining and utilization of the bimetals low alloyed carbon steel -bronze

Cr.Nr	Savings resulted by the utilization of the bimetals low alloyed carbon steel - bronze	Proportion of deposited layer SD, %	
		10 %	20%
1	Value savings	39	24
2	Quantitative savings regarding the alloy of deposited layer SD	81	65
3	Minimum ratio between the price of the deposited alloy SD and the price of the base material MB in order to achieve value savings	4	5

Indicative calculations in order to establish the costs of some half-products and bimetallic bushings carbon steel–copper and carbon steel-bronze with the proportion SD 15%, by comparing with the technological proceedings are presented in the table 2.

Table 2. Comparative costs of the of the half-products and bimetallic bushings depending on the technological proceedings

Cr. Nr	Manufacture proceeding	Estimative cost		
		France, Germany, Sweden	Russia, Ukraine	Romania
1	Method of compound ingot	118%	120%	120%
2	Method of compound package	123%	127%	125%
3	Method of welding in slag bath	!05%	105%	105%
4	Centrifugal methods	100%	100%	100%

From the table 2 it is remarked that the most advantageous proceedings from the economic point of view are those based on centrifugal methods → much more the real possibilities of the immersion and centrifugation proceedings which eliminate operations and equipment necessary to pre-heating, manipulating, casting into spin casting machines, extraction.

Having in view a possible series production in Romania, the products would be competitive on the European market taking into account that for a period of time the expenses with the man power will be low.

In fig.3 the percentage savings (%) are indicatively synthesized in the presented curves, that are achievable by using a ton of bimetallic half-products of low alloyed carbon-steel – stainless steel and of a ton of half-products and of a ton of bimetallic half-products and bushings of low alloyed carbon steel - bronze → instead of a ton of half-products of stainless steel, respectively bronze.

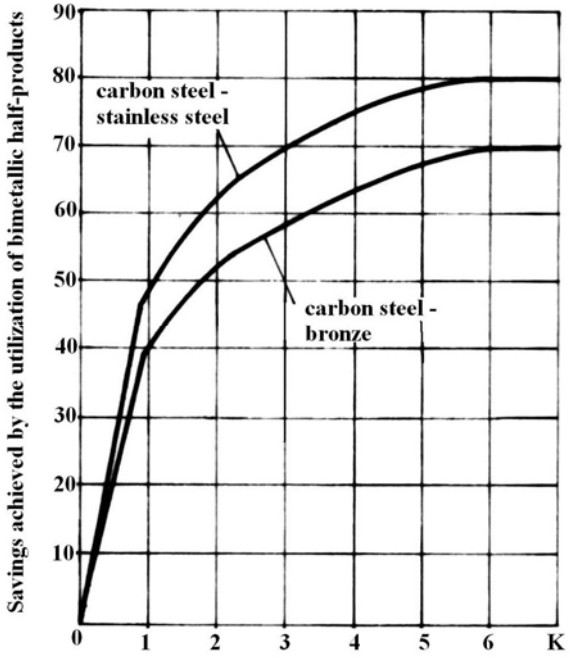

Fig.3. Savings achieved by the utilization of bimetallic half-products

The savings represented in the ordinate have been established depending on the ratio K from the in the abscissa (K= ratio between the surface of the cross section of the carbon steel half-products and the surface of the deposited layer section). As much bigger is K as the obtained savings are higher. In the building machines, energetic and automobile industry the bimetallic half products and bushings of low alloyed steel – anti-friction material are used on a large scale and they have superior characteristics: high and stable friction coefficient at different temperatures, low wearing and long service time, resistance at high temperatures and good thermal conductibility, high resistance at corrosion, ensurance of a slow braking.

The utilization of the bimetallic half-products and bushings of steel bronze achieve a 60-70% average of savings of Cu alloys; in the case of apparatus and machines manufacture (products with a high incorporated intelligence degree) the savings can reach even up to 90% scanty metals and alloys (in which case they are used as thin layers deposited and tight joined by MB of carbon or low alloyed steel).

The economic efficiency is as much bigger as the geometrical dimensions of the products are bigger and the proportion of the deposited layer SD is reduced at minimum values.

4. Conclusions

The actual tendencies in the world in what concerns the bimetallic bushings of carbon steel- bronze and carbon steel-high alloyed steel are:

- the gradual increasing of the geometrical dimensions bushings leads to the increasing of the economical advantages in the case of the utilization for welded constructions of big dimensions;
- the manufacture of the bimetallic half-products and bushings of great dimensions for special utilizations in the petrochemical, energetic and nuclear industry;
- the continuation of the research for the extension of the ranges of MB and SD in the direction of the increasing of the alloying degree for the large utilization in the automobiles industry.

The technological proceedings of immersion and centrifugation impose also from the economical point of view existing a sale market for the bimetallic bushings, the technological proceedings having big possibilities of automation and robots utilization.

REFERENCES

1.Corãbieru P., Predescu C., Velicu S., Corãbieru A., Vasilescu D.D. – Researches concerning the influence of joining temperature on the bimetal layer – The 7th International Conference of Technology and Quality for Sustained Development, May 25-27, 2006, Bucharest, România – organized by University Politehnica of Bucharest in cooperation with Politecnica di Milano, Italy and De Montfort University United Kingdom, Proccedings TQSD06, p. 139-144, ISBN 973-720-035-7, AGIR Publishing House.

2.Corãbieru P, Corãbieru A., Velicu S., Predescu C. – The new bronzes of replacement of the Cu-Be alloys for the increasing of the capacity of plastic deformation and cutting- Proceedings of the 15th International Conference on Manufacturing Systems – ICMaS – Published by Editura Academiei Române, ISSN 1842-3183, pag. 383-386, 26-27.10.2006, Bucuresti, România

3.Corãbieru P., Corãbieru A., Alexandru I., Vrabie I. – The influence of joining temperature on the bimetal layer structure and characteristics, Polytechnic Institute of Iasi, Volume LI (LV), Fascicle 3, Section Metals Science and Engineering – 2005, pag. 77-82, ISSN – 1453-1690.

Received March 15, 2007

SC PRESUM PROIECT SA Iasi, Calea Chisinaului 32
Univ. Politehnica Bucuresti, Splaiul Independenței, nr. 313
SC Procom Iasi, Strada Canta 14

APLICAȚII INDUSTRIALE ALE BUCŞELOR BIMETALICE. ASPECTE ECONOMICE

Abstract

În contextul integrării României în UE creşterea producţiei şi utilizarea produselor bimetalice este aşteptată în diferite domenii datorită îmbunătăţirii proprietăţilor electrice, termice, antifricţiune, îmbunătăţirea posibilităţilor de lipire, aderenţă, economisirea materialelor neferoase. Cercetările actuale în domeniul bimetalelor vizează creşterea treptată a dimensiunilor geometrice ale bucşelor bimetalice, diversificarea sortimentelor materialelor de bază şi straturilor depuse în direcţia creşterii gradului de aliere, dezvoltarea posibilităţilor de automatizare şi robotizare a depunerilor straturilor metalice. Economiile de metale şi aliaje deficitare ajung până la 90% în cazul utilizării semifabricatelor bimetalice în fabricarea aparatelor cu un grad ridicat de inteligenţă înglobată.

BULETINUL INSTITUTULUI POLITEHNIC DIN IAŞI
Tomul LIII (LVII), Fasc. 2, 2007
Secţia
ŞTIINŢA ŞI INGINERIA MATERIALELOR

STUDY OF THE THERMO-PHYSICAL PARAMETERS AND THEIR CORRELATION IN THE RAPID TREATING WITH BORON-CARBON-VANADIUM, ELECTRO-CHEMICALLY CONTROLLED, OF THE COLD PLASTIC DEFORMATION TOOLS

VASILESCU DAN DRAGOS, BACIU CONSTANTIN, LOZOVAN MIHAI, CORABIERU PETRICĂ, CORĂBIERU ANIŞOARA

Abstract

The superficial layers treated with boron-carbon-vanadium of the plastic deformation tools of experimental steel 21MoMnCr12 have been obtained with an electric furnace with electrodes of dimensions 1000x300x270 mm, the heating of the tool being achieved in industrial direct current with the frequency of 50Hz and the closing of the electric circuit between electrodes being made through a granulated mixture with dimensions of 0,1≤d≤0,4 mm, electrically conductive. The thickness of the diffusion layer depends directly on the part polarization, the current density of the electrodes i= 10A/mm^2 so that more than 85% of the active power is transformed in heat. The electric resistivity φ and the relative magnetic permeability μ_r modify depending on the temperature T of the tool. Above the Curie point (727°C) the penetration depth has an accented increase, and the pellicle effect diminishes. The length of the tool and of the heating precincts influences the power variation and the electric power factor.

Keywords: *deformation tools treated with boron-carbon-vanadium*

3. INTRODUCTION

The hardening process by boron-carbon-vanadium treatment in electro-thermal granular environments is based on the direct electric heating method that presents the following advantages by respect to the other known heating electric or non-electric systems: reduced heating time, high output, reduced energy specific consumption. These affirmations are sustained by the data presented in the Table 1.

Table 1. Thermo-physical parameters at different direct heating by electric resistance

Heating procedure	Installation output, %	Start and stop time	Surface decarburation	Scoria forming, %	Heating time, min.	Energy specific consumption, kWh/t	Power factor
Direct heating by electric resistance	0,70 – 0,95	Seconds	Does not present	(0,3 – 0,5)	0,3 – 3,0	200 – 350	0,3 – 0,95

The hardened superficial layers at the deformation tools made of the experimental steel 21MoMnCr12 have been obtained with an electric furnace with

graphite electrodes, the heating of the tool charge being achieved directly, the closing of the electric circuit being made through a granular mixture, electrically conductive.

The granular mixture and the tools charge are the elements of closing an electric circuit of low tension at which the furnace itself is connected.

The direct heating is achieved through the direct current of industrial frequency (50Hz).

Equivalent electric scheme

The equivalent electric scheme of the installation (figure 1) contains the resistance R_{rs} and the reactance X_{rs} of the short net, the contact equivalent resistance R_c of the graphite electrodes, the resistance R and reactance X of the metallic tools, the secondary tension U_2 of the supply transformer, tension U at the terminals of the installation and the heating current I, as per the figure 1.

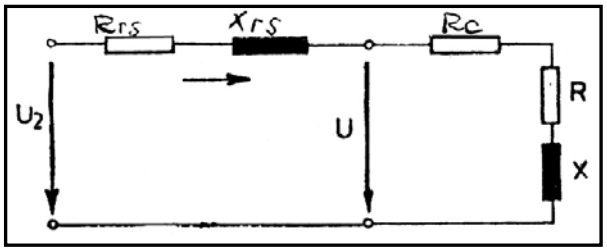

Fig.1.Equivalent electric scheme of the direct heating installation

2. LABORATORY EXPERIMENTS

Thermo-physical parameters – intensity – temperature

From the moment of the putting into function of the heating installation, an attentive following of the physical-electrical parameters variation (tension-intensity) and heating parameters (mixture temperature and charge temperature) has been effected. The values of the thermo-physical parameters are registered and followed during the whole heating, as per the table 2.

Table 2. The monitoring of the thermo-chemical treatment in electro-thermal granular environment of the deformation tools of low alloyed steel 21MoMnCr12

Experimental steel	Dimensions Ø x 1 (mm)	Period start/end therm-chem. Treat.	U (V)	I (A)	T_{solid} granular mixture (^{0}C)	T_{charge} (part) (^{0}C)	Remarks
21MoMnCr12	100x120	Heating start	70	150	20	20	Heating period (t_h)=1 h
	100x120	Heating end	50	700	1000 1100	900	
	100x120	Start maintain temp. boron-carbon-vanadium treatment	50	700	1000	900	Period of maintain

	100x120	End of maintain temp. of boron-carbon-vanadium treatment	50	700	950	900	Total period (t) of carbonization t_i+t_m=5 h

The thermal process of heating of the steel tools in electro-thermal granular environment depends also on the ratio between the weight of the conductive granular mixture and the weight of the metallic tools.

Into the framework of the experiments the ratio between the weight of the granular mixture from the working precincts and the weight of the steel charge submitted to heating has been deliberately altered until an optimum ratio was found that influences positively the heating period.

In the table 3, the variant of charging in the furnace precincts is presented.

Table 3. Overall dimension variants for the furnace charging

Dimensional variant of the furnace Lx1xh, (mm)	Dimensions of exp. Parts Ø x 1, (mm)	Charge weight, (kg)	Weight of the solid granular mixture, (kg)	Ratio weight of granular mixture/charge weight
1000x300x270	Ø 100x120	8,0	16	2/1

Electric output of the installation

Parameters of the metallic tools are established based on the pellicle effect.

Design data:

- Half-product (cylindrical part)- material – MoMnCr12
- Ø 100x120 mm, r_e=50 mm;
- Section area S = π x 50^2 = 7850 mm^2 = 78x$10^{-4}m^2$
- Lateral surface A = 37 x $10^{-3}m^2$
- Part length 1 = 120 mm
- Part weight m = 8 Kg
- To = 20^0C
- Th = 1000^0C

Material sizes: density = 7800kg/m^3; massic heat = 0,220Wh/kgK;
Electric resistivity = 0.2x 10^{-6} Ωm; resistivity la 1000°C = 1,23x10^{-6} Ωm

Table 4. Calculation of the electric parameters of electro-thermal heating

Size	Calculation	Result
Plastic deformation tools parameters		
Initial penetration depth	$\int_o = 503 \sqrt{\frac{0,2x10^{-6}}{50\ x\ 50}}$	4,5x10^{-3}m

		11,1
Function K_{Ro}	$K_{Ro} = \frac{1}{2} x\, 11,1 + \frac{1}{4}$	5,8
Function K_{Xo}	$K_{Xo} = \frac{1}{2} x 11,1 - \frac{3\sqrt{2}}{64} x \frac{1}{11,1}$	5,49
Initial resistance in direct current	$R_{CCo} = \int_0 \frac{l}{s} = 0{,}2x10^{-6} \frac{0{,}12}{78x10^{-4}}$	$0{,}003x10^{-3}\Omega$
Initial resistance	$Ro=5{,}8x0{,}03x10^{-3}$	$0{,}017x10^{-3}\ \Omega$
Initial reactance	$Xo=K_{Xo}Xr_{cco}=5{,}49x0{,}03x10^{-3}$	$0{,}016x10^{-3}\ \Omega$
Final penetration depth	$\int_i = 503\sqrt{\frac{\int_i}{\mu_{ri} xf}} = 503\sqrt{\frac{1{,}23x10^{-6}}{1.x50}}$	$79x10^{-3}$m
	$\frac{r_e}{\int_i} = \frac{50\ x\,10^{-3}}{79\ x\,10^{-3}}$	0,11
Function $K_{Rî}$	$K_{Ri} = 1 + \frac{1}{48}(0,63)^4$	1
Function $K_{Xî}$	$K_{Xi} = \frac{1}{4}(0{,}63)^2\left[1 - \frac{1}{96}(0{,}63)^4\right]$	0,098
Final resistance in direct current	$R_{cci} = \int_c x \frac{1}{s} = 1{,}23x10^{-6} x \frac{0{,}12}{78x10^{-4}}$	$0{,}01x10^{-3}\ \Omega$
Final resistance	$Rh=K_{Rî}Xr_{ccî}=1x0{,}01x10^{-3}$	$0{,}01x10^{-3}\ \Omega$
Final reactance	$Xh=K_{Xî}xRî=0{,}098x0{,}01x10^{-3}$	$0{,}0009x10^{-3}\ \Omega$
Heating electric current	$J=10A/mm^2$ – current density $I=10x10^6x78x10^{-4}$	78KA
Energetic indicators of the heating installation		
Active power	$Po=(Ro+Rc)x78^2x10^6$ $=0{,}027x10^{-3}x78^2x10^6$	164,26 Kw
Reactive power	$Ph=0{,}01x10^{-3}x78^2x10^6$ $Qh=0{,}0009x10^{-3}x78^2x10^6$	60840 W (60,8 Kw) 5,47 Kvar
Electric output	$Co = \frac{0{,}17x10^{-3}}{0{,}17x10^{-3} + 0{,}2x10^{-4}} x100 = 89\%$	89%
Installation output	$C_0 = 0{,}9 \times 0{,}89 \times 100$	80,1%
Energy specific consumption	$e_{tot.} = 0{,}220 / 0{,}89$	0,247Kw/kg =247Kw/t

In the figure 2 the time variation of the surface temperature T_s and the axle temperature T_{ax} of the cylindrical deformation tools of steel 21MoMnCr12.

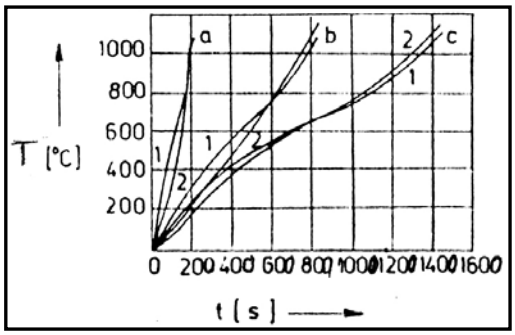

Fig.2.Variation of time of the surface temperature(1) and axle temperature(2) of a part of 21MoMnCr12 having the diameter of Φ 100x120 mm, heated in electro-thermal granular environment.
Heating time: a) 200 s; b) 800 s; c) 1400 s.

As at temperatures under Curie point, the heat sources are distributed at few millimeters from the surface, the temperature of the surface exceeds that of the axle and the thermal flow is oriented towards the interior of the metallic part section.
The specific consumptions of electric power of the electro-thermal heating installation are indicated in the figure 3.

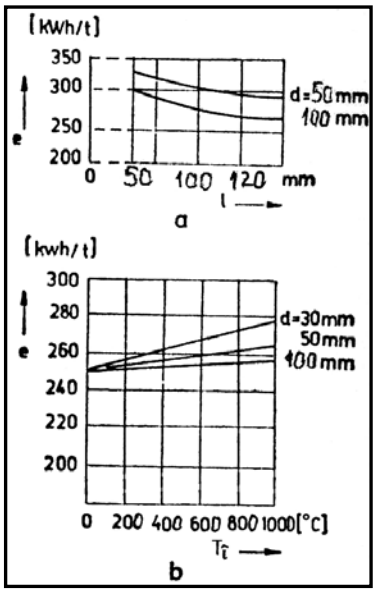

Fig.3. Specific consumption of energy at the electro-thermal heating of the cylindrical tools (diameter d) of steel 21MoMnCr12 depending on the length l (a) and on heating time (b). Heating temperature: T_i=900^{0}C

Conclusions

It was experimentally demonstrated that the thickness of the diffusion layer depends directly on the tool polarization, the current density at the electrodes i= 10A/mm^2 so that more than 85% from the active power is transformed in heat. The electrical micro discharges (electric micro arcs) on the tool surface develop high temperature under whose action atomic active carbon, boron, vanadium are formed depending on the nature of alloying particles that compose the granular environment of electric propagation. The absorption of the atomic element by the tool surface and the creation of the diffusion zone takes place. The electric resistivity φ and the relative magnetic permeability μ_r are modified depending on the temperature T of the plastic deformation tool. Over the Curie point (727°C) the penetration depth increases strongly and the pellicle effect diminishes. The length of the tool and of the heating precincts influences the power variation and the electric power factor. The calculated electric output C_o of

the furnace is 89%. The economic efficiency of the procedure is 2 -3 times higher by respect to the classic technologies and the characteristics of the superficial layer are improved.

REFERENCES

1. Vasilescu D.D., Corăbieru P., Corăbieru A. – Determinarea variaţiei rezistenţei mecanice şi rezistenţei la uzare a subansamblelor de tip arbori pentru motoare cu combustibil ecologic – Simpozionul „Generarea, prevenirea şi procesarea emisiilor poluante în mediu industrial" **(**The determination of the mechanical resistance and of the wear resistance of the shafts type sub-assemblies for motors with ecological fuel. – Symposium "Generation, prevention and processing of the polluting emissions in the industrial environment"), Bucharest, 2005, pag.163 – 169, ISSN 973-718-332-0.

2. Vasilescu D.D., Baciu Constantin, Adomnica Liviu – Cercetări privind posibilitatea de aliere complexă a stratului superficial al oţelurilor prin borocarbovanadizare rapidă controlată electrotermic.- Conferinţa "Cercetarea de Excelenta – Premiză favorabilă pentru dezvoltarea spaţiului românesc de cercetare"(Researches regarding the possibilities of complex alloying of the superficial layer of the steels by rapid treating with boron-carbon-vanadium, electro-thermally controlled – Conference "Research of Excellence – favorable premise for the research Romanian space" –22 – 24 oct. 2006, Brasov.

3. Corăbieru A., Corăbieru P., Alexandru I., Hopulele I., - Cercetări privind durificarea superficială a sculelor pneomatice prin modificări structurale zonale – Researches concerning superficial hardening of pneomatic tools through zonal structural modifications, Revista "Tratamente Termice şi Ingineria Suprafeţelor" (Magazine "Heat Treatments and Surfaces Engineering"), vol.VI, nr.1 – 2/ 2005, pag.11 – 18, ISSN 1221-5678.

Received March 15, 2007

SC Procom Iasi, Strada Canta 14
Univ. Gh. Asachi Iaşi, Bd. Mageron, 63
SC PRESUM PROIECT SA Iasi, Calea Chisinaului 32
INCDFT IASI

ANALIZA PARAMETRILOR TERMOFIZICI ŞI CORELAŢIA LOR ÎN PROCESUL TERMOCHIMIC DE BOROCARBOVANADIZARE RAPIDA CONTROLATĂ ELECTROTERMIC AL SCULELOR DE DEFORMARE PLASTICĂ LA RECE

Abstract

*Straturile superficiale borocarbovanadizate ale sculelor de deformare plastică din oţel experimental 21MoMnCr12 s-au obţinut cu un cuptor electric cu electrozi cu dimensiuni 1000x300x270mm.la care încălzirea sculei se realizează în curent continuu industrial de frecvenţă 50Hz, închiderea circuitului electric dintre electrozi făcându-se prin intermediul unui amestec granular cu dimensiuni 0,1≤d≤0,4mm. conductiv electrotermi*c. *Grosimea stratului de difuzie depinde direct de polarizarea piesei, densitatea de curent de la electrozi i= 10A/mm^2 încât peste 85% din puterea activă se transformă în căldură. Rezistivitatea electrică φ şi permeabilitatea magnetică relativă μ_r se modifică funcţie de temperatura T a sculei. Peste punctul Curie (727°C) creste accentuat adâncimea de pătrundere, iar efectul pelicular scade. Lungimea sculei şi a incintei de încălzire influenţează variaţia de putere şi factorul de putere electrică.*

BULETINUL INSTITUTULUI POLITEHNIC DIN IAŞI
Tomul LIII (LVII), Fasc. 2, 2007
Secţia
ŞTIINŢA ŞI INGINERIA MATERIALELOR

APPLICATIONS OF RHEOCASTING PROCESS TO Al-Si ALLOYS

VIRGIL GEAMĂN, AUREL CRIŞAN, SORIN ION MUNTEANU

Abstract. *Rheocasting process (RC), has been developed for manufacturing near-net shape components of high integrity directly from liquid alloys. The rheocasting process innovatively adapts the well-established high shear dispersive mixing action to the task of in situ creation of semisolid slurry followed by direct shaping of the semisolid slurry into a component using the existing cold chamber die-casting process. The rheocast component has close to zero porosity, fine and uniform microstructure throughout the entire component. Compared with those produced by conventional high-pressure die-casting, rheocasting samples have much improved tensile strength and ductility.*
In the paper are presented the rheocasting process, the microstructure and mechanical properties of rheocast samples made from Al-Si alloys.

Keywords*: semisolid slurry, rheocasting process.*

1. Introduction

Aluminum alloys, as lightweight structural materials, are playing an important role in achieving vehicle weight reduction and improving fuel economy in the automotive industry. Since 1990, the use of Al has been doubled in cars and tripled in the light truck market. Currently, 85% of all Al alloy castings are used by the automotive and mass transport industry, and a large proportion of such castings are produced by high-pressure die-casting (HPDC) process. However, the quality of components manufactured by the HPDC process is limited by the presence of a substantial amount of porosity, which not only excludes the application of HPDC components in high-safety and airtight systems, but also denies the opportunity for further property enhancement by heat treatment. It is clear that further increase in Al application in the transport industry will require a major advance in processing technologies.
The new processes need to be capable of producing components of high integrity and improved performance while being comparable with the HPDC process in terms of production cost and efficiency.
Porosity due to turbulent mould filling could be reduced or even eliminated if the viscosity of the melt could be increased to reduce the Reynolds number sufficiently so that trapped air is minimized [1]. This is the concept of semisolid metal (SSM) processing. Since early 1970s, a number of SSM processing techniques have been proposed [2]. One of the most popular SSM processes is thixocasting, in which non-dendritic alloys pre-processed by electromagnetic stirring are reheated to the semisolid region prior to the shaping process.

As a new processing technique, thixocasting does improve component integrity and performance, but proves to be cost intensive, low efficiency and less flexible. After 30 years of extensive R&D, thixocasting is currently experiencing a decline in acceptance as a viable production technology [2]. Under such circumstances, a new processing concept, rheocasting process, has been developed.

2. The rheocasting process

The rheocasting process is an innovative one-step SSM processing technique to manufacture near-net shape components of high integrity directly from liquid aluminum alloys.
The process innovatively adapts the well-established high shear dispersive mixing action of the twin-screw extruder (originally developed for polymer processing) to the task of *in situ* creation of SSM slurry with fine and spherical solid particles followed by direct shaping of the SSM slurry into a near-net shape component using the existing cold chamber die-casting process.
The rheocasting process starts from feeding predetermined dose of liquid metal from the melting furnace into the slurry maker where it is rapidly cooled to the SSM processing temperature while being mechanically sheared by a pair of closely intermeshing screws converting the liquid into a semisolid slurry with a pre-determined volume fraction of the solid phase dictated by the barrel temperature. The semisolid slurry is then transferred to the shot chamber of the HPDC machine for component shaping. In order to prevent Al-alloy from oxidation, nitrogen gas is used as the protective environment during the slurry-making process.

3. Microstructures

Two commercially aluminum alloys, respectively: AlCu4MgMn and ATSi5Cu1, were used in this work. Alloys were usually melted at 700^{o}C and fed into a slurry maker at the temperature of 40^{o}C above their melting point. A laboratory cold chamber die-casting machine was used for casting the standard tensile test samples. Fig. 1 shows the typical microstructures of rheocast alloys versus the die-casting procedure. Detailed micro structural characterization of various rheocast samples has revealed the following micro structural characteristics:

- Porosity is well below 0.5 vol.%. pores are rarely observed in the rheocast samples. Occasionally observed pores are small in size..
- Primary particles have a fine size, spherical morphology and uniform distribution throughout the entire casting.
- The remaining liquid in the SSM slurry solidifies under high cooling rate in the die resulting in the formation of extremely fine Al-phase (<10μm).
- Oxide particles are fine (few μm), spherical and well dispersed and uniformly distributed, reducing the harmfulness of oxide particle clusters and oxide film in cast components.
- Si-rich phases can be dispersed uniformly without any macro-segregation.

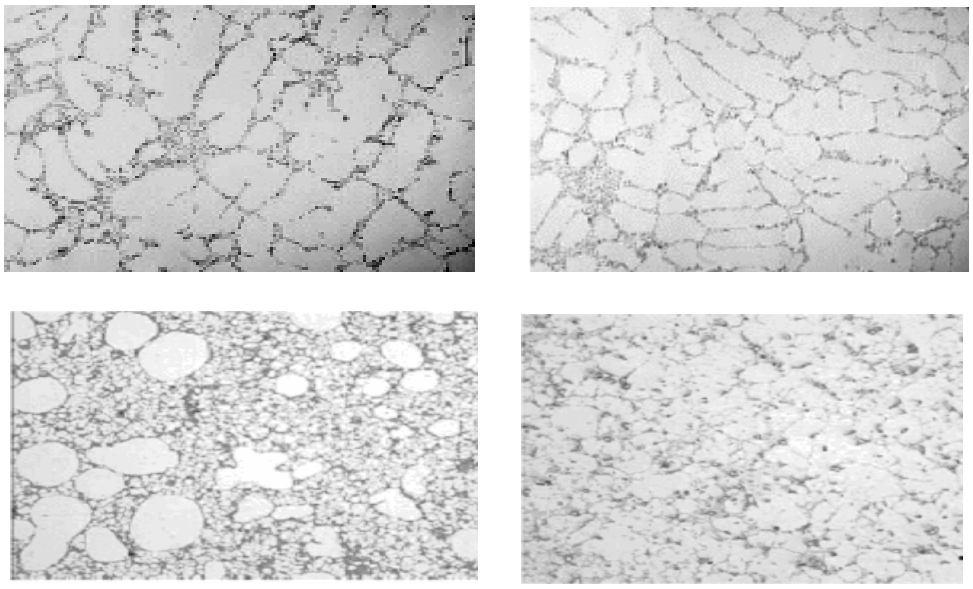

a). b).

Fig. 1. *Microstructures of experimental Al-Si alloys, after die-casting and rheocasting respectively. (a) AlCu4MgMn; (b)ATSi5Cu1.*

4. Mechanical properties

A special die was made to cast standard tensile test samples for mechanical testing. Processing parameters, such as screw rotation speed, shearing time, shot velocity, shot pressure, intensifying pressure and die temperature, were systematically varied. The effects of such processing parameters were assessed against sample quality in terms of microstructure and mechanical properties.

Table 1 summarizes the mechanical properties of the rheocast ATSi5Cu1 and AlCu4MgMn alloys in comparison with those of the same alloys produced by die-casting and sand cast processes. Rheocast ATSi5Cu1 alloy has much improved tensile strength and acceptable ductility.

Table 1. *Experimental data with tensile strength, yield strength and elongation results for ATSi5Cu1and AlCu4MgMn alloys.*

ATSi5Cu1 – alloy			
Casting process	Tensile strength [MPa]	Yield strength [MPa]	Elongation [%]
Rheocast	246	115	7.6
Die-cast	202	105	6.2
Sand cast	171	92	5.1
AlCu4MgMn – alloy			
Casting process	Tensile strength [MPa]	Yield strength [MPa]	Elongation [%]
Rheocast	233	112	7.3
Die-cast	198	96	5.8
Sand cast	163	86	4.7

5. Summary

A new semisolid metal processing technology, rheocasting, has been developed for the production of aluminum alloy components with high integrity. Rheocasting can be easily achieved by adding a slurry maker to the existing cold chamber die-casting machine. The rheocast samples have close to zero porosity, fine and uniform microstructure and are free from other casting defects.
Compared with high pressure die-casting or any available semisolid processing techniques, rheocasting offers components with improved strength and ductility, which can be attributed to micro structural refinement and uniformity, much reduced or eliminated porosity and refined and dispersed oxide particles. Rheocasting process is particularly suitable for production of high safety, airtight and highly stressed components in the automotive industry.

References

1. Metz S. A. and Flemings M. C. - *AFS Trans.,* Nr. 78 (1970), p. 453.
2. Kirkwood D.H. and Kapranos P. - *Proc. 4th Int. Conf. on the Semi-Solid Processing of Alloys and Composites*, Sheffild, England, 1996.
3. Fan Z. - *Inter. Mater. Rev.,* Nr. 47 (2002), p. 49-85
4. Chayong S., Atkinson H.V. and Kapranos P. – *Thixoforming of 7075 aluminum alloys*, Materials Science and Engineering, Series A 390 – 2005, p. 3÷12.
5. Giordano P. and Chiatmetta G. L. - *Proc. 7th S2P,* Tsukuba, Japan, Sept. 25-27, 2002, p. 665-670.
6. Basner T. – *Rheocasting of Semi-Solid A357 Aluminum,* Delphi Automotive Systems, 2006.
7. Zaharia I.I. and Geamăn V. - *Practical aspects regarding to thixoforming process applied to aluminum alloys.* MATEHN'06 - International Conference, Cluj-Napoca (paper in print).

Received March 15, 2007

Transilvania University of Braşov, Romania

APLICAȚII ALE PROCESULUI DE REOTURNARE LA ALIAJELE Al-Si.

Procesul de reoturnare fost dezvoltat ca un proces de execuție a semifabricatelor cu integritate ridicată, direct din aliajul lichid. Procesul de reoturnare adaptează inovativ bine-cunoscutele dispersii de forfecare prin amestecare, cu crearea in situ a pastei semisolide si fasonarea directa intr-un component prin folosirea camerei reci a unei masini de turnare sub presiune. Semifabricatele reoturnate au porozitate redusă către zero, microstructură fină, fără incluziuni. Comparativ cu turnarea clasică sub presiune, noul procedeu oferă o creştere a proprietăților mecanice şi a ductilității.
În lucrare sunt prezentate: procesul de reoturnare, proprietățile mecanice şi microstructurile pentru probe executate din aliaje Al-Si.

BULETINUL INSTITUTULUI POLITEHNIC DIN IAŞI
Tomul LIII (LVII), Fasc. 2, 2007
Secția
ŞTIINȚA ŞI INGINERIA MATERIALELOR

STUDY ON THE DEPENDENCE BETWEEN CHEMICAL COMPOSITION AND CHARACTERISTICS OF CAST IRONS

AUREL CRISAN, SORIN ION MUNTEANU, IOAN CIOBANU, VIRGIL GEAMAN

Abstract: *The paper presents research conducted with the purpose of optimising the chemical composition of cast irons used for the casting of bearing ball machining disks. The technological properties (as castability) and exploitation characteristics(as their durability in ball machining and their capacity of ball machining) of these cast irons were taken into consideration,. The link between these characteristics and the chemical composition of the cast irons was achieved by the Ni contents, the carbon saturation degree S_c and the equivalent eutectic carbon C_{cq}. The paper describes the types of used test pieces, working conditions and presents the interpretation of the experimental results (second degree polynomial regression curves) as well as the consequent conclusions.*

Keywords: *cast iron, micro-shrinkhole, shrinkage, shape factor, solidification, bearing ball machining disks.*

1. INTRODUCTION

The casts from this cast iron are cast parts with forms and dimensions established by internal norms of manufacturers and users [1]. They belongs to category of medium size parts with mass of 100 – 1000 kg and a relatively simple geometric configuration, that is a rim with a single cutting out, optionally consolidated by a girder. As end products the disks have two zones respectively two surfaces with distinctive utility, as shown in figure 1. For disks with H ≥ 70mm, the following dimensional relation is applicable for the usable area: H_U = H - 40 mm. On the working surface there are cut channels to assure the bearing balls circulation during polishing. After a certain time of using , when the channel reach the maximum admitted values, a new cutting operation is carried out in order to achieve a new channel. This operation can be repeated until the usable area of the disk thickness is completely used (see figure 1). On the usable zone of the disk no casting defects detectable by non-destructive control are allowed (like contraction pores, blowholes, inclusions,)

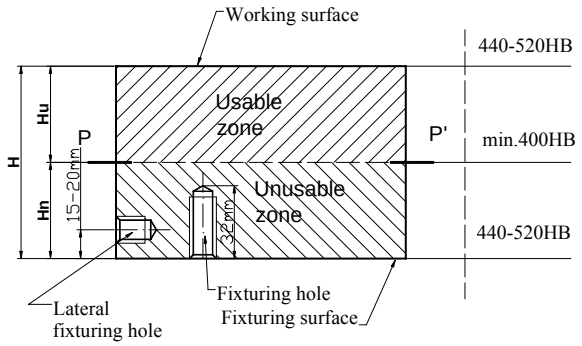

Fig. 1. Using zones and surfaces of the disks

The main exploitation characteristic of bearing ball grinding disks is their capacity of ball machining, which can be expressed by the duration of the operation and the quality of the resulted surface. The actual machining (grinding) of the balls is the result of an induced wear process, following the contact between disk and balls, where the disk is the driving element of the balls, generating their rotation through the channels of its active side.

2. EXPERIMENTAL METHODOLOGY

A set of samples was conceived in order to establish the dependencies between chemical composition of the cast irons used to cast the disks and the tendency to occur of certain specific defects during solidification (fig.2). While samples 1, 2 and 3 were created to study the casting properties of cast irons, the sample 4 was designed to study the material behaviour after the final heat treatment.

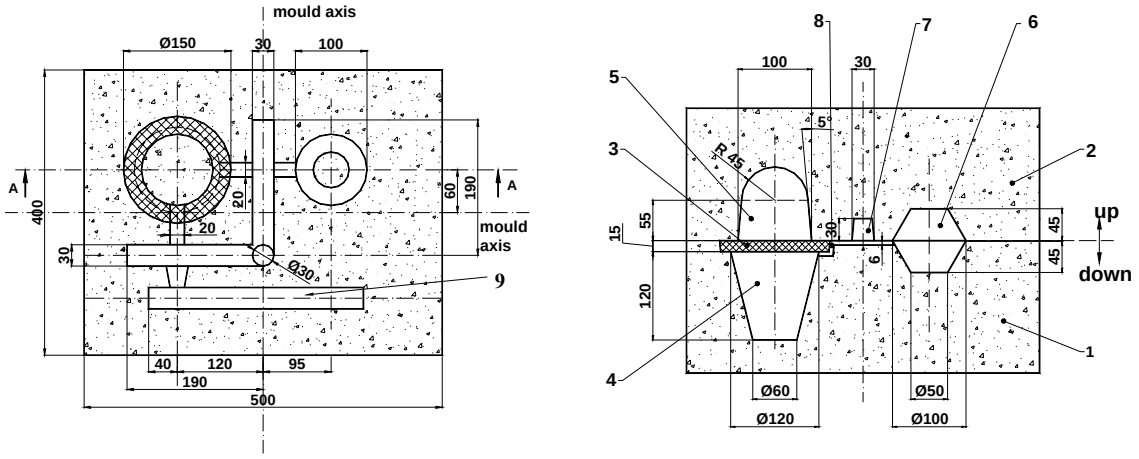

a) b)

Fig. 2. View of the separation plane of the mould, a); Section through mould for casting the samples, b)(section A-A of fig. a)) 1-inferior semi-mould; 2-superior semi-mould;3 – separation core; 4-sample 1; 5-sample 2; 6 –sample 3; 7-distribution channel;8-feeder for sample 1, 9-sample4.

The setting of the cast samples in the mould allowed the analysis of the concentrated shrinkhole volume (in the sample 1, that have a vertically upwards directed solidification under the influence of sample 2), of the shrinkhole volume for inverse directed solidification (for sample 2, its solidification being influenced by sample 1), and of the volume and the aspect of the shrinkholes in the absence of a directed of solidification (for sample 3, its solidification characteristics being close to those of a spherical body)[1]. Table 1 shows the chemical composition of the studied 15 charges of hypoeutectic cast irons. The Ni of their composition was modified, essentially determining the variation of carbon saturation degree S_c, and correspondingly influencing too the tendency of occurrence of certain solidification defects and hardenability of cast iron.

The main casting property monitored during the present study was the tendency of occurrence of shrinkholes during solidification, in the form of macro- or micro-shrinkholes, considering that this type of defect significantly affects the service life of

disks, even if it does not necessarily scrap them (depending on the "healthy" thickness of the cast disk shown in figure 1).

Table 1. Chemical composition of the cast irons after casting [%]

Nr.crt.	C	Si	Mn	P	S	Cu	Cr	Ni	Sc
1	3.111	1.69	0.67	0.053	0.0086	0.43	0.64	**0.56**	0.837
2	3.074	1.74	0.65	0.057	0.027	0.43	0.63	**0.8**	0.831
3	3.063	1.8	0.65	0.053	0.017	0.43	0.63	**0.54**	0.832
4	3.175	1.75	0.71	0.056	0.0128	0.42	0.65	**0.56**	0.859
5	3.009	1.82	0.69	0.131	0.0313	0.33	0.41	**1.73**	0.824
6	2.76	2.1	0.66	0.128	0.0384	0.33	0.41	**1.10**	0.776
7	2.788	2.23	0.66	0.115	0.0211	0.33	0.41	**0.74**	0.792
8	2.685	2.02	0.65	0.131	0.031	0.32	0.41	**3.18**	0.749
9	2.696	2.03	0.64	0.137	0.0316	0.32	0.4	**3.21**	0.753
10	2.816	1.68	0.64	0.130	0.0335	0.32	0.4	**3.29**	0.783
11	2.823	1.84	0.63	0.125	0.0328	0.35	0.51	**3.26**	0.774
12	2.792	1.9	0.63	0.134	0.0429	0.35	0.51	**4.78**	0.770
13	2.896	1.95	0.63	0.139	0.04	0.35	0.52	**5.07**	0.804
14	2.672	1.89	0.63	0.110	0.0208	0.35	0.51	**4.4**	0.735
15	2.674	2.03	0.63	0.120	0.0356	0.34	0.52	**7.26**	0.746

The volume of the open shrinkhole V_{ret} was determined by direct measurement. For the closed shrinkhole, within the context of sample solidification considered a micro-shrinkhole, the volume was determined by weighing the samples in air and water and calculating the porosity P by relation (1):

$$P = \frac{\rho_f (G_R - G_a) - \rho_a \bullet G_R}{(G_R - G) \bullet \rho_f} \times 100\% \qquad (1)$$

where ρ_f is the theoretical density of the cast iron (calculated as depending on the chemical composition), $\rho_a = 1$ [g / cm^3] is the density of water, G_R is the weight of the samples in air, and G_a is the weight of the samples in water.

In order to express as correctly as possible the link between the chemical composition and the tendency of shrinkhole occurrence, both the micro-shrinkhole and open shrinkhole volumes were expressed (by direct measurement and computation) in cm^3 as well as in %. Also, by addition, the total shrinkhole volume was computed V_{tret} (in both expressions). For the % expression the volume of a certain type of shrinkhole was related to the total volume determined for a certain sample. For instance:

$$V_{ret} = \frac{V_{ret}}{V_{probă} + V_{porozitate} + V_{ret}} \times 100 \qquad (2)$$

where V_{ret} is the volume of the open shrinkhole [cm^3],$V_{porozitate}$ is the volume of the micro-shrinkholes [cm^3],$V_{probă}$ is the theoretical volume of the sample [cm^3] (calculated as the ratio of the weight of the samples in air and their theoretical density).

In order to evaluate the possibility of directing solidification under the specific conditions of each type of cast sample, a common indicator was identified, that is the

directing index of solidification I_d, expressed as the ratio of the open shrinkhole volume (V_{ret}) and the total shrinkhole volume (V_{tret}), measured in cm^3 :

$$I_d = \frac{V_{ret}}{V_{tret}} \times 100 \qquad (3)$$

The bearing balls used in the study (to determinate the capacity of ball machining of cast iron) have a standardised chemical composition (STAS 11250-80), shown in table 2.and the samples from cast iron used have the dimensions and form sown in figure 3.

Table 2 Chemical composition of balls

Iron's mark	Chemical composition, [%]								
RUL 1	C	Mn	Si	Cr	Mo_{max}	S_{max}	P_{max}	Ni_{max}	Cu_{max}
	0,95-1,10	0,20-0,45	0,17÷0,37	1,30÷1,65	0,08	0,02	0,027	0,30	0,25

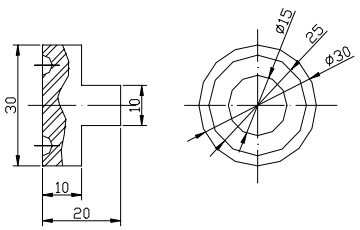

Fig.3 Form and dimensions of cast iron test pieces

Prior to the actual testing within the study, the test pieces were hardened in oil (heated to 850^{o}C, maintained for 30 min and cooled in oil bath), in order to achieve similar characteristics to those of ball grinding disks.

The bearing ball machining capacity of the cast irons was assessed by monitoring the losses due to wear of both cast irons and balls, during the conducted experiment. The computational relationship for these losses is:

$$P_{uz} = (G_i - G_f)/G_i \text{ x } 100, \qquad [\%] \qquad (4)$$

where: -P_{uz} – wear losses, [%]; G_i – initial weight, [g];G_f – final weight, [g];

3.EXPERIMENTAL RESULTS

Correlation between the chemical composition of cast iron and the volume of the open shrinkhole

The increase of S_c generates a concentration of the shrinkhole(see figure 4). Thus the volume of the open shrinkhole may grow. This effect is augmented in the case of directed solidification, so can be noticed at the type 1 samples with vertically directed solidification, in opposition to type 3 samples which solidification was uninfluenced by external factors. The effect of directing can be observed in the type 2 samples too. In this case the directing was achieved vertically but downwards (that is in opposite direction to the natural factors of solidification) the increase of S_c can trigger the concentration of the shrinkhole, but this is not open anymore at the upper side of the samples, as was determined within the present experiment.

In absence of directing in 3 type samples the increase of Ni content reduces the shrinking tendency of the open shrinkhole, in 1 and 2 type samples the situation is entirely different. For a strong directing solidification (as in samples 1) a minimum

volume of the open shrinkhole can be noticed at around 4% Ni. For a reverse directing of solidification (samples 2) the existence of a maximum volume of the open shrinkhole is observed around the value of 3% Ni.

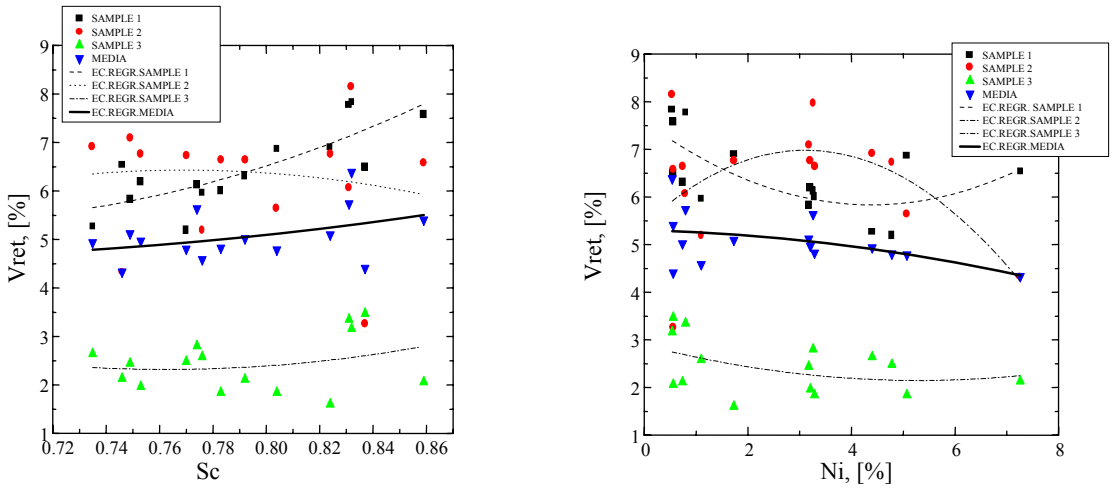

a) *b)*

Fig.4. Influence of the carbon saturation degree S_c- a) and of the Ni content - b), on the volume of the concentrated shrinkhole V_{ret}

The influence of chemical composition on the volumes of micro-shrinkholes (porosity)

In the present study the volume of the micro-shrinkholes was considered the total volume of closed holes in the cast samples.

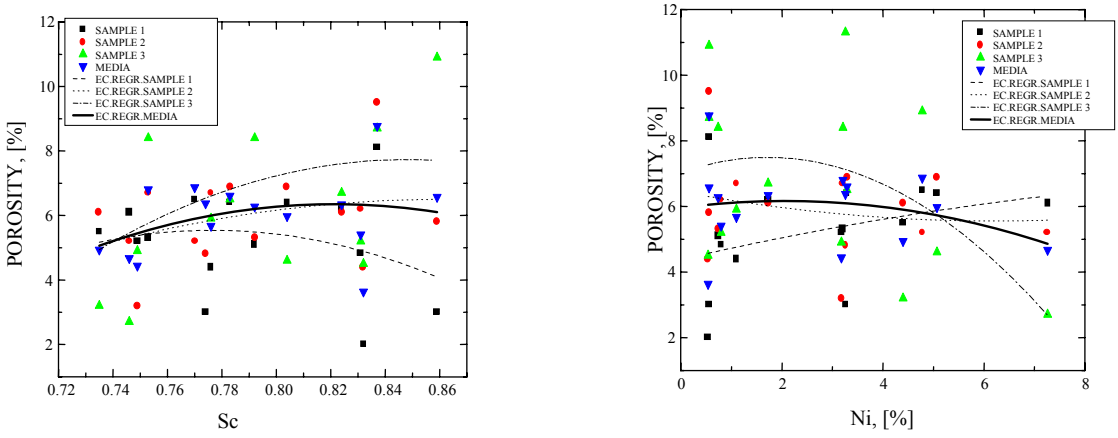

a) *b)*

Fig.5. Influence of the carbon saturation degree S_c- a) and of the Ni content - b), on the volume of micro-shrinkholes (POROSITY)

In figure 5a) it can be noticed that for type 1 samples, with the increase of S_c the tendency of occurrence of micro-shrinkholes decreases. This decrease is augmented at higher values of S_c. In the case of type 2 and 3 samples the tendency of occurrence of microporosity increases with the growth of S_c. This increase however becomes smaller towards the superior values of S_c, and tends to stop entirely over the value of S_c= 0,84. Once with an intensified directing of solidification, the effect of Ni on the occurrence tendency of micro-shrinkholes is modified too. Thus for type 1 samples with directed

solidification the increase in Ni augments the tendency of micro-shrinkholes occurrence. For a reverse directing of solidification, with increasing Ni content, the tendency of micro-shrinkholes occurrence decreases very slowly. The strongest decrease of the tendency of micro-shrinkholes occurrence was observed in type 3 samples. The strongest decrease of the tendency of micro-shrinkhole occurrence with a growing Ni content was observed in type 3 samples.

Influence of the chemical composition on the directing solidification index

The directing solidification index I_d is influenced by the carbon saturation degree S_c in close relation to the mechanism of solidification.

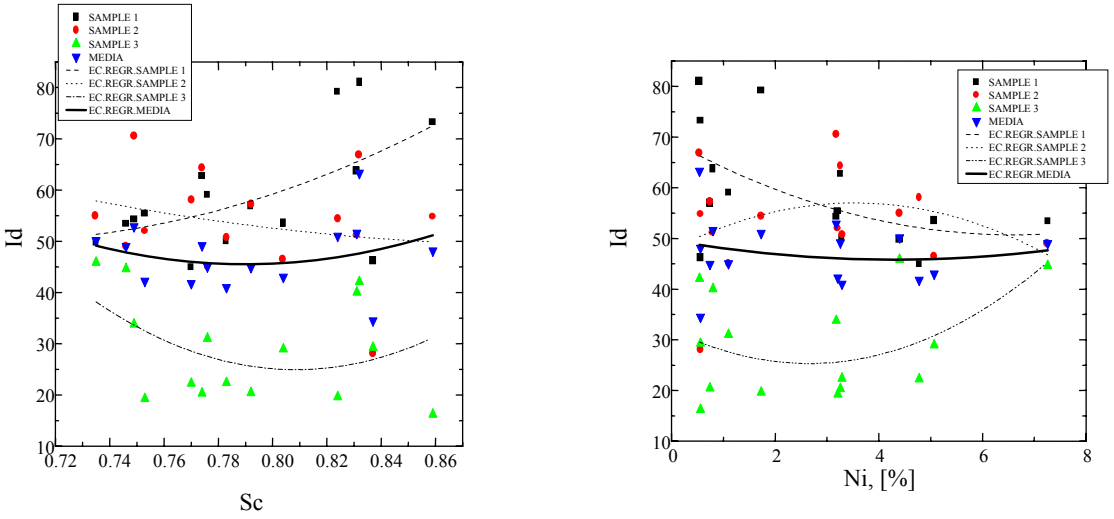

a) *b)*

Fig.6. Influence of the carbon saturation degree S_c a) and of the Ni content b) on the directing solidification index I_d

Thus, for type 1 samples (with a strong directing of solidification) increasing the carbon saturation degree the possibility of directing of the solidification grows (figure 6a). In the type 2 and 3 samples an increasing of carbon saturation degree is associated with a slight decrease of the directing solidification capacity. In type 3 samples this effect occurs only for the inferior range of values of the carbon saturation degree. At carbon saturation values exceeding 0.82 also a growth the capacity of directing solidification is observed.

The dependence between the wear losses and the chemical composition

These dependencies, shown in figures 7 and 8 were processed under the form of second degree polynomial regression curves, such as to highlight the optimum areas. Figure 7 shows on both curves extreme points located between 1.0 and 1,2 % Ni.

In the case of the test pieces the extreme point is a maximum, while for the balls it is a minimum.

This suggests that in this interval both exploitation durability of the cast irons and the machining capacity are minimum. Consequently, in order to maximise cast iron exploitation characteristics, this interval of Ni contents should be avoided. This type of influence can be explained by the effect of Ni on the structure of cast irons in the context of applying the previously described heat treatment

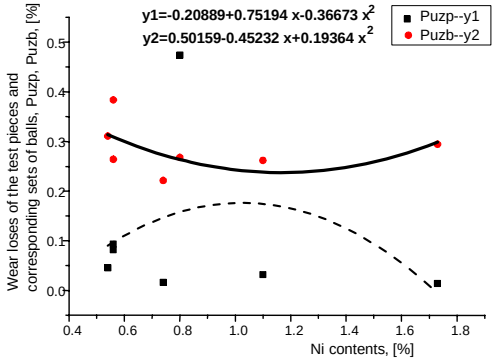

The increase of the carbon saturation degree determines a decrease of cast iron durability (test piece wear losses increase), and at the same time an increase of ball machining capacity (see fig. 9a.). A similar dependence can be noticed also between the equivalent eutectic carbon and the studied wear losses (see fig.9b.).

Fig. 8. Dependence between Ni contents and wear losses

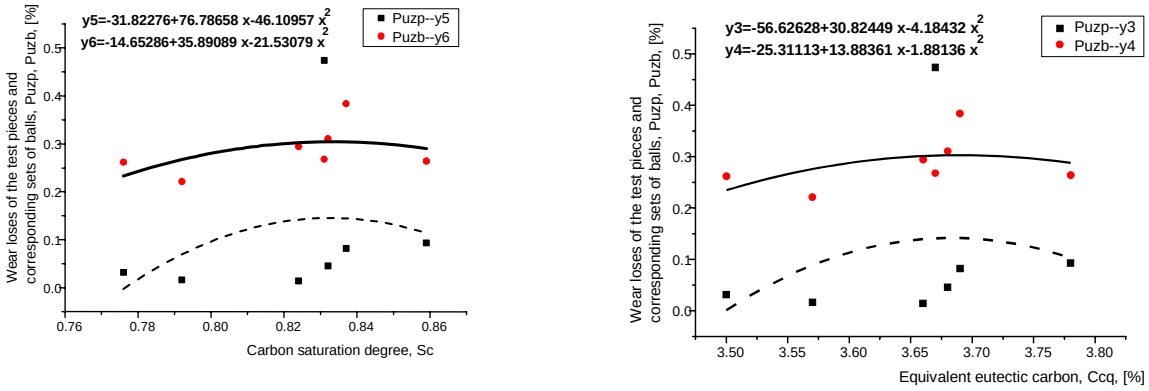

a) b)

Fig. 9. Dependence between carbon saturation degree S_c and wear losses a), end between equivalent eutectic carbon C_{cq} and wear losses b)

4. FINAL CONCLUSIONS

The increase of the degree of carbon saturation S_c has a global decreasing effect of the tendency of shrinkholes occurring in cast samples, associated with their concentration. This effect is augmented in the case of directed solidification, as can be noticed in type 1 samples, where a more significant decrease of the tendency of micro-shrinkhole occurrence is observed for higher values of S_c. A good possibility of controlling the occurrence of solidification defects results for the cast irons of charges 1 to 14 (table 1), which was actually verified on cast disks too.

Strictly according to the present research results, the chemical composition of the cast iron has to be oriented towards Ni contents higher than 1,4 % (1.4 – 1.6%), carbon saturation degrees of S_c= 0.82 – 0.86 and equivalent eutectic carbon C_{cq}= 3.65 – 3.80 %. This orientation however needs to be correlated with research results relative to the technological behaviour of the studied cast irons in the manufacturing process of bearing ball machining disks (casting and heat treatment characteristics). The results of such research carried out by the same authors confirm the validity of the previously specified composition range.

REFERENCES

1. Crisan A., Munteanu S.I., Ciobanu I., Riposan I. *Study about the optimization of chemical composition of cast ironused for casting the bearing ball grinding disks* Eight International Symposium on Science and Processing of Cast Iron- Beijing , China, October 16-19,2006, Proceedings, p424-429.
2. Crişan A., Maşniţă M., Munteanu S. I., Ciobanu I., *Study on the characteristics of cast irons used for the casting of bearing ball grinding disks,* paper presented at Bramat Conference, Brasov, Romania, Vol.I , pp. 244 -249, 13-14-March 2003.
3. Kurz W., Fischer D. J., *Fundamentals of solidification,* Trans tech publication – Switzerland – Germany – UK – USA, 1986.
4. Stefanescu D.M., *Science and engineering of casting solidification,*Kluwer Academic/ Plenum Publisher, New York, Boston, Dordrecht, London, Moscow, 2002.
5. Barton R., *Porosity of Ductil Iron,*Foundry Trade Journal, febr. 1984.
6. Yu S. K., Loper C. R., Cornell H. H., *The effect of Mn, Cu and Ni on the microstructure, hardness and hardenability of ductile irons,* AFS Transactions, vol. 94, 1986.
7. Hecht M., *Tendance à la porosite des fontes à graphite lamellaire,* Fonderie,No. 2, 1980.

Received March 15, 2007

Transilvania University of Braşov, Romania

STUDIU ASUPRA DEPENDENTEI DINTRE COMPOZITIA CHIMICA SI CARACTERISTICILE UNOR FONTE

Rezumat: Lucrarea prezintă o serie cercetări effectuate cu scopul optimizării compoziţiei chimice a fontelor utilizate la turnarea discurilor de pilit bile pentru rulmenti. S-au urmarit proprietăţile tehnologile (în special cele de turnare) şi cele de exploatare (capacitatea de prelucrare a bilelor). Legătura dintre acestea şi compoziţia chimică a fontei s-a realizat prin valoarea conţinutului de Ni, gradul de saturaţie în carbon S_c şi carbonul echivalent C_{cq}. Lucrarea prezintă tipurile de probe utilizate în studiu, condiţiile de lucru, rezultatele cercetărilor experimentale efectuate (sub forma unor dependenţe polinomiale de gradul 2) şi concluziile finale.

BULETINUL INSTITUTULUI POLITEHNIC DIN IAŞI
Tomul LIII (LVII), Fasc. 2, 2007
Secția
ŞTIINȚA ŞI INGINERIA MATERIALELOR

THEORETICAL AND EXPERIMENTAL RESEARCHES ABOUT THE MACROSOLIDIFICATION OF BARS WITH U SECTION

S.I.MUNTEANU, I.CIOBANU, A.CRISAN, M. MASNITA, V.GEAMAN

Abstract: The paper presents a 2D mathematical model, based on finite differences method and software created by authors, to simulate the solidification of castings with translation symmetry. There are presented the hypotheses that are on the basis of the model, the conditions to apply and the basic. There are presented too the results of an experimental research about influence of the inner opening of the U bars on the hot spots position at solidification. The experimental results are compared with the results obtained by solidification simulation.

Keywords: casting, simulation, solidification.

Introduction

During last years the authors realized many research in the domain of mathematical modeling and casting solidification simulation [1÷7]. In the present paper there are presented the mathematical model the simulation software and the results obtained by simulation compared with experimental results. The mathematical model that lay on the basis of the software uses the finite differences method. The software can be used for applied and fundamental studies about to the solidification of casting with translation symmetry, with great length in rapport with the cross section dimensions (bar, tube, plate, and long profile).

In the figure 1 there is presented a cross section throw a mould in which are purred some pieces of bar type with U section. The cross section is perpendicular to the longitudinal axis of the parts. There is presented the mode of sharing the mould assembly section in rectangle finite elements with the dimensions x_i and respectively y_j, where the indexes i =1÷M and j =1÷N, represent the order number for the elements, the numbering being from left to right and from bottom to top.

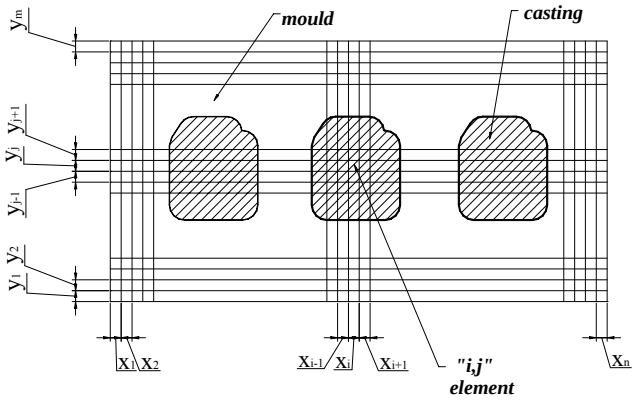

Fig. 1. Cross section through mould-part assembly and the sharing in elementary surfaces.

The time of cooling and solidification process is also divided in finite time intervals $\Delta\tau$. One moment of the process τ_k is expressed as an integer multiple of elementary intervals, $\tau_k=k\cdot\Delta\tau$, where k has values from k=0 to k=kmax. The value $\tau_0=0$ correspond to initial moment, and τ_{kmax} (for $k=k_{max}$) to the final moment of the studied process.

Hypotheses

The mathematical model considers the following hypotheses:

- the contact between the elements is perfect during all the process;
- the heat transmission inside the mould is made only by means of conductivity in perpendicular direction on the sides of the elements;
- the evaporation, re-condensation and burning process inside the walls of the mould are neglected, as well as gases circulation through the pores of the mould;
- the heat exchange between mould-environment is done only by convection;
- the convection currents inside the liquid alloy and at contact surface liquid-solid are neglected;
- there are neglected the variation of the volume with the temperature in solid and liquid state as well as the volume variation at solidification (hypothesis valid in the case when we don't want to calculate the shrinkage cavity volume);
- the alloy solidifies at constant temperature, hypothesis valid for the pure metals and eutectic alloys;
- the mould instantaneous fill with liquid alloy (the liquid alloy flow at the mould filling is neglected);
- the temperature inside the liquid alloy at the initial moment is uniform and equal with the casting temperature T_t
- the temperature in the mould walls at the initial moment is uniform too and equal with T_{0f};
- the flowing and feeding processes during solidification are ignored;

Mathematical model

At one moment $\tau_k=k\cdot\Delta\tau$ the state of a finite surface element with the index „i" on the Ox axis and „j" on Oy axis is characterized by the temperature T_{ij}^{k} and the solidified mass fraction ζ_{ij}^{k}.

The mathematical model is based on thermal balance equation write for an element "i, j" from the mould assembly, corresponding to an elementary time interval $\Delta\tau$, at the moment τ_k.

$$(\Delta Q_{ij}^{k})_s = (\Delta Q_{ij}^{k})_{ced} \qquad (1)$$

The heat changed by the element „i,j" with the four neighbor elements during the time interval $\Delta\tau$ between τ_k and τ_{k+1} is given by the equation:

$$(\Delta Q_{ij}^k)_s = [\alpha_{i-1,i,j,j}^k (T_{ij}^k - T_{i-1,j}^k) y_j + \alpha_{i,i+1,j,j}^k (T_{i,j}^k - T_{i+1,j}^k) y_j + \\ + \alpha_{i,i,j-1,j}^k (T_{i,j}^k - T_{i,j-1}^k) x_i + \alpha_{i,i,j,j+1}^k (T_{i,j}^k - T_{i,j+1}^k) x_i] \Delta\tau \quad (2)$$

In the hypothesis of thermal transfer between the finite elements throw thermal conductivity, the thermal transfer coefficient between two adjoining elements are given by the equations:

$$\alpha_{i,i+1,j,j}^k = \frac{2}{\frac{x_i}{\lambda_{i,j}^k} + \frac{x_{i+1}}{\lambda_{i+1,j}^k}} \quad (3)$$

and respectively

$$\alpha_{i,i,j,j+1}^k = \frac{2}{\frac{y_j}{\lambda_{i,j}^k} + \frac{y_{j+1}}{\lambda_{i,j+1}^k}} \quad (4)$$

In the conditions of uniform sharing in square surface elements ($x_i=y_i=x_{i+1}=y_{i+1}$) and in the case of an element "ij" is partially solidified (ξ_{ij}^k) and partially liquid ($1-\xi_{ij}^k$), at the moment τ_k, the equivalent thermal coefficient is given by the equation:

$$\lambda_{ij}^k = \frac{1}{\frac{\xi_{ij}^k}{\lambda_{Sij}^k} + \frac{1-\xi_{ij}^k}{\lambda_{Lij}^k}} \quad (5)$$

The values for thermal exchange coefficients with environment $\alpha_{0,1,j,j}^k$, $\alpha_{M,M+1,j,j}^k$, $\alpha_{i,i,0,1}^k$ and $\alpha_{i,i,N,N+1}^k$ are introduced as initial data as function of temperature: $\alpha_{o,1,j,j}^k = f_\alpha(T_{0,j}^k; T_{1,j}^k)$, $\alpha_{M,M+1,j,j}^k = f_\alpha(T_{M,j}^k; T_{M+1,j}^k)$, $\alpha_{i,i,0,1}^k = f_\alpha(T_{i,0}^k; T_{i,1}^k)$ and $\alpha_{i,i,N,N+1}^k = f_\alpha(T_{i,N}^k; T_{i,N+1}^k)$.

The mass heat $(\Delta Q_{ij}^k)_{ced}$ released (or received) by the „i,j" element during the elementary time interval $\Delta\tau$, as result of temperature and (or) solidified fraction variation is expressed in function of the temperature $T_{i,j}^k$ and solid fraction $\xi_{i,j}^k$ in the initial state, at the moment τ_k and in function of the temperature $T_{i,j}^{k+1}$ and solid fraction $\xi_{i,j}^{k+1}$ in the final state, at the moment τ_{k+1}. As result, depending on these parameters, 9 situations are possible. So using the thermal balance equation (1), the solid fraction $\xi_{i,j}^{k+1}$ in the "i,j" element, at the moment τ_{k+1} can be calculated with one of the equations:

$$\zeta_{ij}^{k+1} = \left[\frac{\Delta Q_{ij}^{k}}{x_i y_j \rho_{Lij}^{k}} - (T_{ij}^{k} - T_{sij}) c_{Lij}^{k} \right] \frac{1}{L_{ij}} \tag{6}$$

$$\zeta_{ij}^{k+1} = \zeta_{ij}^{k} + \frac{\Delta Q_{ij}^{k}}{x_i y_j \rho_{Lij}^{k} L_{ij}} \tag{7}$$

$$\zeta_{ij}^{k+1} = 1 + \frac{\Delta Q_{ij}^{k} - x_i y_j \rho_{sij}^{k} (T_{ij}^{k} - T_{sij})}{x_i y_j \rho_{sij}^{k} L_{ij}} \tag{8}$$

If the value ζ_{ij}^{k+1} calculated with these equations is not comprised inside the interval [0,1], then the temperature T_{ij}^{k+1} of the „i,j" element at the moment τ_{k+1}, is calculated with one of the next equations.

$$T_{ij}^{k+1} = T_{ij}^{k} - \frac{\Delta Q_{ij}^{k}}{x_i y_i \rho_{Lij}^{k} c_{Lij}^{k}} \tag{9}$$

$$T_{ij}^{k+1} = T_{sij} - \frac{\dfrac{\Delta Q_{ij}^{k}}{x_i y_i} - \rho_{Lij}^{k} (T_{ij}^{k} - T_{sij}) c_{Lij}^{k} - \rho_{Lij}^{k} L_{ij}}{\rho_{Sij}^{k} c_{sij}^{k}} \tag{10}$$

$$T_{ij}^{k+1} = T_{ij}^{k} - \frac{\Delta Q_{ij}^{k} + x_i y_j \rho_{Lij}^{k} L_{ij} \zeta_{ij}^{k}}{x_i y_i \rho_{Lij} c_{Lij}^{k}} \tag{11}$$

$$T_{ij}^{k+1} = T_{ij}^{k} - \frac{\Delta Q_{ij_{ced}}^{k} - x_i y_j \rho_{Lij}^{k} L_{ij} (1 - \zeta_{ij}^{k})}{x_i y_i \rho_{Sij}^{k} c_{sij}^{k}} \tag{12}$$

$$T_{ij}^{k+1} = T_{ij}^{k} - \frac{\Delta Q_{ij}^{k}}{x_i y_j \rho_{Sij}^{k} c_{sij}^{k}} \tag{13}$$

$$T_{ij}^{k+1} = T_{sij} + \frac{x_i y_j \rho_{ij}^{k} c_{sij}^{k} (T_{ij}^{k} - T_{sij}) - x_i y_j \rho_{Sij}^{k} L_{ij} - \Delta Q_{ij}^{k}}{x_i y_j \rho_{Lij}^{k} c_{Lij}^{k}} \tag{14}$$

It is possible that the equations presented above have a simplest aspect if the values of space sharing for the elements are equal in the both directions (x_i=y_j) and also if the volume variation with temperature as well as at the transforming from

liquid to solid is neglected. In this case it can be considered that the alloy has constant density ($\rho_{Lij}^{k}=\rho_{Sij}^{k}=\rho$).

6. Results.

The mathematical model was used to create a computer program to simulate the solidification of a bar with U shape section, cast in eutectic gray cast iron. The geometric shape and the dimensions of the bar are given in the figure 2. The walls thickness for the studied bar is a=20mm. The distance between the parallel arms of the profile is b=20mm. Due to this cause the bar section is noted as U_{axb} that it means U_{20x20}. Because the analyzed piece has a translation symmetry with constant section, and the length L is great comparing with the cross section dimensions (L>6(b+2a)), the cooling throw the bar ends do not influence the solidification in the cross section from the middle of the bar. As result for the solidification simulation of this part a 2D software can be used.

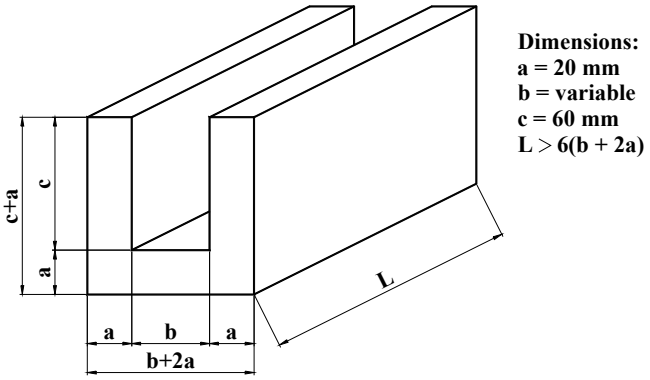

Fig. 2. The geomery of the bars

The part is cast in grey eutectic alloy. The thermal parameters of the cast alloy and of the mould material considered for simulation in this study are:

ρ_L = 7070 kg/m^3, ρ_S = 7286 kg/m^3, λ_L = 30 W/mK, λ_S = 40 W/mK, c_L = 1080 J/kgK, c_S = 850 J/kgK, L = 292800J/kg, ρ_f = 1550kg/m^3, λ_f = 0,7W/mK, c_f = 1200J/kgK, α_{aer} = 30W/m^{2}K, T_T = 1350°C, T_S = 1153°C, T_a = 20°C, T_{0f} = 20°C.

The dimensions of the surface elements, in which the mould and casting were divided, were $x_i=y_j$=2mm. The time step to study the thermal transfer was $\Delta\tau$= 0,1s. The maximum time step number for studying the cooling and solidification was k_{max}=10000 that corresponds to a time interval τ_{max}=1000s.

In the table 1 there are given the results obtained by computer simulation referring to solidification time and hot spots position

In the second part of the research there was realized an experimental research to verify if the results obtained by computer simulation are confirmed by casting praxis. The experimental research try to locate the shot spots position throw shrinkage faults position in castings and to compare the experimental research with those obtained by simulation. In this but there were cast three type of bars, considered representatives U_{20x4}, U_{20x20} and U_{20x120}. The chemical composition of the grey cast iron is given in table 2. The parts are poured in green moulds realized with lost pattern.

Table 1 The hot spots coordinates are measured in rapport with a coordinate system with the origin at the intersection of the section axis and external surface of the crossing part.

No.	Part	Slot dimension	Hot spots coordinates		Solidification time
		b[mm]	*x*[mm]	*y*[mm]	τ[s]
1	U20x0	0	0	40	905.8
2	U20x4	4	-2 and 2	38	838,9
3	U20x8	8	-4 and 4	34	777,3
4	U20x12	12	-6 and 6	30	721,8
5	U20x16	16	-8 and 8	28	679,7
6	U20x20	20	0	20	671,3
7	U20x30	30	0	16	645.1
8	U20x40	40	0	14	632.0
9	U20x60	60	-10 and 10	12	607.3
10	U20x80	80	-24 and 24	12	596.6
11	U20x100	100	-38 and 38	14	593.8
12	U20x120	120	-48 and 48	14	593,5
13	U20x160	160	- 68 and 68	14	593,5
14	U20x200	200	-88 and 88	14	593,5
15	U20x300	300	-138 and 138	14	593,5

Table 2 The chemical composition of the grey cast iron

Material symbolization.			Chemical composition.					Sc
Conf. STAS	Conf. SREN 1561		% C	% Si	% Mn	% P	% S	
	alphanumerical	numerical						
Fc. 250	EN GJL250	EN JL040	3,0 ÷ 3,4	1,8 ÷ 2,5	0,6 ÷0,8	max. 0,3	max. 0,12	0,89

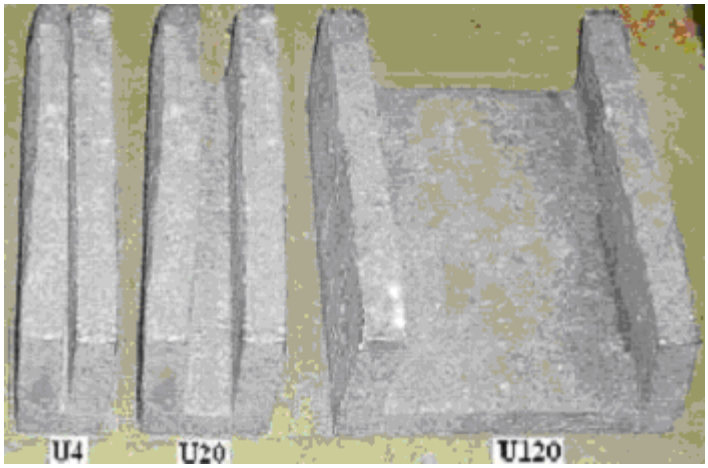

Fig.3 Experimental parts cast in grey cast iron.

The castings are presented in figure 3. To evidence the shrinkage fault position the parts were cut in the cross section at the middle of the length. In the figures 4 there are presented the photos of the sectioned castings and marked the shrinkage position. In the figures 5 there are presented the corresponding isotherms map at the end of solidification determined by computer simulation.

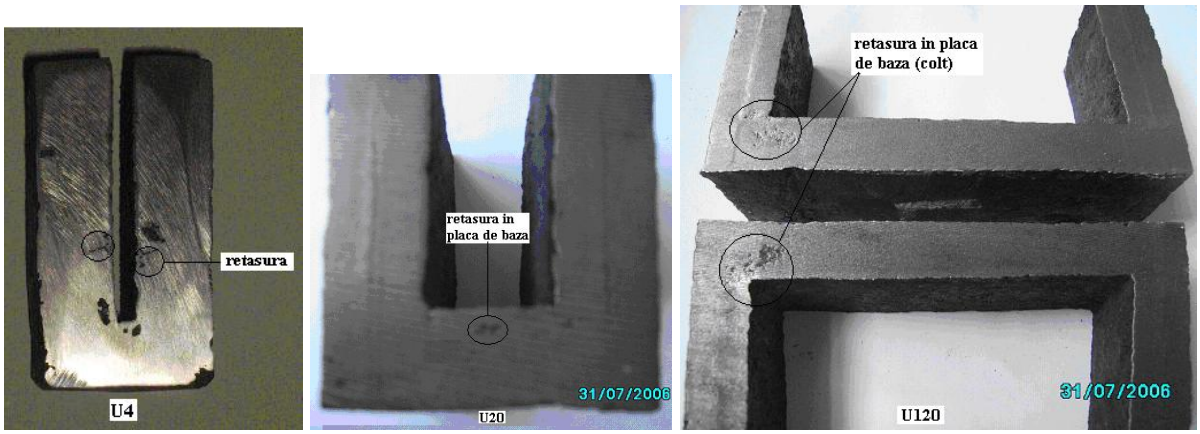

Fig.4 Cross section through the parts U20x4, U20x20 and U20x120 to localize the shrinkage.

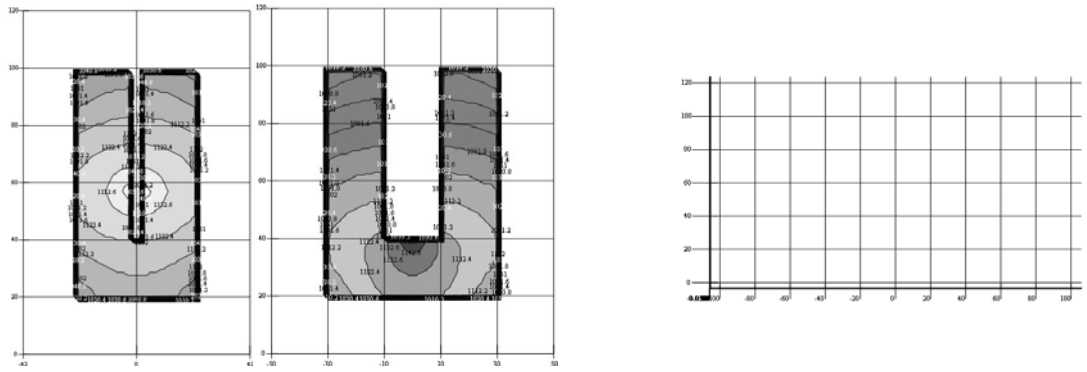

Fig.5 The temperature map obtained by simulation in the cross section through the parts U20x4, U20x20 and U20x120

Analyzing the castings section it was observed the shrinkage are slight dispersed. This is explained by one side by the small solidification shrinkage of the grey cast iron, and on the other side by the reduction of feed capacity (alloy flow) in the solidification zone at the end of part solidification. It can be assumed that the hot spot position correspond to middle zone of porosity. Comparing the shrinkage position in the experimental castings with the hot spot position determined by computer simulation can be observed that in the case of parts U_{20x4}, U_{20x20} and U_{20x120} the shrinkage position of the experimental castings correspond to the position determined by simulation.

Symbols

- x_i, y_j- the length of the finite elements sides in the directions of the two axes 0x, 0y;
- $\Delta\tau$- the elementary time interval for which the thermal balance equations are written;
- i, j – the index number of the finite surface elements with the length x_i and respectively y_j, in the two directions Ox and Oy;
- k – the index number of the elementary time interval $\Delta\tau$;
- M, N – the maxim value of the parameters "i", respectively "j";
- k_{max}- the maximum value the parameter „k";
- T_{ij}^{k} - the temperature of the element with indexes i,j at the τ_k;
- ξ_{ij}^{k} - the solidified fraction in the "ij" element at the moment τ_k;
- T_{Sij} - the solidus temperature of the "ij" element;

• ρ_{Sij}^{k} - the density of the ”ij” element in solid state at the moment τ_k;

• ρ_{Lij}^{k} - the density of the ”ij” element in liquid state at the moment τ_k;

• L_{ij} – the specific latent heat of the element ”ij”;

• c_{Sij}^{k} - the specific heat in solid state for the ”ij”element at the moment τ_k;

• c_{Lij}^{k} - the specific heat in liquid state for the ”ij”element at the moment τ_k;

• $\left(\Delta Q_{ij}^{k}\right)_s$ - the heat changed by the ”ij” element with the neighbor elements, during the elementary time interval $\Delta\tau$;

• $\left(\Delta Q_{ij}^{k}\right)_m$ - the mass heat released by the ”ij” element, during an elementary time interval $\Delta\tau$, as result of temperature or solidified fraction modification, at the moment τ_k;

• λ_{sij}^{k} - the thermal conductibility coefficient in the solid state for the ”ij” element, at the moment τ_k;

• λ_{Lij}^{k} - the thermal conductibility coefficient in the liquid state for the ”ij” element, at the moment τ_k;

• $\alpha_{i-1,i,j,j}^{k}$ - the heat transfer coefficient at the moment τ_k, in 0x direction, between the element ”i-1,j” and the element ”i, j”;

• $\alpha_{i,i,j-1,j}^{k}$ - the heat transfer coefficient at the moment τ_k, in 0y direction, between the element ”i,j-1” and the element ”i, j”;

References:

[1]- **CIOBANU I., MUNTEANU S., CRIŞAN A**. – Mathematical modelling of the cooling process using finite differences method, Eight Israel Materials Engineering Conference, IMEC VIII, Ben Gurion University of Negev, Beer Sheva, Israel 16-17 April 1997, Proceedings pp. 138.

[2]- **CIOBANU I, MUNTEANU S I, CRIŞAN A** - Influența distanței dintre piese în forma de turnare asupra cineticii solidificării la turnarea în forme crude - Buletin ştiințific Conferința Internațională de Ştiința şi Ingineria Materialelor BRAMAT 99 , 3-5 Feb. 1999,Ed. Universității Transilvania Braşov, vol II, ISBN 973-98797-0-5, pag. 44-58,

[3]- **MUNTEANU S. I., CIOBANU I., CRIŞAN A**. - Cercetări prin simulare pe calculator privind repartizarea izotermelor câmpului de temperatură la solidificarea barelor cu secțiune U turnate din fontă cenuşie.- Turnarea şi Solidificarea Metalelor şi Aliajelor TSMA’2004, Ed. U.T. Pres Cluj-Napoca, Tome II 2004, p19-28, ISSN1453-9756

[4]- **MUNTEANU S. I**. - Computer aided simulation of aluminum alloys solidification in continuous electromagnetic casting -Proceedings of the International Conference on The Science of Casting and Solidification, 28-31 May 2001, Brasov, Romania, ISBN 973-9428-67-3, p. 151-157,

[5]- **CIOBANU I., MUNTEANU S. I., CRIŞAN A.**,- Mathematical model and 2D software based on finite differences method for simulation of the solidification of the parts cast from eutectic alloys – Proceedings International Conference on Materials Science & Engineering BRAMAT 2003, 13-14 March, Transilvania University of Braşov Publishing House, vol. I, ISBN 973-635-122-X/973-635-123-8, pp. 250-255.

[6]- **MUNTEANU SORIN ION, CIOBANU IOAN, CRIŞAN AUREL** - Cercetări privind particularitățile solidificării profilelor cu secțiune U20×20 - Revista METALURGIA Nr.12/2004 pag 25-36 ISSN 0461-9579

[7]- **MUNTEANU SORIN ION, CIOBANU IOAN, CRIŞAN AUREL** – Partcularitai privind solidificarea barelor cu sectiune „U” cu deschidere mare intre bratele paralele - METALURGIA Editura ştiințifica F.M.R. Nr. 4, 2005, p 38-52, ISSN 0461-9579

Received March 15, 2007

Transilvania University Brasov

Abstract. *Lucrarea prezinta un model matematic 2D, bazat pe metoda diferentelor finite si un soft creat de autori pentru simularea solidificarii pieselor turnate cu simetrie de translatie. Sunt prezentate ipotezele care stau la baza modelului conditiile de aplicare si ecuatiile de baza. Sunt prezentate de asemenea rezultaele unei cercetari experimentale privind influenta deschiderii unui profil turnat cu sectiune U asupra pozitiei nodurilor termice la solidificare. Rezultatele experimentale sunt comparate cu rezultatele obtinute prin simulare pe calculator*

BULETINUL INSTITUTULUI POLITEHNIC DIN IAŞI
Tomul LIII (LVII), Fasc. 2, 2007
Secția
ŞTIINȚA ŞI INGINERIA MATERIALELOR

TEMPERATURE AND THERMAL STRESS FIELD AT ROLLING LINEAR CONTACT, WITH APPLICATIONS AT ROLLING CYLINDERS

BY

FLORIN TUDOSE SANDU – VILLE, VASILE BULANCEA, OVIDIU CALANCEA

Abstract*. The increase of the industrial products quality is possible trough reliability rising. For machine parts located in enclosure, where premature deteriorations are difficult to record in a non-stop program of work, under thermo-mechanical contact loads, is important to have an evaluating solution for repairs and for the changing parts program. These conditions apply also for non active rolling mill rollers. The paper presents some types of calculations for thermal stresses, the main cause for global thermo-mechanical contact wear. The variable thermo-elastic stresses indicated by a thermal tide determine the faster occurrence of a cracking and pitting field in a contact layer. Some experimental results obtained on a test rig and their mathematical analysis are also presented.*

Keywords: *temperature, thermal stress, global thermo-mechanical contact wear*

I. Theoretical background

Most of the technological processes are carried out with heat release. With the increase of the parameters of machine working processes, the heat transfer from the working medium to the parts or from warmer to colder parts is intensified, the heat stress increasing.

That is why one can notice that, out of the total disturbances of parts determined by static, cyclical, dynamical stresses, as well as by other types of loads, the relative contribution of the defects induced by thermal cyclical loadings increases.

The heat stresses determine thermal stresses in the structure of parts and machine components.

The thermal stresses that appear in a part during its operation or the technological process (for example during a heat treatment) can be higher than those produced by external forces or moments, sometimes resulting in part cracking. Considering this, the calculation of certain machine components taking into account only the mechanical stresses is not enough, being necessary to consider the thermal stresses too.

The thermal stresses also influence the durability, especially in the case of variable strengths. The thermal stress character depends on the temperature field which they provoke. A stationary temperature field will induce static stresses. In the case of time variations of the temperature field, its changing rate is very important. In case of small temperature rates, the thermal stresses can be considered as quasi-static. At higher temperature rate variable thermal stresses will be generated.

If the strains remain within the elastic zone during the loading, the stresses are thermo-elastic, while when the strains enter the elastic-plastic range the stresses are thermo-plastic.
The cyclical temperature variation can induce cracking in machine components (similarly to breaking produced by the stresses created by external forces), a phenomenon called thermal fatigue. Unlike the thermal fatigue which appears after a relatively big number of loading cycles, there is the heat shock (the heat stress induced in a body at its contact with a fluid with a temperature differing from that of the body), which can result in part destruction after a small number of cycles.
The destruction provoked by alternative thermal cyclical loadings- thermal fatigue- can be noticed in a specific form only with the parts which are subjected to an insignificant additional mechanical load.
The damaging action of this kind of loading is revealed in a much more important manner when it is combine with the internal pressure, with centrifugal stresses, external loading (rolling cylinder, gears working under high temperature conditions) or under the conditions of insufficient lubrication or cooling.
In these situations, the thermal-cyclical damage of parts superficial layers usually represents the cause of the appearance of the first destruction centers, which then get generalized under the joint action of the other stress types.
The rolling cylinders represent a category of machine components- tools at which the mechanical and thermal stresses have significant values, presenting a variable character, thus belonging to the above specified working conditions.
One of the important conditions of hardened superficial layer damaging at the rolling cylinders is represented by the very high thermal stresses in their superficial layer. These stresses present a cyclical character due to repeated heating and cooling of this layer during each cylinder rotation.

II. Temperature field in active cylinders

The specialized literature presents data concerning the temperature field in rolling cylinder in terms of:

- Heat exchange conditions
- Rolling speed
- Emulsion flow rate
- Down-time duration.

At the same time, there are data concerning the determination through computation, of the most probable moments when cracks and detachments can appear on the active surface of the rolling cylinders.
The thermal calculus starts from the facts that the strain focus is represented by a heat source. The enthalpy modifications for the plate, ΔQ_b, and cylinder ΔQ_c respectively when the plate passes through the strain focus will be:

$$\Delta Q_b = 2(-Q_1 + Q_2 + Q_3) \quad (1)$$

$$\Delta Q_c = 2(Q_1 + Q_2' + Q_3' + Q_4) \quad (2)$$

where:
Q_1 is the heat given up by the plate to a rolling cylinder if the plate temperature is higher,

Q_2 and Q_2' - the quantities of heat received by the plate and cylinder as the result of the conversion to heat of the mechanical work, due to plate shape change;
Q_3 and Q_3' – the quantities of heat received by the band and cylinder as the result of the conversion to heat, of the friction force mechanical work.
Q_4 – the heat quantity due to mechanical hysteresis.
The temperature of the cylinder surface T_{sc} when leaving the rolling focus will be:

$$T_{s,c} = T_0 + \Delta T_1 + \Delta T_2 + \Delta T_3 \quad (3)$$

where:
T_o – the initial temperature of the cylinder surface,
ΔT_1 – temperature increase due to higher plate temperature,
ΔT_2 – temperature increase due to plate plastic strain,
ΔT_3 – temperature increase due to friction.
The temperature variations are determined taking also into account the existence of the lubricant film between the plate and the cylinder, namely:

$$\Delta T_1 = (T_{b_0} - T_{c_0}) \frac{K_\varepsilon}{1 + K_\varepsilon} F_1(\mathrm{H}) \quad (4)$$

$$\Delta T_2 = \frac{\sigma_{c,med} \cdot \ln \frac{H}{h}}{c_b \gamma_b} \cdot \frac{\tau}{\tau_t} \cdot \frac{K_\varepsilon}{1 + K_\varepsilon} F_3(\mathrm{H}) \quad (5)$$

$$\Delta T_3 = \frac{2q}{\lambda b} \sqrt{a_b \tau} \frac{K_\varepsilon}{1 + K_\varepsilon} \quad (6)$$

where:
T_{bo} and T_{co} are the contact temperatures at the surface of plate and cylinder respectively, in the rolling focus [^{o}K],
$K_\varepsilon = \sqrt{\frac{\lambda_b \rho_b c_b}{\lambda_c \rho_c c_c}}$ – the criterion of thermal diffusivity of the material of plate and rolling cylinder,
λ – the coefficient of thermal conductivity, in [W/m· ^{o}K],
c – the material specific heat, in [J/kg· ^{o}K],
ρ – density, in [kg/m^3]
α – thermal diffusivity, $a = \frac{\lambda}{\rho \cdot c} [m_2 / s]$
$\sigma_{c\,med}$ – the ultimate strength of the plate material in the strain focus,
H and h – the plate thickness before and after the strain,
τ and τ_t – the total elapsed time and the contact time respectively,

$\mathrm{H} = \frac{K\sqrt{a_b \tau}}{\lambda_b}(1 + K_\varepsilon)$ the criterion of contact heat transfer,

K – the coefficient of heat exchange from the plate to the cylinder through the emulsion film ($K = \frac{\lambda_c}{\rho_c}$.),

$\lambda_c = 0{,}6 - 0{,}68 [W / m^0 K]$

For emulsion cooling of the cylinder:

$K = (6-13{,}6)\cdot 10^5 [W/m^{2\cdot 0}K]$ $K = (30-68)\cdot 10^4 [W/m^{2\,0}K]$ (emulsion cooling)

ρ_c = 1- 2μm, the emulsion film thickness.

$$F_1(\mathrm{H}) = 1 - \exp H^2, erfcH \qquad (7)$$

$$F_3(\mathrm{H}) = \frac{1}{H^2}[1 - \exp \mathrm{H}^2 \cdot erfc\mathrm{H} - 2\mathrm{H}(0{,}5642 - 0{,}5\mathrm{H})] \qquad (8)$$

where erfcH= 1- erfH, the Gauss error function

q – the intensity of heat emission at the cylinder- plate contact. The approximate value of q is determined as

$$q = \frac{1}{S}\int_S \tau_x \cdot u \cdot dS \qquad (9)$$

where:

r_s – the instantaneous value of the slip stress

S – the area of the contact surface [m^2]

u – relative slip speed.

The temperature variation on the rolling cylinder surface is presented in Figure 1

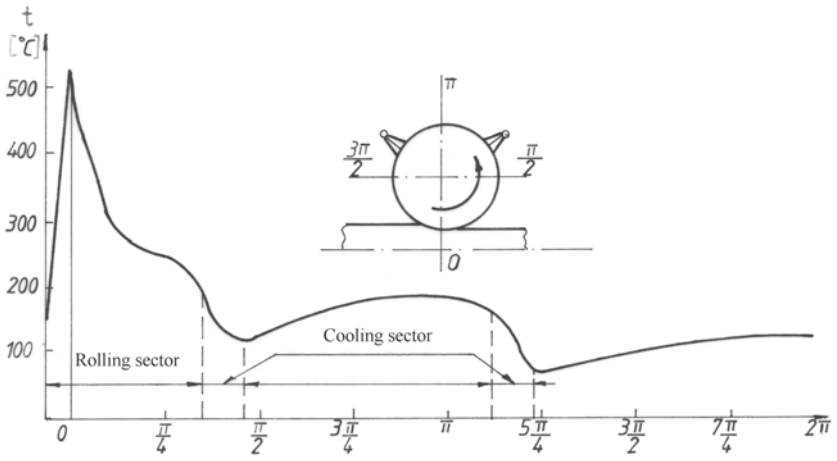

-Figure 1.-

The non-uniform temperature distribution, both in the tangential and radial directions, will generate important thermal stresses.

III. Temperature Stresses

Whenever the expansion or contraction that would normally result from the heating or cooling of a body is prevented, stresses are developed that are called *thermal,* or *temperature, stresses.* It is convenient to distinguish two different sets of circumstances under which thermal stresses occur: (1) The form of the body and the temperature conditions are such that there would be no stresses except for the *constraint of external forces;* in any such case, the stresses may be found by determining the shape and dimensions the body would assume if unconstrained and then calculating the stresses produced by forcing it back to its original shape and. (2) The form of the body and the temperature conditions are such that stresses are produced in the *absence of external constraint* solely because of the incompatibility of the natural expansions or contractions of the different parts of the body.

A number of representative examples of each type of thermal stress will now be considered later in the paper. In all instances the modulus of elasticity *E* and the coefficient of thermal expansion *y* are assumed to be constant for the temperature

range involved and the increment or difference in temperature AT is assumed to be positive; when AT is negative, the stress produced is of the opposite kind.

A long hollow cylinder with thin walls has the outer surface at the uniform temperature T and the inner surface at the uniform temperature $T + \Delta T$. The temperature gradient through the thickness is linear. At points remote from the ends, the maximum circumferential stress is ½ ΔTγE / (1 — ν) (compression at the inner surface; tension at the outer surface) and the longitudinal stress is ½ $\Delta T\gamma E/1$-ν) (compression at the inside; tension at the outside).

A hollow cylinder with thick walls of inner radius b and outer radius c has the outer surface at the uniform temperature T and the inner surface at the uniform temperature $T + \Delta T$. After steady-state heat flow is established the temperature decreases logarithmically with r and then the maximum stresses, which are circumferential and which occur at the inner and outer surfaces, are

$$\sigma_t = \frac{\Delta T\,\gamma E}{2(1-\nu)\,\log_e(c/b)}\left(1-\frac{2b^2}{c^2-b^2}\log_e\frac{c}{b}\right)$$ (Outer surface) – Tension

$$\sigma_t = \frac{\Delta T\,\gamma E}{2(1-\nu)\,\log_e(c/b)}\left(1-\frac{2c^2}{c^2-b^2}\log_e\frac{c}{b}\right)$$ (Inner surface) – Compression

In [2] is presented the expression for the calculation of the thermo-elastic stresses in a cylinder situated in a variable temperature field.

Let's consider a cylinder of internal radius R_1 and external radius R_2 with the temperature variable only in terms of radius and time T(r, τ). At the beginning the cylinder temperature equals zero, while at the moment τ = 0 the cylinder is introduced into two mediums: one from inside the cylinder of temperature T_1 and the other from outside the cylinder of temperature T_2

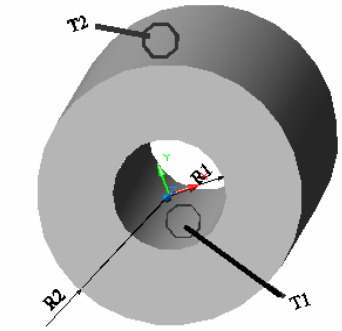

Given the axial symmetry, $\varepsilon_{zz} = 0$ and therefore the stresses can be expressed only in terms of the radial motion u_r. It follows that:

$$\sigma_{rr} = \frac{E\alpha}{2(1-\mu)}(1-\frac{R_1^2}{r^2})[T(R_2\tau)-T(r,\tau)];\ (10)$$

$$\sigma_{\phi\phi} = \frac{E\alpha}{2(1-\mu)}(1+\frac{R_1^2}{r^2})[T(R_2\tau)+(1-\frac{R_1^2}{r^2})T(r,\tau)-2T(r,\tau)];\ (11)$$

where: $T(r,\tau)$ represents the cylinder average temperature reported to the radius r. The stress values calculated for a cylinder with Ø400mm and inside hole with Ø80mm at $\Delta t = 60^oC$ have been around 200 MPa [1].

IV. Experimental results

On the test rig presented in [4] rolling tests were carried out for rolls of $Ø_{ext\ max}$ = 116mm and $Ø_{int\ max}$ = 80mm. The temperatures were measured with a "National Instruments" transducer and software. The measured temperatures ranged between 20 and 100°C for the maximum rolling intervals (continuously) equal to 5 hours.

The maximum normal contact stress was 400 MPa for a contact width ranging between 10 and 20mm. The rotation speed was 125 rpm, the same for all the rolls in contact. The rolls material was OLC45xB3STAS80-88. The experimental results were analyzed by of computation software. The diagrams of thermo-elastic stresses variation in cylinders are presented using various calculation solutions and temperature intervals.

Figure 3

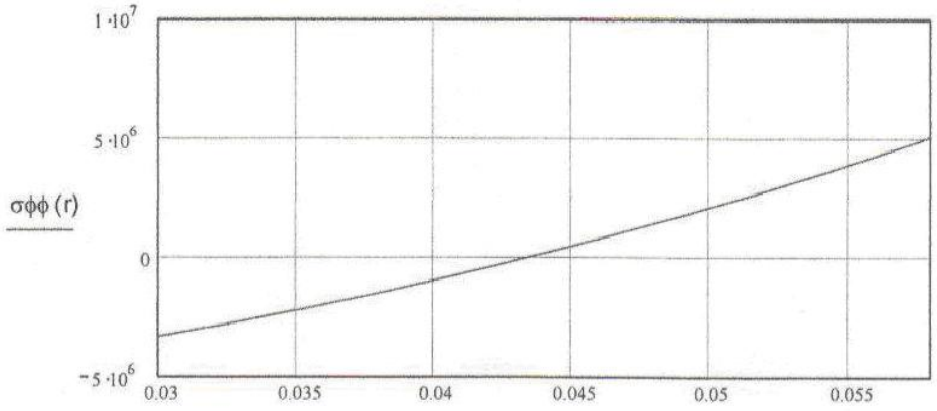

Figure 4

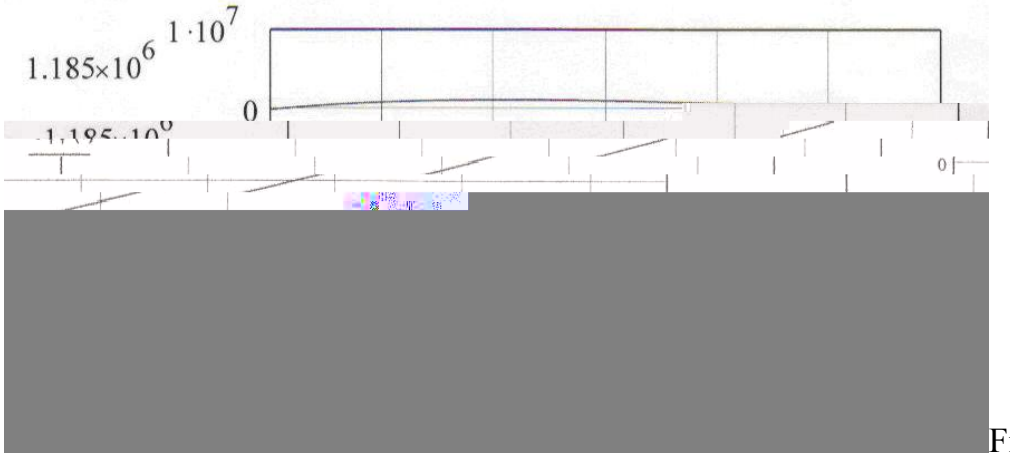

Figure 5

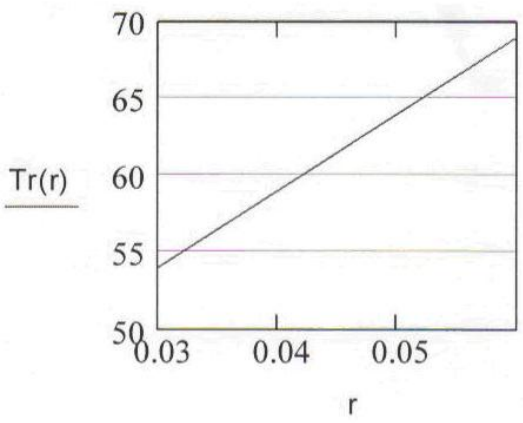

Figure 6

V. Conclusions

The thermal stresses are important components of the resulting equivalent stress, the cause of deterioration of the rolling cylinders working surfaces.

The maximum values of the thermal stresses appears at the beginning of cylinder heating, when the temperature difference between layers of different depth is larger, also due to the cylinder thermal inertia.

The alternative thermo-cyclical tests determine the appearance of localized defects in the superficial layer, which become initiation centers for deteriorations which get generalized later under joint action of the other types of stresses.

The appearance of the thermal shock results in speeding the initiation of deterioration.

The temperature difference between the cylinder internal and external surfaces changes in direct proportion with the value of thermal stresses.

The weight of the thermal deteriorations is higher at the beginning of the process, the other stress types resulting mainly in deteriorations in the next stages of the process.

References

1. Poluhin V.N., Nicolaev V.A., a.o. – "Nadejnost i dolgovecinost valkov holodnoi prokatki", Moskva, Metallurgija, 1976
2. Popa Bazil, Mădărăşanu T., a.o. – "Solicitări termice în construcţia de maşini", Ed. Tehnica, Bucureşti, 1978
3. Racocea C, Tudose-Sandu-Ville Florin – "Thermal Stress Evaluation in Active Rollers for Hot Rolling Mill", Buletinul Institutului Politehnic Iaşi, Tomul XXXIX (XLIII), fasc.1-4, secţia V, Construcţii de maşini, 1993
4. Tudose-Sandu-Ville Florin – "Experimental Research and Statistical Evaluation concerning Linear Contact Reliability", Balkan Journal of Tribology, 2005
5. Warren C. Young – "Roark's Formulas for Stress and Strain", Sixth edition, McGraw, Hill Book Company, 1989

Received April, 2007

Technical University Iaşi

CÂMPUL DE TEMPERATURI ŞI TENSIUNI TERMICE LA CONTACTUL LINIAR CU ROSTOGOLIRE, CU APLICAŢII LA CILINDRI DE LAMINOR

Rezumat. *Lucrarea prezintă componentele temperaturii suprafeţei cilindrului la ieşirea din focarul de laminare, cât şi relaţii de calcul pentru tensiunile din cilindri în diverse situaţii de funcţionare. Rezultate experimentale obţinute pe un stand propriu de încercri sunt prelucrate şi au făcut obiectul unei analize. Apariţia şocului termic determină accelerarea iniţializării deteriorării; diferenţa de temperatură dintre suprafeţele interioare şi exterioare ale cilindrului este direct proporţională cu valoarea tensiunilor termice.*

BULETINUL INSTITUTULUI POLITEHNIC DIN IAŞI
Tomul LIII (LVII), Fasc. 2, 2007
Secția
ŞTIINȚA ŞI INGINERIA MATERIALELOR

THE CONDUCTYNG OF FURNACES FOR THERMIC TREATMENT BY MODELING OF TRANSFORMATION PROCESSES AND THE PREDICTION OF MICROSTRUCTURES AND PROPERTIES OF STEELS.

BY

IULIAN CUCOŞ

Abstract: *The establishment of prediction methods based on the phenomenological description and computer simulation of the transformation processes during heat treatment and the development of software for technological planning has been of major interest.*

The control of furnaces for thermic treatment is a consequence of permanent effort for relief of work through amplify of his capacity in solving problems of productions. The advanced system for conducting the furnaces rof heat treatments has the main importance in different activities developed in hard conditions.

Keywords: *properties prediction, heat treatment of steels, computer simulation, designing and conducting system, computer simulation,. electric furnaces, conduct, property prediction, PID and PlD-predictive controller.*

1. Introduction

The development of computer simulation of heat treatments has been concentrated on two main areas of interest:

- modeling of transformation processes and the prediction of microstructures and/or properties ;
- developing program packages (designed in the majority of cases to be purchased on the market for direct industrial use) to help solve concrete tasks such as material selection, property prediction, and the design of heat-treating operations

By introducing computer methods, steel heat treatments can be analyzed and/or optimized in terms of product quality, property scatter, processing time, and energy consumption.

A proper computer algorithm makes it possible to select the heat-treatment parameters that result in minimum energy consumption and optimum mechanical properties. Because of the many factors involved, reducing energy consumption is an optimization task that can be done only by applying a suitable simulation computer program.

Simulation software can be classified either as on-line programs for process control or as programs to assist decision making and process analysis and can be subdivided into:

- property prediction programs
- process planning programs
- material selection programs and their data bases
- programs for special technical and economic problems in connection with heat treatment .
- finite-element analysis for modelling the effects of quench severfty on distortion and dimensional control of parts.

2. Concept of a Property Prediction System

A property-prediction system used for simulating the metallurgical process occurring during heat treatment and predicting the microstructure and mechanical properties of quenched and tempered or case-hardened steel's is described in this section.

Before starting to design a property-prediction system, first those internal parameters (Ac3 temperature, transformation kinetic data, hardness values of the micro structural elements, and so on) that have the most determinative effects on the properties.

The programs are based on a phenomenological model of kinetics of transformation taking place in no isothermal conditions and permits the prediction of the progress of transformations, of the microstructure, and of the mechanical properties as a function of time and of position in the cross section of the heat-treated work piece. The equations forming the base of the model belong to three main groups as follows:

- the differential equation of heat conduction by a numerical method, the temperature field in the given work piece is solved
- the system of kinetic differential equations for describing the transformation processes occurring in the microstructure
- equations describing the relation between the microstructure and properties

Modelling of transformation kinetics can be done with differential equations such as:

$$\frac{\partial Y_j(r,t)}{\partial t} = g_j\,(Y_1, Y_2, \ldots Y_j, T, t) \qquad (1)$$

where t denotes time;

- r is the vector representing a given point of the work piece (the position vector);
- T is the temperature, which is a function of time t and position r;
- (j = 1,2,. . . J) is a so-called micro structural parameter;
- g = 1,2,. . . J is an appropriately selected real value function.

The micro structural parameters Y in (1) are numerical quantities that may be interpreted within relatively wide limits.

The starting point for predicting mechanical properties such as hardness and yield point is that the properties are related to micro structural parameters. It was assumed that after transformation at a given location r in the work piece, a numerical property P(r) of the steel may be calculated with a precision satisfying practical

demands as a function of a small number of elementary micro structural properties p (j=1,2,. - . M) according to the formula:

$$P(r) = f,(p_1,p_2, \ldots\ldots\ldots\ldots..,P_M) \quad (2)$$

where f, is an appropriately selected function.

In most cases, the so-called generalized linear law of mixture represented by the following Stieltjes integral was used to calculate the elementary micro structural property (j=l,2,...M):

$$p_j = \int \chi(T, Y_j) dY_j \quad (3)$$

where χ [T(r, t), Y_j] is a suitably defined weighting function containing and summarizing the numerical information on the given property of the micro structural parameter Y.

The input data are:

- chemical composition of the work piece to be hardened
- initial state of the work piece (annealed, normalized, quenched, and tempered)
- geometry: shape and size of the work piece (round bar or plate) characterized by its diameter or thickness, or Jominy specimen and the distance from the cooled surface to the point where the microstructure and properties are to be predicted
- heating conditions: heating medium, austenitizing temperature, and the total time spent by the work piece in the austenitizing furnace
- quenching conditions characterized by the HR value (relative heat transfer coefficient specifying the cooling severity) and the temperature of the quenching
- tempering conditions given by the tempering temperature and the duration of tempering

The chemical composition of the work piece is first verified against the specified composition range of the steel type for which the predictor program was developed. From the composition, we calculate A_1, A_3, B_s, M_s, transformation temperatures by formulas based on dilatometrical measurements and regression analysis.

Computation of the heating curve takes into account the furnace features. Calculations are based on the application of an approximate method developed to solve heat conduction problems for simple geometries.

The accuracy of the following Newtonian approximation can also satisfy the requirements:

$$T = (To — Ta)\exp\{- \alpha_h t\} + Ta \quad (4)$$

where: T the austenitization temperature;

- To is temperature at t = 0;
- h is a constant depending on the furnace, mass of work piece, heating medium, quality of the face, and agitation of the medium.

The temperature to austenitization is determined by the initial microstructure and the heating rate. The experimental results may be described with the following equation:

$$Ac_3 = A_3 + a\, v^{1/3} \quad (5)$$

where v is heating rate at temperature A_3 and a is a parameter depending on initial state of microstructure.

Computation of the austenite grain also requires consideration of no isothermal conditions. The extent grain growth taking place during austenitization is known to have a decisive effect is the characteristics of steel.

It was assumed that grain size D_a of steels at constant temperature T is described an isothermal kinetic function of the following type:

$$D_a = \left[\int_o^t k_o \exp\left(-\frac{Q_a}{RT} \right) dt + {D_o}^N \right]^{1/N} \tag{6}$$

The unknown parameters k_0, N, and Q_a can be estimated by regression analysis using measured data.

The characteristics of the isothermal time- temperature transformation chart are calculated as a function of the chemical composition and austenite grain size, also taking into account the temperatures A_1, A_3, B_s and M_s.

One of the most frequently used equations for the isothermal transformation is Avrami's equation:

$$y = 1 — \exp\{—bt^n) \tag{7}$$

where y is the volume fraction of the transformed austenite;

- t is the time spent on the isotherm;

- b and n are temperature, grain size, and composition-dependent constants, evaluated from the isothermal TTT diagram or from measurements with continuous cooling .

Computation of the cooling curve at the given point of the work piece can involve a simple method similar to the one described to use a Newtonian cooling:

$$T = (Ta-Tq)\exp\{-\alpha_c t\}+Tq \tag{8}$$

where Ta is the austenitization temperature;

- Tq is the temperature of the quenching;

- a is the geometry and quenching-dependent parameter.

Calculating the progress of the transformation processing continuous cooling from the TTT characteristics is a crucial part in property prediction. Estimation of the ferritic, pearlitic and bainitic fractions during each step.

Information about transformation temperature defined for the initiation of the ferrite-pearlite faction and for the beginning temperature range, B, of the bainite reaction is first provided by this program.

When the hardness after quenching is calculated on the basis of microstructure and e carbon content, many investigations are necessary to ascertain the best rule of mixing.

In the calculation of the hardness after quenching, the transformed amounts of austenite on each isothermal step, and their individual isothermal hardness can be taken into account.

The amounts of the micro structural elements are calculated by the help of the stepwise method. The individual hardness's of the micro structural elements are taken from a hardness-temperature table or function valid for the actual steel, and the resultant as-quenched hardness Hq is composed from these components with the formula:

$$Hq = \sum_{i=1}^{v} y_i(T_i) H(T_i) + y_m \cdot H_m + y_a \cdot H_a \tag{9}$$

where T, is the temperature of the this step;

- $y_i(T_i)$ is the transformed amount at temperature T_i
- $H(T_i)$ is the isothermal hardness;
- v is the number of isothermal steps, until temperature reaches M_s
- Y_m is the volume fraction of martensite;
- Y_a is the volume fraction of retained austenite;
- H_m is the hardness of martensite;
- H_a is the hardness of retained austenite.

The tempering of steels forms a significant part of practical heat treatment, and therefore its study and mathematical description are of greatest importance. Several generally applied methods are available for the isothermal case. From computational considerations, it is assumed that the kinetic equation describing the change in hardness under no isothermal conditions is of the form:

$$H_t = f_4 (P_g) \quad (10)$$

where H_t stands for the instantaneous hardness after tempering;

- f_4 is a suitably selected function;
- P_g is the so-called generalized time-temperature parameter, which is applicable to the description of tempering processes with changing temperature

The form of the parameter P_g can be selected in many ways.

This chart can be applied to convert from one tempering time and temperature to any other, on the basis that combinations of tempering temperature and time having the same value of tempering parameter will produce the same hardness.

For tempering at varying temperatures, Eq the value of the parameter P required to achieve the specified hardness may be determined with the deferent figures. For isothermal tempering, the various time-temperature combinations for the given parameter value PD, which may be used to achieve the specified hardness.

In the kinetic function employed for the phenomenological description of hardness decrease occurring during tempering, the value of the apparent activation energy (Q_D = 250 kJ/mol) is essentially identical to the activation energy for the self-diffusion of ferrite in steel that is not alloyed with molybdenum.

It follows from this assumption that the lower chart in figures may be used generally for all hardenable steels free of molybdenum. However, the upper chart representing the so-called master curve must be deduced and plotted individually for the various steel types from measured data.

Mechanical Property Estimates not only the hardness, but also the other mechanical properties, namely the tensile strength, yield strength, elongation, reduction in area, and the Charpy value of the impact energy with the following formulas:

$$R_m = 3.412 \text{ HV } 64.3 \quad (11)$$

where R_m is the ultimate tensile strength in MPa, and HV is the Vickers hardness.

For the calculation of the yield point R (MPa), elongation A_{50} (%) in 50 mm, reduction in area Z (%), and Charpy value KU(Joules), the equations below have been suggested:

$$R = (1{,}17\text{-}0{,}0007Y_m)*R_m + 3{,}72Y_m - 484 \quad (12)$$

$$R_m = 3{,}412HV\text{-}64{,}3$$

$$A_{50} = 40\text{-}(0{,}03\text{-}0{,}0001Y_m)R_m$$

$Z=100-(0,06-0,00024Y_m)R_m$
$KU=296-(0,285-0,00098Y_m)R_m$
where Y_m is the volume fraction of martensite in %.

3. The control of furnaces for thermic treatment

The process computer which conducts the electric furnaces lakes the initial and current data through the system of acquisition of data from human operator and sensor in furnaces then the computer analyses on the base of mathematical model of transformation process and the prediction of microstructures and properties a optimum strategy for conduct the industrial strategy for conduct the industrial furnaces.

The program of the property prediction of microstructure and mechanical properties are based on a phenomagnetical model of kinetics of transformation taking plane in no isothermal conditions.

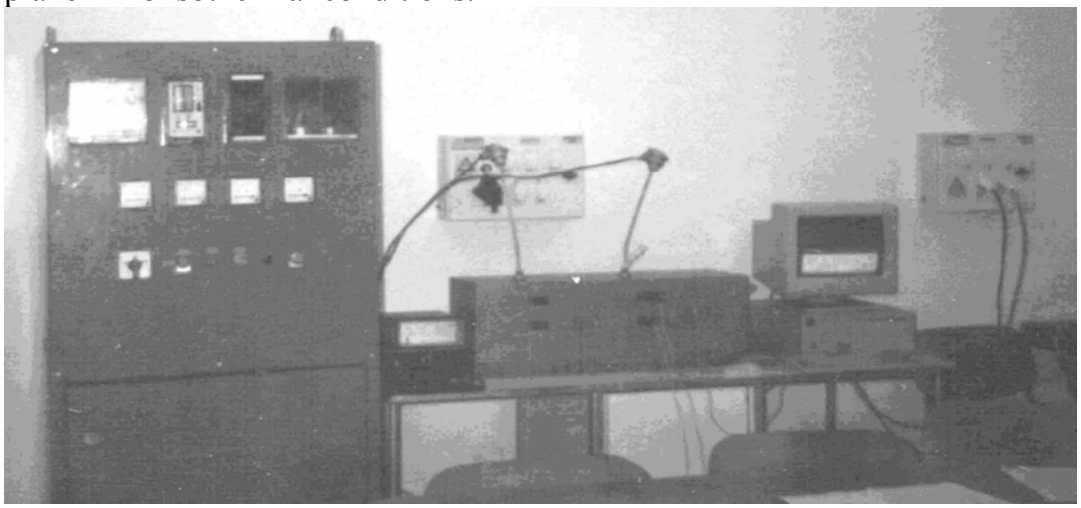

Fig.1 *The system for conduct the electric furnace for heat treatments.*

The functions offered through conduct system are :

- the modelation and simulation of heat transfer in electric furnace ;
- the sequential regulation of furnaces parameters ;
- the complete imagine above the process, checking of start / stop of furnaces, the function for alarm and safety stopping ;
- this system post parameters value from a certain part of process which is interesting at certain moment, on display are the references values, the sizes for actions and the signal of entrances in the limits ;
- the system offers possibility of work with a system of menus .

The computer which conduct the furnaces takes the initial and current data through the system of acquisition of data from sensors in the furnace then the computer analyses on the base of mathematical model a optimum strategy for conduct the electric furnaces .

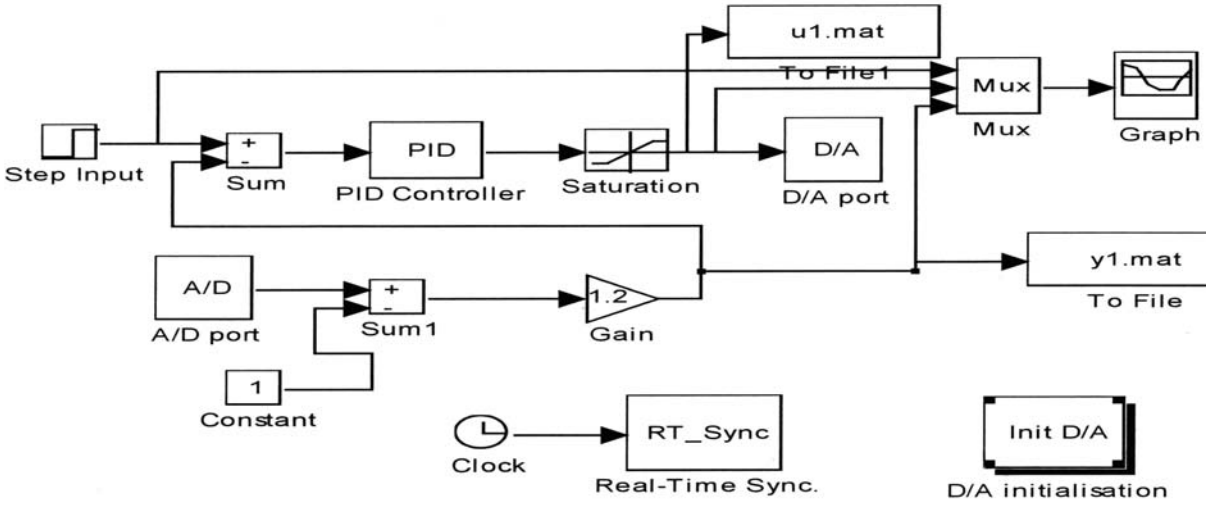

Fig.2 *The system block scheme for conduct the electric furnace.*

The structure of initial database is :

- the steel marks and the semi-products number and size ;
- the temperature of furnaces and semi-product .

In next figures we present the result of conduct the chamber type electric furnace for heat treatments with PID and PID – predictive algorithm.

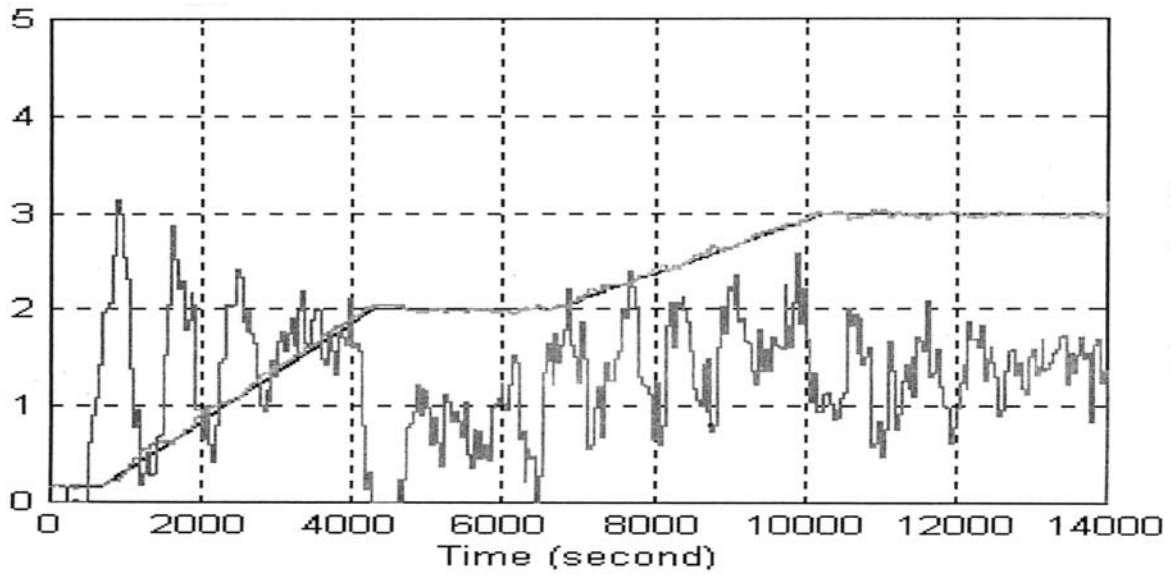

Fig.3 *Results of conduct with PID algorithm.*

The equations forming the base of model are :

- the system of kinetic differential equation for describing the transformation process ;
- the differential equations of heat transfer ;
- the relation between the properties and microstructure .

The tuning algorithm PID together with the supervision system was implemented on a PC with system of acquisition of data from conducted system.

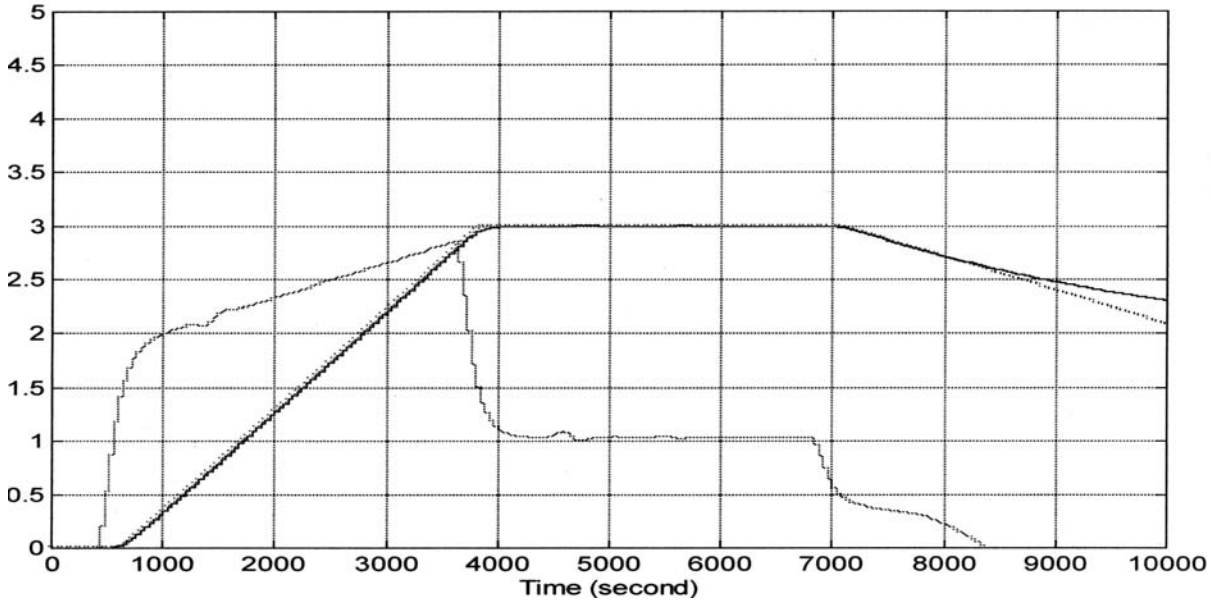

Fig.4 *Results of conduct with PID - predictive algorithm.*

The results show the improvement of the performances of controlled system with delay time as well as the increase of economical efficiency.

REFERENCES

1.Cucoş I., Dănilă R., Catarschi V. – *Matematichal modelling, optimisation and simulation assisted by personal computer of the heat transfer from the heat treatment furnaces* I Congres International de Ştiița şi Ingineria Materialelor Iaşi , mai 1994.

2.Ungureanu Şt., Cucoş I. Dima A – *Evoluated system computer assisted for designing and conducting the chamber type furnaces heat treatments* , I Congress International de Ştiința şi Ingineria Materialelor, Iaşi, mai 1994

3. Chiriac F., Leca A. - *Procese de transfer de căldură şi masă în instal ţiile industriale* , Ed.Tehnică, Bucureşti , 1982

4.Gheorghely M., Reti T. Somogyi S., Konkoly T. – *Aide au choix d'acier par calcul des caracteritique mecanique*, Traitement thermique, Franța, sept. 1992

IULIAN CUCOŞ The "Gh.Asachi" Technical University Iaşi

CONDUCEREA CUPTOARELOR DE TRATAMENT TERMIC PRIN MODELAREA PROCESELOR DE TRANSFORMARE SI PREDICTIA MICROSTRUCTURII SI A PROPRIETATILOR OTELULUI.

Rezumat: Sistemul pentru predicția proprietăților este folosit pentru simularea proceselor metalurgice care apar în timpul tratamentelor termic şi pentru prevederea microstructurii şi proprietăților mecanice, sistemul are o structură modulată. Modelul matematic permite prevederea evoluției transformării şi microstructurii, a proprietăților mecanice ca funcție de timp şi de poziția în secțiunea pieselor tratate termic.

Problema principala a conducerii cuptoarelor de tratament termic o reprezinta controlul temperaturii din cuptor astfel incat aceasta sa evolueze dupa profilul impus de tehnolog. Proiectarea sistemului de regalare automata presupune:

- caracterizarea matematica a comportarii procesului condus din cuptor;
- stabilirea obiectivelor reglarii si optimizarea valorilor parametrilor reglarii;
- modelarea matematica a proprietatilor fizico-mecanice a piesei dupa tratamentul termic;
- implementarea algoritmului de reglare PID-predictiv si validarea solutiei propuse pe baza analizei performantelor sistemului.

BULETINUL INSTITUTULUI POLITEHNIC DIN IAŞI
Tomul LIII (LVII), Fasc. 2, 2007
Secția
ŞTIINȚA ŞI INGINERIA MATERIALELOR

STATE OF ART OF CAD/CAM IN PROSTHETICS

BY

OCTAVIAN CIOBANU

Abstract. *The paper examines the current state of art of CAD/CAM technologies in prosthetics. The flexibility and speed of these technologies have made them useful for a wide range of applications; such as, prosthetic socket design, wheelchairs, spinal orthoses, and foot orthoses. Characteristics of some CAD/ CAM systems for prosthesis are showed and an overview of opinions of researchers involved in this area is presented. CAD/CAM systems reduce fabrication time, but sometines compromise the accuracy of the fit of a custom made orthosis. Although research continues into advanced fabrication techniques, the prosthetics and orthotics industry has not yet taken advantage of all possibilities in the computer-assisted manufacturing side.*

Key words: CAD/CAM, prosthesis, overview

1.Introduction

CAD/CAM technologies have become a tool for the field of prosthetics and orthotics. Prosthetists use CAD/CAM to produce a positive model of a residual limb from which a prosthetic socket can be manufactured. The CAD/CAM technologies provide controlled methods for shape and dimensions modification, more accurate methods for positive mould fabrication and a decrease in production time. The processes using CAD/CAM may include some of the following steps:

- determination of the residual limb shape by means of a measuring system or device;
- prosthesis (socket) design based on measurements using some type of CAD computer software;
- machining a positive mold for the prosthesis; the prosthetic socket can be made by conventional methods including plastic forming, milling, stereolithography etc.

At present, three main methods exist of measuring the residual limb defining initial socket shape prior to CAD modifications and constructions:

1. Manual measurements of the residual limb's dimensions and circumference using caliper and tape have been used to define a primitive socket selected from a set of stored socket models. These models can then be scaled, tapered, and modified in shape and compression areas using a CAD program;

2. In mixed method, a more complete but time consuming recording of the residual limb shape is obtained by first taking a plaster cast of the limb in the conventional manner and then digitizing points along the inner surface of the cast. This is followed by a CAD modification of an average rectification pattern based on information obtained from several amputee residual limbs.
3. In modern non-contacting methods of determining residual limb shape are used different techniques as video cameras, ultrasounds, 3D scanners etc.

The CAD/CAM technologies in prosthetics became in some bioengineering research centers, computer aided socket design and computer aided socket manufacturing CASD/CASM.

2. Method

There are presented some well known CAD/CAM systems for prosthesis from all over te world with their characteristics and performances: the CAPOD system, the DELCAM system, the Biosculptor system, the Rodin 4D system and CANFIT-PLUS system.

The CAPOD system produced and used in Sweden includes:

- a scanner for limb measurement;
- a CAD/CAM workstation to control the scanning of the limb to perform socket design modifications or constructions and to control the socket-mold machining;
- a numerically-controlled (NC) milling machine to cut the socket mold.

The CAPOD measuring system [1] consists of a CCD video camera and a laser-light source mounted to a rotatable frame, and a cover to completely contain the frame except where the amputee's limb is located in the center of the frame. A plane of laser light is directed toward the coplaner central axis of the rotatable frame and intersects with the limb to form a line contour on the limb's surface (Fig.1). To view this intersection as a contour rather than as a straight line, the camera is positioned at a 45° angle to the plane of light. In order to view the full length of the limb while maintaining a compact device, the camera is positioned to obtain a reflected image of the limb's contour via two plane mirrors. This results in an optical axis with a virtual angle of 56° in respect to the rotation axis.

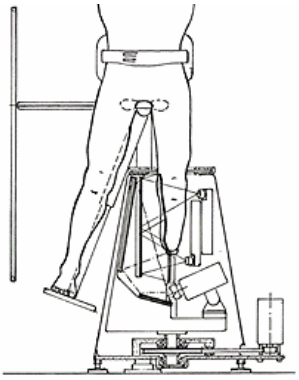

Fig. 1 The CAPOD measuring system

To measure the limb's shape, the frame containing the video camera and a laser light source is rotated around the limb under the control of a PC. The frame-grabber is used to obtain 100 images of the stump-shape dependent line contour at 3.6° intervals. Raw planar coordinates of the leading edge of the contour image are stored for processing. For the residual limb, this edge is represented by approximately 350 points, while the system permits up to 512 points per contour or 51,200 points for complete shape representation. The planar coordinates are then filtered and transformed into three-dimensional (3-D) position coordinates to obtain be complete shape of the limb. Once the final socket shape is determined, cylindrical coordinates describing its shape are sent to an NC milling machine to cut the positive mold. The mold blank is currently made from equal parts by volume of plaster and microballoons. The NC machine was specially designed and built for the CAPOD system. It is known that commercial machines generally have higher specifications than required and are highly expensive. Machining is carried out with the mold plug stationary. The cutter itself is stepped radially, while its carriage is stepped longitudinally corresponding to each line contour scanned, as shown in Figure 2.

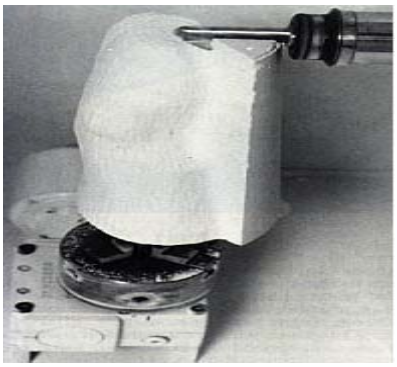

Fig. 2 The milling machine of CAPOD system

The DELCAM system (www.delcam.com) range from the scanning system to the production of the final prosthesis. The company has grown steadily since being founded formally in 1977, after initial development work at Cambridge University, UK. It is now the largest developer of product design and manufacturing software in the UK, with subsidiaries in North America, Europe and Asia.

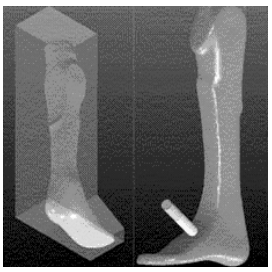

Fig. 3 Prosthesis fabrication by DELCAM system

The system allows the user to look into the database for a suitable mould that fits with the specific requirements. The model can then be sent directly to production or modified if necessary and than sent to production. The DELCAM software for the

reverse engineering is called CopyCAD and is a comprehensive solution to manage point cloud data. It will allow the prosthesists to fill the gap between the digital and the physical world, reading every set of data, which have been generated by optical, laser or mechanical devices. Once the model has been modified, with a CNC machine tool called PowerMILL (5 axis), it is possible to generate the work cycle to create the thermoforming mould for the orthesis or prosthesis.

BioSculptor (www. biosculptor.com) is a complete CAD/CAM solution for the prosthetic and orthotic profession. The system includes a four axis CNC non-contact laser imager, a software for CAD modification and visualization and a 4.5 axis CNC mill. Biosculptor system can perform next actions:

- scans with a dual camera scanner for non-contact solution which minimizes user errors and allows the model to be digitized more efficiently and accurately in a shorter amount of time and displays a real time image of the object being scanned. (Fig. 4)
- imports data and images into the BioSculptor CAD package; adds customized modifications to patient data;
- send the CAD model to any CNC compatible facility for production.

Fig. 4 The scanner used in BioSculptor system

The Seattle Shape Maker Computer Aided Design and Computer Aided Manufacturing equipment is a rapid prototyped system using Fused Deposition Modelling (FDM). FDM is a technique of rapid prototype manufacture which involves the depositing of auto-adhering material in specific computer controlled sequence as to build a prototype in space. The first FDM Fused Deposition Modeling prosthesis has been built by REHABTech in Australia (http://rehabtech.eng.monash.edu.au/cadcam) The modified socket, desired cosmesis and alignment details are used to build a digital image of the prosthesis. This information is then converted using a specifically built software program developed at REHABTech so it can be read by the FDM software. The whole prosthesis, socket, cosmesis and structure are then built as one by the Fused Deposition machine out of ABS (Acetyl Butyl Styrene - an engineering grade plastic that can be machined, glued, painted and is both strong and light). The prosthesis should be modified to avoid high stresses. It is anticipated that a full FEM-analysis on multiple prostheses may provide some basic rules in order to avoid high stresses.

Secondly these basic rules can then be applied on new designs. This also could be done for common modifications the prosthetist wants to make such as holes for straps or other attachments. The wall thickness can also be specified.

.

Fig. 5 Prosthesis made of ABS

Rodin 4D is a complete CAD/CAM system for orthopaedics. te system is capable of importing the main industrial formats (STL, 3DS) or those specific to orthopaedics (AOP, AP2). Rodin4D is a complete and open system. Each CAD station includes its own CAM module (preparation for machining) including a block manager for the optimization of machining operations.

Fig.6 The Rodin scanning system

Rodin system has no-contact 3D digitizer which enables prosthesists to digitize freely and easily the most complex forms (Fig.6). The milling machine is controlled in real time by an onboard PC (Fig. 7). During the machining cycle, the milling machine enclosure is inaccessible to the operator, protecting him from the moving parts. It has large capacity (1100mm x 600 mm) means that it can mill body jackets, corsets, aesthetic prostheses, lower limbs, standing frames etc. Characteristics: spindle motor: 3000/10000 rpm, power supply: 380v, 60Hz , 25A, average cycle time: 20 minutes.

Fig. 7 Rodin Milling machine with on board PC

The CANFIT-PLUS system (www.vorum.com/P&O_System) uses data for prosthesis socket obtained by fitting an appropriate brim to the patient, and taking a series of circumferential measurements under weight bearing conditions. Since no cast is required, it is eliminated the use of plaster in the design process. Also the system uses uses a non-contact, optical scanner to image virtually any part of the human body with a level of accuracy comparable to traditional methods of clinical shape measurement (scanning system in Fig. 8). The measurement data entered into the CAD program (CANFIT PLUS design sofware) generates a modified socket and displays it on the computer screen. The CANFIT-PLUS Remote Communications program transmits designed socket data via modem or internet/e-mail to the manufacturing facility. Prosthetic and orthotic positive shapes are carved in this system with carver machine.

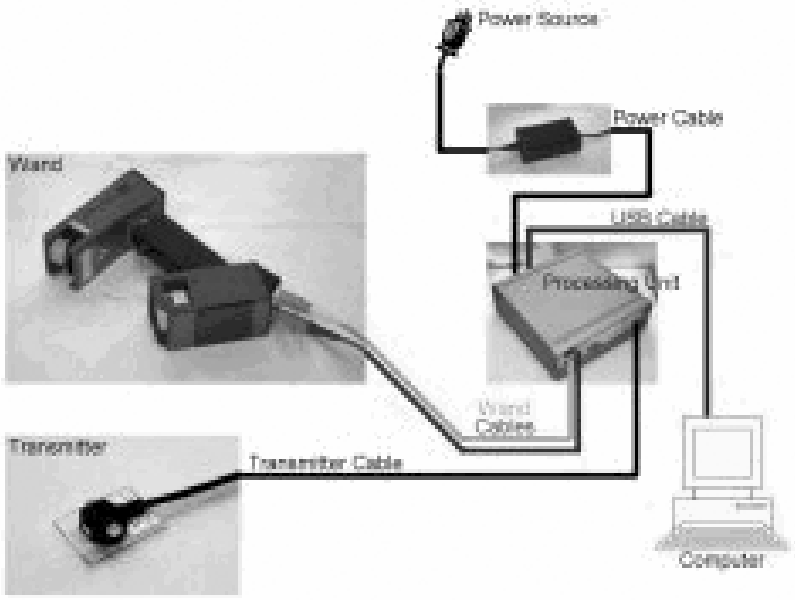

Fig. 8 CANFIT-PLUS Scanning system

3. Discussion

Opinions of specialists on CAD/CAM technologiues are controversial and sometimes pesimistic. On the optimistic side, a lot of scientific papers showed that the advance in computer technology over the past years, combined with reductions in cost, have helped make CAD/CAM a succesfull reality in prosthetic practice. Computer aided design and manufacturing has the ability to combine the accuracy of custom made with the speed and labor savings of off-the-shelf systems [2,3,4,5].

Smith and Burgess [6] showed that an exact mold of the residual limb is not a good socket. The socket must be accurately indented in areas that can better tolerate the transfer of forces, and the socket must be relieved out away from the residual limb in areas that are less tolerant of force and pressure. These special areas of the socket that require modification are called regions. Once the digital representation of the residual limb is obtained, software is used to add the modifications that transform the digital shape from an exact mold of the amputated limb, to the shape of a functioning prosthetic socket. This process is called rectification, and introduces indentations on

regions that can tolerate more weight, and relief in regions that cannot tolerate weight as well. Most software packages have templates that will identify these regions and add these modifications in a similar fashion even for different sized and shaped limbs. There are literally thousands of variations and theories about the exact location and shape of these regions, and on how to describe the subtle details of gradual versus more abrupt modification, and the location of the apex and the magnitude of the change. Most software packages will allow an individual prosthetist to personally refine the rectification process. Prosthetists can create their own templates, so that their favorite or most successful rectifications can be reproduced for other patients.

John Michael [7] showed that current CAD/CAM techniques in prosthetics provide mediocre-quality prostheses at greater cost than conventional methods. CAD/CAM works only for the cases that currently present few difficulties. computer-aided approaches to prosthetics and orthotics have to be adapted starting immediately. There are many reasons for this recommendation, but the primary one is that, if we fail to accept and enhance this technology, other less-qualified individuals will simply fill the domain.

Edward Lemaire [8] wrote that clinical CAD/CAM applications has shown that the transfer of manual prosthetic modification skills to a computer system is not an easy or time-efficient task. This knowledge-transfer problem is expanded when the individuality of clinical modification procedures are considered (i.e., each prosthetist has a slightly, or very, different modification approach). In most cases, a prosthetist will learn to modify a shape on a CAD system by trial and error. The inability to define how individual prosthetists modify a socket can impede the transition from manual techniques to CAD/CAM.

Lilia Magnus [9] showed that there are tibial movements inside a prosthetic socket, large enough to influence the prosthetic fitting and that CAD /CAM technique had no major advantage compared with traditional technique from the patient's point of view. Also she showed that proper time for definitive prosthetic fitting after transtibial amputation was approximately three to four months after operation.

Bill Contoyannis [10] wrote that the use of Rapid Prototyping technology and in particular of Fused Deposition Modelling was investigated for the production of a trans tibial prosthetic socket and how this would effect the clinical delivery of the device. It was found that although it was quite feasible to produce and trial the socket, it had no significant impact on the key aspects of speed, quality and design of the socket.

4. Conclusions

The rapid advance in computer technology over the past years, combined with reductions in cost, have helped make Computer Aided Design and Computer Aided Manufacturing a clinical reality in prosthetic practice. Technicians in the field felt their jobs may be jeopardized by automated fabrication techniques. Prosthetists who use CAD-CAM techniques are finding they have more time for patient care and clinical

assessment. CAD/CAM systems [11-15] reduce fabrication time, but sometines compromise the accuracy of the fit of a custom made orthosis. Computer aided design and manufacturing has the ability to combine the accuracy of custom made with the speed and labor savings of modern systems. This would be a substantial benefit to patients, practitioners, and third party payors as well. Although research continues into advanced fabrication techniques, the prosthetics and orthotics industry has not yet taken advantage of all possibilities in the computer-assisted manufacturing side.

REFERENCES

1. Oberg K J., Kofman, A., Sigblad G. The CAPOD System-A Scandinavian CAD/CAM System for Prosthetic Sockets, **JPO**, Vol. 1, Num. 3, pp. 1989, 139-148
2. Brncick M. Computer automated design and computer automated manufacture. **Phys Med Rehabil Clin N Am.** 2000 Aug;11(3):701-13
3. Topper AK, Fernie GR. Computer-aided design and computer-aided manufacturing (CAD/CAM) in prosthetics. **Clin Orthop Relat Res**. 1990 Jul;(256):39-43.
4. Goh JC, Lee PV, Toh SL, Ooi CK. Development of an integrated CAD-FEA process for below-knee prosthetic sockets. **Clin Biomech** (Bristol, Avon). 2005 Jul;20(6):623-9.
5. Carroll K. Lower extremity socket design and suspension.**Phys Med Rehabil Clin N Am**. 2006 Feb;17(1):31-48
6. Smith DG, Burgess EM. The use of CAD/CAM technology in prosthetics and orthotics--current clinical models and a view to the future. **J Rehabil Res Dev**. 2001 May-Jun;38(3);327-34
7. Mitchel J. Reflections on CAD/CAM in Prosthetics and Orthotics, **JPO**, Vol. 1, Num.3 1989,116-121
8. Lemaire E. A Quantitative Method For Designing Manual Socket Modifications, **Rev. mex. ortop. traumatol**; 9(4), 1995, 237-44
9. Contoyannis B, PROSTHESIS DESIGN and CONSTRUCTION, Seminario "Tecnologie al servizio dell'uomo",Universita La Sapienza, 1999
10. Magnus L. Volumetric determinations with CAD/CAM in prosthetics and orthotics: Errors measurement **J Rehabil Res Dev** Vol . 32 No. 2, May 1995 Pages 141-148
11. www.delcam.com
12. www. biosculptor.com
13. http://rehabtech.eng.monash.edu.au/cadcam
14. www.rodin4d.com
15. www.vorum.com/P&O_System

Received March 15, 2007

Gr. T. Popa University of Medicine and Pharmacy, Iasi
Faculty of Medical Bioengineering

Stadiul actual al utilizării tehnologiilor CAD/CAM în protezare

Rezumat. Lucrarea abordează stadiul actual al tehnologiilor CAD/CAM în fabricarea protezelor. Flexibilitatea şi viteza acestor tehnologii le-au permis să devină utile într-un mare număr de aplicaţii ca proiectarea manşoanelor protezelor, proiectarea scaunelor cu rotile, proiectarea ortezelor spinale şi a ortezelor pentru picioare. Sunt trecute în revistă caracteristicile unor sisteme CAD/CAM pentru proteze şi sunt prezentate opiniile unor cercetători implicaţi în acest domeniu. Sistemele CAD/CAM reduc timpul de fabricare dar de multe ori precizia în potrivirea pe pacient este compromisă, comparativ cu ortezele făcute manual. Deşi cercetările continuă în direcţia optimizării tehnicilor avansate de fabricare, industria protezelor şi a ortezelor nu a putut profita pe deplin de toate avantajele oferite de sistemele de fabricare cu ajutorul calculatorului.

BULETINUL INSTITUTULUI POLITEHNIC DIN IAŞI
Tomul LIII (LVII), Fasc. 2, 2007
Secția
ŞTIINȚA ŞI INGINERIA MATERIALELOR

OPTIMIZATION OF THE POWER FACTOR IN METAL AND ALLOY CASTING SECTORS

BY

IOAN CARCEA, COSTEL ROMAN, ROMEO CHELARIU, MATEI GHERGHE

ABSTRACT
In addition to the active power materialized in the torque developed in engine shafts or the heat energy released by resistors, a large amount of reactive power is necessary for the electromagnetic circuits such as coils. The reactive energy required for the operation of such a unit may be supplied by the local power supplier, in which case the power costs are extremely high, or it may be produced by the insertion in the circuit of compensation banks. The setup of a compensation bank designed to bring the power factor to values higher to the neutral one, has many advantages.

KEYWORDS: optimization, power factor, compensation system.

1. Introduction

The alternating current electrical wirings, whose operation circuit diagram includes active elements, such as resistors, and also reactive elements, such as coils or condensers, are large reactive power consumers. In addition to the P, [W] active power materialized in the torque developed in engine shafts or the heat energy released by resistors, a large amount of Q, [VA] reactive power is necessary for the electromagnetic circuits such as coils. The main reactive energy consumers in a metal and alloy development and casting sector are: induction heated electrical furnaces, arc heated electrical furnaces, transformers, coils, non-synchronous motors, metal fumes discharge lamps, etc.

The reactive energy required for the operation of such a unit may be supplied by the local power supplier, in which case the power costs are extremely high, or it may be produced by the insertion in the circuit of compensation banks. If the main consumer is an induction heated melting electrical furnace, depending on its characteristics, its operation may be impossible without the use of compensations systems. The explanation is that the interferences caused in the regional electrical system are so powerful that they may alter its proper operation. In the absence of compensation or its improper performance, it may be possible to have reactive energy consumption in kVArh, close to the active energy consumption in kWh.

2. Power factor

The main cause of the high reactive energy consumption is the phase difference between voltage and current, this magnitude being defined as power factor and symbolized by cos φ.

In an inductor (1) – metal part (2) system, the impedance $\underline{Z}$ is given by the ratio [1]:

$$\underline{z} = \frac{\underline{U}}{\underline{I}} = R + jX \tag{1}$$

where:

- $R = R_1 + p^2R_2$ is the total resistance in the inductor-part system, where R_1 is the inductor resistance and R_2 is the metal part resistance
- $X = X_1 + p^2X_2 + X_a$ is the total reactance in the inductor-part system, where X_1 is the inductor reactance and p^2X_2 is the metal part reactance
- $p^2 = N^2(\alpha_M/\alpha_2)^2$ is the transformation ratio of the inductor-part system at high frequencies
- α_M is the mutual inductance correction factor, which is determined by experiments depending on the diameter and height of the d_1 and h_1 inductor, as well as the height of the part subjected to heating
- α_2 is the correction coefficient depending on field unevenness at the ends of the part subjected to heating
- N is the number of inductor windings
- X_a is the air (or insulation material) reactance between inductor and part

The electric output in an inductor-metal part system is:

$$\eta_c = \frac{P_2}{P_1} \tag{2}$$

where:

- $P_1 = RI_1^2 = (R_1 + p^2R_2)I_1^2$ is the active power fed by the mains to the inductor
- $P_2 = R_2I_2^2 = R_2p^2I_1^2$ is the power turned into heat in the metal part
- I_1 is the sinusoidal line current
- I_2 is the current induced in the deep δ_2 layer of the eddies.

It results:

$$\eta_c = \frac{p^2R_2}{R_1 + p^2R_2} \tag{3}$$

The electric output increases with the increase of p^2, which is the inductor-part system transformation ratio, and R_2, which is the electrical resistance of the batch, and with the decrease of the electrical resistance of the inductor.

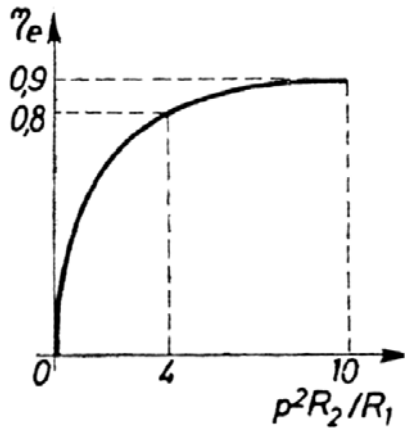

Figure 1. Shows the variation of the electrical output depending on the $p^2 R_2/R_1$ ratio.

Since the transformation ratio increases with the increase of the ω frequency, while the latter decreases with the δ_2 eddies penetration depth, which means that the η_e electrical output increases with the d_2/δ_2 ratio.

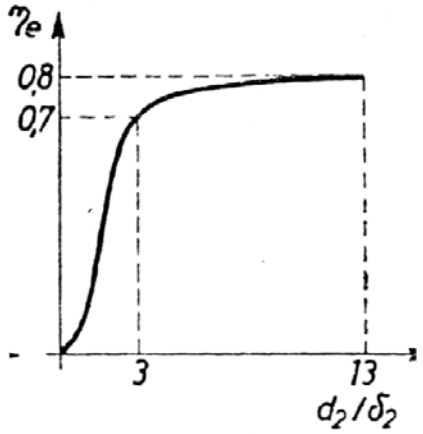

Figure 2. Shows the variation of the electrical output depending on the d_2/δ_2 ratio.

According to the (1) ratio , the power factor of the inductor-metal part system is:

$$\cos\varphi = \frac{R}{Z} = \frac{R}{\sqrt{R^2 + X^2}} \tag{4}$$

The closer the part diameter to the inductor diameter and the higher the d_2/δ_2 ratio, the highest the power factor.

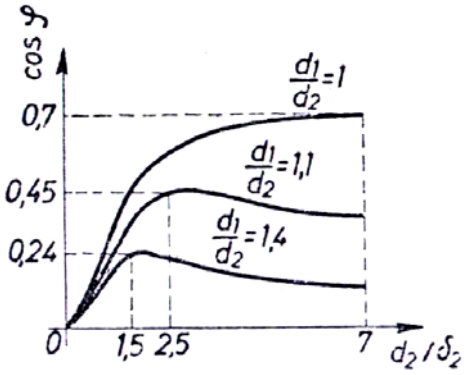

Figure 3. Shows the variation of the power factor depending on the d_2/δ_2 ratio.

The highest value of the power factor is reached when X = R and cos φ = 0.707. This is actually possible when $d_1/d_2 = 1$, and $d_2/\delta_2 \geq 10/\sqrt{2}$.

Since these values are not satisfactory from the energetic standpoint, special power factor and electrical output improvement actions are necessary.

3. Compensation system determination

If, theoretically, the power factor of an induction heated electrical furnace cannot exceed the maximum 0.707 value, it means that in practice cos φ have even lower values. Given the fact that the power consumption of the induction heated electrical furnace is more than 50% of the total power consumption, then cos φ = 0.50÷0.65, which is entirely unsatisfactory.

The power factor, below which a consumer is fed with power from the mains without the provision of compensation measures, is called natural power factor and it corresponds to a φ_{nat} phase difference angle. In order to prevent the negative effects mentioned above, the power consumers should operate at a neutral power factor corresponding to a φ_n phase difference angle.

The improvement of the power factor is achieved by means of the banked capacitor banks that may be adjusted during operation. The compensation may be performed on the spot, when each consumer is fed reactive energy from a condenser linked to it by multiple connections, or at the central level, when the compensation is achieved at the general switchboard level by means of an automatic battery. The advantage of centralized compensation is that is requires only a single capacitor bank able to wire by means of switches as many condensers as necessary.

For a P_c active power required by the consumer, the capacitor bank should supply:

$$Q_c = P_c\left(tg\varphi_{nat} - tg\varphi_n\right) \text{ [kvar]} \quad (5)$$

In this case, the active power losses of 2÷5 W/kvar in the capacitor bank were neglected. The automatic capacitor bank is chosen according to the data in Table 1.

Table 1 – Qc [kvar] energy required for compensation, designed to bring the power factor to cos φ≥ 0.92 from:

P (kW)	Q, [kvar]							
	$\cos\varphi_0$=0,50	$\cos\varphi_0$=0,55	$\cos\varphi_0$=0,60	$\cos\varphi_0$=0,65	$\cos\varphi_0$=0,70	$\cos\varphi_0$=0,75	$\cos\varphi_0$=0,80	$\cos\varphi_0$=0,85
50	65-87	55-76	45-67	37-59	30-51	23-51	16-38	10-31
100	130-173	109-192	90-133	74-117	59-102	45-88	32-75	19-62
150	195-260	164-228	135-200	111-176	89-153	68-132	48-113	29-93
200	260-346	218-304	180-266	148-234	118-204	90-176	64-150	38-124
250	325-433	273-380	225-333	185-293	148-255	113-220	80-188	48-155
300	390-519	327-456	270-399	222-351	177-306	135-264	96-225	57-186
350	455-606	382-532	315-466	259-410	207-357	157-308	112-263	67-217
400	520-692	436-608	360-532	296-468	236-408	180-352	128-300	76-248
450	585-779	491-684	405-599	333-527	266-459	203-396	144-338	86-279
500	650-865	545-760	450-665	370-585	295-510	225-440	160-375	95-310
550	715-952	600-836	495-732	407-644	325-561	248-484	176-413	105-341
600	780-1038	654-912	540-798	444-702	354-612	270-528	192-450	114-372
650	845-1125	709-988	585-864	481-761	384-663	293-572	208-488	124-403
700	910-1211	763-1064	630-901	518-819	413-714	315-616	224-525	133-434
750	975-1298	818-1140	675-962	555-878	443-765	338-660	240-563	143-465
800	1040-1384	872-1216	720-1034	592-936	472-816	360-704	256-600	152-496
850	1105-1471	927-1292	765-1101	629-995	502-867	383-748	272-638	162-527
900	1170-1557	981-1368	810-1167	666-1053	531-918	405-792	288-675	171-558
950	1235-1644	1036-1444	855-1234	703-1112	561-969	428-836	304-713	181-589
1000	1300-1730	1090-1520	900-1330	740-1170	590-1020	450-1020	320-750	190-620

A concrete example is the foundry of the RANCON trade company of Iasi where before the mounting of a capacitor bank the natural power factor was cos φ_{nat} = 0.65÷0.70, when only the machines tools, arc-welding sets, transformers, etc. were working, or cos φ_{nat} = 0.55÷0.65, when the induction heated electrical furnace was working as well. It is edifying the fact that in this case, for an average active energy consumption P_c = 25343 kW, there was a reactive energy consumption Q_c = 23098 $kvar_h$. According to the ratio (5) the reactive energy that the capacitor bank is supposed to supply was determined and an automatic 5 step 200 kvar installed capacity bank was ordered.

4. Conclusions

The setup of a compensation bank designed to bring the power factor to values higher to the neutral one, cos $\varphi_n \geq 0.92$, has following advantages:

- there are no reactive energy costs;
- the invoiced active energy decreases by 1÷3% due to the reduction of the active power losses caused by the reactive power transfer;
- conventional duty rating at the highest output, due to the improvement of the local level of the mains voltage;
- the transformers' loading capacity is increased.

References:

1. Saimac, A., Roşu, E., Gostian, C., *Utilizarea energiei electrice în metalurgie,* Editura Didactică şi pedagogică, Bucureşti, 1980
2. Samoilă, C., Ionescu, M.S., Drugă, I., *Tehnologii şi utilaje moderne în metalurgie,* Editura Tehnică, Bucureşti, 1986
3. ****Soluţii economice pentru compensarea energiei reactive,* Alfa Energ, Bucureşti, 2004

Received March 15, 2007

*Technical University „Gh. Asachi" Iasi,
**S.C. RANCON S.R.L.

OPTIMIZAREA FACTORULUI DE PUTERE IN SECTOARELE DE ELABORARE A ALIAJELOR

Rezumat

În afara puterii active, care se caracterizează în cuplul din arborele motoarelor sau energia termică degajată în cazul rezistorilor, o mare cantitate de putere reactivă este necesară în cazul circuitelor electromagnetice de genul bobinelor. Energia reactivă necesară funcţionării unei astfel de unităţi poate fi preluată de la furnizorul de energie electrică, situaţie în care cheltuielile energetice sunt foarte mari şi se obţine prin intercalarea în circuit a unor baterii de condensatoare. În urma instalării unei baterii de compensare care să aducă factorul de putere la valori superioare celei neutre, se obţin numeroase avantaje.

BULETINUL INSTITUTULUI POLITEHNIC DIN IAŞI
Tomul LIII (LVII), Fasc. 2, 2007
Secția
ŞTIINȚA ŞI INGINERIA MATERIALELOR

MATHEMATICAL MODEL CONCERNING THE SOLID-LIQUID INTERFACE STABILITY AND THE DETERMINATION OF THE THERMAL STRESSES IN THE ELECTRIC ARC HARDFACING PROCESSES

BY

MIREA CONSTANTIN, AGOP MARICEL

Abstract. *In accordance with the results of some theoretical researches, in this paper are presented some theoretical problems in relation with the solidification of the deposed metal in the electric arc hardfacing processes. These theoretical problems relate to the interface solid-liquid stability, the determination of the stability conditions in the case of the undercooling melt and the determination of the thermal stresses induced in the facing process.*

For determination of the stability conditions of the solid-liquid interface it was used one equation system coupled in for concentrations and temperatures, being obtained the stability conditions in linear approximation. Particularly, for the undercooling melt case, results that interface stability depends both the plasma characteristics and the interface characteristics, that particularly implies the matrix (base metal). The influence of the plasma is find again in the imposed restrictions, restrictions which was introduced by assimilation of the solidification speed with diffusion speed of the plasma electrons from the electric arc welding column.

For the thermal stresses determination was elaborated one complex mechanism for the realization of one deformation thermodynamics and the construction of one macroscopic potential function, and on the basis of the quantic mechanics the Navier-Stokes analogous of this.

Key words: *hardfacing, arc welding, solidification, interface solid-liquid, thermal stresses*

1. Introduction

The residual stresses evaluation from the metallic materials is one important factor that is reflected in exploitation performances of the equipments. The friction-wear phenomena, that have place with a significance weight in the equipments function, are greatly influenced by a series of parameters, these including and stresses state and structure.

The surface damage decrease by wear is possible with the application of some different surface technologies that includes, with a significant weight, and hardfacing. In the welding technologies field, this technological process suppose the deposition of one added material on substratum (base metal) with the purpose to confer this latter properly properties for resistance to the considered wear applications.

In this context, this paper present, for beginning, some aspects that aims the interaction of the electric arc with the solid surface of the base metal, the weld pool solidification, the overlay microstructure and the stress state induced by the welding process, correlating in this way the anterior researches results, [1], [2], [3].

As regards the deposited metal by welding, the properties and the characteristics of this are in first place determined by the microstructure, determined it self by the chemical composition and the thermal influence exercised from welding process.

In the case of the melting welding processes, the microstructure developed in the deposited metal depends to the solidification characteristics of the melted pool. Therefore, the microstructure development of the deposed metal is determined by the growth speed of the crystals, temperature gradient, undercooling degree and alloy composition.

The microstructure particularities of the welding deposited metal are controlled by the solid-liquid interface configuration in the time of the solid phase growth in welding pool. The nature and the stability of this interface are determined especially by the thermal and constitutional undercooling from immediate proximity of the interface, [5], [6].

Also, the melted pool solidification and the deposited metal microstructure are decisive influenced by the physical processes produced at the interaction between the thermal source and the metal in the welding process, these processes including the stresses and the deformations.

The thermal stresses that appear in the time of the welding processes are due to the localized application of the heating, which produce a non uniform local heating of the base metal. The heating and cooling respectively after welding lead to the volume modifications, their effect being the deformations and the stresses. The thermal stresses appear due to impede deformations and they not disappear when the temperature revert to the initial temperature, producing residual stresses.

Seeing the determinant role of the deposited metal microstructure in the wear processes of the surfaces, and the fact that microstructural particularities depends on the solid-liquid interface form, it is rise the problem of conditions determining for the stability of this interface. The interface stability was studies for the case of the arc welding processes, considering a series of restrictions imposed by the electric arc plasma, [1]. Thus, it can determine the electrical parameters for that it is suppose that the interface is stable.

To determine the thermal stresses it was elaborated one complex mechanism, [1], [2], [3], with the help of this it was developed one thermodynamic of the deformation, and on the basis of the quantic mechanics, the Navier-Stokes analogous of this.

2. Stability conditions and the development of one thermodynamic for the deformation

In the hardfacing processes, the thermal activation, necessary for overlay materialization and connection realizing between base metal and added metal, is produced by the heated generated in the welding arc. In the case of the welding processes with direct arc welding, the discharge plasma appear at the contact electrod-

solid surface, being generated by an ensemble of physical processes with physical characteristics determined that was established in reference [1]. The raise temperature developed from electric arc produce the forming of a commune melted pool (resulted from the mixing of a certain quantity from base metal and added metal) that solidify later.

In the process of the melting pool solidification, both the form and the stability of the solid-liquid interface in the time of solid faze growth are characteristic elements of the solidification process that suffer the influence of the interaction between thermal source and metal in the time of welding.

In the basis of the restrictions imposed by the electric arc plasma, it can study the stability of the solid-liquid interface in linear approximation. This chose can be treaty from mathematic point of view using a non-stationary equation set coupled in concentrations and temperatures. Considering that the stability of the solid-liquid interface is described by such as equations system, on obtained, [1], the stability conditions of the interface in the linear proximity under the form:

$$U > \frac{m_e\left(\omega^2 + v_{en}\right)d}{e v_{en}}\left[\frac{L_v k_L^2}{K_L T_M \Gamma} + \frac{D_L\left(k-1\right)m' C_\infty}{k' k T_M T}\right] \quad (1)$$

where:

- U: electric arc tension;
- m_e: electron weight;
- ω: pulsația electric field ;
- e: electron charge;
- ν_{en}: the frequency of the electron-neutron collision;
- d: the distance between electrode and solid surface;
- L_v: the volume latency heat of solidification;
- k_L: the thermal diffusivity of the liquid;
- K_L: the conductivity coefficient of the liquid;
- T_m: melting temperature of the base metal;
- Γ: capillary lenght (solid-liquid interfacial stress related to the solidification latency heat of the volume unity);
- D_L: diffusion coefficient associated with the liquid faze;
- k: segregation coefficient;
- C_∞: the liquid concentration far away from contact zone;
- T: temperature;
- $m' = \partial T_E / \partial C_L$, T_E being the equilibrium temperature and C_L the liquid concentration;
- $k' = \partial C_S / \partial C_L = k + (C_\infty / k)(\partial k / \partial C_L)$, C_S being the solid concentration.

Was resulted in this way that in the case of the undercooling melt the stability conditions depends both the discharge plasma and the interface characteristics, which particularly implies the matrix (base metal). The influence of discharge plasma is finding again in the imposed restrictions, the restrictions that were introduced with assimilation of the solidification speed with diffusion speed of the plasma electrons from the welding arc column.

The solid-liquid interface state is reflected and on the uniformity or non-uniformity of the stresses field: so, but the interface is stable, the stresses field induced by the thermal field (thermal stresses) is uniform, and but the interface in unstable then the stresses field is non-uniform.

Maintaining the analogy with the thermodynamics of the non-equilibrium processes, it was developed, [2], one deformation thermodynamics. In such context, it was show that for certain thermodynamics potentials and particularly in order to reduce the enthalpy to the usually thermodynamics form U + pV, when the constrictions are hydrostatics, it is necessary to chose the thermodynamics state variables of the body (base metal + deposed metal), $V_{\alpha\beta}$, so that they matrix determinant to be proportional with the 3/2 exponent of the metric tensor determinant of the body geometrical configuration, and this for any configuration. This fact represents an intrinsic correlation between the geometry and the deformation thermodynamics and in particular in the form, [2]:

$$V_{\alpha\beta} = \frac{1}{3\bar{\rho}} h_{\alpha\beta}^{3/2} \tag{2}$$

where:

- $V_{\alpha\beta}$: the variables of the body thermodynamics state;
- $\bar{\rho}$: the specific density of the reference configuration;
- $h_{\alpha\beta}$: metric tensor;

Allowing for this, the thermodynamics stresses form can be write in the following form, [1]:

$$\sigma_{\alpha\beta} = -pJh_{\alpha\beta}^{3/2} \tag{3}$$

where:

- p: hydrostatic pressure;
- J: $\bar{\rho}/\rho$, ρ being the density on the loading actual state;

Which desire to comment are some observations, namely:

• first of all, it is obviously that the thermodynamics stresses, that is those constrictions that actions inside of the solid differ from mechanics constrictions and it's up to our to choice, in such manner, so that in a given state they to coincide (for other details can be seen the references [6], [10], [11], [13]). The dependence for temperature is realized now with the densities ρ, that is some approximate. In this acceptation it can be admitted that the exterior constriction state $T_{\mu\nu}$, from relation, [2]:

$$\dot{U} - T\dot{S} = VT_{\mu\nu}d_{\mu\nu}, \tag{4}$$

where:

- U: the free energy of the body;
- T: the temperature;

- S: the entropy;
- $d_{\mu\nu}$: dissipative element in a internal friction phenomenon,

not represent stresses but a tensor that to represent the anisotropy of the crystalline lattice in a generalized co-ordinates system. As we see later, indeed, this same to be the case from thermodynamics and quantic point of view a expression as the type, [2]:

$$d_{\mu\nu} = \frac{1}{2}\left(\frac{\partial u_{\mu}}{\partial x^{\nu}} + \frac{\partial u_{\nu}}{\partial x^{\mu}}\right), \tag{5}$$

where:

- u_{μ}, u_{ν}: the displacements;
- x^{μ}, x^{ν}: the coordinates,

represent, until a factor ħ, even the "dissipation" energy that result from a Schrodinger equation for solid, [5, [8], [11];

- an other point that must be remarked is that the deformations is not directly obtained like in geometrical theories, like with the help of the canonic variables concerted to stresses $V_{\mu\nu}$ that have a tensor structure much complex than the deformations $\varepsilon_{\mu\nu}$. Once knowing $V_{\mu\nu}$ it can find $h_{\mu\nu}$ and hence the deformation tensor $S_{\mu\nu}$, which is $\varepsilon_{\mu\nu}$ just in the case when the initial state correspond to a indefinite configuration;
- finally, it is interesting to observe that in our considerations not interval the deformation tensor $\sigma_{\mu\nu}$ but only the metric tensor of the present state. This shows the fact that the situation can be generalized to include a metric tensor of the initial configuration, different from $\delta_{\mu\nu}$.

Because the determination of the thermodynamics stresses means enthalpy implies the existence of a potential, on write, [3], the macroscopic potential function and on the basis of quantic mechanics the Navier-Stokes analogous of this.

The key for determination of the macroscopic potential function is the assertion according to the fact that are known the constriction under the form of the stresses in assumption with a matrix 3 x 3 and that the their elements, inclusive the principals elements in a some situation, are measurable in any point of the material. With other words, we desire to explicit the idea in accordance with the deformations is unique determined by the constrictions state and the material structure.

In accordance with the macroscopic potential theory of the deformation must be search to a energetic function that not vary from point to point in the space of the respective body, that is strictly depend only the external limit conditions expressed in a certain matrix σ that depend from point on the external surface of the material.

The key for solution entire problem consist in the assumption that the stresses are represented in any point with a matrix 3 x 3 with measurable elements. This fact implies that the matrix have proper real value. In such context, using the properties of the cubic indexes, it writes the potential function beginning from the values on the principal axes of the thermodynamic stresses. This function will depend both the invariants s_1, s_2 of the stresses and the Novojilov angle ξ, [3]:

$$h = \frac{1}{3}\left\{s_1 + \sqrt{3s_2}\sin 3\xi - i\sqrt{3s_2}\cos 3\xi\right\} \tag{6}$$

Using the Schrodinger equation, writed in a hydrodynamic model, on see that this is equivalent with an equation type Navier-Stokes where the stresses tensor have the known form:

$$\sigma_{ij} = \eta\left(\frac{\partial u_i}{\partial x_j} + \frac{\partial u_j}{\partial x_i}\right) \tag{7}$$

with $\vec{u}$ (a cinematic „quasi-speed which not represent the real mechanical movement, but contribute to the impulse transfer and to the energy concentration) that have the form:

$$\vec{u} = \frac{\hbar}{2m}\nabla \ln \rho, \tag{8}$$

and the cinematic and dynamic viscosity in the form:

$$\nu = \frac{1}{4m\hbar}, \qquad \eta = \frac{1}{4}\hbar\rho, \tag{9}$$

where:

- ν: cinematic viscosity;
- η: dynamic viscosity;
- m: repose weight of the test particle from Bohm potential expression;
- ħ: reduced constant of Plank.

It is poses in evidence a special potential, namely Bohm potential, that contribute to the impulse and energy transfer with a very special mechanism.

In conditions in that the intern structure of the material have a coherent structure then the Bohm potential must be identified with potential function in the macroscopic case, function that determine, [2], the thermal stresses state.

3. Conclusions

- the study of the solid-liquid interface implies, from mathematic point of view, the usage of a equation set coupled in concentrations and temperatures, the influence of discharge plasma at the electrode-solid surface contact being pose in evidence through the identification of the solidification rate with the diffusion rate of the electrons;
- for the case of the undercoolind melt the stability conditions depend both the discharge plasma characteristics and the solid-liquid interface characteristics;
- the thermal stresses analyze induced in the welding processes is make on the basis of one deformation thermodynamics (developed with preservation the of the analogy with non-equilibrium thermodynamics processes) by which the temperature

dependences are introduced by means of the densities, and the stresses tensor is substituted with one tensor that represent the lattice anisotropy;

• the thermal stresses determination will implies the writing of the macroscopic potential function and the Navier-Stokes analogous of this.

REFERENCES

1. Agop, M., Mirea, C., Aspecte teoretice asupra stabilității interfeței solid-lichid la încărcarea prin sudare cu arc electric. Metalurgia, nr. 7, 2005, p. 47-56.

2. Agop, M., Mirea, C., Mazilu, N., Asupra unei termodinamici a deformației prin analogie cu termodinamica proceselor de neechilibru. I: Fundamente teoretice. Metalurgia, 2007 (în curs de publicare).

3. Agop, M., Mirea, C., Mazilu, N., Asupra unei termodinamici a deformației prin analogie cu termodinamica proceselor de neechilibru. II: Construcția funcției de potențial şi analogul Navier-Stokes al mecanicii cuantice. Metalurgia, 2007 (în curs de publicare).

4. Agop, M., Mirea, C., Mazilu, N., Asupra unei termodinamici a deformației prin analogie cu termodinamica proceselor de neechilibru. III: Transferul energiei către termostat şi corespondența mersului la întâmplare cu potențialul Bohm. Metalurgia, 2007 (în curs de publicare).

5. Bohm, D., Phisycal Revue, vol. 85 (2), 1952, p. 166.

6. Cernikov, N., A., Preprint Dubna, PZ-9714 şi PY-9631.

7. Flemings, M., C., Solidification Processing. McGraw, New York, 1974.

8. Harvey, R., J., Physical Revue, vol. 152, 1966, p. 1115.

9. Kurz, W., Fisher, D., J., Fundamentals of Solidification. Trans. Tech. Publications, Aederrmannsdorf, Switzerland, 1986.

10. Landan, Lifschitz, E., M., Mecanique des fluids. Moscova, 1971.

11. Messiah, A., J. Mecanica cuantica. Vol. I, Editura Ştiințifică, Bucureşti, 1973.

12. Socs, E., Modele discrete şi continue ale solidelor. Editura Ştiințifică, Bucureşti, 1974.

13. Truesdell, C., Noll, N., The Non-Linear Theories of Mechanics. Handbook der Physik, ed. S. Flugge, Springer Verlag, 1963

Received March 15, 2007

Technical University "Gh. Asachi" Iassy

Rezumat. În acord cu rezultatele unor cercetări teoretice anterioare, sunt prezentate unele aspecte teoretice ale problemelor legate de solidificarea metalului depus în procesele de sudare cu arc electric. Acestea vizează stabilitatea interfeței solid-lichid, determinarea condițiilor de stabilitate în cazul topiturii subrăcite şi determinarea tensiunilor termice induse în procesul de depunere.

Pentru determinarea condițiilor de stabilitate ale interfeței solid-lichid s-a utilizat un sistem de ecuații cuplate pentru concentrații şi temperaturi, obținându-se condițiile de stabilitate în aproximație liniară. În particular, pentru cazul topiturilor subrăcite, rezultă că stabilitatea interfeței depinde atât de caracteristicile plasmei de descărcare cât şi de caracteristicile interfeței, ceea ce în particular implică matricea (metalul de bază). Influența plasmei de descărcare se regăseşte prin restricțiile impuse, restricții care s-au introdus prin asimilarea vitezei de solidificare cu viteza de difuzie a electronilor plasmei din coloana arcului electric de sudare.

Pentru determinarea tensiunilor termice s-a elaborat un mecanism complex, prin care s-a dezvoltat o termodinamică a deformațiilor şi construcția unei funcții de potențial macroscopic, iar pe baza mecanicii cuantice analogul Navier-Stokes al acesteia.

BULETINUL INSTITUTULUI POLITEHNIC DIN IAŞI
Tomul LIII (LVII), Fasc. 2, 2007
Secţia
ŞTIINŢA ŞI INGINERIA MATERIALELOR

MECHANICAL CHARACTERISTICS OF ALUMINUM ALLOYS PREDICTION BY ELECTRICAL CONDUCTIVITY AND HARDNESS MEASUREMENTS

BY

ADRIAN COMANICI

ABSTRACT: *In this paper we propose a no destructible method for mechanical resistance characteristic evaluation and prediction for wrought Al alloys. Based on conductivity and hardness measurement we can evaluate the heat treatment of aluminum different specimens.*

KEYWORDS**:** aluminum, no destructible method, mechanical resistance characteristics

INTRODUCTION

One of the uses of eddy current instruments is for the measurement of electrical conductivity. The value of the electrical conductivity of a metal depends on several factors, such as its chemical composition and the stress state of its crystalline structure. Therefore, electrical conductivity information can be used for sorting metals, checking for proper heat treatment, and inspecting for heat damage. The technique usually involves nulling an absolute probe in air and placing the probe in contact with the sample surface. For nonmagnetic materials, the change in impedance of the coil can be correlated directly to the conductivity of the material. The technique can be used to easily sort magnetic materials from nonmagnetic materials but it is difficult to separate the conductivity effects from the magnetic permeability effects, so conductivity measurements are limited to nonmagnetic materials. It is important to control factors that can affect the results such as the inspection temperature and the part geometry. Conductivity changes with temperature so measurements should be made at a constant temperature and adjustments made for temperature variations when necessary. The thickness of the specimen should generally be greater than three standard depths of penetration. This is so the eddy currents at the back surface of the sample are sufficiently weaker than the variations in the specimen thickness that are not seen in the measurements. Generally large pancake type, surface probes are used to get a value for a relatively large sample area. The instrument is usually setup such that a ferromagnetic material produces a response that is nearly vertical. Then, all conductive but nonmagnetic materials will produce a trace that moves down and to the right as the probe is moved toward the surface. Think back to the discussion on the impedance plane and these type of responses make sense. Remember that inductive reactance changes are plotted along the y-axis and resistance changes are plotted in the x-axis.

Since ferromagnetic materials will concentrate the magnetic field produced by a coil, the inductive reactance of the coil will increase. The effects on the signal from the magnetic permeability overshadow the effects from conductivity since they are so much stronger. When the probe is brought near a conductive but nonmagnetic material, the coil's inductive reactance goes down since the magnetic field from the eddy currents opposes the magnetic field of the coil. The resistance in the coil increases since it takes some of the coil's energy to generate the eddy currents and this appears as additional resistance in the circuit. As the conductivity of the materials being tested increases, the resistance losses will be less and the inductive reactance changes will be greater. To sort materials using an impedance plane device, the signal from the unknown sample must be compared to a signal from a variety of reference standards. However, there are devices available that can be calibrated to produce a value for electrical conductivity which can then be compared to published values of electrical conductivity in MS/m or percent IACS (International Annealed Copper Standard). Please be aware that the conductivity of a particular material can vary significantly with slight variations in the chemical composition and, thus, a conductivity range is generally provided for a material. The conductivity range for one material may overlap with the range of a second material of interest, so conductivity alone can not always be used to sort materials. The electrical conductivity values for a variety of materials can be found in the material properties reference tables. Electrical Impedance (Z), is the total opposition that a circuit presents to alternating current. Impedance is measured in ohms and may include resistance (R), inductive reactance (XL), and capacitive reactance (XC). However, the total impedance is not simply the algebraic sum of the resistance, inductive reactance, and capacitive reactance. Since the inductive reactance and capacitive reactance are 90 degrees out of phase with the resistance and, therefore, their maximum values occur at different times, vector addition must be used to calculate impedance. The relationship between impedance and its individual components (resistance and inductive reactance) can be represented using a vector as shown below. The amplitude of the resistance component is shown by a vector along the x-axis and the amplitude of the inductive reactance is shown by a vector along the y-axis. The amplitude of the the impedance is shown by a vector that stretches from zero to a point that represents both the resistance value in the x-direction and the inductive reactance in the y-direction. Eddy current instruments with impedance plane displays present information in this format.

The impedance in a circuit with resistance and inductive reactance can be calculated using the following equation. If capacitive reactance was present in the circuit, its value would be added to the inductance term before squaring.

The impedance in a circuit with resistance and inductive reactance can be calculated using the following equation. If capacitive reactance was present in the circuit, its value would be added to the inductance term before squaring.

$$Z = \sqrt{\left(XL^2 + R^2\right)} \tag{1}$$

The phase angle of the circuit can be calculated using the equation below. If capacitive reactance was present in the circuit, its value would be subtracted from the inductive reactance term.

$$Tan\phi = \frac{X_L}{R} \tag{2}$$

Impedance and Ohm's Law. When there is inductive reactance or capacitive reactance also present in the circuit, Ohm's Law must be written to include the total impedance in the circuit. Therefore, Ohm's law becomes I = V / Z
Ohm's law now simply states that the current (I), in amperes, is proportional to the voltage (V), in volts, divided by the impedance (Z), in ohms and in form (1).
Standard Depth of Penetration must be written by formula:

$$\delta \approx \frac{1}{\sqrt{\pi f \mu \sigma}} \tag{3}$$

where:
δ = Standard Depth of Penetration (mm); f = Test Frequency (Hz); Q = Magnetic Permeability (H/mm); Q = Electrical Conductivity (% IACS).

HARDNESS MEASUREMENTS

The internal structural changes described previously produce substantial changes in the mechanical properties of aluminum and its alloys. Tensile properties are among those most affected. Work-hardening curves for several non-heat-treatable alloys illustrate the increase in strength that accompanies cold work. This increase is obtained at the expense of ductility, as measured by the per cent elongation in the tensile test and by reduced formability in operations such as bending and drawing. Cold working also increases shear strength, creep strength at low temperatures, and smooth-specimen fatigue strength. It has little effect on notch fatigue strength, but increases notch tensile strength in about the same proportion as smooth-specimen tensile strength. Limited use is made of strain hardening to increase the strength of heat treatable alloys. The principal applications are in extruded and drawn products, such as wire, rod, and tube. Heat treated Al-Mg-Si alloys are employed extensively in such products, which are sometimes drawn after heat treatment to increase strength and improve surface finish. The low ductility and poor workability of other artificially aged, heat treatable alloys have restricted cold working as a procedure for obtaining higher strengths. In the aluminum-copper alloys, however, small amounts of cold work are employed after solution heat treatment to obtain increased response during artificial aging. The effect of strain hardening on the electrical conductivity of aluminum is small and generally less than that of alloying or of the heat treatments used for many aluminum alloys. The electrical conductivity of conductor-grade aluminum is decreased from a typical value of 63% IACS in the annealed condition to 62.5% in the strain-hardened and temper.

EDDY CURRENT INSTRUMENT

Eddy current instruments can be purchased in a large variety of configurations. Both analog and digital instruments are available. Instruments are commonly classified by the type of display used to present the data. The common display types are analog meter, digital readout, impedance plane and time versus signal amplitude. Some instruments are capable of presenting data in several display formats. The most basic

eddy current testing instrument consists of an alternating current source, a coil of wire connected to this source, and a voltmeter to measure the voltage change across the coil. An ammeter could also be used to measure the current change in the circuit instead of using the voltmeter. In eddy current probes and cables, it is commonly stated that capacitance is negligible. However, even circuits not containing discreet components for resistance, capacitance, and inductance can still exhibit their effects. When two conductors are placed side by side, there is always some capacitance between them. Thus, when many turns of wire are placed close together in a coil, a certain amount of stray capacitance is produced. Additionally, the cable used to interconnect pieces of electronic equipment or equipment to probes, often has some capacitance, as well as, inductance. This stray capacitance is usually very small and in most cases has no significant effect. However, they are not negligible in sensitive circuits and at high frequencies they become quite important.

Figure. 1. Conductivity Meters and Standard References Blocks

Figure 2. AutoSigma 3000 Conductivity Meter

If the eddy current circuit is balanced in air and then placed on a piece of aluminum, the resistance component will increase (eddy currents are being generated in the aluminum and this takes energy away from the coil, which shows up as resistance) and the inductive reactance of the coil decreases (the magnetic field created by the eddy currents opposes the coil's magnetic field and the net effect is a weaker magnetic field to produce inductance), see fig.3. If a crack is present in the material, fewer eddy currents will be able to form and the resistance will go back down and the inductive reactance will go back up. Changes in conductivity will cause the eddy current signal to change in a different way. Analog instruments see fig.1 are the simplest of the instruments available for eddy current inspections. They are used for crack detection, corrosion inspection, or conductivity testing. These types of instruments contain a simple bridge circuit, which compares a balancing load to that measured on the test specimen. If any changes in the test specimen occur which deviate from normal you will see a movement on the instruments meter. Based on this principle is the construct of digital instruments see fig.2.

EXPERIMENTAL

With some materials, such as solution heat treatable aluminum alloys, conductivity measurements are often made verifying that parts and materials have received the proper heat treatment. High purity aluminum is soft and ductile, and gains strength and hardness with the addition of alloying elements. A few such aluminum alloys are the 2000 series (2014, 2024, etc.), 6000 series (6061, 6063, etc.), and 7000 series (7050, 7075, etc.). The 2xxx series aluminum alloys have copper, the 6xxx series have magnesium, and the 7xxx have zinc as their major alloying elements.

Heat treatment of aluminum alloys is accomplished in two phases - solution heat treatment and then aging. In the solution heat treatment step, the alloys are heated to an elevated temperature to dissolve the alloying elements into solution. The metal is then rapidly cooled or quenched to "freeze" the atoms of the alloying elements in the lattice structure of the aluminum. This distorts and stresses the structure, making electron movement more difficult, thereby decreasing the electrical conductivity. In this condition, the alloys are still relatively soft but start to gain strength as the alloying elements begin to precipitate out of solution to form extremely small particles that impede the movement of dislocations within the material. The formation of the precipitates can be controlled for many alloys by heating and holding the material at an elevated temperature for a period of time (artificial aging). As the alloying elements precipitate out of solid solution, the conductivity of the material gradually increases. By controlling the amount of precipitated particles within the aluminum, the properties can be controlled to produce peak strength or some combinations of strength and corrosion resistance. Sometimes, the material must be annealed or put into the softest, most ductile condition possible in order to perform forming operations. Annealing allows all of the alloying elements to precipitate out of solution to form a course, widely spaced precipitate.

The electrical conductivity is greatest when the material is in the annealed condition. Since solution heat-treated and aged materials are stronger, components can be made using less material. A lighter or more compact design is often of great importance to the designer and well worth the cost of the heat treating process. However, think of the consequences that could arise if a component that was supposed to be solution heat-treated and aged somehow left the manufacturing facility and was put into service unheat-treated or annealed. This is a real possibility since heat-treated aluminum parts look exactly like unheat-treated parts. Consider 2024 aluminum as an example. Select tensile properties and its electrical conductivity for various heat treatment conditions are given in Table 1.

Table 1. Experimental values of electrical conductivity of Al alloys

Heat Treatment Condition	Ultimate Strength	Yield Strength	Electrical Conductivity
Annealed (O)	26 ksi (180 MPa)	11 ksi (75 MPa)	50 % IACS
Solution Heat Treated and Naturally Aged (T42)	64 ksi (440 MPa)	42 ksi (290 MPa)	30 % IACS
Solution Heat Treated, Coldworked and Artificially Aged (T861)	70 ksi (485 MPa)	66 ksi (455 MPa)	38 % IACS

It can be seen that the yield strength for the material is 42 kilopounds/square inch (ksi) (290 MPa) in the solution heat-treated and naturally aged condition (T42 condition). The yield strength can be increased to 66 ksi (455 MPa) when coldworked and artificially aged (T861 condition). But in the annealed condition, the yield strength is reduced to 11 ksi (75 MPa). If an annealed part were accidentally used where a part in the T42 or T861 was intended, it would likely fail prematurely. However, a quick check of the conductivity using an eddy current instrument of all parts prior to shipping would prevent this from occurring.

Table 2. Properties for Alclad 2024 Aluminum (experimental values)

Material Clad	H. T.	Conductivity %IACS	Hardness HV
2024	T0	48.20	70
2024	T3	31.75	100
2024	T351	28	123
2024	T4	30	111
2024	T42	31.75	135
2024	T6	40.00	117
2024	T72	44.00	105
2024	T8	42.00	130
2024	T86	39.00	159

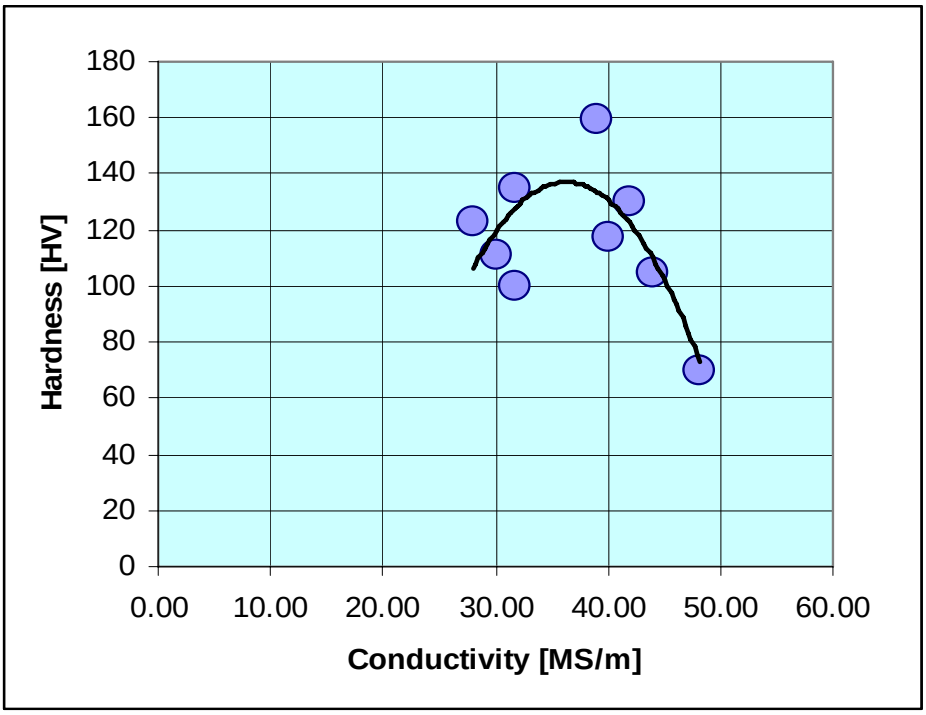

Figure 3. Graphic aspects results

Electric resistivity is slightly higher than in the ternary aluminum-magnesium-silicon alloys and of the order of 3,0-3,2 x 10-8Ωm (50-55% IACS) for alloys with 0.4-0.5% Mg and a slight excess of silicon, in the artificially aged condition. Higher magnesium, manganese and copper reduce this conductivity, which is also lower in the naturally

aged temper, but may reach values of 55-60% IACS in annealed material. Alloys with lower magnesium and silicon contents have better conductivity but lower strengths. Increasing the iron or the silicon from 0.2 to 2% decreases the conductivity by some 10%. Chromium, manganese and especially titanium, vanadium and zirconium markedly reduce the electric conductivity. Additions of boron, which precipitates these elements as borides, are used to remove them in conductor material

CONCLUSIONS

Stress relief. The inverse relation between propagation energy and yield stress is to be expected; as the yield stress is increased, the extent to which the stress concentration ahead of a crack or notch may be relaxed by plastic deformation is decreased. It is, therefore, one of these processes which is affecting the observed toughness. It has been postulated that the mechanical properties of Al-Zn-Mg based alloys should be sensitive to matrix microstructures. G.P. zones, being coherent, are sheared by dislocations and this process favors the formation of coplanar dislocation arrays and pile-ups at boundaries. Although η' plates are thought to be partially coherent and hence should permit considerable shearing, the deformation of η' dispersions has been shown to occur in bands rather than by coplanar flow. Stress concentrations at boundaries should hence be greater for G.P. zone dispersions than for η' dispersions. It is well established that one major variable is strength, since as strength is increased there is an accompanying decrease in toughness. There is also evidence that fracture is sensitive to heat treatment, and particularly that the toughness associated with an underaged structure is superior to that of an overaged structure having the same yield stress. However, considerable use is being made commercially of over-aged tempers, particularly two-step overaged tempers such as T73; although these were developed primarily to improve stress-corrosion resistance, alloys thus aged have significantly greater toughness than those aged to maximum strength. The published information is hence somewhat confusing and little attempt has been made to relate these effects to microstructural differences. Knowing the effect of mechanical deformation on properties, more efficient stress relieving procedures can be developed. Stress relief of hand forgings by cold deformation is, of course, quite straightforward. After being solution treated and quenched, the cold forging is placed between cold flat dies, and reduced in thickness by the desired amount. It is then aged, which results in the TXX52 temper. With hand forgings, it is relatively easy to control the extent of reduction, thus protecting the final properties in the 7000 series alloys. One practice would be to aim for 1 to 2% deformation in alloys like 7075 or 7049. A true 0.5% reduction is probably just as effective as some greater percentage in minimizing distortion. In alloys like 2024, where the cold deformation is also needed to achieve desired strengths, higher percentages of reduction are naturally used. In die forgings, because of widely varying section sizes and the more precise requirements for final forging dimensions, stress relief by cold deformation becomes more complicated.

Chemical composition. Obvious gains in toughness can be obtained by reducing Fe, Si and other trace elements. Limits to such reductions are set by cost and availability of high purity materials. Alternatively, minor benefits can be derived from achieving a more uniform distribution of whatever second phase particles are present. The reduction of Fe and Si should be treated with some caution since it may also affect the

ISSN 1453-1690